NCC-based SERS Substrate: Fundamentals, Preparation and Applications

Segun Ajibola Ogundare

2018

Dissertation submitted in fulfilment of the academic requirements for the degree of Doctor of Philosophy

School of Chemistry & Physics, College of Agriculture, Engineering and Science, University of KwaZulu-Natal, Durban

As the candidate's supervisor I have approved this dissertation for submission.

[redacted]

28 November 2018

Prof. W. E. van Zyl

Date

Abstract

This study reports the isolation and characterization of nanocrystalline cellulose (NCC) produced from discarded cigarette filters (DCF). The DCF were processed into cellulose *via* ethanolic extraction, hypochlorite bleaching, alkaline deacetylation, and then converted into NCC by sulphuric acid hydrolysis. The morphological structures of the isolated NCC, established with TEM, showed that the nanocrystals were needle-like with length in the range of between 62–258 nm. FEGSEM showed the morphological transition of the micro-sized DCF to a self-assembled NCC, while EDX revealed the presence of Ti (as TiO_2) in DCF, which was retained in the NCC. A NCC sample that was freeze-dried showed a specific surface area of ~8 m^2/g. The crystallinity of the NCC film and the freeze-dried samples were ~97% and ~94%, respectively. Crystallite sizes of the freeze-dried (8.4 nm) and film (7.6 nm) samples correlated with the mean width (8.3 nm) of the NCC, observed with the TEM.

The isolated NCC was used in the dual role as a reducing- and stabilizing agent in the formation of silver nanoparticles (AgNPs). By this method, a notable size variation of the synthesized AgNPs was found over the pH range of between 5–10, ranging from 4.61 nm at pH = 9 and increasing to 19.93 nm diameter at pH = 5. The size and yield of the AgNPs were also affected by the reaction time and concentration. The spherically shaped AgNPs induced a localized surface plasmon resonance (LSPR) at around 416 nm. The Ag content in the dry AgNPs was 81.9 wt%, which correlated with 82.1 wt% mass left at 600 ºC. Further analysis showed that the dry AgNPs were macroporous with reduced surface area and porosity upon calcination. The sensitivity of the AgNPs showed excellent surface-enhanced Raman scattering (SERS) of riboflavin. The limit-of-detection (LOD) for riboflavin, based on a signal-to-background ratio of 3:1, was found to be 3×10^{-7} M. The intensities of SERS signals increased with increase in concentration.

In addition, clusters of AgNPs were synthesized with NCC isolated from Whatman cellulose filter paper, which behaved as a dual reducing- and stabilizing agent, and Stöber silica (SiO_2) provided a suitable anchoring surface. The synthesized nanocomposite (AgNPs/SiO_2/NCC) was evaluated as a substrate for surface-enhanced Raman scattering (SERS) of malachite green (MG) and compared with AgNPs/NCC nanocomposite. The FTIR spectra of both nanocomposites showed a weak carbonyl band (1754 cm^{-1}), indicating partial oxidation of the NCC. The UV-vis spectrum of AgNPs/NCC showed a narrow peak at 412 nm, characteristic

of LSPR of monodispersed AgNPs. However, this peak was broad with a shoulder at 490 nm in the spectrum of the AgNPs/SiO_2/NCC, which indicated clustering of the plasmonic nanoparticles. TEM micrographs showed that the plasmonic nanoparticles were monodispersed with a mean diameter of 19.5 nm in AgNPs/NCC, while they aggregated into clusters on SiO_2 in AgNPs/SiO_2/NCC resulting in an approximately 20 nm increase in the mean diameter of the SiO_2. The SEM/EDX spectra and XRD diffractograms of the nanocomposites showed Ag as the predominant element. The SERS performance of the nanocomposites was evaluated by using MG as a probe, showed AgNPs/SiO_2/NCC as a superior substrate with significant improvement in intensities of Raman peaks of MG and high sensitivity as the LOD was 0.9 nm, while AgNPs/NCC showed a LOD of 5.2 nm, based on a signal-to-background ratio of 3:1. This result underscores the huge contribution of SERS "hot spots" as AgNPs assembled into clusters in contrast to monodispersed AgNPs in the absence of SiO_2.

Declarations

Declaration 1: Plagiarism

I, Segun Ajibola Ogundare, declare that:

1. The research reported in this thesis, except where otherwise indicated, is my original research.
2. This thesis has not been submitted for any degree or examination at any other university.
3. This thesis does not contain other persons' data, pictures, graphs or other information, unless specifically acknowledged as being sourced from other persons.
4. This thesis does not contain other persons' writing, unless specifically acknowledged as being sourced from other researchers. Where other written sources have been quoted, then:
    a. Their words have been re-written but the general information attributed to them has been referenced
    b. Where their exact words have been used, then their writing has been placed in italics and inside quotation marks, and referenced.
5. This thesis does not contain text, graphics or tables copied and pasted from the Internet, unless specifically acknowledged, and the source being detailed in the thesis and in the References sections.

Signed



26th November, 2018

Segun Ajibola Ogundare

Declaration 2: Publications

DETAILS OF CONTRIBUTION OF PUBLICATIONS that form part and/or include research presented in this thesis (include publications in preparation, submitted, *in press* and published with details of the contributions of each author to the experimental work and writing of each publication).

Publication 1 (published)

Segun A. Ogundare, Vashen Moodley and Werner E. van Zyl. **Nanocrystalline Cellulose Isolated from Discarded Cigarette Filters.** *Carbohydr. Polym.* **2017**, *175*, 273-281.

Contributions: I synthesized, carried out most of the characterizations and wrote the initial draft of the manuscript and carried out subsequent modifications towards publication of the paper. Vashen Moodley carried out certain part of the characterizations.

Publication 2 (published)

Segun A. Ogundare and Werner E. van Zyl. **Nanocrystalline Cellulose as Reducing- and Stabilizing Agent in the Synthesis of Silver Nanoparticles: Application as a Surface-Enhanced Raman Scattering (SERS) Substrate**. *Surfaces and Interfaces* **2018**, *13*, 1-10.

Contributions: I carried out the synthesis and characterisation of the nanocomposites. I prepared and modified the draft through to publication.

Publication 3 (submitted)

Segun A. Ogundare and Werner E. van Zyl. **A review of cellulose-based substrates for SERS: fundamentals, design Principles, applications.** Manuscript submitted to *Cellulose* (The submission ID is: CELS-D-19-00139).

Contributions: I carried out the collation of the all the literature cited, prepared and modified the draft through to submission of the paper for publication.

Publication 4 (submitted)

Segun A. Ogundare and Werner E. van Zyl. **Amplification of SERS "hot spots" by silica clustering in a silver-nanoparticle/ nanocrystalline cellulose sensor applied in malachite green detection.** Manuscript submitted to *Colloids and Surfaces A: Physicochemical and Engineering Aspects.* (Ms. Ref. No.: COLSUA-D-19-00280)

Contributions: I carried out the synthesis and characterisation of the nanocomposites. I prepared and modified the draft towards publication of the paper.

Signed:  26th November, 2018

Segun Ajibola Ogundare

Declaration 3: Conference and workshop proceedings

1. Segun A. Ogundare, Vashen Moodley and Werner E. van Zyl. **Nanocrystalline Cellulose Isolated from Discarded Cigarette Filters. Physicochemical Properties of Nanocrystalline Cellulose Isolated from Recycled Cigarette Filters *via* a "Green" Approach.** (Poster presented at UKZN Nanotechnology Platform Workshop, Westville Campus, Durban, South Africa, 2016).

2. Segun A. Ogundare and Werner E. van Zyl. **NCC Isolated from Discarded Cigarette Filters: A Template for Green Synthesis of Silver Nanoparticles as a Sers Substrate**. (Oral presentation at Research Day UKZN, Westville Campus, Durban, 2017).

3. Segun A. Ogundare and Werner E. van Zyl. **NCC Isolated from Discarded Cigarette Filters: A Template for Green Synthesis of Silver Nanoparticles as a Sers Substrate**. (Poster presentation at Research Day UKZN, Westville Campus, Durban, 2018).

Dedication

To my family

Acknowledgements

- I will like to appreciate the Almighty God for the love, strength and wisdom to complete successfully, this programme.
- My sincere gratitude to Professor Werner van Zyl, for giving me the opportunity to be a part of his research team and for providing the required support and guidance to make this study programme successful.
- I remain indebted to my family especially my wife, Olamide Ogundare, my rare gem, Mofifoluwa Ogundare and my mother, Olatundun Ogundare who have had to endure my long absence during the course of this programme and to my siblings and other relatives who have contributed, in no small measure, towards this programme, I remain grateful.
- I acknowledge the University of Kwazulu-Natal for the opportunity to study for this PhD programme under the Fee remission programme for three years. The entire staff of School of Chemistry and Physics as well as MMU staff are highly appreciated for their kind support always.
- I acknowledge Olabisi Onabanjo University for granting me the study leave to enable me to complete this programme. My sincere gratitude to the entire staff of Chemical Sciences Department, Olabisi Onabanjo University for their moral support and guidance.
- My appreciation to my laboratory colleagues and members of the SUSWEB research group, Sicelo Sithole, Dr. Michael Pillay, Dr. Fezile Potwana, Dr. Vashen Moodley, Dr. Tomilola Ajayi, Dr. Eric Gwaza, Chrisanne Naicker, Lewis Yussuf, Denisha Gounden, Emmanuel Mkumbuzi, Nadia Nirmal, Thaveshan Gounden, Greg Muungani, Serena Naicker and Erick Bakare.
- I am most grateful to the Deeper Life Campus Fellowship (DLCF), UKZN for their prayer and support, and to my Nigerian friends with Dr. Olushola Bodede, Paul Awolade, Amaku James, Ayomide Labulo, Dr. Adeyinka Gbadebo, Ejalonibu Muritala, Abimbola Adeleke, Illiya Yerima and others, I am most grateful for all the love.

List of Figures

Fig. 2.1: Schematic illustrations of (A) chemical enhancement mechanism, (B) electromagnetic enhancement mechanism and (C) plasmonic “hot spot”. 14

Fig. 2.2: Schematic illustration of modified drop cast method of paper-based SERS substrate.. 23

Fig. 2.3: Schematic illustration of *in-situ* fabrication of paper-based SERS substrate and its application.....27

Fig. 2.4: (a) Schematic illustration of laser-induced photothermal formation of metal nanoparticles on silicon, glass and filter paper substrates. Photographic images of metal nanoparticles (Ag (top); Au (down)) formed on silicon (b), glass (c), filter paper (d) and photographic paper (e) with different number of laser shots......29

Fig. 2.5: Coating of Au nanorods stabilized with CTAB on filter paper (A), illustration of H_2O/DCM interface self-assembled Ag nanoparticles on filter paper by immersion (B). 31

Fig. 2.6: (1) Inkjet printing of Ag nanoparticles on paper substrate and schematic illustration of chromatographic separation of analytes in a mixture, (2) screen printing of Au-Ag bimetallic SERS substrate and microfluidic channels on paper. 34

Fig. 2.7: (1) Spray coating of Ag nanoparticles on paper, (2) writing of metal nanoparticles on paper, and (3) Ag nanoparticles coated on paper by brushing.....36

Fig. 2.8: Bioanalytical application of a paper-based SERS substrate in: (1) Oral-cancer diagnostics, (2) Tear screening for Gouty arthritis diagnosis and (3) Pre-natal diseases detection.....40

Fig. 2.9: CA-based SERS substrate fabricated by (A) electrospraying and (B) co-electrospinning techniques.....48

Fig. 2.10: Schematic illustration of NCC-based SERS substrate. 53

Fig. 3.1: ^{1}H NMR (A) and ^{13}C NMR (B) spectra of CA-DCF and DCF run at 60°C in DMSO-d_6. 87

Fig. 3.2: ATR-FTIR spectra of NCC-CF (film and freeze-dried (FD)), Cel-CF and DCF. 89

Fig. 3.3: TEM micrograph (A), and distributions graphs for length (B), width (C) and aspect ratio (D) of NCC-DCF. 90

Fig. 3.4: FEGSEM micrographs of DCF (A), Cel-DCF (B), NCC-DCF freeze dried (C1-C3), film (D1-D3) and ash at 700°C (E1-E3). 92

Fig. 3.5: X-ray diffractograms of NCC-DCF film, freeze-dried (FD), Cel-DCF and DCF.....93

Fig. 3.6: The thermograms (A) and DTA curves (B) of NCC-DCF film, freeze-dried (FD), Cel-DCF and DCF. 95

Fig. 3.7: BET Isotherms of NCC-DCF (freeze-dried (FD) and film samples), Cel-DCF and DCF. 97

Fig. 4.1: Images and absorption spectra of synthesized AgNPs at different; pHs (A1 and A2), time intervals (B1 and B2), concentrations of $AgNO_3$ (C1 and C2) and AgNPs colloid (D1, D2 and D3).....111

Fig. 4.2: TEM micrographs and Size distributions of synthesized AgNPs for; (A) different pH ($AgNO_3$: 0.20 M, time: 15 min.); (B) time interval ($AgNO_3$: 0.10 M, pH 10); (C) concentration (time: 15 min., pH 10). AgNPs colloid TEM and HRTEM. 113

Fig. 4.3: SEM micrographs and EDX spectra of dried AgNPs (A1 and A2) and calcined AgNPs (B1 and B2).....115

Fig. 4.4: FTIR spectra of NCC, dry and calcined AgNPs.....116

Fig. 4.5: XRD difractogram of the dry and calcined AgNPs.....117

Fig. 4.6: BET isotherms (A) and pore size distributions (B) of dry and calcined AgNPs.....118

Fig. 4.7: TGA thermogram (A) and DTA curve (B) of dry and Inset: thermal analysis data. 119

Fig. 4.8: Raman spectra of NCC, NCC-AgNPs, riboflavin (RBF) and SERS spectrum of 5 µM RBF (A), SERS spectra of RBF in concentration range 10–0.00001 µM (B), plots of peaks intensities against concentration (C) and Calibration plot of 1352 cm^{-1}peak intensity against concentration (D). 121

Fig. 5.1: FTIR spectra of NCC, SiO_2, AgNPs/NCC and AgNPs/SiO_2/NCC.....136

Fig. 5.2: Absorption spectra and images (inset) of NCC, SiO_2, AgNPs/NCC and AgNPs/SiO_2/NCC. 137

Fig. 5.3: TEM micrographs of NCC (A), AgNPs/NCC (B), HRTEM micrograph of AgNPs/NCC (C), TEM micrographs SiO_2 (D). AgNPs/SiO_2/NCC (E) and HRTEM micrograph AgNPs/SiO_2/NCC (F) 139

Fig. 5.4: SEM micrographs of dilute NCC dried on glass (A), SiO_2 (B), AgNPs/NCC (C), AgNPs/SiO_2/NCC (D) and dilute AgNPs/SiO_2/NCC dried on glass (E).....140

Fig. 5.5: X-ray diffractograms of NCC, SiO_2, AgNPs/NCC and AgNPs/SiO_2/NCC.....141

Fig. 5.6: The thermograms (A) and DTA curves of NCC, SiO_2, AgNPs/NCC and AgNPs/SiO_2/NCC. 142

Fig. 5.7: SERS spectra of MG on AgNPs/SiO_2/NCC substrate in concentration range 0.001–10000 nM (A) and the corresponding plots of peak intensities against concentration (B). SERS

spectra of MG on AgNPs/NCC substrate in concentration range 0.001–10000 nM (C) and the corresponding plots of peak intensities against concentration (D). Raman spectra of MG, SERS spectra of MG (1000 nM) on the nanocomposites (E) and the calibration plots of 1621 cm^{-1} peak intensity against concentration. 145

Fig. S3.1: ATR-FTIR spectra of SAT-DCF and SAT-LR. LR (Laboratory reagent). 156

Fig. S3.2: FEGSEM micrographs, EDX spectra and mapping of constituent elements of DCF (A1-A3), the obtained cellulose (B1-B3), NCC-DCF freeze-dried (C1-C3), NCC-DCF film (D1-D3) and NCC-DCF ash (E1-E3). 158

Fig. S3.3: Gaussian fit X-ray diffractograms of DCF, the obtained cellulose (Cel-DCF), NCC-DCF freeze-dried (NCC-DCF FD) and film (NCC-DCF Film). 159

Fig. S4.1: Absorption spectra of synthesized AgNPs at different time intervals for pH 5 (B1), pH 6 (B2) pH 7 (B3), pH 8 (B4) and pH 9 (B5). 161

Fig. S4.2: Absorption spectra of synthesized AgNPs at different concentrations for pH 5 (B1), pH 6 (B2) pH 7 (B3), pH 8 (B4) and pH 9 (B5). 162

Fig. S4.3: EDX mapping of elements present in the synthesized dry AgNPs. 163

Fig. S4.4: EDX mapping of elements present in the calcined AgNPs. 163

Fig. S4.5: SEM micrograph, EDX spectrum and mapping of elements present in the AgNPs adsorbed on filter paper. 164

Fig. S4.6: ICP OES calibration for quantification of AgNPs after digestion. 164

Fig. S4.7: Gaussian fits of XRD diffractograms of dry and calcined AgNPs 165

Fig. S4.8: Raman spectra of FP, FP-NCC-AgNPs, FP-riboflavin (RBF) and SERS spectrum of 5 µM RBF (A), SERS spectra of RBF in concentration range 10–0.00001 µM on filter paper

(B), plots of peaks intensities against concentration (C) and Calibration plot of 1352 cm^{-1}peak intensity against concentration (D). 165

Fig. S5.1: Length (A), width (B) and aspect ratio distributions of isolated NCC from filter paper.....166

Fig. S5.2: Size distributions of SiO_2 (A), AgNPs/SiO_2/NCC (B) and AgNPs/NCC (C).....167

Fig. S5.3: Representative HRTEM micrograph of AgNPs/NCC showing lattice fringes. 168

Fig. S5.4: EDX mapping of elements present in AgNPs/NCC composite. 169

Fig. S5.5: EDX mapping of elements present in AgNPs/SiO_2/NCC composite. 170

Fig. S5.6: Gaussian fits of XRD diffractograms of NCC, AgNPs/NCC and AgNPs/SiO_2/NCC. 171

Fig. S5.7: Raman spectra of neat nanocomposites indicating background intensity levels. .171

List of Schemes

Scheme 1.1. Illustration of Cellulose as a Green SERS Substrate: Fundamentals, Design Principles, Applications. 4

Scheme 1.2. Stepwise isolation of NCC-DCF from DCF. 4

Scheme 1.3. Synthesis of AgNPs using NCC isolated from DCF as both reducing- and stabilizing agent and SERS study of riboflavin (RBF). 5

Scheme 1.4. Synthesis of AgNPs clusters using NCC isolated from FP as both reducing- and stabilizing agent in the presence of Stöber silica and SERS study of malachite green (MG). .. 6

Scheme 2.1. Methods of preparing micro- and nanocellulose, and common names associated with the morphology or process. 18

Scheme 3.1. Stepwise isolation of NCC-DCF from DCF 83

Scheme 4.1. Synthesis of AgNPs using NCC isolated from DCF as both reducing and stabilizing agent and SERS application in detection of riboflavin. 109

Scheme 5.1. Graphical illustration of the preparation and application of AgNPs/SiO_2/NCC. 135

List of Tables

Table 3.1. Comparison of thermal analysis data for NCC-DCF (film and freeze-dried), Cel-DCF and DCF. 95

Table 5.1. Comparison of thermal analysis data for NCC, AgNPs/NCC and AgNPs/SiO_2/NCC 142

Table S3.1. Elemental compositions of DCF, Cellulose-DCF and NCC-DCF (freeze-dried (FD), film and ash) from EDX.....159

Table S5.1. A representative weight percent of constituent elements in the nanocomposites 170

List of Abbreviations

AgNPs	Silver Nanoparticles
ATR	Attenuated Total Reflection
BC	Bacterial Cellulose
BNC	Bacterial Nanocellulose
ca.	circa
CNC/ synonymous to **NCC**	Cellulose Nanocrystal/ Nanocrystalline Cellulose
CNW	Cellulose Nanowire
CNF	Cellulose Nanofibrillated
CMF	Cellulose Microfibrillated
DCF	Discarded Cigarette Filters
DMSO	Dimethyl Sulphoxide
EDX	Energy Dispersive X-ray
EtOH	Ethanol
FCC	Face-centered cubic
FP	Filter Paper
FTIR	Fourier Transform Infrared
HRTEM	High Resolution Transmission Electron Microscope
LSPR	Localised Surface Plasmon Resonance
MG	Malachite Green
NC	Nanocellulose
NMR	Nuclear Magnetic Resonance
ppm	parts per million
SEM	Scanning Electron Microscope
SERS	Surface-Enhanced Raman Scattering
SILAR	Successive Ionic Layer Absorption and Reaction
SNC	Spherical Nanocellulose
UV/Vis	Ultra Violet/ Visible

Table of Contents

Abstract ii

Declarations iv

Declaration 1: Plagiarism iv

Declaration 2: Publications v

Declaration 3: Conference and workshop proceedings vi

Dedication vii

Acknowledgements viii

List of Figures ix

List of Schemes xiv

List of Tables xv

List of Abbreviations xvi

Table of Contents xvii

Chapter 1 1

Introduction 1

1.1 Background 1

1.2 Aims and objectives of the study 2

1.3 Overview 3

1.4 Significance of the study 6

1.5 References 7

Chapter 2 10

A review of cellulose as a green SERS substrate: Fundamentals, design principles, applications 10

2.1 Introduction 10

2.2 Fundamentals of the SERS mechanism 12

2.2.1 Charge transfer enhancement mechanism 12
2.2.2. Electromagnetic enhancement mechanism 13
2.3 Cellulose and Nanocellulose 15
2.3.1 Source of cellulose 15
2.3.2 Nanocellulose isolation 16
2.4 Plasmonic SERS substrate design 19
2.5 Contributions of cellulose in SERS substrate design 20
2.5.1 Cellulose paper-based SERS substrate 21
2.5.1.1 Drop casting 21
2.5.1.2 Thermal evaporation 23
2.5.1.3 In-situ coating 24
2.5.1.4 Laser induced photothermal deposition 27
2.5.1.5 Immersion deposition 29
2.5.1.6 Inkjet printing 31
2.5.1.7 Screen printing 33
2.5.1.8 Physical vapor deposition 34
2.5.1.9 Spray Coating 34
2.5.1.10 Pen-on-paper 35
2.5.1.11 Brushing 35
2.6 Applications of paper-based SERS substrate 36
2.6.1 Bioanalysis 36
2.6.2 Water quality assessment 41
2.6.3 Adulteration of illicit drugs 41
2.6.4 Food safety 42
2.6.5 Dye identification in artworks 44
2.7 Other forms of cellulose for SERS substrate design 44
2.7.1 Cellulose fabrics and membranes 45
2.7.2 Surface modified cellulose 46
2.7.3 Cellulose nanofibrils 49
2.7.4 Bacterial cellulose 51
2.7.5 Nanocrystalline cellulose 53
2.8 Conclusions and outlook 54

2.9 References 55

Chapter 3 80

NCC isolated from discarded cigarette filters 80

3.1 Introduction 80

3.2 Experimental 81

3.2.1 Materials 81

3.2.2 Extraction of cellulose from Discarded CF 81

3.2.3 Isolation of NCC-DCF 82

3.3 Characterization 83

3.3.1 ^{1}H and ^{13}C NMR spectroscopy 83

3.3.2 Fourier transform infrared spectroscopy (FTIR) 84

3.3.3 Morphological structure analysis. 84

3.3.4 Powder X-ray diffraction analysis 84

3.3.5 Thermogravimetric analysis (TGA) 85

3.3.6 Specific surface area and porosity measurements 85

3.4 Results and Discussion 86

3.4.1 Nanocrystalline cellulose yield 86

3.4.2 NMR and FTIR Spectroscopies 86

3.4.2.1 NMR Spectroscopy 86

3.4.2.2 ATR-FTIR spectroscopy 88

3.4.3 TEM study 89

3.4.4 FEGSEM and EDX study 90

3.4.5 X-Ray powder diffraction study 92

3.4.6 Thermogravimetric analysis (TGA) and Differential thermal analysis (DTA) 94

3.4.7 BET measurements 96

3.5 Conclusion 97

3.6 References 98

Chapter 4 103

NCC as reducing- and stabilizing agent in the synthesis of silver nanoparticles: Application as a SERS substrate 103

4.1 Introduction 103
4.2 Experimental 105
4.2.1 Materials 105
4.2.2 Isolation of NCC 105
4.2.3 Synthesis of silver nanoparticle 105
4.3 characterization of the synthesized AgNPs 106
4.3.1. UV-vis spectroscopy 106
4.3.2 Microwave digestion and ICP-OES analysis 106
4.3.3 Morphological studies 106
4.3.4 Fourier transform infrared spectroscopy (FTIR) 107
4.3.5 Powder X-ray diffraction analysis 107
4.3.6 Specific surface area and porosity measurements 107
4.3.7 Thermogravimetric analysis (TGA) 108
4.4 SERS spectroscopic study 108
4.5 Results and Discussion 109
4.5.1 Optical study 109
4.5.2 TEM/HRTEM study 112
5.5.3 FEGSEM and EDX study 114
4.5.4 FTIR study 115
4.5.5 Powder XRD study 116
4.5.6 BET study 117
4.5.7 Thermogravimetric and differential thermal analyses (TGA/DTA) 118
4.5.8 Detection of riboflavin via surface enhanced Raman scattering (SERS) 119
4.6 Conclusion 121
4.7 References 123
Chapter 5 128
Silver nanoparticles produced from nanocrystalline cellulose on SiO_2-supports and their application in malachite green detection by SERS 128
5.1 Introduction 128
5.2 EXPERIMENTAL 130
5.2.1 Materials 130

5.2.2 Isolation of NCC 130
5.2.3 Synthesis of silica (SiO_2) 131
5.2.4 Synthesis of AgNPs/SiO_2/NCC composite 131
5.3 Characterization of the synthesized nanomposites 131
5.3.1 UV-vis spectroscopy 131
5.3.2 Zeta potential measurements 131
5.3.3 Microwave digestion and ICP-OES analysis 132
5.3.4 Morphological studies 132
5.3.5 Fourier transform infrared spectroscopy (FTIR) 133
5.3.6 Powder X-ray diffraction analysis 133
5.3.7 Thermogravimetric and differential thermal analyses (TGA/DTA) 133
5.4 SERS spectroscopic study 134
5.5 Results and Discussion 134
5.5.1 Synthesis of nanocomposites 134
5.5.2 FTIR study 135
5.5.3 Optical study 136
5.5.4 Stability study of colloidal solutions of nanocomposites 137
5.5.5 TEM/HRTEM study 138
5.5.6 SEM/EDX study 139
5.5.7 Powder XRD study 140
5.5.8 Thermogravimetric and Differential thermal analyses (TGA/DTA) study 141
5.5.9 Detection of malachite green (MG) via surface-enhanced Raman scattering (SERS) 143
5.6 Conclusion 145
5.7 References 146
Chapter 6 154
Conclusions and future work 154
6.1 Conclusions 154
6.2 Future work 155
Appendices 156

Appendix A: Supplementary information to Chapter 3 156

Appendix B: Supplementary information to Chapter 4 161

Appendix C: Supplementary information to Chapter 5 166

Chapter 1

Introduction

1.1 Background

Cellulose, especially in its nanocrystalline form, has attracted huge research interest in recent time. This is due to its diverse and ever-increasing applications in medicine (drug delivery, microfluidic diagnostic devices, biosensors, cellular bioimaging, vascular grafting, medical implantation, tissue engineering nanoscaffolds and nanosponges), electronics (flexible transistors, organic light-emitting diodes (OLED), high performance loud speakers, printed antenna and radiofrequency identification devices (RFID)). In addition to these applications are: sustainable energy (high performance solar cell, dye sensitized solar cell (DSSC), batteries, electrochemical- and super-capacitors,), water decontamination and bio-based antimicrobial food packaging, which have been extensively reviewed.[1-9] Being an abundant polysaccharide in nature, coupled with its sustainability and environmental friendliness, it has the potential to replace most petroleum-based polymers that are non-biodegradable once modified to suit the required needs. The capacity of cellulose to function efficiently in numerous applications is strongly dependent on its remarkable properties, which include: biocompatibility, biodegradability, relatively high strength, stiffness, specific surface area, low toxicity and density some of which vary with cellulose hierarchical structural dimension (macro-, micro-, and nano-fibrilated cellulose) and crystallinity (amorphous and crystalline cellulose).[2-3, 10-11] With increasing emerging applications, necessitate better understanding of the variations between cellulose morphology and properties.[1, 12]

The advent of nanotechnology has brought significant advancement in the study of nanocrystalline cellulose (NCC): a form of cellulose with nanoscale dimension and high degree of crystallinity, which provides the basis for the unique properties. On isolation, NCC showed improvement in virtually all properties when compared to other forms of cellulose and this has resulted in a flurry of research in the isolation and characterization of this nanomaterial. NCC is produced from different cellulose sources, which include, but not limited to, recycled cellulosic man-made materials (waste tissue paper[13], old corrugated container[14] and old newspaper[15-16]) and agricultural wastes[17-21] in order to serve as alternative to the conventional sources[22-23] and to minimize the cost of production towards making NCC more accessible at affordable cost.

Most applications of NCC involve the chemical interaction of its reactive surface hydroxyl groups. The hydroxyl groups facilitate the use of NCC and other related forms of cellulose as alternative green stabilizing and/or reducing agents in the synthesis of Ag, Au, Pt, Pd and Cu nanoparticles.[24-27] In principle, NCC prevents the aggregation of such nanoparticles, leading to the enhancement of their catalytic performance,[28-29] antimicrobial activities[30-31] and improved sensitivity when employed as an analytical tool in the detection of analytes *via* surface enhanced Raman spectroscopy (SERS).[32-33] The rich hydroxyl groups have also enabled the grafting and formation of NCC with other agents, thereby leading to the formation of biopolymer grafts and composites with improved electrical, optical and mechanical properties, which have found applications in advanced medical, electronic and sustainable energy studies. Among these materials, are: NCC/SiO_2 composites in the production of materials with photonic properties[8] and NCC/ZnO composites used in the production of materials with UV-blocking properties and photocatalytic activities.[34] Similarly, in medicine, NCC grafted to peptide has been employed for the detection of human neutrophil elastase, NCC labelled with fluorescein isothiocyanate and grafted with folic acid was used in the detection of tumour cells in human and rat brains, while NCC/hydroxyapatite composite has been used in bone replacement.[3] The potential applications of NCC are enormous and highly sustainable, making it an evergreen nanomaterial.

1.2 Aims and objectives of the study

As a contribution to the recent research on the isolation of NCC from recycled materials and its aforementioned applications, this thesis focuses on the isolation of NCC from discarded cigarette filters (DCF) and Whatman® cellulose filter paper (FP) by using acid hydrolysis. The isolated NCC-DCF were employed as reducing- and stabilizing agent in the synthesis of silver nanoparticles (AgNPs), which were used in the detection of riboflavin (vitamin B2) *via* surface enhanced Raman spectroscopy (SERS). NCC-FPs were used as reducing- and stabilizing agent in synthesis of AgNPs clusters on silica support. The synthesized nanoclusters were used as SERS substrate for the detection of malachite green.

The research objectives of this thesis are:

- Provision of a comprehensive literature review on the use of cellulose-based materials in the design of SERS substrates and applications.
- Isolation of NCC from DCF and FP *via* acid hydrolysis by using sulphuric acid as catalyst.

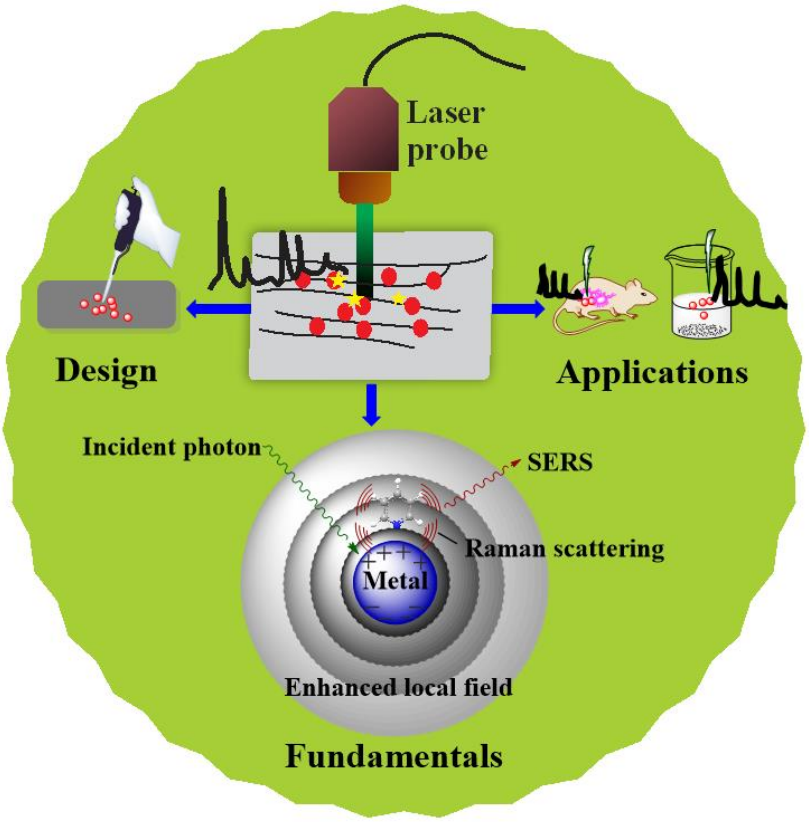
- Characterization of NCC isolated with microscopic techniques (TEM, HRTEM and SEM/EDX), spectroscopic techniques NMR (^{1}H and ^{13}C) and FTIR, powder X-ray diffraction technique, thermogravimetric and differential thermal analyses (TGA/DTA), specific surface area and porosity analyses (BET measurement).
- Synthesis of AgNPs by using the isolated NCC from DCF as reducing- and stabilizing agent.
- Characterization of the synthesized AgNPs using TEM, HRTEM, SEM/EDX, spectroscopic techniques such as: UV-vis and FTIR, powder X-ray diffraction technique, thermogravimetric and differential thermal analyses (TGA/DTA), inductive coupled plasma optical emission spectrometry (ICP-OES), specific surface area and porosity analyses (BET measurement).
- Detection of riboflavin by using synthesized AgNPs/NCC above as a SERS substrate.
- Synthesis of AgNPs clusters by using the isolated NCC from FP as reducing- and stabilizing agent and SiO_2 as support for the clusters.
- Characterization of the synthesized AgNPs clusters by using TEM, HRTEM, SEM/EDX, spectroscopic techniques UV-vis and FTIR, powder X-ray diffraction technique, thermogravimetric and differential thermal analyses (TGA/DTA), inductive coupled plasma optical emission spectrometry (ICP-OES) and zeta potential analyzer.
- Detection of malachite green by using the synthesized AgNPs/SiO_2/NCC above as a SERS substrate in comparison with AgNPs/NCC synthesized without SiO_2.

1.3 Overview

This thesis contains 6 chapters and a brief description of each chapter is as follows:

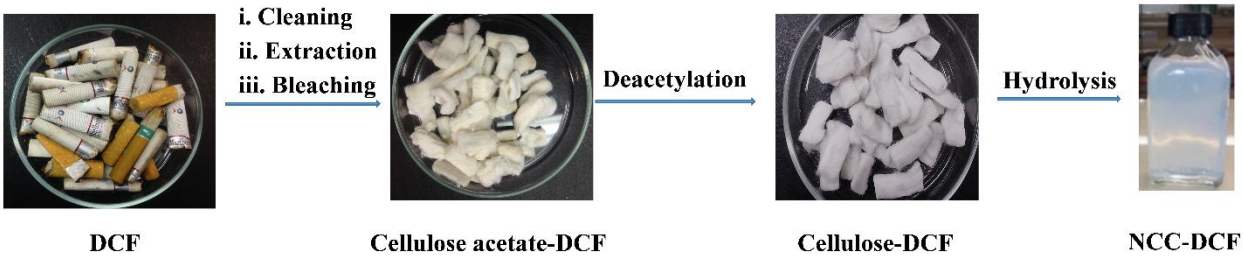
Chapter 1: Background on cellulose, its unique properties and numerous applications. This chapter also includes the aims and objectives of the thesis as well as the scope and coverage of the thesis.

Chapter 2: This chapter contains a comprehensive review on the fundamentals of cellulose and its various morphological forms, description of surface-enhanced Raman scattering (SERS) mechanisms, the design of cellulose-based SERS substrates and their applications.



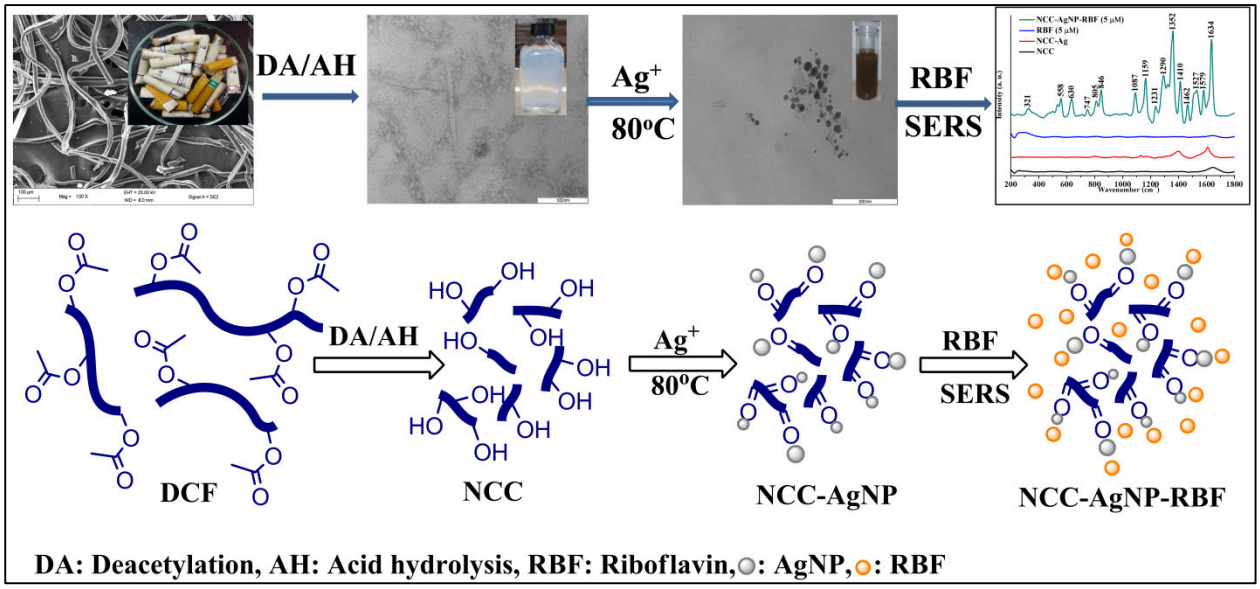
Scheme 1.1. Illustration of Cellulose as a Green SERS Substrate: Fundamentals, Design Principles, Applications.

Chapter 3: This chapter includes the isolation and characterization of NCC from DCF. DCF were collected and processed into cellulose via ethanolic extraction, hypochlorite bleaching and alkaline deacetylation and NCCs were isolated from the cellulose-DCF obtained by acid hydrolysis, as summarized in Scheme 1.2. The cellulose acetate, obtained cellulose-DCF and the isolated NCC-DCF as well as the by-product of deacetylation ($CH_3COONa \cdot 3H_2O$) were fully characterized. The study showed how DCF, an environmental pollutant, could be transformed into a useful and environmentally-friendly nanomaterial (NCC), in order to mitigate its hazardous environmental impact at minimal cost.



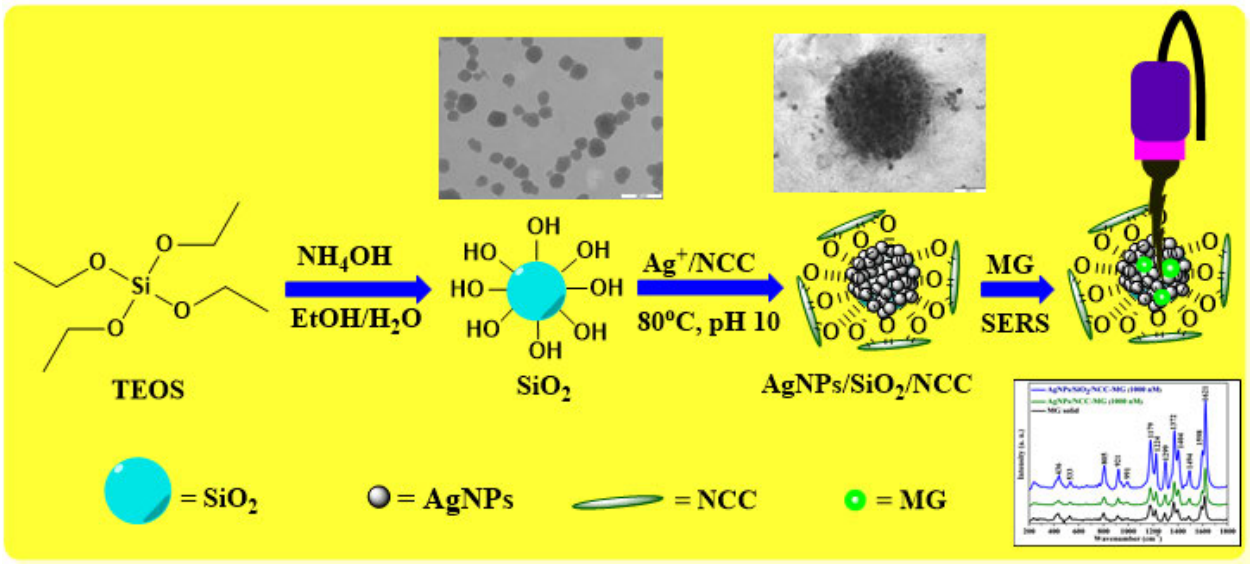
Scheme 1.2. Stepwise isolation of NCC-DCF from DCF.

Chapter 4: This chapter describes NCC-DCF as a template for green synthesis of AgNP used as a SERS substrate for the detection of riboflavin. Silver nanoparticles (AgNPs) were synthesized by using NCC-DCF isolated from DCF as a reducing- and stabilizing agent over a pH range of between 5–10 at 80 ºC for different durations (15–75 minutes). The synthesized AgNPs used in surface enhanced Raman spectroscopic (SERS) detection of riboflavin (RBF), were characterized. The SERS study was carried out by using Raman spectrometer equipped with charge coupled device (CCD) detector. The study demonstrated an approach to produce cheap analytical tool from most littered items (DCF).



Scheme 1.3. Synthesis of AgNPs by using NCC isolated from DCF as a reducing- and stabilizing agent and SERS study of riboflavin (RBF).

Chapter 5: This chapter entails the synthesis of AgNPs clusters by using NCC isolated from FP as a reducing- and stabilizing agent in the presence of Stöber silica as an anchoring surface for the clusters. The nanocomposite was used as a SERS substrate in order to enhance the Raman signal of malachite green in comparison with monodispersed AgNPs prepared in the same manner in the absence of Stöber silica. The nanocomposites were well characterized. This study demonstrated the significant enhancement of SERS signals by using the substrate with high population of "hot spot".



Scheme 1.4. Synthesis of AgNPs clusters by using NCC isolated from FP as a reducing- and stabilizing agent in the presence of Stöber silica and SERS study of malachite green (MG).

Chapter 6: This chapter contains the conclusion and recommendations derived from the study based on the findings of this study.

1.4 Significance of the study

The significance of this study is shown in the following perspectives:

1. This study demonstrated for the first time stepwise isolation of NCC from DCF as a way of ameliorating the environmental hazard associated with DCF, which is arguably the most littered item in the world.

2. The study added more value to the isolated NCC-DCF by using it as a reducing and in the same vain, as a stabilizing agent in the synthesis of AgNPs, which was further applied in the detection of riboflavin (a highly fluorescence molecule with poor Raman signal) *via* SERS study.

3. The study demonstrated the design of AgNPs clusters as a SERS substrate with high sensitivity for the detection of malachite green (MG), a fungicide with genotoxic and carcinogenic tendencies, illicitly used in some aquaculture industries.

1.5 References

(1) Zhu, H.; Luo, W.; Ciesielski, P. N.; Fang, Z.; Zhu, J.; Henriksson, G.; Himmel, M. E.; Hu, L. Wood-Derived Materials for Green Electronics, Biological Devices, and Energy Applications. *Chem. Rev.* **2016**, *116*, 9305–9374.

(2) Lin, N.; Huang, J.; Dufresne, A. Preparation, Properties and Applications of Polysaccharide Nanocrystals in Advanced Functional Nanomaterials: A Review. *Nanoscale* **2012**, *4*, 3274–3294.

(3) Rojas, J.; Bedoya, M.; Ciro, Y., Current Trends in the Production of Cellulose Nanoparticles and Nanocomposites for Biomedical Applications. *InTech OpenScience*, Chapter 8, **2015**.

(4) Olivera, S.; Muralidhara, H. B.; Venkatesh, K.; Guna, V. K.; Gopalakrishna, K.; Kumar, Y. Potential Applications of Cellulose and Chitosan Nanoparticles/Composites in Wastewater Treatment: A Review. *Carbohydr. Polym.* **2016**, *153*, 600–618.

(5) Azeredo, H. M.; Rosa, M. F.; Mattoso, L. H. C. Nanocellulose in Bio-Based Food Packaging Applications. *Ind. Crop. Prod.* **2016**, *97*, 664–671

(6) Abdul Khalil, H.; Saurabh, C. K.; Adnan, A.; Fazita, M. N.; Syakir, M.; Davoudpour, Y.; Rafatullah, M.; Abdullah, C.; Haafiz, M.; Dungani, R. A Review on Chitosan-Cellulose Blends and Nanocellulose Reinforced Chitosan Biocomposites: Properties and their Applications. *Carbohydr. Polym.* **2016**, *150*, 216–226.

(7) Brinchi, L.; Cotana, F.; Fortunati, E.; Kenny, J. Production of Nanocrystalline Cellulose from Lignocellulosic Biomass: Technology and Applications. *Carbohydr. Polym.* **2013**, *94*, 154–169.

(8) Abitbol, T.; Rivkin, A.; Cao, Y.; Nevo, Y.; Abraham, E.; Ben-Shalom, T.; Lapidot, S.; Shoseyov, O. Nanocellulose, a Tiny Fibre with Huge Applications. *Curr. Opin. Biotechnol.* **2016**, *39*, 76–88.

(9) Bella, F.; Galliano, S.; Falco, M.; Viscardi, G.; Barolo, C.; Grätzel, M.; Gerbaldi, C. Approaching Truly Sustainable Solar Cells by the Use of Water and Cellulose Derivatives. *Green Chem.* **2017**, *19*, 1043–1051.

(10) Jonoobi, M.; Oladi, R.; Davoudpour, Y.; Oksman, K.; Dufresne, A.; Hamzeh, Y.; Davoodi, R. Different Preparation Methods and Properties of Nanostructured Cellulose from Various Natural Resources and Residues: A Review. *Cellulose* **2015**, *22*, 935–969.

(11) Bledzki, A.; Gassan, J. Composites reinforced with cellulose based fibres. *Prog. Polym. Sci.* **1999**, *24*, 221–274.

(12) Moon, R. J.; Martini, A.; Nairn, J.; Simonsen, J.; Youngblood, J. Cellulose Nanomaterials Review: Structure, Properties and Nanocomposites. *Chem. Soc. Rev.* **2011**, *40*, 3941–3994.

(13) Maiti, S.; Jayaramudu, J.; Das, K.; Reddy, S. M.; Sadiku, R.; Ray, S. S.; Liu, D. Preparation and Characterization of Nano-Cellulose with New Shape from Different Precursor. *Carbohydr. Polym.* **2013**, *98*, 562–567.

(14) Tang, Y.; Shen, X.; Zhang, J.; Guo, D.; Kong, F.; Zhang, N. Extraction of Cellulose Nano-Crystals from Old Corrugated Container Fibre Using Phosphoric Acid and Enzymatic Hydrolysis Followed by Sonication. *Carbohydr. Polym.* **2015**, *125*, 360–366.

(15) Takagi, H.; Nakagaito, A. N.; Bistamam, M. S. A. Extraction of Cellulose Nanofibre from Waste Papers and Application to Reinforcement in Biodegradable Composites. *J. Reinf. Plast. Compos.* **2013**, *32*, 1542–1546.

(16) Mohamed, M.; Salleh, W.; Jaafar, J.; Asri, S.; Ismail, A. Physicochemical Properties of "Green" Nanocrystalline Cellulose Isolated from Recycled Newspaper. *RSC Adv.* **2015**, *5*, 29842–29849.

(17) Nagalakshmaiah, M.; Mortha, G.; Dufresne, A. Structural Investigation of Cellulose Nanocrystals Extracted from Chili Leftover and Their Reinforcement in Cariflex-IR Rubber Latex. *Carbohydr. Polym.* **2016**, *136*, 945–954.

(18) Fahma, F.; Iwamoto, S.; Hori, N.; Iwata, T.; Takemura, A. Effect of Pre-Acid-Hydrolysis Treatment on Morphology and Properties of Cellulose Nanowhiskers from Coconut Husk. *Cellulose* **2011**, *18*, 443–450.

(19) Khawas, P.; Deka, S. C. Isolation and Characterization of Cellulose Nanofibres from Culinary Banana Peel Using High-Intensity Ultrasonication Combined with Chemical Treatment. *Carbohydr. Polym.* **2016**, *137*, 608–616.

(20) Lu, P.; Hsieh, Y.-L. Cellulose Isolation and Core–Shell Nanostructures of Cellulose Nanocrystals from Chardonnay Grape Skins. *Carbohydr. Polym.* **2012**, *87*, 2546–2553.

(21) Bano, S.; Negi, Y. S. Studies on Cellulose Nanocrystals Isolated from Groundnut Shells. *Carbohydr. Polym.* **2017**, *157*, 1041–1049.

(22) Pönni, R.; Kontturi, E.; Vuorinen, T. Accessibility of Cellulose: Structural Changes and Their Reversibility in Aqueous Media. *Carbohydr. Polym.* **2013**, *93*, 424–429.

(23) Tarrés, Q.; Oliver-Ortega, H.; Llop, M.; Pèlach, M. À.; Delgado-Aguilar, M.; Mutjé, P. Effective and Simple Methodology to Produce Nanocellulose-Based Aerogels for Selective Oil Removal. *Cellulose* **2016**, *23*, 3077–3088.

(24) Lokanathan, A. R.; Uddin, K. M. A.; Rojas, O. J.; Laine, J. Cellulose Nanocrystal-Mediated Synthesis of Silver Nanoparticles: Role of Sulphate Groups in Nucleation Phenomena. *Biomacromolecules* **2013**, *15*, 373–379.

(25) Garza-Navarro, M.; Aguirre-Rosales, J.; Llanas-Vázquez, E.; Moreno-Cortez, I.; Torres-Castro, A.; González-González, V. Totally Ecofriendly Synthesis of Silver Nanoparticles from Aqueous Dissolutions of Polysaccharides. *Int. J. Polym. Sci.* **2013**, *2013*, 1–8

(26) Lin, X.; Wu, M.; Wu, D.; Kuga, S.; Endo, T.; Huang, Y. Platinum Nanoparticles Using Wood Nanomaterials: Eco-Friendly Synthesis, Shape Control and Catalytic Activity for p-Nitrophenol Reduction. *Green Chem.* **2011**, *13*, 283–287.

(27) Kaushik, M.; Li, A. Y.; Hudson, R.; Masnadi, M.; Li, C.-J.; Moores, A. Reversing Aggregation: Direct Synthesis of Nanocatalysts from Bulk Metal. Cellulose Nanocrystals as Active Support to Access Efficient Hydrogenation Silver Nanocatalysts. *Green Chem.* **2016**, *18*, 129–133.

(28) Kaushik, M.; Moores, A., Review: Nanocelluloses as Versatile Supports for Metal Nanoparticles and Their Applications in Catalysis. *Green Chem.* **2016**, *18*, 622–637.

(29) Wu, X.; Lu, C.; Zhou, Z.; Yuan, G.; Xiong, R.; Zhang, X. Green Synthesis and Formation Mechanism of Cellulose Nanocrystal-Supported Gold Nanoparticles with Enhanced Catalytic Performance. *Environ. Sci.: Nano* **2014**, *1*, 71–79.

(30) Shi, Z.; Tang, J.; Chen, L.; Yan, C.; Tanvir, S.; Anderson, W. A.; Berry, R. M.; Tam, K. C. Enhanced Colloidal Stability and Antibacterial Performance of Silver Nanoparticles/Cellulose Nanocrystal Hybrids. *J. Mater. Chem. B* **2015**, *3*, 603–611.

(31) Azizi, S.; Ahmad, M. B. H.; Hussein, M. Z.; Ibrahim, N. A. Synthesis, Antibacterial and Thermal Studies of Cellulose Nanocrystal Stabilized ZnO-Ag Heterostructure Nanoparticles. *Molecules* **2013**, *18*, 6269–6280.

(32) Soliveri, G.; Ardizzone, S.; Yüksel, S.; Cialla-May, D.; Popp, J.; Schubert, U. S.; Hoeppener, S. Microwave-Assisted Silver Nanoparticle Film Formation for SERS Applications. *J. Phys. Chem. C* **2016**, *120*, 1237–1244.

(33) Jiang, F.; Hsieh, Y.-L. Synthesis of Cellulose Nanofibril Bound Silver Nanoprism for Surface Enhanced Raman Scattering. *Biomacromolecules* **2014**, *15*, 3608–3616.

(34) Jiang, Y.; Song, Y.; Miao, M.; Cao, S.; Feng, X.; Fang, J.; Shi, L. Transparent Nanocellulose Hybrid Films Functionalized with ZnO Nanostructures for UV-Blocking. *J. Mater. Chem. C* **2015**, *3*, 6717–6724.

Chapter 2

A review of cellulose as a green SERS substrate: Fundamentals, design principles and applications

2.1 Introduction

Surface enhanced Raman spectroscopy (SERS) has become one of the most versatile analytical techniques available due to its sensitivity and specificity on the identification of target molecules *via* unique vibrational information referred to as "fingerprint", which is based on structure, conformation and the environment of the target molecule. The potential of SERS to detect analytes at low concentration supports its wide applications.[1-6] The discovery of SERS in 1928 stemmed from Raman scattering (i.e. inelastic scattering of light by molecules) reported by Raman.[7] However, the first report on SERS as a phenomenon was in 1974 by Fleischmann *et al.*,[8] who observed that the Raman scattering of pyridine adsorbed on a roughened silver surface was significantly enhanced. Two independent research groups had, shortly thereafter, reported greater enhancement of pyridine Raman scattering on a roughened silver surface and concluded that the observed increase in enhancement was more than could be accounted for only through an increase in surface area. Instead, it was affirmed that this was due to an increase in the electromagnetic field[9] and charge transfer[10] interaction, between the silver surface and the adsorbed molecules. The two concepts remained the mainstay of the SERS debate within the research community, and are part of the current vernacular, as electromagnetic- and chemical mechanisms.

Although the concept of SERS was established by using a roughened silver metal surface, the advent of nanotechnology has brought an expansion to SERS applications with the use of metal nanoparticles as SERS substrates. Metal nanoparticles, especially the Group 11 coinage metals (Ag, Au, Cu) are capable of generating strong surface plasmon resonance (SPR) in the visible and near infrared regions, and have been exploited as SERS substrates. In 1979, Ag and Au nanoparticle colloids, synthesized *via* sodium borohydride ($NaBH_4$) reduction of their respective metal salts, were used to enhance the Raman scattering of pyridine. The enhancement was improved when the excitation wavelength used in the study was close to the observed localized surface plasmon resonance (LSPR) of the nanoparticles.[11] This clearly underscores the significant contribution of metal nanoparticles to SERS. Similarly, Ag nanoparticles synthesized by using the citrate reduction method were employed as SERS

substrates in the detection of single molecules of crystal violet[12] and rhodamine 6G (R6G).[13] These findings opened the door for numerous applications of SERS in medical diagnostics and bioanalytical studies.[3, 6, 14-16] With recent advancement in size and shape control of metal nanoparticles during preparation, using different reducing and stabilizing agents, plasmonic nanoparticles that are capable of inducing high SERS enhancement, have evolved with time. Commonly used reducing agents, include: $NaBH_4$, hydrazine (NH_2NH_2), hydroxyl amine (NH_2OH), triethanol amine (TEA), poly (ethylene amine), glucose, sodium citrate, and dimethyl formamide (DMF). Stabilizing agents include polyvinylpyrrolidone (PVP), poly(ethylene glycol)-block-poly(propylene glycol)-block-poly(ethylene glycol), silanes, and other compounds with functional groups, such as thiol (-SH), carboxylic acid (-COOH) and amino ($-NH_2$), that can serve as an anchor for the plasmonic nanoparticle to minimize aggregation.[17-18] However, the use of chemical reducing and stabilizing agents can introduce interferences as a result of the agents or their by-products that may compete with intended targets during SERS measurement. This is circumvented by using support materials which are stable, with minimal interference during measurement as stabilizing and reducing agent. Cellulose as a biodegradable naturally abundant biopolymer has tremendous benefits as a green reducing- and stabilizing agent in the synthesis of metal nanoparticles. With a surface rich in hydroxyl functional group, cellulose has been used as a reducing- and stabilizing agent as well as solid support in the preparation of substrate for SERS measurements. Remarkable features of cellulose among others, include its: i) availability as the most abundant biopolymer on earth, ii) flexibility with which it can be refined from macro- to nanoparticles with varying degree of crystallinity, iii) ease of functionalization to introduce different functional groups to its surface, iv) biocompatibility and biodegradability. Cellulose has a very weak SERS response, hence it has low interference and background signals during measurement. As a fibre (paper), it can be used as solid platform for SERS substrate and as colloid suspension (nanocellulose) and hence, it can be used as stabilizing and/or reducing agent. When functionalized, it can induce the synthesis of metal nanoparticles with various shapes and dimensions, towards improved SERS signals. Being cheap and readily available, cellulose serves as a basic component in the fabrication of many point-of-care (POC) medical diagnostic kits,[19-21] an area where SERS is gaining tremendous attention in recent time.[22]

A number of reviews are available on SERS, but to date none has focused on the significant contribution of cellulose in SERS development. In this review, the fundamental principle of SERS, the use of cellulose in its various forms in the preparation of SERS substrates, and the applications of these substrates in SERS are discussed. An insight into how cellulose combines

the role of reducing and stabilizing agents in the preparation of metal nanoparticles to guide in the fabrication of SERS substrates is presented. Challenges associated with the use of cellulose in order for it to perform these roles have been identified and suggestions made to overcome them. The review aims to shed more light on the synthesis and design of improved and reliable SERS substrates that will attract market value in the near future *via* the use of cellulose and/or its derived products.

2.2 Fundamentals of the SERS mechanism

Several mechanisms have been proposed to unravel the influence of roughened metal surface for the enhancement of Raman scattering of molecules, but only two have been well established,[1] namely: i) the chemical (charge transfer) and ii) electromagnetic enhancement mechanisms. They have an independent mode of action but often occur simultaneously. Their influence on Raman scattering strongly depends on the proximity of the target molecule to the roughened metal surface, hence the need to ensure absorption of the target on the surface of the metal. For an in depth description of SERS mechanisms, the principle of Raman scattering is required. Inspired by Compton's concept of inelastic scattering of X-ray by molecules, Raman hypothesized that the visible light of the electromagnetic spectrum should also experience similar inelastic scattering when focused on molecules. He observed the inelastic scattering of visible light focused on molecules in liquid and gaseous states in a classic experiment.[7] However, the intensity of the inelastic scattering was very weak since only one in ten million photons was scattered *via* this process. This inelastic scattering of light was later named after Raman.[7] The discovery of SERS was as a result of a deliberate effort towards enhancing the Raman scattering of molecules with the assumption that with more molecules involved in the scattering, the Raman intensity could be amplified. This was demonstrated by the absorption of pyridine on a roughened silver surface.[8] Although an increase in the absorption of molecules, led to an increase in intensity, it was discovered that the metal surface further provided additional enhancement *via* electromagnetic and charge transfer mechanisms.[9, 10]

2.2.1 Charge transfer enhancement mechanism

The charge-transfer enhancement mechanism stems from electronic interactions between a metal surface and absorbed molecules, caused by the overlap of orbitals. Electronic transitions occur within and between the orbitals of the metal and the absorbed molecules under the influence of light energy, thereby leading to enhancement of Raman scattering (Fig. 2.1A).

This observation is more prominent in molecules with electronic absorption in the near ultraviolet region, which experience a change in molecular orbital energy level when either in close proximity or absorbed on metal nanoparticles. The resultant enhancement *via* charge transfer mechanism is estimated[5, 23-24] to be in the range of between 10–10^3 folds.

2.2.2. Electromagnetic enhancement mechanism

The electromagnetic mechanism arises from the absorption and scattering of incoming photons by delocalized electrons in the conducting band of metal nanoparticle surface. This interaction results in a coherent oscillation of the electrons if the frequency of the incoming photons is the same as the frequency of the oscillating electrons, which is known as localized surface plasmon resonance (LSPR). LSPR depends on the size, shape and the nature of metal nanoparticle. The local electromagnetic field on the metal surface is enhanced through the LSPR. Molecules absorbed at the metal surface or in proximity to the local enhanced field will experience strong Raman scattering due to induced dipole from the enhanced local field. The Raman scattered intensity from the molecule is further amplified by the enhanced field, hence leading to SERS (Fig. 2.1B). Essentially, there are two steps in the electromagnetic enhancement mechanism, i) enhancement of the local field where the metal nanoparticle acts as a receiving antenna and ii) enhancement of the Raman signal that is scattered off the molecule where the metal nanoparticle acts as a transmitting antenna. The resultant enhancement factor (ratio of SERS intensity to normal Raman intensity) is approximately proportional to 10^4 of the enhanced local field when the frequencies of the incident photons and the observed Raman scattering are very close. Unlike the charge transfer mechanism, the electromagnetic enhancement is estimated to be in the range of between 10^4 to 10^{12} for molecules absorbed on the metal surface, making it the dominant enhancement often observed.[1, 25-28] It is important to note that the above SERS description is for a single metal nanoparticle. With two neighbouring nanoparticles (dimer), the enhancement of the local field is more intense, especially at the gap or crevice, commonly referred to as the "hot spot" between the nanoparticles, leading to stronger SERS signals (Fig. 2.1C). The intensity of the SERS signal is also affected by the distance between the target molecule and nanoparticle surface. The shorter the distance, the greater the intensity of the signal. However, there is a limit to which the gap size can be reduced in order to avoid quantum effects between the coupled nanoparticles, which can adversely distort the signal band and intensity.[3-4, 29]

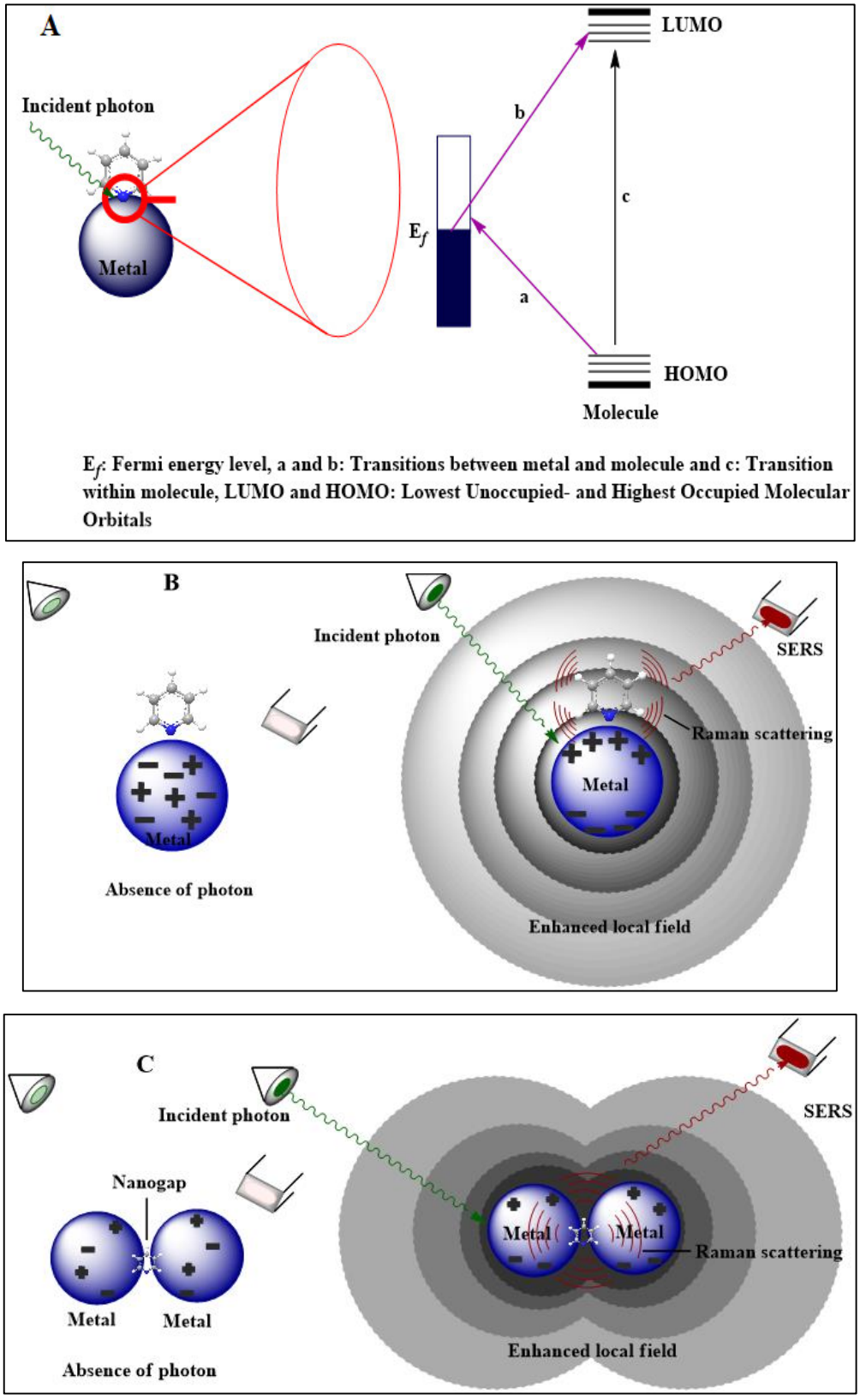


Fig. 2.1: Schematic illustrations of: (A) chemical enhancement mechanism, (B) electromagnetic enhancement mechanism and (C) plasmonic "hot spot".

2.3 Cellulose and Nanocellulose

Cellulose is the most abundant and perhaps, the most explored biopolymer on earth, consisting of β-D-glucopyranose ($C_6H_{10}O_5$) units, linked by β-1,4-glycosidic bond. The basic unit is called cellobiose, comprising of two β-D-glucopyranose units inverted by 180º along the vertical plane.[30] Cellulose is rich in hydroxyl functional groups with six of these groups present in each cellobiose unit. The hydroxyl groups provide a medium for intra- and intermolecular hydrogen bonding within and between the cellulose chains, which combine to form elementary fibrils. In the structural hierarchy, the elementary fibrils combine to form microfibrils, which assemble in combination with hemicellulose and lignin into macrofibrils.[17, 30] This structural arrangement provides the strength for the plant framework with cellulose as the backbone.

Morphologically, cellulose consists of rigid and well-ordered (crystalline) regions connected by less-ordered (amorphous) regions.[31-32] The amorphous regions are susceptible to hydrolysis under the influence of concentrated acid and can also be easily oxidized. In the context of nanocellulose acid hydrolysis, the crystalline regions could be referred to as nanocrystalline cellulose (NCC), cellulose nanocrystal (CNC) or cellulose nanowhiskers (CNW). However, when cellulose is subjected to mechanical treatment under high pressure, fibrillation occurs, leading to formation of cellulose nanofibrils (CNFs) and/or cellulose microfibrils (CMFs), which consist of alternating amorphous and crystalline regions with the fibril length in the submicron range. These materials are more flexible and longer, with higher aspect ratios (length/width) than NCC. Generally, NCC, CNF and CMF are considered as nanocellulose, based on the dimension classification.[33] NCCs are basically rod-like in shape with lengths in the range of between 50–500 nm and widths in the range of between 3–20 nm, while CNF and CMF have widths in the range of between 5–100 nm with lengths in the submicron and micrometer ranges, respectively.[31, 33-35] The source of cellulose, pre-treatment and treatment, as well as the duration of treatment are among several factors that will ultimately, influence the dimensions of nanocellulose (Scheme 2.1). However, all forms of nanocellulose are chemically identical, except for the purposeful surface modification arising from various chemical reagents employed during treatment processes.

2.3.1 Source of cellulose

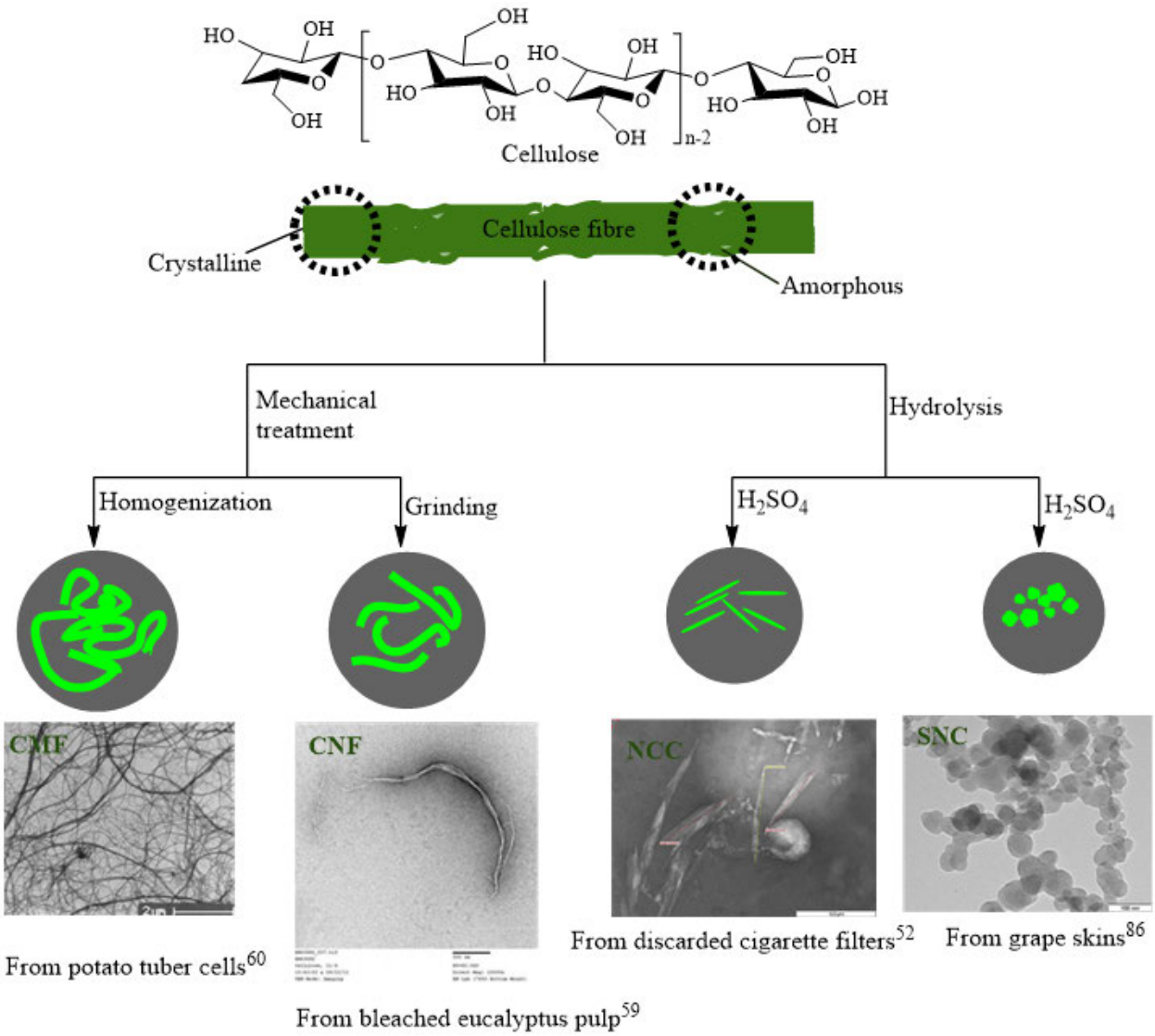
The primary source of cellulose is plant material in which it co-exists with lignin and hemicellulose in a complex structure. There are several modified industrial wood-pulping processes used in the extraction of cellulose from plants. These processes, basically involve the removal of extractives, lignin and hemicellulose, followed by bleaching in order to obtain

bleached pulp with high cellulose content. However, in nature, cellulose can be found in almost pure state in cotton and with a 'bottom-up' approach, cellulose can be synthesized from simple sugar and other basic requirements *via* bacterial propagation. This type of cellulose is referred to as bacterial cellulose (BC).[36-39] Due to its high purity and water content, BC has been explored for biomedical applications. Other known sources of cellulose are tunicate[40-42] and algae.[43-46] The necessity of recycling in order to reduce waste, has brought about new sources of cellulose that are non-conventional. These include: agricultural wastes,[34, 47-49] man-made wastes, such as old newspaper,[50] corrugated paper[51] and even discarded cigarette filters[52] (Scheme 2.1). This demonstrates that there is sufficient supply of raw material, available for the isolation of nanocellulose.

2.3.2 Nanocellulose isolation

CNF and CMF are produced *via* mechanical processes, which include grinding, steam explosion, microfluidization, cryocrushing, high pressure homogenization, electrospinning and ultrasonication (Scheme 2.1).[53-60] These processes involve fibrillation of cellulose by using high frictional force, temperature, pressure, ultrasound energy and electric field with specialized equipment. The high power required and cost of equipment tend to impose restraints on the commercial viability of these processes.[61] Hence, chemical and enzymatic pre-treatments are introduced in order to reduce power consumption.[32, 34, 62-64] Unlike CNF and CMF, NCC is isolated by hydrolysis, catalyzed by acid or induced *via* oxidation. With strong acid, such as H_2SO_4, the amorphous region is hydrolyzed, leaving the crystalline region with high resistance to hydrolysis. The preference for H_2SO_4 in the hydrolysis of cellulose, is due to the introduction of surface charge through sulphate hemi-ester groups on the isolated NCC, which assist in stabilizing the NCC when dispersed in water. However, the introduction of the sulphate hemi-ester groups also reduces the thermal stability of the NCC. Other mineral acids, such as HCl, HBr and H_3PO_4 have also been reported, but they showed less stabilizing effect on NCC in water.[65] A combination of these acids have also been employed in cellulose hydrolysis.[66] The dimension and yield of NCC as well as other physical characteristics depend on acid type, concentration of the acid, source of cellulose, acid volume-to-cellulose mass ratio, reaction time and temperature.[67-68] Higher acid concentration, temperature and increase in acid to cellulose ratio, as well as longer reaction time result in shorter length of NCC with reduced aspect ratio.[69] Generally, 64–65 wt% of H_2SO_4 at 45ºC with 45 min reaction time, results in NCC with length in the range of between 50–300 nm and width in the range of between 5–10 nm.[70]

Apart from the use of strong acid, NCC has also been isolated with oxidizing agents, which induce hydrolysis *via* oxidation of the glycosidic bond of the amorphous region of the cellulose. Ammonium persulphate ($(NH_4)_2S_2O_8$) (APS), sodium periodate ($NaIO_4$) and 2, 2, 6, 6-tetramethyl-1-piperidinyloxy radical (TEMPO), in combination with sodium hypochlorite (NaOCl) and sodium bromide (NaBr) have been successfully used to isolate NCC *via* oxidation.[71-75] However, the process can be cumbersome requiring more reaction time and surface oxidation thereby leading to the inevitable introduction of carboxylic (COOH) and aldehyde (–CHO) groups on the surface of the isolated NCC. With TEMPO, further mechanical treatment is often required in order to ensure complete fibrillation. The advantage of the APS method over other methods is the possibility of isolating NCC directly from feedstock with lignin-containing cellulose, without pre-treatments as required by other methods.[76] In addition, the advent of ionic liquid has afforded the opportunity to produce regenerated cellulose of nano-dimension and morphology with the advantage of recovering the ionic liquid.[77-78] Ionic liquid dissolves cellulose by interacting with the hydroxyl groups, leading to a reduction in the intra- and intermolecular hydrogen bonding. The dissolved cellulose is subsequently precipitated with water and the ionic liquid recovered. Within the principles of green chemistry and with the aim to improve the yield of nanocellulose, dicarboxylic acids (exemplified by maleic and oxalic acids), have also been shown to be suitable candidates in isolating nanocellulose.[68, 79-82] The hydrolysis requires high temperature and acid concentration with longer reaction time than when sulphuric acid is used for the hydrolysis. The surface of the isolated nanocellulose is also modified with hemi-esters of the carboxylic acids, which improves the thermal stability and crystallinity of the nanocellulose in comparison to NCC isolated with inorganic acids. The recovery of the acids and the by-product (sugar) of hydrolysis *via* crystallization shows the green nature of the process.[83-84] It is important to note that nanocellulose with a spherical morphology can also be isolated.[72, 85-87] In comparison, with the use of TEMPO, organic acids and ionic liquids produce nanocellulose with longer lengths and wider widths and belong to the class of CNF different from nanocellulose with shorter lengths and narrower widths through the use of inorganic acids, hence it is classified as NCC.[83, 88]



Scheme 2.1. Methods of preparing micro- and nanocellulose, and the common names associated with the morphology or process. CMF: Reproduced with permission from ref. 60. Copyright 2000 John Wiley and Sons, CNF: Reprinted by permission from ref. 59. Copyright 2012 Springer Nature, NCC: Reprinted from ref. 52. Copyright 2017 with permission from Elsevier, SNC: Reprinted from ref. 86. Copyright 2012 with permission from Elsevier.

The forms and extent of surface modification arising from pre-treatment and treatment processes during the isolation of nanocellulose, are typically studied by spectroscopic techniques, such as ^{1}H and ^{13}C nuclear magnetic resonance (NMR) and Fourier transform infrared (FTIR). NMR and FTIR as well as conductometric titration analysis have been used to determine the degree of oxidation of a nanocellulose surface isolated by using ammonium persulphate.[71,72,76,89] Additional techniques, such as UV-vis absorption and photoluminescence spectroscopies, are employed when nanocellulose surfaces are modified with chromophoric and luminescence moieties in order to suit particular requirements.[76,90,91] The description and

dimensions of nanocellulose are acquired by using microscopy techniques, including transmission electron microscopy (TEM), scanning electron microscopy (SEM), and atomic force microscopy (AFM). Similarly, dynamic light scattering (DLS) has also been employed to estimate nanocellulose dimension.[92] Generally, the TEM, SEM and AFM are indispensable tools in the classification and dimension analysis of nanocellulose, especially to observe the variations resulting from the use of different parameters towards improving quality and yield of NCC.[69, 93, 94] Zeta potential and powder X-ray diffraction (XRD) techniques are used to determine nanocellulose surface charge and degree of crystallinity, respectively. The thermal stability of nanocellulose is studied *via* thermal gravimetric analysis (TGA), differential scanning calorimetry (DSC) and differential thermal analysis (DTA).[95] Although, there are limitations associated with some of these techniques when used individually, when combined together, they provide a suitable platform for characterization of nanocellulose of different functionalities designed to meet specific needs.

2.4 Plasmonic SERS substrate design

Substrate design is one of the key factors considered to achieve SERS with high sensitivity and reliability. Substrates with high sensitivity show strong enhancement for specific target molecules with reproducible signals and minimum variation to ensure reliability. Plasmonic (metal nanoparticle) SERS substrates provide a great advantage in achieving highly sensitive and reliable SERS signals. The local surface plasmon resonance (LSPR) of the metal nanoparticle can be tuned to a wavelength range between that of the exciting incident laser and the Raman scattering signal of the target molecule. This is required for maximum enhancement of the local field on the metal nanoparticle surface, leading to a highly enhanced signal. Several metals, such as: Li, Na, K, Rb, Cs, Pt, In, Ga, Rh, Al, Cu, Ag and Au have been studied[5, 96] for their SERS enhancement effects, but the coinage metals (Au, Ag and Cu) are most attractive since they produce highly enhanced and reliable SERS signals for a broad variety of target molecules.[1] This is due to the fact that their LSPR, in the visible and near infrared regions can be readily tuned to the wavelengths of commercial lasers used in SERS studies. The LSPR can be tuned by varying the size, shape, surface roughness and distance between nanoparticles. Recent developments in nanotechnology have made it possible to design nanoparticles with regular shapes, which include sphere, triangle, cube, cuboid, cylinder, hallow, octahedral, cuboctahedra, sphere and other related shapes that can be likened to flowers and dendrites.[2, 97, 98] A combination of metals in plasmonic substrate design can also result in multicomponent substrates. Core-shell, which has gained attention because it provides a means the SERS

enhancement effect of two different metals and create platforms for coating substrates with a protective layer in order to reduce cytotoxicity when used for *in vivo* and *in vitro* biomedical applications.[2-3, 99] Gold (Au) has proven to be the best choice when compared to Ag and Cu in biomedical SERS studies, due to its biocompatibility, lower cytotoxicity and wider tunable LSPR to the near infrared region, which is less invasive on tissue, but with a deeper penetration than ultraviolet and visible radiations.[6] However, Ag provides a stronger enhancement when compared to Au and it is also cheaper, hence it accounts for a higher percentage of SERS substrates. Copper (Cu) is seldom used due to its low resistance to oxidation under ambient condition, thus limiting its stability.[5]

SERS substrates are coated or printed on solid supports, such: as glass, silicon wafer, adhesive tape, polymers (nylon, polyacrylonitrile, polyethylene terephthalate, polydimethylsiloxane, polyethylene, poly(ethylene oxide), polyvinyl alcohol, polyacrylamide and polyvinylidene fluoride filter membranes), graphene, carbon nanotube or cellulose.[100-110] They are also used as a colloidal solutions when stabilized by using different agents. Cellulose has played a significant role as a solid platform, also as stabilizing- and reducing agent in the design of SERS substrate. However, it contributes more when considered as a solid platform on which synthesized plasmonic nanoparticles are immobilized *via* different techniques such as thermal evaporation, vapor deposition, laser induced photothermal deposition, dip coating, inkjet printing and screen printing.[107] Recently, cellulose in its various forms has been employed as stabilizing agent to prevent coagulation during synthesis of plasmonic nanoparticle in the presence of reducing agent and it has also been reported that cellulose simultaneously plays the dual role of a reducing and stabilizing plasmonic nanoparticles under suitable reaction conditions.[17, 111] With this perspective in mind, it is imperative to consider the enormous contributions of cellulose in SERS substrate design towards realizing commercially viable, sustainable, flexible and green substrates in the near future. In this review, insight is provided on the use of cellulose in its various forms not only as solid support but also as a stabilizing- and reducing agent in the design of SERS substrate.

2.5 Contributions of cellulose in SERS substrate design

The first use of cellulose in the design of a SERS substrate was reported independently in 1984 by Tran *et al.*[112] and Vo-Dinh *et al.*[113] by using different techniques in the fabrication of the substrate. Tran and co-workers employed filter paper as a stabilizing agent to obtain the SERS of organic dyes at subnanogram level by using $NaBH_4$ reduced Ag colloid with LSPR of 400 nm and particle size in the range 10–30 nm as plasmonic nanoparticle. Vo-Dinh *et al.* studied

the SERS of trace organic compounds using Ag immobilized through thermal evaporation technique on a filter paper spin-coated with Teflon or polystyrene latex as a substrate. The approaches of the two different studies showed not only the independence of the research findings, but also established the preference of filter paper in SERS substrate design since filter paper with other materials, such as: plastic sheets, metal and glass plates were compared.[112, 113] More recently, new cellulose-based SERS substrates have evolved parallel to new developments in nanotechnology and these substrates have been shown to be successful in numerous applications. With well-developed proof-of-concept scenarios, SERS has become an emerging technology in the detection of trace analytes in the study of pesticide residue in food, dye identification in artwork, forensic analysis of samples during investigation, DNA analysis, detection of explosives and bio-warfare, and others. This review addresses the techniques of fabricating cellulose-based SERS substrates and their applications.

2.5.1 Cellulose paper-based SERS substrate

Cellulose paper, including office paper, newspaper, Kraft paper and filter paper of various grades has been explored in the design of SERS substrates. The fabrication processes with which these papers were coated with plasmonic nanoparticles in the substrate design, are quite innovative, simple and economical when compared to known conventional methods. Some of these processes have been highlighted.[107, 114] However, a comprehensive review is required in order to understand the basic principles adopted in these fabrication processes.

2.5.1.1 Drop casting

The first SERS substrate on cellulose paper was made by dropping a premixed colloid solution of the analytes (dyes) and Ag nanoparticles on filter paper, which provided support for the Ag nanoparticles. SERS spectra for sub-nanogram quantities of various dyes were obtained while the substrates were wet in order to take advantage of the dielectric environment offered by water, which produces better enhancement when compared to air.[112] When a solution of gold nanostars stabilized by sodium citrate was cast on filter- and printing papers, the filter paper-based SERS substrate produced better enhanced SERS signal with crystal violet as SERS probe due to higher porosity. Higher enhancement was also reported for the signals with a wet probe on both printing- and filter papers due to higher dielectric constant of water when compared to air.[115] On the contrary, printing paper was observed to show improved SERS enhancement with Ag nanostars when compared to filter paper.[116] A number of factors are responsible for these variations in performance; some of these factors are inherent in paper morphology, composition

and porosity as well as variation in deposition techniques, especially the effect of drying time. However, filter paper dominated other forms of papers in SERS substrate design probably due to its porosity and high cellulose composition. In separate studies, SERS of *p*-hydroxybenzoic acid[117] and Sudan III azo dye[118] were studied by using citrate stabilized Ag nanoparticles deposited on filter paper by continuous dropping and drying until the desired volume was transferred. The analytes were deposited in the same manner. The results showed that the dried filter paper substrate produced better resolved SERS signals when compared to Ag nanoparticle colloidal solution as well as other solid substrates investigated. The SERS spectra obtained on a filter paper-based substrate were also in agreement with those based on theoretical calculations.[117, 119-120] Further study was carried out by using the same substrate design to investigate the influence of adsorption configurations for *p*-, *m*- and *o*-hydroxybenzoic acids on SERS signals.[121] Theoretical calculations based on density function theory (DFT) as well as experimental studies using filter paper-based substrate, with Au nanoparticles, showed a difference in adsorption configurations of *p*-, *m*- and *o*-nitroaniline on filter paper and in colloidal solutions. Adsorption was *via* the nitro group oxygen in colloidal solution in a perpendicular manner, while on filter paper, the corresponding SERS signals suggested tilting of the aromatic ring at an angle, the degree of tilting varies with the position of the amino group.[122, 123]

It is noteworthy that the concentration of plasmonic nanoparticles deposited on paper by drop casting, strongly influenced the intensity of SERS signals. This was demonstrated when the SERS of fullerenes (C_{60} and C_{70}) was obtained by using Au nanoparticles cast on filter paper in different volume *via* this method. The intensities of the SERS signals of the analytes gradually increased with increase in volume until a saturation point was reached, after which the intensity decreased. The saturation points indicated that sufficient aggregate of Au nanoparticles was attained.[124] The advantage of a solid substrate is that it enables the study of SERS of analytes, which are not soluble in water as demonstrated when the SERS of single wall carbon nanotube (SWCNT) was obtained for the first time on Ag, and Au nanoparticles coated filter paper. The study showed the possibility of using SERS to estimate the diameter of SWCNT and monitor the reaction mechanism during production.[125] The SERS signal of C_{70} in Au nanoparticles-pyridine colloidal solution was dominated by pyridine signals, however, when deposited and dried on filter paper, the interference signals from pyridine were not observed.[126]

Although the drop casting technique is simple, the uniformity of the plasmonic coating remains a challenge and also the uneven spreading of samples results in variation in SERS signals. A

method was developed to ensure uniform distribution of plasmonic nanoparticles on casting. In order to achieve this, a paper was placed between two Teflon templates, designed to restrict the spread of Au nanoparticles on paper and heat was applied to reduce drying time. The improved SERS substrate was used in the detection of nicotine and uric acid in aqueous solution[127] as well as uric acid in synthetic urine.[128] Another method developed to restrict the spreading of plasmonic nanoparticles on casting, was by first calendaring a filter paper in order to reduce the surface roughness. The paper was then treated with alkyl ketene dimer (AKD) in order to make the surface hydrophobic as illustrated in Fig. 2.2. The paper surface had an improved contact angle on coating with AKD leading to the retention of Ag nanoparticles and analytes on filter paper. The substrate showed improved SERS enhancement for the detection of pesticides (thiram and ferbam) in water. Thiram and ferbam were detected to limits of 0.46 and 0.49 nM respectively.[129]

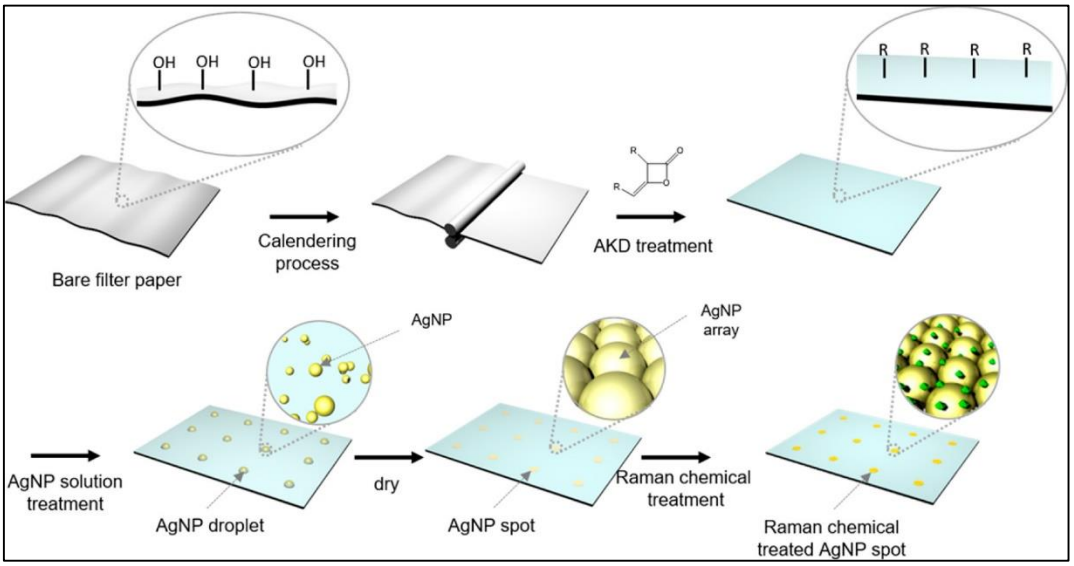


Fig. 2.2: Schematic illustration of modified drop cast method of paper-based SERS substrate. Reprinted with permission from ref. 129. Copyright (2018) American Chemical Society.

2.5.1.2 Thermal evaporation

Thermal evaporation in a vacuum chamber was employed in order to deposit Ag on filter paper spin-coated with polystyrene latex. The filter paper provided a solid and flexible support for the polystyrene sphere on which the plasmonic nanoparticles were coated. The spherical polystyrene aided distribution and uniformity of the Ag. With this substrate, the SERS spectra of trace amount of organic compounds were obtained.[113] It was also used to obtain the SERS of nitro-polynuclear carcinogenic aromatic compounds.[130] A substrate designed without pre-coating of filter paper with polystyrene before thermal evaporation of Ag was employed for

identification of anthraquinone dyes in artworks.[131] However, thermal evaporation of Ag on filter paper without pre-coating with polystyrene resulted in substrate damage on exposure to the laser beam and poor signal reproducibility, which was due to the non-uniformity of the surface coating, unlike when pre-coated with polystyrene.[132] In another study, ZnO nanorods were also grown on paper, prior to thermal evaporation of Ag nanoparticles onto the nanorods, in order to induce a "hot spot" on the surface. The designed SERS substrate was capable of detecting rhodamine 6G (R6G) to a detection limit of 9 nM.[133] Concurrent low temperature thermal evaporation of Ag and Au on filter paper led to plasmonic nanoparticles SERS substrate. By varying the composition of the metals, the plasmonic resonance of the alloy was tuned to different wavelength. The SERS substrate showed strong enhancement for the detection of adenine and folic acid, down to pM level.[134] However, this technique is not very popular in SERS substrate design due to the time requirement and cost of facilities.

2.5.1.3 *In-situ* coating

The hydroxyl groups on cellulose paper provide the necessary anchor for Ag^+ ions for *in-situ* coating. The procedure, first developed by Berthod *et al.*,[135] simply involved immersion of filter paper in an aqueous solution of Ag^+ ions, followed by spraying the wet paper with sodium borohydride as reducing agent. The paper turned black, indicating the reduction of Ag^+ ions. Taking advantage of the dielectric environment provided by water, the substrate was used wet in order to obtain the SERS of *p*-aminobenzoic acid and other related nitrogen containing compounds.[136] The substrate was further explored to analyze mixture of the nitrogen containing compounds by using the unique SERS characteristic vibrational modes of each compound as identification tags.[137-138] With this substrate design, the influence of analyte spatial distribution on SERS signals was studied. The observed non-uniformity in the spatial distribution was attributed to the difference in analyte affinity for solvent in which it was dissolved, and the substrate.[139] SERS signals also vary with pore sizes and chemical composition of the paper when using "*in-situ* coating" in substrate design.[140] Another challenge associated with this method is the polydispersed nature of the Ag nanoparticles since the particles size varied at different locations on the paper due partly to non-uniform distribution of the reducing agent on spraying.[141] This can lead to poor reproducibility of the SERS spectra and wrong interpretations. In order to minimize such effects, filter paper was pre-coated with alumina before *in-situ* coating with plasmonic nanoparticles. The modified filter paper showed an improved SERS signal compared to unmodified filter paper.[142]

An alternative to spraying of a reducing agent was demonstrated by vertically mounting filter paper in solution containing Ag^+ ions and glucose (reducing agent) at a set temperature and time to *in-situ* coat the filter paper with Ag nanoparticle. The filter paper was also pre-treated in basic and acidic solutions to improve the coating. The paper pre-treated with ammonia showed improved SERS signal for tyrosine with a detection limit of 625 nM.[143] Agarose was used as a reducing agent to coat filter paper with Ag nanoparticle *in-situ*. A filter paper was dipped into a solution of Ag^+ ions and agarose for 5 seconds after which it was incubated in the dark at 28°C for 72 hours in order to obtain a dark-brown filter paper coated with Ag nanoparticles. This study showed improved SERS signals for crystal violet, trinitrotoluene and chlorpyrifos compared to those fabricated by dip coating with detection limit of 10 pM, 10 nM and 1 nM, respectively. The improved performance was attributed to the shrinkage of the agar on drying leading to the aggregation of Ag nanoparticles into the "hot spot" and the hydrophobic surface provided by the agar prevented uncontrolled spreading of analyte on the substrate.[144]

Photochemical reduction of Ag^+ ions in aqueous solution in the presence of sodium citrate and NaOH was used to coat a filter paper with Ag nanoparticles *in-situ* under a light emitting diode (LED) at room temperature. The paper fabricated under optimized conditions was used to detect adenine to a low concentration of ~160 nM.[145] Successive ionic layer absorption and reaction (SILAR) method was also demonstrated for the *in-situ* synthesis of Ag nanoparticles on SERS paper-based substrate. The concept involved an initial introduction of hydrophobic and hydrophilic arrays on filter paper by wax printing, followed by the successive adsorption of metal ions (Ag^+ or Au^{3+}) and reduction with $NaBH_4$ by floating of the pretreated filter paper in different solutions containing the metal ions and $NaBH_4$ in order to aid adsorption of the metal ions and their subsequent reduction. Multiple cycles (6) were required to obtain the best coverage. The paper played a significant role in the adsorption of metal ions into its porous structure and rough surface in order to ensure a uniform coating, unlike the glass, silicon wafer and polydimethylsiloxane (PDMS) substrates investigated. The fabricated Ag nanoparticles paper substrate showed a reproducible limit of detection in the fM range with a relative standard deviation of 4.2% and an enhancement factor of 1.1 $x10^9$ for rhodamine B.[146] The Au nanoparticle paper showed a detection limit in the pM range with a relative standard deviation of 7.5% and an enhancement factor of 7.8 $x10^8$ for 2-naphthalenethiol.[147] SILAR was also demonstrated in the fabrication of Ag@Au core-shell nanoparticles coated *in-situ* on paper. The Ag@Au paper-based SERS showed a limit of detection below acceptable maximum range

set by the Environmental Protection Agency (EPA) for aniline, NaN_3 and malachite green in aqueous environment.[148]

Further study on the application of SILAR for the fabrication of paper-based SERS substrate showed that SERS signal enhancement increased with an increase in the number of cycles and the highest enhancement was observed after 6 cycles. As the number of cycles increased the particle size increased and the inter-particle distance decreased, leading to a "hot spot".[149] An *in-situ* interfacial triphasic system was developed to promote the accumulation of "hot spot" on hydrophobic paper. The system involved the formation of an oleic acid-Ag complex by reaction of aqueous $AgNO_3$ solution with oleic acid. The complex formed was gradually dropped on hydrophobic paper, floating on ascorbic acid solution. The oleic acid-Ag complex migrated through the pores on the paper to the aqueous/paper interphase where Ag^+ ions in the complex were reduced by ascorbic acid and capped with oleic acid, making the synthesized nanoparticles hydrophobic. The nanoparticles then migrated through pores back to the oil/paper interphase where they assembled forming a "hot spot". The paper substrate was used in chromatographic separation and SERS measurement of crystal violet and methylene blue dyes.[150]

The concept of *in-situ* seed-mediated growth was developed in order to increase the nanoparticle size on paper, towards achieving high enhancement. For this purpose, Au nanoparticles were grown on cellulose paper pre-coated with poly(γ-glutamic acid) in order to increase the adsorption of Au^{3+} ions, which were reduced with $NaBH_4$. The paper was then mounted in a growing solution containing Au^{3+} in order to increase the nanoparticles size. The SERS substrate was able to achieve 10 pM detection limit for 4-mercaptophenylboronic acid and was further used to detect and quantify the level of brassinosteroids (plant growth regulators) in plant.[151] In another study, *in-situ* seed-mediated growth was adopted to fabricate Ag nanoflowers (AgNFs) on paper. Successive dipping of cellulose paper in acidic $SnCl_2$ and $AgNO_3$ led to the formation of Ag nanoseeds on the paper with the reduction of Ag^+ ions by Sn^{2+} ions. The seeds were grown into AgNFs by immersing in a mixture of ascorbic acid and $AgNO_3$ solution. The fabricated paper-based AgNFs SERS substrate showed strong enhancement for rhodamine 6G (R6G) and crystal violet, which could be detected down to 10^{-20} and 10^{-19} M, respectively. The application of the substrate to detect crystal violet on spiked fish surface showed that crystal violet could be detected to a limit of 10^{-17} M, when the substrate is used as swab.[152] The stability of the substrate was improved by coating with graphene oxide. The graphene oxide-treated substrate maintained its enhancement of SERS signals with a higher stability over a period of time, when compared to untreated substrate.[153]

Leveraging on the reducing capacity of cellulose, Ag^+ ions were reduced to Ag nanoparticles on cellulose paper without any other reducing agent. Filter paper was immersed in a solution containing $Ag(NH_3)_2(OH)$ for adsorption and the temperature of the solution was maintained at 80°C for a specific duration in order to bring about *in-situ* reduction and deposition of Ag nanoparticles with the hydroxyl groups on the filter paper serving as reducing agent. The SERS substrate was used in the detection of anticancer drugs.[154] In another study, filter paper was first oxidized with sodium periodate ($NaIO_4$) to form dialdehyde cellulose (DAC), leading to improved adsorption of Ag^+ ions, which were further reduced by aldehyde and hydroxyl groups (Fig. 2.3). The substrate SERS showed capacity to detect R6G and *p*-aminothiophenol down to 10^{-11} and 10^{-9} M, respectively.[155] Moreover, Au^{3+} ions were also reduced on printer paper as SERS substrate without any reducing agent and the influence of halides was studied.[156] This showed the capacity of cellulose as both stabilizing and reducing agent in the synthesis of metal nanoparticles. With this method, the interference sometimes associated with reducing and stabilizing agents was avoided during SERS analysis.

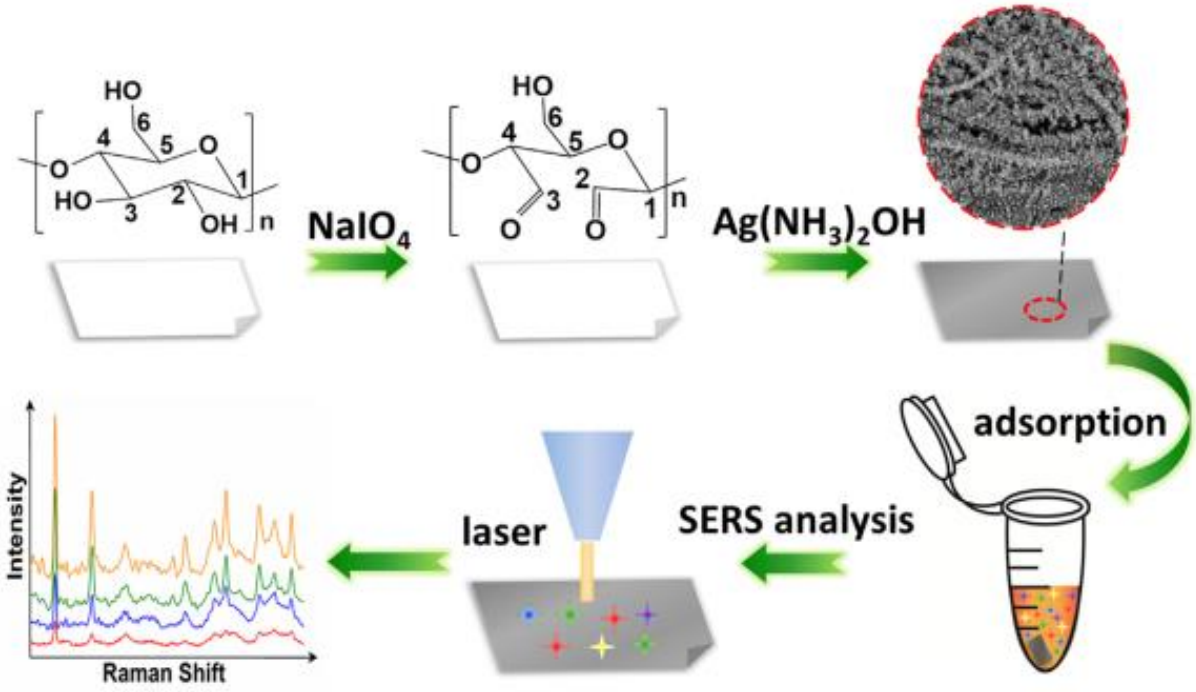


Fig. 2.3: Schematic illustration of *in-situ* fabrication of paper-based SERS substrate and its application. Reprinted from ref. 155. Copyright 2016 with permission from Elsevier.

2.5.1.4 Laser induced photothermal deposition

Apart from the use of a chemical reduction method for *in-situ* nanoparticle deposition on filter paper for SERS study, laser photo-reduction of Ag^+ ions on filter paper has also been reported.

The reduction was aided by photocatalytic hydrolysis of water, leading to the generation of electrons and hydrogen radicals, which effectively reduced the Ag^+ ions on filter paper within the laser region. The substrate prepared was used to obtain the SERS signal of alizarin dye by reducing fluorescence interference from the dye.[157] A laser-induced photothermal effect was also used to fabricate nanoparticles on a filter paper, pre-coated with Ag or Au film by sputter coating. The surface roughness, porous nature and low thermal conductivity of the filter paper, strongly influenced the nucleation of the metal nanoparticles. The rough surface served as nucleation sites, while the pore size controlled the size distribution, and the low thermal conductivity ensured the effective adsorption of the laser leading to a high density of nanoparticles with a single laser shot, unlike silicon wafer and glass that require several shots, Fig. 2.4. The filter paper-based designed substrate showed superior performance compared to silicon wafer and glass with 10^{-15} and 10^{-18} M SERS detection limits observed for R6G and 4-aminothiophenol, respectively.[158] Simultaneous reduction of Ag^+ and SERS measurement was achieved with laser. A mixture of Ag^+ ions and *p*-aminothiophenol on a filter paper under laser showed simultaneous reduction of Ag^+ ions to Ag nanoparticles which induced a local magnetic effect to enhance the Raman signal of *p*-aminothiophenol. The observed phenomenon was adopted to measure Hg^{2+} in aqueous solution. In the presence of Hg^{2+}, the intensity of the observed SERS signals of *p*-aminothiophenol decreased in proportion to the concentration of Hg^{2+} ions due to stronger affinity of the thiol moiety on *p*-aminothiophenol for Hg^{2+} ions. Other related thiol containing organic compounds such as dithizone and *p*-mercaptobenzoic acid showed similar phenomena, unlike R6G and crystal violet which do not have thiol moiety.[159]

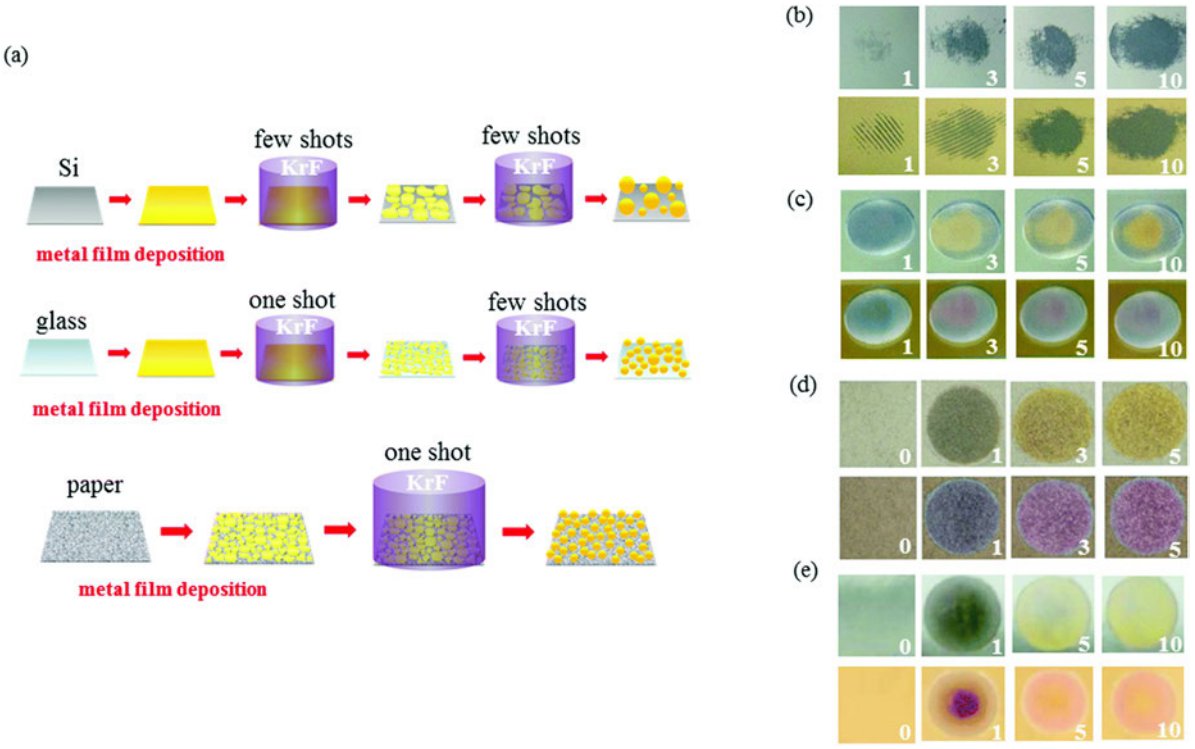


Fig. 2.4: (a) Schematic illustration of laser-induced photothermal formation of metal nanoparticles on silicon, glass and filter paper substrates. Photographic images of metal nanoparticles (Ag (top); Au (down)) formed on silicon (b), glass (c), filter paper (d) and photographic paper (e) with different number of laser shots. Reproduced from ref. 158. Copyright 2015 with permission from Royal Society of Chemistry.

2.5.1.5 Immersion deposition

The immersion (dipping) of filter paper in solution of freshly prepared nanoparticles is another simple technique of depositing plasmonic nanoparticles on filter paper for SERS studies.[160] With this method, Grasseschi *et al.*,[161] deposited freshly prepared Au nanoparticles mixed with diphenylthiocarbazone on filter paper for SERS detection of heavy metals. Hg^{2+} ions were detected down to 10^{-12} g level and with a better resolved SERS when spectra compared to that obtained by using a Au nanoparticles colloid solution. The paper-based substrate was able to immobilize the heavy metal ions within the region of detection when compared to a diluted environment in solution. The concept of detecting heavy metal ions was based on the ability of the ions spotted on the filter paper to displace Au nanoparticles complexed to the dye, leading to the reduction in SERS signals of the dye. Hg^{2+} proved most successful among the ions tested.[161] Multi-branched Au nanoantenna (MGN) with protrusions, synthesized by using 4-(2-hydroxyethyl)-1-piperazineethanesulfonic acid (HEPES) was coated on filter paper by immersion. The LSPR of the MGN was tuned to the near infrared region with HEPES, enabling

the SERS substrate to have improved induced magnetic field with the Raman laser employed. The flexibility of the paper substrate made it possible to detect 4-aminothiophenol by swabbing on a contaminated surface to a limit of 62.5 pg.[162]

The coverage of the filter paper by Au nanoparticles depends on the concentration of the colloidal solution. With higher concentration, the Au deposit is often denser and more uniform, giving rise to an improved SERS signal, when compared to lower concentrations.[163-164] The immersion method proved successful for the uniform coating of filter paper with cetyltrimethylammonium bromide (CTAB), stabilized Au nanorods used in a reported swab SERS experiment.[165] The positively charged CTAB provided a medium of interaction with the hydroxyl groups of the cellulose (filter paper), on which the Au nanorods are strongly anchored (Fig. 2.5A). The flexibility of the filter paper was preserved even after coating, making it suitable for swab sampling of trace analyte from surfaces, unlike the situation for rigid silicon substrates. The SERS study showed that the paper substrate could detect 1,4-benzenedithiol residue as low as 140 pg within a small area.[165] The flexibility of this substrate made it superior to most conventional solid substrate as demonstrated in the SERS study of *trans*-1,2-bis(4-pyridyl)ethane where a reproducible detection limit of 0.5 nM was observed.[166] Similar to CTAB, sodium citrate and cationic polyacrylamide have been used to aid uniform coating of Au and Ag nanoparticles, while chloride ion was also reported for aiding uniform coating of Ag nanoparticles. The paper surfaces were found to have improved homogeneity with a high-density nanoparticle coating, leading to improved SERS signals.[167-171]

It is important to note that the surface composition of nanoparticles contributes more to homogeneity of coating than nanoparticle size. A study in this regard showed that the surface charge of nanoparticles strongly affects the affinity of the nanoparticles for a paper substrate, which invariably affects SERS sensitivity and reproducibility.[172] in order to minimize the number of coating cycles in achieving homogeneity *via* immersion, self-assembly of Ag nanoparticles was induced with tetrabutyl ammonium nitrate (TBA^+ NO_3^-) at the water/dichloromethane (H_2O/DCM) interface (Fig. 2.5B). The self-assembled Ag nanoparticles showed a remarkably uniform coverage on paper in a single coating, resulting in an improved SERS signal of 4-mercaptobenzoic acid with a 10 nM detection limit.[173] Au nanoparticles were also self-assembled without any inducer, but simply by shaking the Au colloid in H_2O/DCM in order to create an emulsion of self-assembled Au nanoparticles at the interface. The self-assembled Au was adsorbed and concentrated on a tip of the arrow-shaped filter paper. The SERS fabricated substrate was able to separate and concentrate the analyte from sample solution with the capacity to produce highly enhanced SERS signal at the tip of

the detection zone, leading to a 10^{-18} M detection limit for R6G.[174] The paper-based microfluidic device designed in star-like shape, having protruding ends was coated with Au nanorods by immersion. With this fabrication, mixed analytes were separated to different protruding ends, called "fingertips" *via* induced electrostatic charge and the wicking power of the paper. A detection limit of sub-atto-molar was achieved using by R6G as a probe, making the device a cheap, but highly sensitive analytical tool.[175] The immersion method of coating provides a great advantage for trace chemical and biological real-time analysis with no pre-treatment or concentration of analyte. Limitations associated with the immersion method are that it requires highly concentrated plasmonic nanoparticles and longer duration (2 days) to achieve uniform and stable coating.

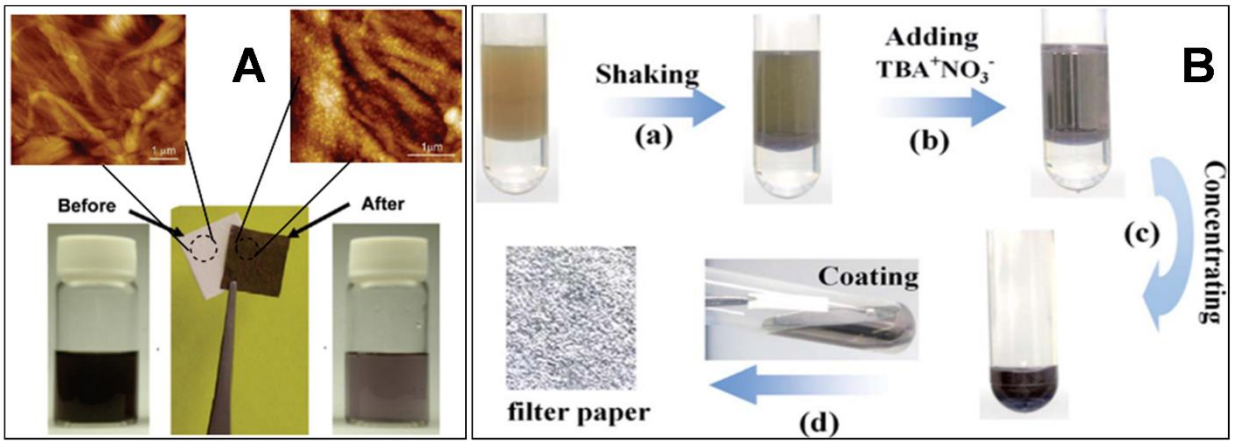


Fig. 2.5: Coating of Au nanorods stabilized with CTAB on filter paper (A). Reprinted with permission from ref. 165. Copyright (2010) American Chemical Society. Illustration of H_2O/DCM interface self-assembled Ag nanoparticles on filter paper by immersion (B). Reproduced from ref. 173. Copyright 2014 with permission from The Royal Society of Chemistry.

2.5.1.6 Inkjet printing

Inkjet printing of plasmonic nanoparticle on cellulose paper helps to provide a medium to coat paper as SERS substrate with a relatively short preparation time when compared to the immersion method and it also affords the opportunity to introduce various type of patterns, as found in microfluidic devices. With inkjet printing, the limitation associated with the spreading of analyte and the uneven distribution of plasmonic nanoparticles can easily be overcome by the introduction of hydrophobic patterns on paper *via* printing. This concept of SERS substrate

design was successfully demonstrated for the first time by Wei and White[103] by using a consumer inkjet printer to design SERS active regions on cellulose paper. The paper was made hydrophobic with hexadecenyl succinic anhydride to prevent spread of analytes prior to the printing of Ag nanoparticles on the paper. Multiple printing of Ag nanoparticles was carried outin order to ensure uniformity. The SERS substrate was able to detect R6G down to 10 femtomoles.[103] Similarly, Au nanoparticles printed on filter paper was used as a SERS substrate for the detection of trace explosives[176] and multiple printing of Au nanorods on printer paper was used to induce a SERS "hot spot" (as the nanorods aligned side-by-side) for detection of chemicals.[177] Ag nanoparticles with mixed shapes were also printed on paper in order to fabricate a SERS substrate that is capable of inducing enhancement at different wavelengths in the visible and near infrared regions.[178]

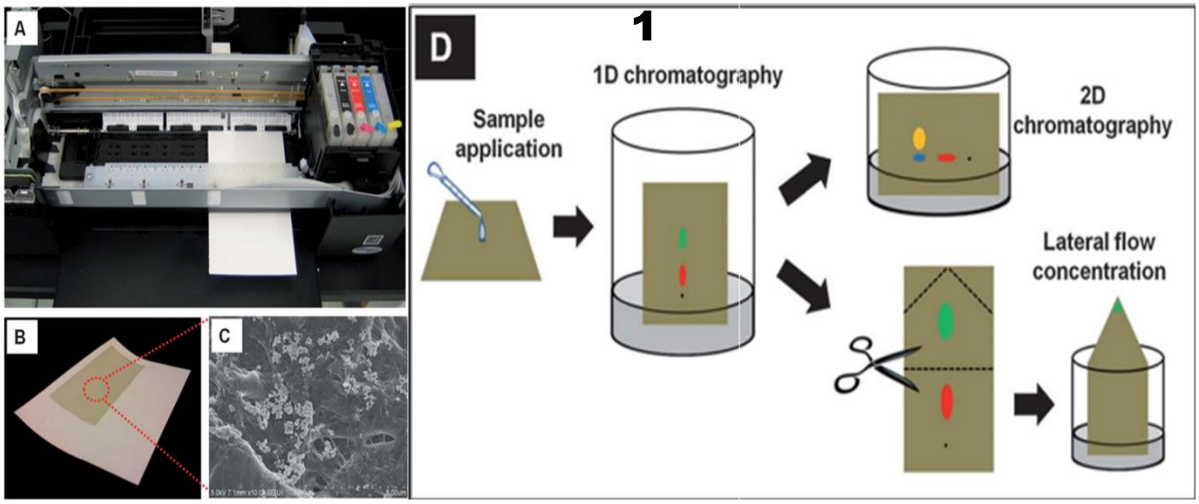
The concept of "dipstick concentration" of analytes from a relatively large volume of diluted sample to a small SERS-active region was demonstrated with inkjet printing of a SERS substrate on cellulose paper. The wicking ability of cellulose served as a "pump" to concentrate analytes at SERS-active region.[179] This concept provided a simple model of concentrating analytes in order to achieve strong and reproducible signal for multiplexed genetic detection and pesticides analysis in water and on solid surfaces that were previously swabbed with SERS substrate for sample collection.[180] As in paper chromatography, a SERS substrate printed on a cellulose paper was used to separate and identify mixture of dyes (R6G, malachite green and methylene blue). The chromatographic separation as well as the dye concentration at the SERS-active zone were made possible by the capillary action of cellulose paper, while Ag nanoparticles printed on the paper provided the field enhancement required in SERS identification of the separated dyes (Fig. 2.6 (1)).[181] A SERS substrate was also fabricated by inkjet printing of reduced graphene-oxide/Ag nanoparticle ink on a weighing paper. The substrate showed enhanced signals for R6G and malachite green when compared to a paper-based substrate having only Ag nanoparticle ink printed on it.[182]

SERS enhancement effects were compared for Ag nanoparticles and Ag nanowires by inkjet printing of halides (KCl or KI/KBr) and $AgNO_3$ applied consecutively on paper. The KI/KBr mixture induced the formation of nanowires on reduction of Ag^+ ions, while KCl induced the formation of nanoparticles. A SERS study using malachite green as probe, showed that the enhancement effect of nanoparticles (6.1×10^5) was higher than that of nanowire (3.7×10^5); the difference was attributed to the multifaceted structures observed in the nanoparticles.[183] The influence of Ag^+ ion on the localized surface plasmon resonance (LSPR) of Au nanoparticles was studied by inkjet printing of Au nanoseeds on filter paper. Seeds were grown

in solution where different concentrations of Ag^+ were added in order to vary the LSPR of the resulting Au nanoparticles. The LSPR Au nanoparticles varies with increase in concentration of Ag^+, however, the Au nanoparticles with LSPR (650 nm), close to the laser wavelength (633 nm) provided the most enhanced SERS signal for R6G. The SERS substrate was also able to detect thiram, a pesticide, to a limit of 0.1 nM.[184]

2.5.1.7 Screen printing

Screen printing is another printing technique that offers the fabrication of disposable SERS substrate on filter paper at a relatively low cost. Similar to inkjet printing, the plasmonic nanoparticles are printed on the filter paper with the aid of a screen in order to fabricate the desired arrays of SERS-active sites on filter paper. The uniformity of the coating and the corresponding SERS signal enhancement strongly depend on the concentration of the nanoparticles and the number of printing cycles.[185] With Ag colloid screen printed on the filter paper, a reproducible detection limit of 160 fM was achieved with R6G.[102] Screen printing was also used to develop microfluidic channels between Ag-Au bimetallic "dumbbells" (SERS zone) and a hydrophilic sampling zone encircled with a hydrophobic wall in order to prevent the spreading of samples outside the detection zone (Fig. 2.6 (2)). The microfluidic paper-based SERS substrate showed a 110 fM limit of detection for R6G.[186] The screen printing provides a fast and simple way of fabricating SERS substrates on filter paper, but the need for highly concentrated plasmonic nanoparticles in solution and multiple printing causes a barrier to the use of this method, like inkjet printing.



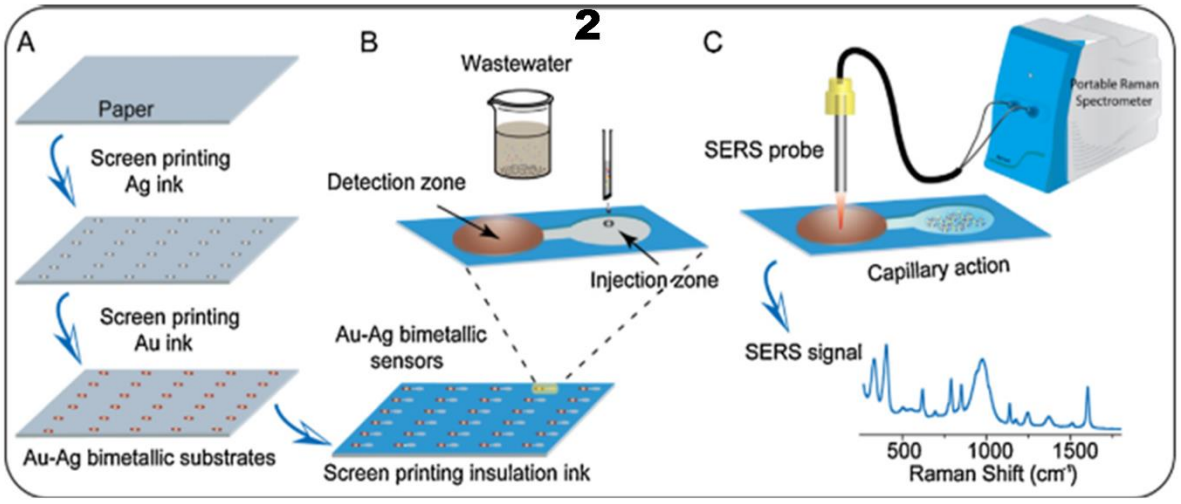


Fig. 2.6: (1) Inkjet printing of Ag nanoparticles on paper substrate and schematic illustration of chromatographic separation of analytes in a mixture. Reproduced from ref. 181. Copyright 2013 with permission from The Royal Society of Chemistry. (2) screen printing of Au-Ag bimetallic SERS substrate and microfluidic channels on paper. Reprinted from ref. 186. Copyright 2013 with permission from Elsevier.

2.5.1.8 Physical vapor deposition

Silver was deposited by physical vapor deposition in a vacuum chamber on different types of cellulose papers with the aim of using their wrinkled and fibrous nature to induce aggregation of Ag leading to a "hot spot" on deposition. All the papers tested (filter, napkin, sulphate, Kraft, newspaper and printing papers) showed high SERS sensitivity, once fully coated with Ag in order to prevent the paper component interfering with analyte signals. With these substrates, SERS detection of R6G down to a concentration of ~10^{-10} M, was achieved.[187] However, the stability of the SERS substrates was a challenge since they started degrading under ambient conditions within 24 hours of fabrication.

2.5.1.9 Spray Coating

The long time required for the deposition of plasmonic nanoparticle *via* immersion and the uneven distribution associated with drop casting thereby, leading to the "coffee ring" effect, prompted the use of spray coating, which involves the spraying of plasmonic nanoparticles from a pressure container onto the cellulose paper. This method was adopted to coat different types of cellulose papers with Ag nanoparticles after the introduction of hydrophobic and hydrophilic pattern on the papers (Fig. 2.7(1)). In comparison with drop casting, the spray coating showed better reproducibility and high accuracy. Ag distribution on spray coated

samples was more uniform when compared to that of drop cast samples. Although the method was successful with all the papers, the filter paper gave the highest signal enhancement. The method involves the multiple cycles of spraying; a minimum of 25 cycles was required to reach optimum performance.[188] This implies the use of more reagent and longer preparation time.

2.5.1.10 Pen-on-paper

The pen-on-paper approach was demonstrated in the coating of plasmonic nanoparticles on paper by Polavarapu *et al.,* with inspiration from recent developments in conductive ink-pen technology for writing electronic devices on paper.[189] Synthesized solutions of Au or Ag nanoparticles from the reservoir of a ball pen were coated on paper *via* the pen nib (Fig. 2.7(2)). This approach provided a simple and convenient way of generating SERS paper at point-of-need and at a relatively low cost. The ink could be fabricated to give the desired LSPR by varying the shape and size of the nanoparticles. SERS ball pens containing ink with Au nanospheres and nanorods as well as Ag nanospheres, have been produced at very low cost. The pen-on-paper approach was proven to be successful with different laser wavelengths and was demonstrated to show a limit of detection of 1 and 0.1 nM for malachite green on Au nanorods, and Ag nanosphere coated papers, respectively.[189]

2.5.1.11 Brushing

Brushing of plasmonic nanoparticles on filter paper was demonstrated by Zhang *et al.,* to fabricate simple and efficient SERS substrate.[190] The fabrication involved the introduction of microfluidic channels with the aid of wax printing on filter paper in order to prevent the spreading of analytes. Concentrated Ag nanoparticles were applied on a detection zone within the hydrophilic region by using a paint brush of appropriate dimension and about 14 cycles of this process was shown to result in a good coverage (Fig. 2.7 (3)). The microfluidic channel provided a path for a lateral flow of analyte to the detection zone by the capillary action of the paper. With the substrate, a reproducible limit of detection of 1 and 10 nM were recorded for R6G and malachite green, respectively.

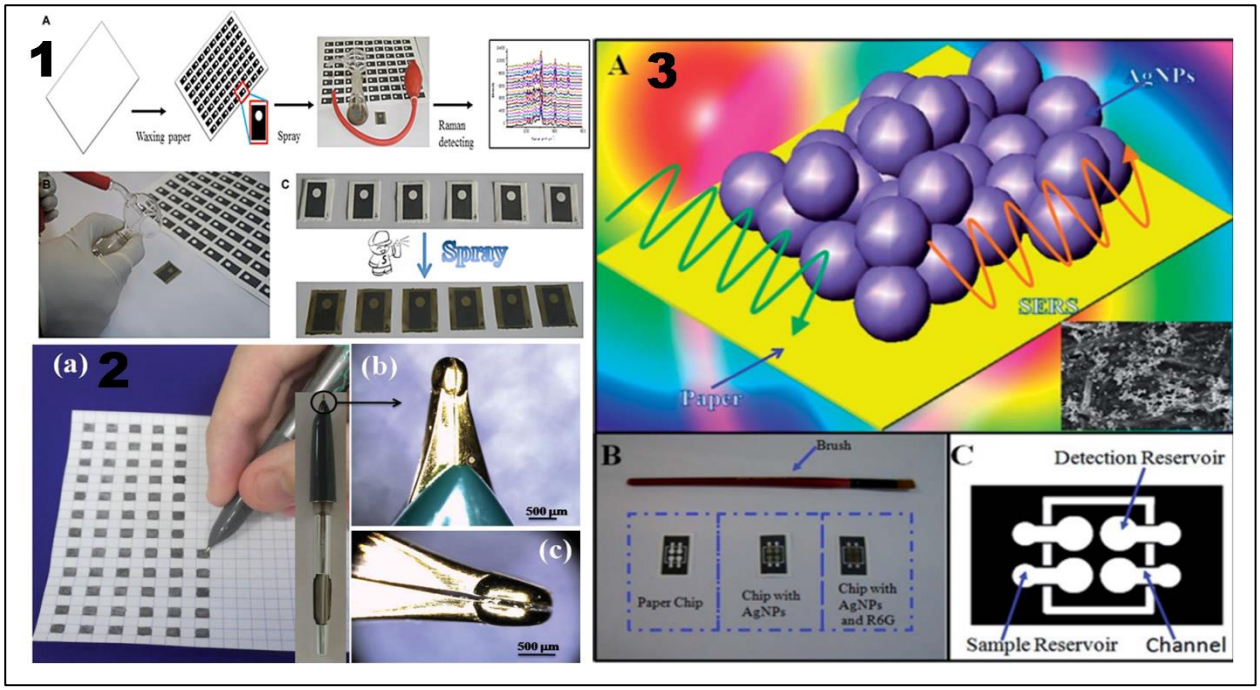


Fig. 2.7: (1) Spray coating of Ag nanoparticles on paper. Reproduced with permission from ref. 188. Copyright 2013 John Wiley and Sons, (2) writing of metal nanoparticles on paper. Reproduced with permission from ref. 189. Copyright 2014 John Wiley and Sons, and (3) Ag nanoparticles coated on paper by brushing. Reproduced from ref. 190. Copyright 2014 with permission from Royal Society of Chemistry.

2.6 Applications of paper-based SERS substrate

The early stages of paper-based SERS substrate focused on substrate design and optimization towards achieving improved SERS signals with different SERS probes. More recently, research interest has been on the applications of paper-based SERS substrate in biomedical, food, textile dye, painting, pharmaceutical and forensic analyses. These numerous applications show the huge potential in paper-based SERS substrates.

2.6.1 Bioanalysis

The role of SERS in bioanalysis is well established and paper-based SERS has contributed significantly to this development. Hoppmann and White demonstrated the detection of genetic targets by using a low cost paper-based substrate.[191] The oxidative products of apomorphine (a drug used in the treatment of Parkinson's disease), were detected by using paper-based SERS substrates coated with Au nanostars.[167] In combination with solid phase extraction, paper-based SERS substrates containing Ag nanoparticles were used to detect 6-thioguanine, an anticancer drug.[154] Similarly, a combination of HPLC and paper-based SERS was used to monitor 2'-deoxy-2'-fluoro-2'-C-methyluridine (PSI–6260), the metabolite of sofosbuvir (hepatitis C

drug). A gold nanoparticles colloid was used as ink to develop SERS substrate on A4 size paper. Blood samples spiked with varying amount of PSI–6260 were separated by using HPLC and at the retention time of PSI–6260, the eluate was detected by using the SERS paper, mass spectrometer (MS) or diode array detector (DAD). The paper-based SERS substrate was found to show improved sensitivity when compared to DAD and it was comparable to that of the expensive MS.[192] Paper-based SERS coated with Au nanoparticles was also used in the detection methrotrexate (an anticancer drug) in spiked human serum.[193]

Glucose was quantified in aqueous solution by using label-free Ag nanoparticles coated on printing paper as SERS substrate.[194] However, glucose determination in whole blood was achieved by using nitrocellulose paper-based SERS substrate with microfluidic channels, constructed by wax-printing in order to introduce hydrophobic walls. The detection zone in the hydrophilic enclosure was coated with Au nanorods modified with 4-mercaptophenylboronic acid and 1-decanethiol in order to aid quantification of glucose level. Nitrocellulose paper entrapped the blood cell and protein in the blood sample, but allowed the glucose to flow to the detection zone. The glucose level in a reference blood sample, as determined by SERS, was not statistically different from the quoted certified level.[195] Similarly, nitrocellulose paper was used in the fabrication of SERS substrate, consisting of functionalized Au nanostars, coated with silica for the diagnosis of traumatic brain injury by monitoring of neuron-specific enolase, a protein biomarker in blood.[196] SERS spectra of erythrocytes in blood samples were also obtained by using polydispersed Ag nanoparticles of various shapes, cast on cellulose paper.[197] Human serum albumin (HSA) was detected after dipstick concentration from a diluted sample with the wicking power of paper coated with multi-branched Au nanoantenna. With the substrate, a remarkable detection limit of 100 fM was achieved for HAS.[162]

In a comparative study of quantitative detection of bovine serum albumin (BSA), paper-based SERS fabricated by photo-reduction of Ag^+ ions on filter paper showed higher sensitivity with lower detection limit (1 mg/mL) when compared to the conventional UV-vis spectroscopic quantification (10 mg/mL).[198] Antigen-antibody detection for bio-diagnostic application was developed with Au nanoparticles coated on paper substrate, followed by functionalization with relevant biomolecules. The reproducibility of the SERS spectra allowed for the quantification of the targets.[199] Mucin-1, a biomarker for cancers, such as: breast, prostate, ovarian and pancreatic, was detected in human blood with aptamer-functionalized Au nanoparticles, deposited on paper pre-coated with carbon dots in order to aid assemblage of Au nanoparticles. The aptamer was hybridized with complementary DNA, which could be readily displaced by mucin-1 in order to facilitate the adsorption of the target to the SERS substrate. With the

substrate, mucin-1 was detected to a limit of 50 ng/mL with a recovery of 90-110% in human blood, even in the presence of other interfering proteins.[200] Oral cancer detection was accomplished with Au nanorods, coated by immersion on filter paper (Fig. 2.8(1)). A clear difference in the lipid and protein content of the examined normal vs. cancerous cells was observed in the diagnosis by using paper-based SERS. While the normal cells showed an intense signal due to high lipid content, the tumor cells showed intense signals associated with high protein and DNA contents.[201]

Based on basic concepts derived from microfluidics and the wicking power of paper, protein samples were detected to low concentrations of ~10^{-15} M by using functionalized Ag core-Au shell (Ag@Au) nanoparticles. The microfluidic channels separately directed the flow of the protein and the functionalized Ag@Au nanoparticles to the detection zone, where aggregation of the nanoparticles induced by the protein, resulted into a "hot spot" for enhanced and reproducible SERS signals.[202] Ag-coated paper-based SERS fabricated with the methodology of SILAR was used in the clinical diagnosis of human papillomavirus (HPV) infection, which is associated with cervical cancer by using samples from human cervical fluid. It was also used for the detection of malachite green, a known human carcinogenic agent, in solution. Differences in SERS signal markers showed the capacity of the substrate to distinguish various types of HPV investigated. The substrate also achieved a 0.004 ppb limit of detection when compared to a 2 ppb tolerance limit stipulated for malachite green, making the substrate, a potential clinical and environmental diagnostic tool.[146] The SILAR concept was also used to fabricate a Au nanoparticles paper-based SERS substrate, used in the identification of biomarker in cerebrospinal fluid for clinical diagnostics of cerebral vasospasm and hydrocephalus development associated with subarachnoid haemorrhage-induced complications. Improved signal enhancement was observed when the cellulose paper surface acquired significant negative charge at pH 3, leading to a strong adsorption of the positively charged Au^{3+} species and a densely Au-nanoparticle coated paper after the reduction with $NaBH_4$. A difference in SERS signals associated with amino acids, glycogen and nucleic acids of cerebrospinal fluids samples of patients and controls provided a platform for SERS diagnostics of complications after subarachnoid hemorrhage.[203]

A clinical diagnostic of Gouty arthritis (painful inflammation of joints) was demonstrated by using Au thin nanofilm thermally evaporated on cellulose paper as a SERS substrate in order to measure the concentration of uric acid in human tears, collected by using the substrate. The cellulose micro/nanopores provided the required absorption channels for the collection of tears from the eyes of normal subjects and Gouty arthritis patients. The SERS substrate showed a

satisfactory result since there was a good correlation between uric acid level in tears and in blood, which is the conventional sample for clinical diagnostics of the disease (Fig. 2.8(2)).[204] Clinical diagnosis of intra-amniotic infection (IAI) and preterm delivery (PTD) in pregnant women was carried out by SERS studies of amniotic fluid from selected subjects by using ZnO nanorods (decorated with Au nanoparticles) coated on cellulose paper with the concept of SILAR (Fig. 2.8(3)). The variations in the SERS signals of the principal components of amniotic fluids of control and patients were used to detect and identify IAN and PTD.[205] For early detection of heparin-induced thrombocytopenia (a blood coagulation disorder) resulting from heparin therapy, P-selectin (the associated biomarker) was monitored by using paper-based SERS coated with Ag ink. The observed SERS limit of detection (0.7 nM) for P-selectin was within the clinical relevant range, making the SERS substrate a potential tool for early detection of blood coagulation disorder.[206]

Similarly, Au coated paper-based SERS substrates were used in clinical diagnostics of ocular infections.[147, 185] Au nanorods capped with *p*-aminothiophenol combined with Au nanoparticles coupled with 1,8-diaminonaphthalene were used to fabricate paper-based SERS for the detection of nitrite ions in human urine.[207] Therapeutic drug monitoring of flucytosine (an antifungal drug) in undiluted human serum was demonstrated by using vertical flow system paper-based SERS with inkjet printed Ag nanoparticles. Layers of nitrocellulose membranes were stacked on the plasmonic region of the paper for the separation of the target analyte from other serum components. While the serum flowed through the membranes, protein components, known to cause fouling of the plasmonic surface were trapped within the micropores of the membranes and the target analyte was allowed to flow through to the plasmonic region on the paper. With this technique, flucytosine was detected and quantified in a linear range of between 10-150 µg/mL, which covered the commonly recommended therapeutic dose range (20-80 µg/mL) and also lower than 100 µg/mL stipulated as an acceptable toxicity threshold in undiluted serum for clinical monitoring of the drug.[208] Quantitative analyses of acetylsalicylic acid and nicotinamide in commercial products were carried out by using Ag nanoparticles coated on filter paper as SERS substrate. The results from the SERS substrate were in close agreement with those of the conventional method (HPLC-UV).[209-210] Paper-based SERS substrates have also been employed to detect the presence of illicit dyes in medicinal herbs. Often, dyes are incorporated into medicinal herbs in order to improve their market value. A paper-based SERS substrate coated with Ag nanoparticles was used as swab to identify medicinal herbs contaminated with illicit dyes. The

swab showed excellent performance towards the detection of simulated adulterated herb samples with different dyes examined.[211]

Recently, a paper-based substrate coated with mono-6-thio-cyclodextrin functionalized Au nanorods was used as a swab for the detection of Sudan dyes in a spiked medicinal herb. The paper provided the micropores for adsorbing the plasmonic Au nanorods, while mono-6-thio-cyclodextrin served as the host for trapping the hydrophobic dyes. The substrate showed improved SERS performance for the detection of Sudan III and IV when compared to paper-based substrate coated with Au nanorods without mono-6-thio-cyclodextrin.[212] Analytical technique was developed for microRNA detection by using DNA-encoded anisotropic Ag nanoparticles cast on paper substrate. While the DNA encoding resulted in shape modification of the Ag nanoparticles and tuning of the plasmonic wavelength, the paper provided a 3-D porous structure with abundant hydroxyl groups, which facilitated fluid accessibility and provided high surface area for the assemblage of the nanoparticles, leading to strong signal enhancement for the detection of microRNA.[213]

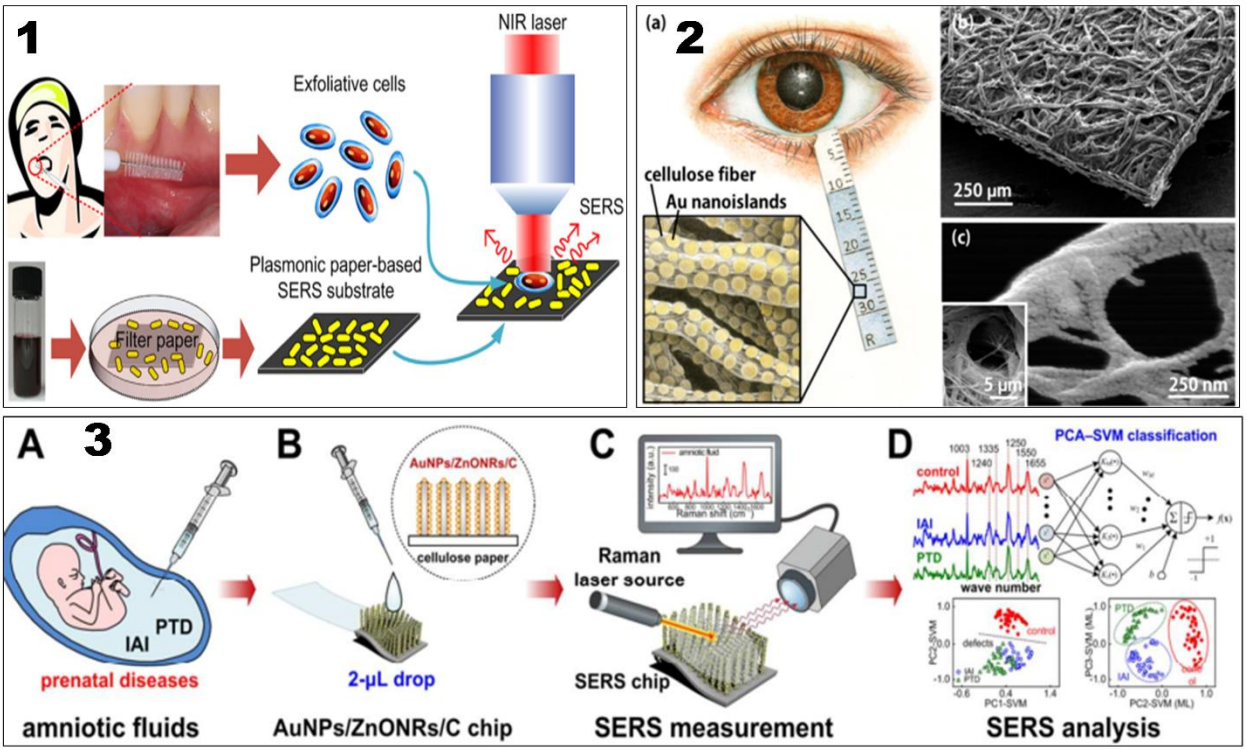


Fig. 2.8: Bioanalytical application of a paper-based SERS substrate in: (1) Oral-cancer diagnostics. Reprinted from ref. 201. Copyright 2014 with permission from Elsevier. (2) Tear screening for Gouty arthritis diagnosis. Reprinted with permission from ref. 204. Copyright (2017) American Chemical Society and (3) Pre-natal diseases detection. Reprinted with permission from ref. 205. Copyright (2018) American Chemical Society.

2.6.2 Water quality assessment

A paper-based SERS substrate with microfluidic channel was developed to quantitatively analyze aromatic pollutants in wastewater. The capillary action of paper served as a "pump" in order to drive the trace pollutants from the injection zones to the SERS active zones for detection. Sample pre-treatment was not required in industrial wastewater, prior to its introduction to this substrate as the suspended particulates were trapped at the injection zone. The paper-based SERS achieved detection limits of: 8.3, 10, 74 and 88 nM for benzidine, pyrocatechol, aniline and *p*-aminobenzoic acid, respectively, showing the excellent capacity of the substrate for trace analysis in wastewater.[186] In a similar manner, pesticide malathion was detected in water. The wicking property of cellulose paper was leveraged to concentrate the pesticide to SERS-active zone from a highly diluted sample. With this concept, a detection limit of 413 pg was achieved for malathion in water.[179] A SERS paper substrate fabricated by brushing of Ag nanoparticles on filter paper, showed a reproducible recovery of malachite green from spiked local lake water at different concentrations. The substrate showed a detection limit of 10 nM for malachite green with a relative standard deviation of 13.7%.[190] Moxifloxacin was detected and quantified in spiked tap water by using a paper-based substrate coated *in-situ* with hydrazine-reduced Ag nanoparticles. The porous and fibrous nature of the paper ensured the uniform assemblage of Ag nanoparticles on it, leading to enhanced SERS signals.[214] Microcystin-LR, a toxin produced by cyanobacteria in freshwater, was detected by using a SERS substrate fabricated with a pen-loaded with Au nanoparticles. Microcystin-LR was detected to a limit of 1 nM on paper at a relatively low cost.[215]

2.6.3 Adulteration of illicit drugs

SERS and chromatographic separations, based on paper substrates, have been shown to detect and quantify the presence of heroin in samples where it has been masked with highly fluorescence dye to prevent its detection. The wicking power of paper provides a means to separate the drug from its contaminants and also concentrate it in a SERS-active region on a Ag printed paper. This method achieved a detection limit of 25 ng of heroin in the contaminated sample.[181, 216] Moreover, on Ag printed paper, heroin and cocaine samples were collected and concentrated by lateral-flow through capillary action to the SERS-active region and were detected with good reproducibility to a limit of 9 and 15 ng, respectively.[179]

2.6.4 Food safety

Gold nanoparticles generated *in-situ* on a printer paper were used as a SERS substrate for the detection of residual pesticides in orange. The SERS substrate was fabricated by printing of the reducing agent on the paper and immersion of the paper in $HAuCl_4$ solution for *in-situ* growth of Au nanoparticles. The combination of the two methods was proposed in order to avoid the multiple printing associated with coating of paper with synthesized nanoparticles. The limits of detection achieved with this substrate for malachite green (10 µM) and iprodione (1 nM) were found to be less than the maximum residue limits set by European Union.[217] Methyl parathion adsorbed on apple was detected by swabbing with paper coated with multi-branched Au nanoantenna. With the substrate, methyl parathion was detected to a limit of 26.3 µg.[162] Similarly, with a focus to bring SERS closer to a real world application, a pen-on-paper approach was developed, such that SERS substrate can be made available when and where needed. With this approach, thiabendazole, a fungicide and parasiticide added as preservative to food, was detected down to a concentration of ~20 ppb.[189] In another study, a paper substrate fabricated by *in-situ* reduction of Ag^+ ions with formaldehyde was used to obtain SERS signals of thiram samples collected from the surfaces of banana, apple and tomato by swabbing. This, simple but highly sensitive substrate, showed detection limits of 7.2, 24 and 36 ng/cm^2 thiram in banana, apple and tomato, respectively.[218] Thiram was also detected in adulterated tea by using a paper-based SERS substrate fabricated with a combination of microfluidic and SERS concepts. A three-chamber microfluidic channel was fabricated on paper by using wax printing to introduce hydrophobic walls. On deposition of sample in the sample zone and Au@Ag nanoparticles in another zone, the two components were allowed to flow to the reaction chamber by capillary action of paper for SERS measurement. This substrate showed a detection limit of 1 nM for thiram with a recovery range of between 95–110% in adulterated tea.[219] Filter paper immersed in Ag nanoparticles colloid was used to wipe surfaces of apple, pear and grape contaminated with thiram. The extracted thiram was quantified by using the filter paper as SERS substrate. Thiram limits of detection by using this wipe on the fruits were: 4.6, 5.2 and 5.7 ng/mL, respectively, which were below the 50 ng/mL recommended limits.[220]

The illegal use of rhodamine B to enhance chili appearance was investigated. A substrate was designed by coating self-assembled Ag nanoparticles on paper in order to detect the presence of rhodamine B from chili extract in a relatively lower time when compared to the conventional analytical methods.[221] Prohibited colorants in fruit drinks were detected by using Ag nanoparticle paper-based SERS substrate coated with poly(sodium 4-styrenesulfonate) in order to effectively separate and concentrate the colorants from the fruit drinks. Sunset yellow and

lemon yellow were detected to limits of 10 and 100 µM in both orange and mango juices.[222] SO_2 gas in wine was quantified by using a gas diffusion microfluidic paper-based SERS substrate, coated with sea urchin-like ZnO nanoparticles in order to trap the released SO_2 from the wine samples. SERS measurement of the released SO_2 by using Au nanoparticles drop cast on the surface after adsorption of the released SO_2, showed no statistical difference when compared to those obtained by the conventional method. In addition, the SERS method reduced the time of sample preparation and eliminated interference associated with other volatile components in wine samples, known to interfere.[223] The SO_2 released from wine was also measured by using a complex hybrid of 4-mercaptopyridine-modified Au nanorods with reduced graphene oxide and starch-iodine complex, coated on filter paper. The fabricated paper was able to achieve both colorimetric and SERS detections of the released SO_2. The decomposition of the starch-iodine complex on adsorption of SO_2 from wine, resulted in a decrease in colour intensity of the fabricated paper, leading to colorimetric detection, while 4-mercaptopyridine conversion to pyridine methyl sulphate led to SERS enhanced signals of the resulting complex. The substrate was able to detect the SO_2 released in the range of between 5–200 µM and with the change in color intensity and in combination with SERS, released SO_2 detection range was 0.1–5000 µM, which was better than the conventional UV-vis spectroscopic range of 10–1000 µM.[224]

A combination of microfluidic and SERS-based on paper substrates was used to identify and measure the presence of beta-agonist, a prohibited livestock feed additive. The substrates were designed with microfluidic channels to enable the separation of analytes from extraneous materials in the extractive *via* filtration. By doping of analytes and comparison of SERS signals, clenbuterol, ractopamine and salbutamol were identified in a multiplexed study with detection limits of 20, 20 and 30 ng/mL in swine hair, respectively. Although primary concern is for the levels of these beta-agonists in tissues, the studies showed that the quality of livestock with respect to illicit application of beta-agonists can be accessed directly at farm sites with paper-based SERS.[225-226] Melamine in milk was detected to a limit of 10 ppm by using a specially designed paper-based SERS substrate in combination with microfluidic mechanism under centrifugal force, which effectively separated melamine from milk prior to SERS measurement.[227] Melamine in milk was also detected by using paper-based SERS fabricated by first using a fountain pen to introduce hydrophobic patterns on the paper, followed by coating with Ag nanoparticles by using fountain pen containing Ag nanoparticles. This simple innovation made it possible to produce a SERS substrate at point-of-need without any formal training by the end-user. The SERS substrate could detect melamine in milk to a limit of

detection of 0.27 mg/L without any sample pretreatment.[228] Chitosan modified paper, coated with AgNP was also used as SERS substrate for chromatographic separation and SERS detection of melamine, sodium sulfocyanate and dicyandiamide in milk. The substrate showed improved performance and the observed analytes detection limits were below the maximum allowed concentrations.[229] Moreover, Ag nanocubes encapsulated in silica was adsorbed on filter paper in order to fabricate SERS substrate for the quantification of melamine in milk. The assemblage of the nanocubes facilitated by fibrous nature of filter paper was considered as a key factor in the enhancement provided by the substrate in the detection of melamine below the permissible limit.[230] Paper-based SERS substrate was fabricated by coating paper with Au nanoparticles obtained by plant extract-mediated reduction of Au^{3+}. The paper fibrous morphology provided platform for the assemblage of the Au nanoparticles, which showed significant SERS signal enhancement in the detection of tyrosine and melamine with detection limits of 10^{-10} M and 10^{-9} M, respectively.[231]

2.6.5 Dye identification in artworks

The study of artworks, especially paintings, drawings and archaeological textiles, involves the identification of dye in order to authenticate individual items and determine their origins. Paper-based SERS have shown a potential in the identification of historic dyes, commonly found in artworks. Ag thermally evaporated on filter paper stained with lac, alizarin and carminic acid dyes showed improved SERS signals and quenched the associated fluorescence of the dye.[131] Components of inks from historical felt-tip pens were analyzed with paper-based SERS substrate coated with Ag nanoparticles obtained by citrate reduction of Ag^{+} ions. Lines drawn on paper by using the pens were coated with Ag nanoparticles and allowed to dry before SERS measurements. The dye components of different inks from the historical felt-tip pens, were identified by matching their corresponding SERS signals with those of known dyes.[232]

2.7 Other forms of cellulose for SERS substrate design

The use of cellulose paper in SERS substrate design pre-dated and dominated the use of all other forms of cellulose and its derivatives. However, in recent times, the uses of other forms of cellulose-based materials, especially those with nano-dimensions, have become significant. The emerging innovations used in the fabrication of these substrates are worth appraising in order to further explore their applications in SERS.

2.7.1 Cellulose fabrics and membranes

The flexibility and the porous nature of cellulose fabrics and membranes have made them suitable in SERS substrate design for concentration and detection of analytes from highly diluted gaseous or liquid samples. A cellulose fabric-based SERS substrate was designed by coating the fabric with Ag nanoparticles ink, followed by heating at 180ºC in order to induce a "hot spot" within the fabric. The substrate was used to detect nicotine from cigarette smoke filtered through the SERS substrate, and also to detect albuterol, a component of an asthma metered dose inhaler, from air mixture. The porosity of the SERS substrate fabric played a significant role in the trapping of the analytes, leading to their SERS detection.[233] Cotton swabs were used to fabricate SERS substrates that are suitable for the detection of analytes from a contaminated surface. The cotton swabs-based SERS substrates were prepared *via* three routes, thus: by firstly modifying with (3-aminopropyl)trimethoxysilane, followed by self-assembling of Ag nanoparticles on the modified swabs. Secondly, an *in-situ* method was adopted to grow Ag nanoparticles on cotton swabs by using $NaBH_4$ as reducing agent, and thirdly a combination of self-assembling and *in-situ* methods was also adopted. The combined methods afforded a uniform coating of the cotton swab with Ag nanoparticles with improved SERS performance when compared to other substrates for the detection of trace amounts (1.2 ng/cm^2) of 2,4-dinitrotoluene from a contaminated glass surface. The soft and flexible nature of the cotton swab aided the sampling of the analyte from the contaminated surface.[105] The soft and flexible nature of cotton fabric was also explored to fabricate a SERS swab for the detection of carbaryl (a pesticide) on apple fruit. Cotton fabric was first swollen in NaOH solution at 90 ºC in order to improve the absorption capacity of the fabric for Ag^+ ions, which was later reduced *in-situ* with sodium citrate.[234] It is obvious that the soft and flexible nature, as well as the ease of fabrication of cellulose cotton-based SERS substrates transform to an emerging prominent analytical tool.

Regenerated fibres from de-inked pulp have been considered as a low cost substrate in the fabrication of SERS substrate. Fibres from de-inked pulp were functionalized with glycidyltrimethylammonium chloride in order to induce a cationic surface for uniform coating of Ag nanoparticles. The SERS substrate was used to detect rhodamine 6G and melamine to nM concentration levels.[235] A recent report has also shown the possibility of using cellophane (a regenerated, transparent, smooth and flexible cellulose membrane) in the fabrication of a SERS substrate. Cellophane was coated *in-situ* with Ag nanoparticles by immersion in a solution of Ag^+ ions followed by glucose reduction. The cellophane-based substrate showed similar SERS enhancement to a paper-based substrate when used to obtain the SERS signals

of crystal violet dye and acetamiprid (a pesticide), down to a concentration of 10^{-9} and 10^{-6} M, respectively.[236] Similar to how cellulose can serve as SERS substrate, it also has the capacity to host SERS nanocomposites consisting of plasmonic nanoparticles on the substrate. A SERS substrate was fabricated by hosting a nanocomposite of Ag nanoparticles, deposited on amine-functionalized spherical silica within cellulose micropores. The substrate showed improved SERS signals of rhodamine B since several "hot spots" were induced due to the proximity of the Ag nanoparticles on silica, unlike Ag nanoparticles on cellulose.[237]

2.7.2 Surface modified cellulose

Chemical modification of cellulose makes it possible to introduce non-inherent physical and chemical properties for the fabrication of cellulose-based materials in order to meet specific needs. A few of the modified cellulose materials find application in SERS substrate designs. These include: cellulose acetate (CA), methylcellulose (MC), nitrocellulose, hydroxyethylcellulose (HEC) and hydroxymethylcellulose (HMC). Cellulose acetate (CA) is a derivative of cellulose, which can be dissolved in a suitable solvent system to form a membrane. Such membranes have been shown to serve as a platform for SERS substrates, either as hydrogel or transparent film. Kurokawa in 1991 first reported the use of CA-based SERS substrate. A membrane of CA was obtained by dissolving CA in formamide-acetone solvent mixture, followed by gelation in an ice-cold water bath. The membrane was impregnated with hydrous Ag_2O by diffusion of $AgNO_3$ and NaOH across its surface. A SERS substrate was obtained after immersion of the impregnated membrane in $NaBH_4$ solution for *in-situ* reduction of the hydrous Ag_2O. The fabricated CA-based SERS substrate was used to obtain SERS spectra of pyridine and SCN^- from aqueous solution.[238] The same fabrication method, a CA-based SERS substrate was prepared and used to detect trace amounts of: uridine, nicotine, ellipticine and quinacrine hydrochloride, in the concentration range of between 10^{-5}–10^{-7} M.[239] In other reports, it was used for the detection of picolinic and nicotinic acids,[240] bipyridine, phthalimide, phenylethylamine and theobromine,[241] as well as benzoic and thiosalicylic acids.[242]

The concepts of electrospraying and electrospinning have been adopted in CA-based SERS substrate design (Fig. 2.9). Ag nanocubes were embedded in CA microspheres formed by electrospraying of a solution containing the nanocubes and CA in dimethylacetamide. However, co-electrospinning of solutions containing the nanocubes and CA resulted in the formation of nanofibres. The SERS substrate fabricated by electrospraying techniques showed higher loading of Ag nanocubes, accumulated within the CA microspheres when compared to

the electrospun substrate where the nanocubes were distributed on the nanofibres. The Ag nanocube embedded microsphere showed improved SERS performance for the detection of *p*-aminothiophenol (a probe molecule) and methyl parathion (a toxic pesticide), down to concentrations of 10^{-9} and 10^{-6} M, respectively.[243] The nanoporous nature of the CA membrane was exploited to accumulate Au nanoparticles when a solution containing the nanoparticles was filtered by using CA membrane. The substrate obtained was used for detection of carboxylated single-wall carbon nanotubes to a limit of 10 µg/L in water.[244] A mixed cellulose ester (MCE) membranes has also been used as a substrate to monitor the development of biofilms, which is a bacteria colony-causing fouling in membrane. The development and competition between *Brevundimonas diminuta* and *Staphylococcus aureus* were monitored as single- and dual-species biofouling agent on MCE by using Au nanoparticles cast on the membrane.[245]

Another important class of modified cellulose in SERS substrate design is methyl cellulose (MC), which is a water soluble polymer obtained by the substitution of the cellulose hydroxyl groups, resulting in low crystallinity. The gelatinous nature of wet MC and its non-sticky nature on drying, makes it suitable for the fabrication of non-invasive SERS substrate for artwork. A removable SERS substrate was designed for the detection of dye components in artworks by doping MC gel with Ag nanoparticles, reduced with glucose. The SERS substrate obtained was allowed to dry on a small area of an artwork to be investigated for its dye components. After SERS measurement, the substrate was easily removed without any visible damage to the artwork.[246] However, further investigation showed that on removal of the substrate, a few layers of painting (approximately 60 µm) was lost. Following the optimization of the substrate design, the loss of painting layer was reduced to less than 20 µm after detachment. It should be noted that the substrate was found not to be suitable for dye analysis on coloured paper because the substrate gel penetrated the paper matrix and could not be easily removed after SERS measurement.[247] A MC-based substrate was also designed to detect rhodamine 6G in water; the study showed the shape-directing influence of MC in the synthesis of Ag nanoparticles in the presence of citrate as reducing agent. Ag nanoparticles of various shapes were obtained with varying concentrations of MC, leading to the formation of "hot spots" for the detection of rhodamine 6G.[248] Similar to MC, nitrocellulose was also employed in SERS substrate design. A SERS substrate fabricated by inkjet printing of Au nanoparticles on nitrocellulose showed improved performance when compared to paper-based SERS for the detection of 1,2-bis(4-pyridyl)ethylene and thiram.[180]

The need to prolong the storage lifetime of plasmonic nanoparticles for SERS applications makes hydroxyethylcellulose (HEC) an important class of modified cellulose in SERS substrate design. The ability of HEC to dry as thin films and swell into a hydrogel in an aqueous environment makes it suitable for the fabrication of a free-standing film, which not only allows metal nanoparticles to be stored and stabilized for longer period in a dry state under ambient conditions, but also makes them available when required for SERS measurement by swelling with aqueous samples. With this substrate design, Ag nanoparticles stabilized in HEC was used to obtain SERS spectra of: adenine, crystal violet, nicotine, potassium thiocyanate, melamine and tris(bispyridine)ruthenium(II) nitrate as proof-of-concept. It was further applied in the monitoring of theophylline, a therapeutic drug, and a concentration as low as 1.8 mg/L could be discerned from SERS signal, which was below the sensitivity range (10–20 mg/L) required for the monitoring of the drug.[249] The same substrate was employed in other studies for the detection of psychoactive substances in seized drug samples[250] and in the monitoring of phenytoin,[251] a therapeutic drug. However, the stronger influence of Ag nanoparticles for Cl^- ions limited the application of the SERS substrate in a phosphate-buffered saline solution during the monitoring of phenytoin. This limitation was overcome by using similar SERS substrate-containing Au nanoparticles instead of Ag. Hydroxypropylcellulose (HPC) is another modified cellulose used in substrate design for the stabilization of photo-reduced Ag nanoparticles. A hydrogel of HPC-containing Ag^+ ions was irradiated with UV light in order to induce the *in-situ* synthesis of Ag nanoparticles and the subsequently formed HPC-Ag nanoparticle hydrogel was used as a SERS substrate in the detection of organic dyes and pigments in artworks[252] and aqueous solution.[253]

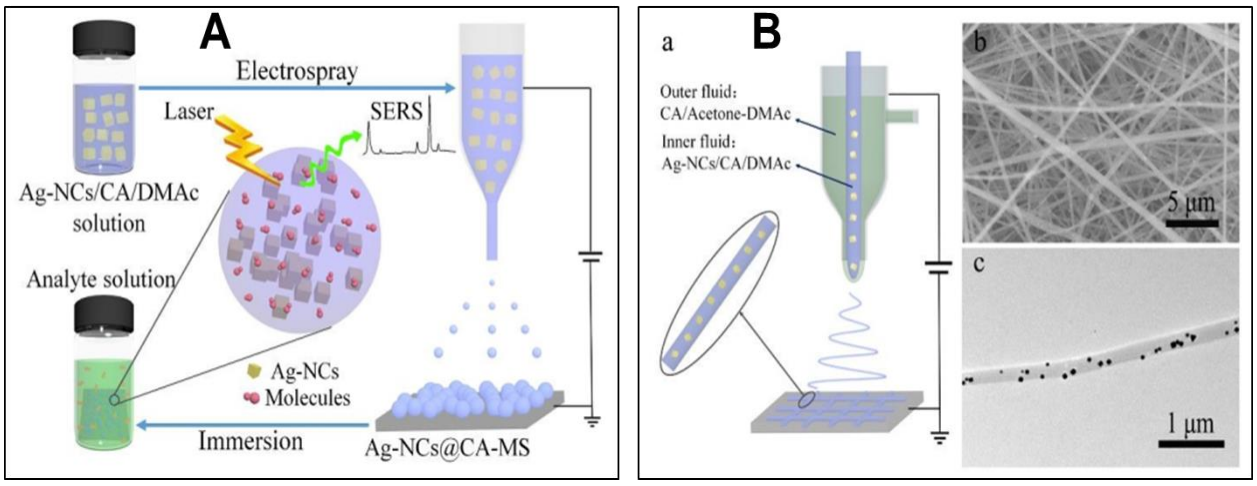


Fig. 2.9: CA-based SERS substrate fabricated by (A) electrospraying and (B) co-electrospinning techniques. Reproduced from ref. 243. Copyright 2017 with permission from Royal Society of Chemistry.

2.7.3 Cellulose nanofibrils

Cellulose nanofibrils (CNFs) obtained by TEMPO-mediated oxidation of cellulose, followed by homogenization with mechanical blending have been known to serve as capping and shape-inducing agents in the synthesis of metal nanoparticles through the surface carboxylate groups resulting from oxidation process.[17] CNFs isolated from rice straw were used in the synthesis of Ag nanospheres by using $NaBH_4$ as reducing agent. The nanospheres were converted to nanoprisms using H_2O_2 as while CNFs served as a shape-inducing agent, directing the formation of the nanoprisms with the surface of carboxylate groups, thus passivating the capped facets [111] of the Ag nanospheres, while the uncapped facets etched-off. The CNF-Ag nanoprisms composite solution was filtered under vacuum over a membrane in order to obtain a SERS nanocomposite film. Unlike the CNF-Ag nanospheres that showed LSPR at 402 nm, the CNF-Ag nanoprisms showed UV-vis absorption characteristics peaks at 334 nm (associated with out-of-plane quadruple resonance) and in the range of between 762–866 nm (associated with in-plane dipole resonance) making it suitable for probing low concentrations of rhodamine 6G with a 785 nm laser beam wavelength which was within the range 762–866 nm observed in the CNF-Ag nanoprisms film, leading to strong SERS enhancement.[254] In addition to the capping and shape-inducing capacity of CNF in the synthesis of metal nanoparticles, CNF can also act as a reducing agent due to the presence of surface hydroxyl groups and auto-hydrolysis of CNF at high temperature under hydrothermal conditions. Based on this concept, a CNF-Ag nanoparticle composite was fabricated by hydrothermally reducing Ag^+ ions on CNF, isolated from kenaf core. On freeze-drying the product obtained, a porous fibrous material was obtained, which served as a SERS substrate probed with rhodamine B and also as catalyst in the reduction of rhodamine B with $NaBH_4$.[255] Similarly, when CNF obtained from banana pseudo stem combined with trisodium citrate as both reducing and co-stabilizing agent, flower-like Ag nanoparticles were obtained, which showed strong enhancement for the detection of *p*-aminothiophenol down to 10^{-17} M in colloidal solution.[256] Besides the reducing capability of CNF, aggregation of metal nanoparticles can also be induced by CNF to create a "hot spot" on SERS substrate. The nanoscale width of CNF and the surface hydroxyl groups provided a mean of immobilizing metal nanoparticles. A substrate was fabricated by using CNF obtained from softwood pulp in order to induce aggregation of citrate stabilized Au nanoparticles on glass to generate a "hot spot", which showed strong and reproducible SERS enhancement for *p*-aminothiphenol.[257] The SERS substrate was also employed to detect rhodamine B and dopamine to a concentration limit of 10^{-12} M for both analytes.[258] A CNF

aggregated citrate stabilized Au nanoparticles was also used as SERS substrate to detect melamine in milk, down to 0.5 ppm.[259]

The role of CNF on preventing uncontrolled aggregation of metal nanoparticles in SERS substrate design was also studied by using CNF/PVA composite film coated *in-situ* with Ag nanoparticles by reduction of adsorbed Ag^+ ions. When analyte solution was introduced to the composite, it was observed that CNF minimized the disruption of the "hot spot", leading to reproducible SERS signals. The surface hydroxyl groups and porous nature of CNF were observed to immobilize Ag nanoparticles and prevent uncontrolled aggregation at low pH leading to the detection of thiabendazole pesticide in a spiked apple at a pH below its pKa. This could not be detected at neutral pH since thiabendazole is a neutral molecule at higher pH, making its SERS detection difficult due to poor interaction with the Ag nanoparticle surface.[260]

With nanopores and rich hydroxyl surface, a CNF membrane was used as a nanofilter-SERS substrate to pre-concentrate plasmonic Au nanorods and analytes on its surface. The capacity of the CNF membrane as nanofilter, showed that it could retain 95% of rhodamine 6G molecules from 100 nM solution, making it suitable for the detection of the dye, down to a detection limit of 10^{-12} M. The SERS membrane also retained biological cells of *E. coli* when a solution containing the bacteria was filtered through it. SERS signals associated with amino acids present in *E. coli* cells were detected by using a 785 nm laser as excitation wavelength.[261]

The power of attraction of CNF for metal nanoparticles can be improved by making CNF acquire a net positive charge on the surface to electrostatically attract negatively charged metal nanoparticles. With this idea, SERS spectra of thiram pesticide in spiked apple juice were studied by using CNF modified with (2,3-epoxypropyl)trimethylammonium chloride to form a net positive charge on the surface for the electrostatic attraction of negatively charged Au nanoparticles, stabilized with citrate. The modified CNF was uniformly coated with Au nanoparticles, leading to a homogenous distribution of the "hot spot", which provided an enhanced SERS signal of thiram in apple juice, with a detection limit of 52 ppb. In addition, the intensity of *p*-aminothiophenol was found to be 20 times higher when compared to paper-based substrate.[262] Although paper-based SERS has been used extensively, a recent study showed that its sensitivity and reproducibility were found to improve when coated with CNF because it reduces the surface roughness of the paper. The study revealed that the CNF-coated paper showed improved sensitivity and reproducibility for SERS detection of *p*-aminothiophenol, with a limit of 1.56 nM and a relative standard deviation (RSD) of 9%, unlike the untreated paper with a limit of detection of 20.02 nM and RSD of 27%.[263]

2.7.4 Bacterial cellulose

Cellulose nanofibres with a 3-D network produced by bacteria, especially *Acetobacter xylinus* have been used in the design of SERS substrate. A bacterial cellulose (BC)-based SERS substrate was first reported by Marques *et al.*, in 2008, who observed that the high water holding capacity of these nanofibres made them suitable to adsorb Ag^{+} ions from solution which, were later reduced *in-situ* with sodium citrate to form a SERS substrate. For comparison, wood cellulosic fibres, obtained from *Eucalyptus globulus*, were also used to prepare a SERS substrate by *in-situ* reduction of Ag^{+} with the same experimental conditions. Unlike colloidal solution of Ag nanoparticles, the BC-based substrates required no aggregating agent for Ag nanoparticles before SERS measurements. The BC SERS substrate showed improved SERS signals for thiosalicylic acid and 2,2'-dithiodipyridine when compared with wood cellulose-based substrate. The observed improvement was attributed to the nanofibrous nature of BC, unlike wood cellulose that consists of microfibres with low surface area for Ag nanoparticles adsorption. The potential of the BC SERS substrate was further evaluated by using it to detect amino acids in aqueous solution.[264] Similarly, BC was used to prepare a SERS substrate nanocomposite, consisting of Au nanoparticles. The substrate was prepared by *in-situ* reduction of Au^{3+} ions by using sodium citrate as reducing agent. At high concentration of $HAuCl_4$, Au nanoplates were formed, while at low concentration Au nanospheres were obtained. It was observed that the nano-dimension of BC fibres provided a large volume fraction for the adsorption of the nanoparticles. The hydroxyl groups of BC also played a significant role by forming hydrogen bonds with the carboxylate of citrate-stabilized Au nanoparticles. The substrate was probed by using malachite green isothiocyanate and rhodamine 6G. The study showed that as the SERS substrate dried over time, the SERS signals of the probes improved significantly. This observation was attributed to the formation of a "hot spot" as adjacent Au nanoparticles coupled on the elimination of interstitial water within the BC. The substrate applicability was demonstrated for quantification of atrazine (an environmental contaminant) at pH 1.3 with a linear range of between 0.25–250 µM.[265]

The stability of Au nanoparticles on BC at low pH provides a suitable medium to detect neutral organic environmental pollutants, which cannot be detected at neutral or basic pH. A SERS Au/BC nanocomposite substrate prepared by *in-situ* reduction of Au^{3+} ions in a boiling solution of sodium citrate was employed at very low pH (< 2) below the pKa of targets analytes to detect atrazine and carbamazepine to limits of 11 and 3 nM, respectively. At such pH, the analytes were in their cationic forms, making them to be electrostatically attached to the Au nanoparticles, hence enhancing the SERS signals of the analytes, which were not significantly

enhanced at higher pH.[266] A SERS substrate was also fabricated by *in-situ* reduction of Au^{3+} ions on BC, however, the reduction was photoinduced in an ice-bath under a Xenon lamp without the use of any chemical agent. On drying the substrate, a nanopaper was obtained, which showed strong enhancement for SERS of rhodamine 6G with a detection limit of 10^{-10} M. The nanopaper was also used in identifying dyes present in ballpoint pens and dyed cotton fabrics.[267] The rich surface hydroxyl groups on BC was used as reducing- and stabilizing agent when BC was dipped in a boiling solution of $HAuCl_4$. The Au^{3+} ions were reduced *in-situ* within the BC interlayers. The influence of the drying rate on SERS performance of the BC-substrate was demonstrated by probing the wet and dry BC-substrates with phenylacetic acid. At low concentration (10^{-7} M), no SERS signal was observed with wet BC-substrate hydrogel while with the dry substrate, SERS signals were observed. The observed difference in SERS performance was attributed to the formation of "hot spots" in dry BC-SERS since the interlayer distance shrank on drying into nano-gaps. A similar improvement in SERS enhancement was observed when the BC-substrate was probed with 4-fluorobenzenethiol.[268]

Although *in-situ* coating of BC ensures uniform distribution of plasmonic nanoparticles within the micropores, SERS enhancement capacity of BC-based SERS substrate can be greatly improved if plasmonic nanoparticles are concentrated on the surface and subsurface of BC, since SERS is a surface phenomenon. Against this background, Au nanorods were filtered through hydrated BC film. The nanorods were densely retained on the surface and trapped within the subsurface layers, resulting in a 10 times improved performance of the BC-SERS substrate with rhodamine 6G as a SERS probe, when compared to a similarly treated paper-based substrate. The substrate also showed improved SERS performance for the detection of *E. coli* bacteria collected from a leaf surface by swabbing. The SERS signals of amino acids and DNA present in *E coli* cells served as an identification tag.[269] Unlike drying of BC at ambient temperature, freeze drying of BC at low temperature results in the formation of aerogel with 3-D porous nanofibres and high metal nanoparticles loading capacity. A freeze-dried BC-Au nanorod composite SERS substrate showed a 10 times improved performance for vapor sensing of 2-naphthalenethiol when compared to plasmonic paper. The higher performance of the aerogel was attributed to the accessibility of the Au nanorods to analyte vapor and higher volume distribution due to the 3-dimensional porous structure of the aerogel, unlike the 2-D plasmonic paper.[270]

2.7.5 Nanocrystalline cellulose

Nanocrystalline cellulose (NCC) isolated by acid hydrolysis of cellulose is well known as an important class of nanocellulose, due to its high crystallinity and mechanical strength however its application in SERS substrate design is limited. The first use of NCC in SERS substrate design was as a composite obtained by electrospinning of a precursor suspension containing polyacrylonitrile, NCC, Si and Ag nanoparticles.[271] The composite nanofibres were obtained immersed in HF in order to etch off the embedded Si nanoparticles and introduce nanopores on the fibres. The presence of the NCC improved the thermal stability of the composite material and served as a stabilizing agent for the Ag nanoparticles. With the composite as substrate, the SERS signals of *p*-aminothiophenol was obtained with an enhancement factor of 3.9 x 10^3. Recently, the use of NCC isolated from discarded cigarette filters in the synthesis of Ag nanoparticles with the dual role of functioning as reducing- and stabilizing agent without any other additives was reported. It was observed that the size and yield of Ag nanoparticles varied with pH, concentration and reaction time. The sensitivity of the NCC-Ag nanocomposite colloid showed a reproducible SERS signal of riboflavin with a limit of detection of 3 x 10^{-7} M, based on a signal-to-noise ratio of 3:1. The NCC-Ag nanocomposite colloid remained stable and SERS active for more than a year without aggregation and can also be easily coated on paper as SERS substrate.[272] Although NCC is well known for its unique properties and diverse applications, its use in SERS substrate design is new, making it a versatile area to be explored for fabrication of new improved SERS substrate with prolific applications in real-life.

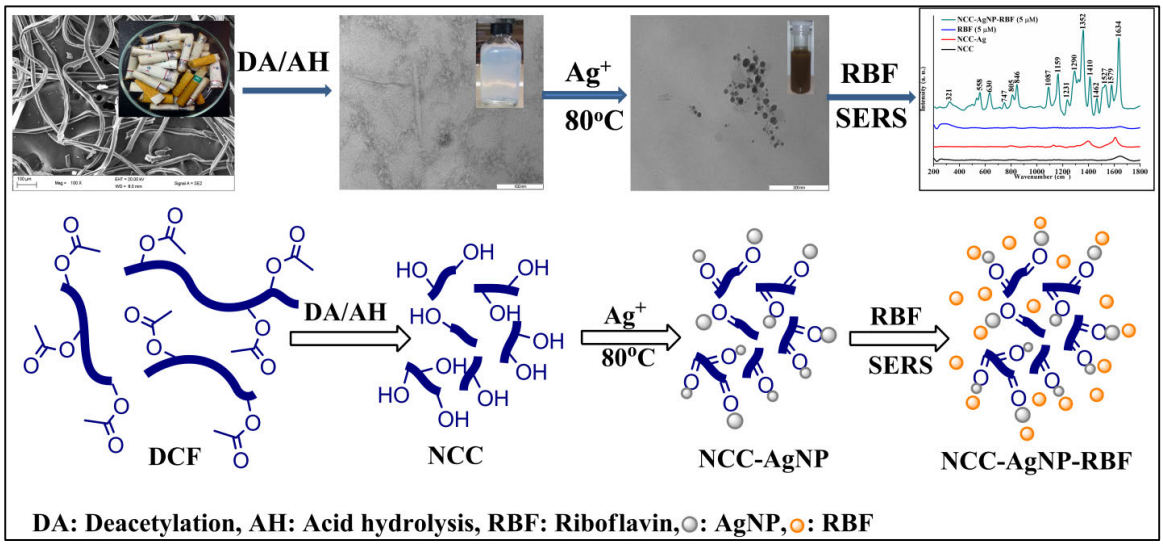


Fig. 2.10: Schematic illustration of NCC-based SERS substrate. Reprinted from ref. 272. Copyright 2018 with permission from Elsevier.

2.8 Conclusions and outlook

The contributions of cellulose in SERS substrate design since its first use in 1984, has been astonishing and also very consistent over the years with promising and innovative applications in many fields of life, demanding fast, accurate, reliable sensing devices at low cost. These remarkable contributions have been highlighted in this review with conscious efforts to present a summary of the advancements made in fabricating improved sensing devices towards accomplishing a platform where a SERS substrate can be made ubiquitous to end-users at home. This ideal is fast becoming a reality since portable Raman spectrometers are now available at affordable prices. However, the need to circumvent the scarcity of affordable and reliable SERS substrates remain elusive and a barrier to overcome for actualization of this technology. In order to achieve this, the diverse and rich research findings on SERS substrates, especially cellulose-based substrates must be converged towards fabricating an end-user friendly SERS substrate that can attract market value.

A cellulose paper-based substrate looks most promising in this regard, however, much is still required to make it more attractive with multifunctional SERS sensing capacity that will serve the everyday purpose of potential consumers. This can only be achieved if a universal testing standard is set, on which new SERS substrates can be evaluated. Currently, many techniques of fabricating SERS substrates exist but there are associated challenges in relation to sensitivity and reproducibility. Although efforts have been made to address many of these challenges in paper-based substrates, the corresponding outcomes cannot be substantiated beyond laboratory level due to the absence of universal testing standard.

Cellulose-based SERS substrates, especially those combined with NCC, which is still in its infancy in SERS applications, should foresee a bright future, not least because NCC has unique properties not found in other forms of cellulose. These include the chiral nematic arrangement of nanocrystals upon drying to form iridescent films[273] with tunable optical properties, which can be transferred to other materials. The response of NCC to external magnetic and electrical fields[65] can also show an unprecedented impact to explore SERS substrate design.

2.9 References

(1) Zong, C.; Xu, M.; Xu, L.-J.; Wei, T.; Ma, X.; Zheng, X.-S.; Hu, R.; Ren, B. Surface Enhanced Raman Spectroscopy for Bioanalysis: Reliability and Challenges. *Chem. Rev.* **2018**, *118*, 4946–4980.

(2) Li, J.-F.; Zhang, Y.-J.; Ding, S.-Y.; Panneerselvam, R.; Tian, Z.-Q. Core–Shell Nanoparticle-Enhanced Raman Spectroscopy. *Chem. Rev.* **2017**, *117*, 5002–5069.

(3) Radziuk, D.; Moehwald, H. Prospects for Plasmonic Hot Spots in Single Molecule SERS towards the Chemical Imaging of Live Cells. *PhysChemChemPhys.* **2015**, *17*, 21072–21093.

(4) Schlücker, S. Surface-Enhanced Raman Spectroscopy: Concepts and Chemical Applications. *Angew. Chem. Int. Ed.* **2014**, *53*, 4756–4795.

(5) Sharma, B.; Frontiera, R. R.; Henry, A.-I.; Ringe, E.; Van Duyne, R. P. SERS: Materials, Applications, and the Future. *Mater. Today* **2012**, *15*, 16–25.

(6) Laing, S.; Jamieson, L. E.; Faulds, K.; Graham, D. Surface-Enhanced Raman Spectroscopy for *in vivo* Biosensing. *Nat. Rev. Chem.* **2017**, *1*, 0060.

(7) Raman, C. V.; Krishnan, K. S. A New Type of Secondary Radiation. *Nature* **1928**, *121*, 501.

(8) Fleischmann, M.; Hendra, P. J.; McQuillan, A. J. Raman Spectra of Pyridine Adsorbed at a Silver Electrode. *Chem. Phys. Lett.* **1974**, *26*, 163–166.

(9) Jeanmaire, D. L.; Van Duyne, R. P. Surface Raman Spectroelectrochemistry: Part I. Heterocyclic, Aromatic, and Aliphatic Amines Adsorbed on the Anodized Silver Electrode. *J. Electroanal. Chem. Interfacial Electrochem.* **1977**, *84*, 1–20.

(10) Albrecht, M. G.; Creighton, J. A. Anomalously Intense Raman Spectra of Pyridine at a Silver Electrode. *J. Am. Chem. Soc.* **1977**, *99*, 5215–5217.

(11) Creighton, J. A.; Blatchford, C. G.; Albrecht, M. G. Plasma Resonance Enhancement of Raman Scattering by Pyridine Adsorbed on Silver or Gold Sol Particles of Size Comparable to the Excitation Wavelength. *J. Chem. Soc., Faraday Trans. 2* **1979**, *75*, 790–798.

(12) Kneipp, K.; Wang, Y.; Kneipp, H.; Perelman, L. T.; Itzkan, I.; Dasari, R. R.; Feld, M. S. Single Molecule Detection Using Surface-Enhanced Raman Scattering (SERS). *Phys. Rev. Lett.* **1997**, *78*, 1667.

(13) Nie, S.; Emory, S. R. Probing Single Molecules and Single Nanoparticles by Surface-Enhanced Raman Scattering. *Science* **1997**, *275*, 1102–1106.

(14) Bjerneld, E. J.; Földes-Papp, Z.; Käll, M.; Rigler, R. Single-Molecule Surface Enhanced Raman and Fluorescence Correlation Spectroscopy of Horseradish Peroxidase. *J. Phys. Chem. B* **2002**, *106*, 1213–1218.

(15) Haynes, C. L.; Yonzon, C. R.; Zhang, X.; Van Duyne, R. P. Surface-Enhanced Raman Sensors: Early History and the Development of Sensors for Quantitative Biowarfare Agent and Glucose Detection. *J. Raman Spectros.* **2005**, *36*, 471–484.

(16) Henry, A.-I.; Sharma, B.; Cardinal, M. F.; Kurouski, D.; Van Duyne, R. P. Surface-enhanced Raman Spectroscopy Biosensing: *In vivo* Diagnostics and Multimodal Imaging. *Anal. Chem.* **2016**, *88*, 6638–6647.

(17) Kaushik, M.; Moores, A. Review: Nanocelluloses as Versatile Supports for Metal Nanoparticles and their Applications in Catalysis. *Green Chem.* **2016**, *18*, 622–637.

(18) Shervani, Z.; Ikushima, Y.; Sato, M.; Kawanami, H.; Hakuta, Y.; Yokoyama, T.; Nagase, T.; Kuneida, H.; Aramaki, K. Morphology and Size-Controlled Synthesis of Silver Nanoparticles in Aqueous Surfactant Polymer Solutions. *Colloid. Polym. Sci.* **2008**, *286*, 403–410.

(19) Maxwell, E. J.; Mazzeo, A. D.; Whitesides, G. M. Paper-Based Electroanalytical Devices for Accessible Diagnostic Testing. *MRS Bull.* **2013**, *38*, 309–314.

(20) Martinez, A. W.; Phillips, S. T.; Whitesides, G. M.; Carrilho, E. Diagnostics for the Developing World: Microfluidic Paper-based Analytical Devices. *Anal. Chem*. **2010**, *82*, 3–10.

(21) Cate, D. M.; Adkins, J. A.; Mettakoonpitak, J.; Henry, C. S. Recent Developments in Paper-Based Microfluidic Devices. *Anal. Chem.* **2014**, *87*, 19–41.

(22) Marks, H.; Schechinger, M.; Garza, J.; Locke, A.; Coté, G. Surface Enhanced Raman Spectroscopy (SERS) for *in vitro* Diagnostic Testing at the Point of Care. *Nanophotonics* **2017**, *6*, 681–701.

(23) Campion, A.; Kambhampati, P. Surface-Enhanced Raman Scattering. *Chem. Soc. Rev.* **1998,** *27*, 241–250.

(24) McNay, G.; Eustace, D.; Smith, W. E.; Faulds, K.; Graham, D. Surface-Enhanced Raman Scattering (SERS) and Surface-Enhanced Resonance Raman scattering (SERRS): A Review of Applications. *Appl. Spectrosc.* **2011**, *65*, 825–837.

(25) Ding, S.-Y.; Yi, J.; Li, J.-F.; Ren, B.; Wu, D.-Y.; Panneerselvam, R.; Tian, Z.-Q. Nanostructure-Based Plasmon-enhanced Raman Spectroscopy for Surface Analysis of Materials. *Nat. Rev. Mater.* **2016**, *1*, 1–16.

(26) Alonso-González, P.; Albella, P.; Schnell, M.; Chen, J.; Huth, F.; García-Etxarri, A.; Casanova, F.; Golmar, F.; Arzubiaga, L.; Hueso, L. Resolving the Electromagnetic Mechanism of Surface-Enhanced Light Scattering at Single Hot Spots. *Nat. Commun.* **2012**, *3*, 1–7

(27) Schatz, G. C.; Van Duyne, R. P. *Electromagnetic Mechanism of Surface-Enhanced Spectroscopy;* John Willey and Sons, Ltd. New York, 2006: pp 19–41.

(28) Haynes, C. L.; McFarland, A. D.; Van Duyne, R. P. Surface-Enhanced Raman Spectroscopy. *Anal. Chem.* **2005**, 77, 338 A–364 A.

(29) Nam, J.-M.; Oh, J.-W.; Lee, H.; Suh, Y. D. Plasmonic Nanogap-Enhanced Raman Scattering with Nanoparticles. *Acc. Chem. Res.* **2016**, *49*, 2746–2755.

(30) Klemm, D.; Heublein, B.; Fink, H. P.; Bohn, A. Cellulose: Fascinating Biopolymer and Sustainable Raw Material. *Angew. Chem. Int. Ed.* **2005**, *44*, 3358–3393.

(31) Moon, R. J.; Martini, A.; Nairn, J.; Simonsen, J.; Youngblood, J. Cellulose Nanomaterials Review: Structure, Properties and Nanocomposites. *Chem. Soc. Rev.* **2011**, *40*, 3941–3994.

(32) Zhu, H.; Luo, W.; Ciesielski, P. N.; Fang, Z.; Zhu, J.; Henriksson, G.; Himmel, M. E.; Hu, L. Wood-Derived Materials for Green Electronics, Biological Devices, and Energy Applications. *Chem. Rev.* **2016**, *116*, 9305–9374.

(33) Jonoobi, M.; Oladi, R.; Davoudpour, Y.; Oksman, K.; Dufresne, A.; Hamzeh, Y.; Davoodi, R. Different Preparation Methods and Properties of Nanostructured Cellulose from various Natural Resources and Residues: A Review. *Cellulose* **2015**, *22*, 935–969.

(34) Brinchi, L.; Cotana, F.; Fortunati, E.; Kenny, J. Production of Nanocrystalline Cellulose from Lignocellulosic Biomass: Technology and Applications. *Carbohydr. Polym.* **2013**, *94*, 154–169.

(35) Lin, N.; Huang, J.; Dufresne, A. Preparation, Properties and Applications of Polysaccharide Nanocrystals in Advanced Functional Nanomaterials: A Review. *Nanoscale* **2012**, *4*, 3274–3294.

(36) Junka, A.; Fijałkowski, K.; Ząbek, A.; Mikołajewicz, K.; Chodaczek, G.; Szymczyk, P.; Smutnicka, D.; Żywicka, A.; Sedghizadeh, P. P.; Dziadas, M. Correlation between Type of Alkali Rinsing, Cytotoxicity of Bio-Nanocellulose and Presence of Metabolites within Cellulose Membranes. *Carbohydr, Polym.* **2017**, *157*, 371–379.

(37) Leitch, M. E.; Li, C.; Ikkala, O.; Mauter, M. S.; Lowry, G. V. Bacterial Nanocellulose Aerogel Membranes: Novel High-Porosity Materials for Membrane Distillation. *Environ. Sci. Tech. Lett.* **2016**, *3*, 85–91.

(38) Cerrutti, P.; Roldán, P.; García, R. M.; Galvagno, M. A.; Vázquez, A.; Foresti, M. L. Production of Bacterial Nanocellulose from Wine Industry Residues: Importance of Fermentation Time on Pellicle Characteristics. *J. Appl. Polym. Sci.* **2016**, *133*, 1–9.

(39) Guo, X.; Chen, L.; Tang, J.; Jönsson, L. J.; Hong, F. F. Production of Bacterial Nanocellulose and Enzyme from [AMIM] Cl-Pretreated Waste Cotton Fabrics: Effects of Dyes on Enzymatic Saccharification and Nanocellulose Production. *J. Chem. Technol. Biotechnol.* **2016**, *91*, 1413–1421.

(40) Zhang, D.; Zhang, Q.; Gao, X.; Piao, G. A Nanocellulose Polypyrrole Composite Based on Tunicate Cellulose. *Int. J. Polym. Sci.* **2013**, *2013*,1–6.

(41) Azizi Samir, M. A. S.; Alloin, F.; Sanchez, J.-Y.; El Kissi, N.; Dufresne, A. Preparation of Cellulose Whiskers Reinforced Nanocomposites from an Organic Medium Suspension. *Macromolecules* **2004**, *37*, 1386–1393.

(42) Uetani, K.; Okada, T.; Oyama, H. T. Thermally Conductive and Optically Transparent Flexible Films with Surface-Exposed Nanocellulose Skeletons. *J. Mater. Chem. C* **2016**, *4*, 9697–9703.

(43) Xiang, Z.; Gao, W.; Chen, L.; Lan, W.; Zhu, J.; Runge, T., A comparison of Cellulose Nanofibrils Produced from *Cladophora glomerata* Algae and Bleached Eucalyptus Pulp. *Cellulose* **2016**, *23*, 493–503.

(44) Chen, Y. W.; Lee, H. V.; Juan, J. C.; Phang, S.-M. Production of New Cellulose Nanomaterial from Red Algae Marine Biomass *Gelidium elegans*. *Carbohydr. Polym.* **2016**, *151*, 1210–1219.

(45) Hua, K.; Strømme, M.; Mihranyan, A.; Ferraz, N. Nanocellulose from Green Algae Modulates the *in vitro* Inflammatory Response of Monocytes/Macrophages. *Cellulose* **2015,** *22*, 3673–3688.

(46) Hua, K.; Carlsson, D. O.; Ålander, E.; Lindström, T.; Strømme, M.; Mihranyan, A.; Ferraz, N. Translational Study between Structure and Biological Response of Nanocellulose from Wood and Green Algae. *RSC Adv.* **2014**, *4*, 2892–2903.

(47) García, A.; Gandini, A.; Labidi, J.; Belgacem, N.; Bras, J. Industrial and Crop Wastes: A New Source for Nanocellulose Biorefinery. *Ind. Crops and Prod.* **2016**, *93*, 26–38.

(48) Henrique, M. A.; Silvério, H. A.; Neto, W. P. F.; Pasquini, D. Valorization of an Agro-Industrial Waste, Mango Seed, by the Extraction and Characterization of its Cellulose Nanocrystals. *J. Environ. Management* **2013**, *121*, 202–209.

(49) Tsukamoto, J.; Durán, N.; Tasic, L., Nanocellulose and Bioethanol Production from Orange Waste Using Isolated Microorganisms. *J. Brazil. Chem. Soc.* **2013**, *24*, 1537–1543.

(50) Danial, W. H.; Majid, Z. A.; Muhid, M. N. M.; Triwahyono, S.; Bakar, M. B.; Ramli, Z. The Reuse of Wastepaper for the Extraction of Cellulose Nanocrystals. *Carbohydr. Polym.* **2015**, *118*, 165–169.

(51) Tang, Y.; Shen, X.; Zhang, J.; Guo, D.; Kong, F.; Zhang, N. Extraction of Cellulose Nano-crystals from Old Corrugated Container Fibre using Phosphoric Acid and Enzymatic Hydrolysis followed by Sonication. *Carbohydr. Polym.* **2015**, *125*, 360–366.

(52) Ogundare, S. A.; Moodley, V.; van Zyl, W. E. Nanocrystalline Cellulose Isolated from Discarded Cigarette Filters. *Carbohydr. Polym.* **2017**, *175*, 273–281.

(53) Zhu, H.; Helander, M.; Moser, C.; Stahlkranz, A.; Soderberg, D.; Henriksson, G.; Lindstrom, M. A Novel Nanocellulose Preparation Method and Size Fraction by Cross Flow Ultra-Filtration. *Curr. Org. Chem.* **2012**, *16*, 1871–1875.

(54) Dimic-Misic, K.; Puisto, A.; Gane, P.; Nieminen, K.; Alava, M.; Paltakari, J.; Maloney, T. The Role of MFC/NFC Swelling in the Rheological Behavior and Dewatering of High Consistency Furnishes. *Cellulose* **2013**, *20*, 2847–2861.

(55) Filson, P. B.; Dawson-Andoh, B. E. Sono-Chemical Preparation of Cellulose Nanocrystals from Lignocellulose Derived Materials. *Bioresour. Technol.* **2009**, *100*, 2259–2264.

(56) Li, W.; Zhao, X.; Huang, Z.; Liu, S. Nanocellulose Fibrils Isolated from BHKP Using Ultrasonication and their Reinforcing Properties in Transparent Poly(Vinyl Alcohol) Films. *J. Polym. Res.* **2013**, *20*, 1–7.

(57) Kumar, V.; Bollström, R.; Yang, A.; Chen, Q.; Chen, G.; Salminen, P.; Bousfield, D.; Toivakka, M. Comparison of Nano-and Microfibrillated CelluloseFilms. *Cellulose* **2014**, *21*, 3443–3456.

(58) Deepa, B.; Abraham, E.; Cherian, B. M.; Bismarck, A.; Blaker, J. J.; Pothan, L. A.; Leao, A. L.; De Souza, S. F.; Kottaisamy, M. Structure, Morphology and Thermal Characteristics of Banana Nanofibres obtained by Steam Explosion. *Bioresour. Technol.* **2011**, *102*, 1988–1997.

(59) Wang, Q.; Zhu, J.; Gleisner, R.; Kuster, T.; Baxa, U.; McNeil, S. Morphological Development of Cellulose Fibrils of a Bleached Eucalyptus Pulp by Mechanical Fibrillation. *Cellulose* **2012**, *19*, 1631–1643.

(60) Dufresne, A.; Dupeyre, D.; Vignon, M. R. Cellulose Microfibrils from Potato Tuber Cells: Processing and Characterization of Starch–Cellulose Microfibril Composites. *J. Appl. Polym. Sci.* **2000**, *76*, 2080–2092.

(61) Rojas, J.; Bedoya, M.; Ciro, Y., Current Trends in the Production of Cellulose Nanoparticles and Nanocomposites for Biomedical Applications. *InTech OpenScience*, Chapter 8, **2015**.

(62) Mishra, S. P.; Thirree, J.; Manent, A.-S.; Chabot, B.; Daneault, C. Ultrasound-Catalyzed TEMPO-Mediated Oxidation of Native Cellulose for the Production of Nanocellulose: Effect of Process Variables. *BioResources* **2010**, *6*, 121–143.

(63) Sehaqui, H.; Zhou, Q.; Ikkala, O.; Berglund, L. A., Strong and Tough Cellulose Nanopaper with High Specific Surface Area and Porosity. *Biomacromolecules* **2011**, *12*, 3638–3644.

(64) Wu, C.-N.; Saito, T.; Fujisawa, S.; Fukuzumi, H.; Isogai, A. Ultrastrong and High Gas barrier Nanocellulose/Clay-layered Composites. *Biomacromolecules* **2012**, *13*, 1927–1932.

(65) Habibi, Y.; Lucia, L. A.; Rojas, O. J. Cellulose Nanocrystals: Chemistry, Self-Assembly, and Applications. *Chem. Rev.* **2010**, *110*, 3479–3500.

(66) Zhang, P. P.; Tong, D. S.; Lin, C. X.; Yang, H. M.; Zhong, Z. K.; Yu, W. H.; Wang, H.; Zhou, C. H. Effects of Acid Treatments on Bamboo Cellulose Nanocrystals. *Asia-Pac. J. Chem. Eng.* **2014**, *9*, 686–695.

(67) Brito, B. S.; Pereira, F. V.; Putaux, J.-L.; Jean, B. Preparation, Morphology and Structure of Cellulose Nanocrystals from Bamboo Fibres. *Cellulose* **2012**, *19*, 1527–1536.

(68) Deepa, B.; Abraham, E.; Cordeiro, N.; Mozetic, M.; Mathew, A. P.; Oksman, K.; Faria, M.; Thomas, S.; Pothan, L. A. Utilization of various Lignocellulosic Biomass for the Production of Nanocellulose: A Comparative Study. *Cellulose* **2015**, *22*, 1075–1090.

(69) Lu, P.; Hsieh, Y.-L. Preparation and Characterization of Cellulose Nanocrystals from Rice Straw. *Carbohydr. Polym.* **2012**, *87*, 564–573.

(70) Rosa, M.; Medeiros, E.; Malmonge, J.; Gregorski, K.; Wood, D.; Mattoso, L.; Glenn, G.; Orts, W.; Imam, S. Cellulose Nanowhiskers from Coconut Husk Fibres: Effect of Preparation Conditions on their Thermal and Morphological Behavior. *Carbohydr. Polym.* **2010**, *81*, 83–92.

(71) Oun, A. A.; Rhim, J.-W. Characterization of Carboxymethyl Cellulose-based Nanocomposite Films Reinforced with Oxidized Nanocellulose Isolated Using Ammonium Persulphate Method. *Carbohydr. Polym.* **2017**, *174*, 484–492.

(72) Cheng, M.; Qin, Z.; Liu, Y.; Qin, Y.; Li, T.; Chen, L.; Zhu, M. Efficient Extraction of Carboxylated Spherical Cellulose Nanocrystals with Narrow Distribution through Hydrolysis of Lyocell Fibres by using Ammonium Persulphate as an Oxidant. *J. Mater. Chem. A* **2014**, *2*, 251–258.

(73) Xu, Q.; Li, W.; Cheng, Z.; Yang, G.; Qin, M. TEMPO/NaBr/NaClO-mediated Surface Oxidation of Nanocrystalline Cellulose and its Microparticulate Retention System with Cationic Polyacrylamide. *BioResources* **2013**, *9*, 994–1006.

(74) Hua, K.; Rocha, I.; Zhang, P.; Gustafsson, S.; Ning, Y.; Strømme, M.; Mihranyan, A.; Ferraz, N. Transition from Bioinert to Bioactive Material by Tailoring the Biological cell Response to Carboxylated Nanocellulose. *Biomacromolecules* **2016**, *17*, 1224–1233.

(75) Carlsson, D. O.; Lindh, J.; Nyholm, L.; Strømme, M.; Mihranyan, A. Cooxidant-free TEMPO-Mediated Oxidation of Highly Crystalline Nanocellulose in Water. *RSC Adv.* **2014**, *4*, 52289–52298.

(76) Leung, A. C.; Hrapovic, S.; Lam, E.; Liu, Y.; Male, K. B.; Mahmoud, K. A.; Luong, J. H. Characteristics and Properties of Carboxylated Cellulose Nanocrystals Prepared from a Novel One-step Procedure. *Small* **2011**, *7*, 302–305.

(77) Man, Z.; Muhammad, N.; Sarwono, A.; Bustam, M. A.; Kumar, M. V.; Rafiq, S. Preparation of Cellulose Nanocrystals Using an Ionic Liquid. *J. Polym. Environ.* **2011**, *19*, 726–731.

(78) Kilpeläinen, I.; Xie, H.; King, A.; Granstrom, M.; Heikkinen, S.; Argyropoulos, D. S. Dissolution of Wood in Ionic Liquids. *J. Agric. Food Chem.* **2007**, *55*, 9142–9148.

(79) Thomas, M. G.; Abraham, E.; Jyotishkumar, P.; Maria, H. J.; Pothen, L. A.; Thomas, S. Nanocelluloses from Jute Fibres and their Nanocomposites with Natural Rubber: Preparation and Characterization. *Intern. J. Bio. Macromol.* **2015**, *81*, 768–777.

(80) Cherian, B. M.; Leão, A. L.; de Souza, S. F.; Costa, L. M. M.; de Olyveira, G. M.; Kottaisamy, M.; Nagarajan, E.; Thomas, S. Cellulose Nanocomposites with Nanofibres Isolated from Pineapple Leaf Fibres for Medical Applications. *Carbohydr. Polym.* **2011**, *86*, 1790–1798.

(81) Shimizu, M.; Saito, T.; Nishiyama, Y.; Iwamoto, S.; Yano, H.; Isogai, A.; Endo, T. Fast and Robust Nanocellulose Width Estimation Using Turbidimetry. *Macromol. Rapid Comm.* **2016**, *37*, 1581–1586.

(82) Xu, W.; Grénman, H.; Liu, J.; Kronlund, D.; Li, B.; Backman, P.; Peltonen, J.; Willför, S.; Sundberg, A.; Xu, C. Mild Oxalic-Acid-Catalyzed Hydrolysis as a Novel Approach to Prepare Cellulose Nanocrystals. *ChemNanoMat* **2017**, *3*, 109–119.

(83) Chen, L.; Zhu, J.; Baez, C.; Kitin, P.; Elder, T. Highly Thermal-Stable and Functional Cellulose Nanocrystals and Nanofibrils Produced Using Fully Recyclable Organic Acids. *Green Chem.* **2016**, *18*, 3835–3843.

(84) Li, D.; Henschen, J.; Ek, M. Esterification and Hydrolysis of Cellulose Using Oxalic Acid Dihydrate in a Solvent-Free Reaction Suitable for Preparation of Surface-Functionalised Cellulose Nanocrystals with High Yield. *Green Chem.* **2017**, *19*, 5564–5567.

(85) Yan, C.-F.; Yu, H.-Y.; Yao, J.-M. One-Step Extraction and Functionalization of Cellulose Nanospheres from Lyocell Fibres with Cellulose II Crystal Structure. *Cellulose* **2015**, *22*, 3773–3788.

(86) Lu, P.; Hsieh, Y.-L. Cellulose Isolation and Core–Shell Nanostructures of Cellulose Nanocrystals from Chardonnay Grape Skins. *Carbohydr. Polym.* **2012**, *87*, 2546–2553.

(87) Hsieh, Y.-L. Cellulose Nanocrystals and Self-Assembled Nanostructures from Cotton, Rice Straw and Grape Skin: A Source perspective. *J. Mater. Sci.* **2013**, *48*, 7837–7846.

(88) Liu, C.; Li, B.; Du, H.; Lv, D.; Zhang, Y.; Yu, G.; Mu, X.; Peng, H. Properties of Nanocellulose Isolated from Corncob Residue Using Sulphuric Acid, Formic Acid, Oxidative and Mechanical Methods. *Carbohydr. Polym.* **2016**, *151*, 716–724.

(89) Castro-Guerrero, C. F.; Gray, D. G. Chiral Nematic Phase Formation by Aqueous Suspensions of Cellulose Nanocrystals Prepared by Oxidation with Ammonium Persulphate. *Cellulose* **2014**, *21*, 2567–2577.

(90) Peng, B. L.; Dhar, N.; Liu, H.; Tam, K. Chemistry and Applications of Nanocrystalline Cellulose and its Derivatives: A Nanotechnology Perspective. *Can. J. Chem. Eng.* **2011**, *89*, 1191–1206.

(91) Kalita, E.; Nath, B.; Deb, P.; Agan, F.; Islam, M. R.; Saikia, K. High Quality Fluorescent Cellulose Nanofibres from Endemic Rice Husk: Isolation and Characterization. *Carbohydr. Polym.* **2015**, *122*, 308–313.

(92) Braun, B.; Dorgan, J. R.; Chandler, J. P. Cellulosic Nanowhiskers. Theory and Application of Light Scattering from Polydisperse Spheroids in the Rayleigh−Gans−Debye regime. *Biomacromolecules* **2008**, *9*, 1255–1263.

93. Jiang, F.; Hsieh, Y.-L., Chemically and Mechanically Isolated Nanocellulose and their Self-assembled structures. *Carbohydr. Polym.* **2013**, *95*, 32–40.

(94) Jiang, F.; Hsieh, Y.-L. Assembling and Redispersibility of Rice Straw Nanocellulose: Effect of Tert-Butanol. *ACS Appl. Mater. Interfaces* **2014**, *6*, 20075–20084.

(95) Habibi, Y.; Goffin, A.-L.; Schiltz, N.; Duquesne, E.; Dubois, P.; Dufresne, A. Bionanocomposites Based on Poly (ε-Caprolactone)-Grafted Cellulose Nanocrystals by Ring-Opening Polymerization. *J. Mater. Chem.* **2008**, *18*, 5002–5010.

(96) Van Duyne, R.; Hulteen, J.; Treichel, D. Atomic Force Microscopy and Surface-Enhanced Raman Spectroscopy. I. Ag Island Films and Ag Film over Polymer Nanosphere Surfaces Supported on Glass. *J. Chem. Phys.* **1993**, *99*, 2101–2115.

(97) Mulvihill, M. J.; Ling, X. Y.; Henzie, J.; Yang, P. Anisotropic Etching of Silver Nanoparticles for Plasmonic Structures Capable of Single-Particle SERS. *J. Am. Chem. Soc.* **2009**, *132*, 268–274.

(98) Sun, Y.; Xia, Y. Shape-Controlled Synthesis of Gold and Silver Nanoparticles. *Science* **2002**, *298*, 2176–2179.

(99) Nguyen, B. H.; Nguyen, V. H.; Tran, H. N. Rich Variety of Substrates for Surface Enhanced Raman Spectroscopy. *Adv. Nat. Sci: Nanosci. Nanotechnol.* **2016**, *7*, 033001.

(100) Chen, J.; Huang, Y.; Kannan, P.; Zhang, L.; Lin, Z.; Zhang, J.; Chen, T.; Guo, L. Flexible and Adhesive Surface Enhance Raman Scattering Active Tape for Rapid Detection of Pesticide Residues in Fruits and Vegetables. *Anal. Chem.* **2016**, *88*, 2149–2155.

(101) Wei, W. Y.; White, I. M. A Simple Filter-Based Approach to Surface Enhanced Raman Spectroscopy for Trace Chemical Detection. *Analyst* **2012**, *137*, 1168–1173.

(102) Qu, L.-L.; Li, D.-W.; Xue, J.-Q.; Zhai, W.-L.; Fossey, J. S.; Long, Y.-T. Batch Fabrication of Disposable Screen Printed SERS Arrays. *Lab Chip* **2012**, *12*, 876–881.

(103) Yu, W. W.; White, I. M. Inkjet Printed Surface Enhanced Raman Spectroscopy Array on Cellulose Paper. *Anal. Chem.* **2010**, *82*, 9626–9630.

(104) Eshkeiti, A.; Narakathu, B.; Reddy, A.; Moorthi, A.; Atashbar, M.; Rebrosova, E.; Rebros, M.; Joyce, M. Detection of Heavy Metal Compounds Using a Novel Inkjet Printed Surface Enhanced Raman Spectroscopy (SERS) Substrate. *Sensors and Actuators B* **2012**, *171*, 705–711.

(105) Gong, Z.; Du, H.; Cheng, F.; Wang, C.; Wang, C.; Fan, M. Fabrication of SERS Swab for Direct Detection of Trace Explosives in Fingerprints. *ACS Appl. Mater. Interf.* **2014**, *6*, 21931–21937.

(106) Wang, P.; Zhang, L.; Xia, Y.; Tong, L.; Xu, X.; Ying, Y. Polymer Nanofibres Embedded with Aligned Gold Nanorods: A New Platform for Plasmonic Studies and Optical Sensing. *Nano Lett.* **2012**, *12*, 3145–3150.

(107) Polavarapu, L.; Liz-Marzán, L. M. Towards Low-Cost Flexible Substrates for Nanoplasmonic Sensing. *PhysChemChemPhys.* **2013**, *15*, 5288–5300.

(108) Huang, L. B.; Zhou, Y.; Han, S. T.; Yan, Y.; Zhou, L.; Chen, W.; Zhou, P.; Chen, X.; Roy, V. Controlled Assembly of Silver Nanoparticles Monolayer on 3D Polymer Nanotubes and their Applications. *Small* **2014**, *10*, 4645–4650.

(109) Fierro-Mercado, P.; Renteria-Beleño, B.; Hernández-Rivera, S. Preparation of SERS Active Substrates Using Thermal Inkjet Technology. *Chem. Phys. Lett.* **2012**, *552*, 108–113.

(110) Jahn, S. F.; Blaudeck, T.; Baumann, R. R.; Jakob, A.; Ecorchard, P.; Rüffer, T.; Lang, H.; Schmidt, P. Inkjet Printing of Conductive Silver Patterns by Using the First Aqueous Particle-Free MOD Ink without Additional Stabilizing Ligands. *Chem. Mater.* **2010**, *22*, 3067–3071.

(111) Oluwafemi, O. S.; Mochochoko, T.; Leo, A. J.; Mohan, S.; Jumbam, D. N.; Songca, S. P. Microwave Irradiation Synthesis of Silver Nanoparticles Using Cellulose from *Eichhornia crassipes* Plant Shoot. *Mater. Lett.* **2016**, *185*, 576–579.

(112) Tran, C. D., Subnanogram Detection of Dyes on Filter Paper by Surface-Enhanced Raman Scattering Spectrometry. *Anal. Chem.* **1984**, *56*, 824–826.

(113) Vo-Dinh, T.; Hiromoto, M.; Begun, G.; Moody, R. Surface-Enhanced Raman Spectrometry for Trace Organic Analysis. *Anal. Chem.* **1984**, *56*, 1667–1670.

(114) Betz, J. F.; Wei, W. Y.; Cheng, Y.; White, I. M.; Rubloff, G. W. Simple SERS Substrates: Powerful, Portable, and full of Potential. *PhysChemChemPhys.* **2014**, *16*, 2224–2239.

(115) He, S.; Chua, J.; Tan, E. K. M.; Kah, J. C. Y. Optimizing the SERS Enhancement of a Facile Gold Nanostar Immobilized Paper-Based SERS Substrate. *RSC Adv.* **2017**, *7*, 16264–16272.

(116) Oliveira, M. J.; Quaresma, P.; De Almeida, M. P.; Araújo, A.; Pereira, E.; Fortunato, E.; Martins, R.; Franco, R.; Águas, H. Office Paper Decorated with Silver Nanostars-

an Alternative Cost Effective Platform for Trace Analyte Detection by SERS. *Sci. Reports* **2017**, *7*, 2480.

(117) Wu, D.; Fang, Y. The Adsorption Behavior of *p*-Hydroxybenzoic Acid on a Silver-Coated Filter Paper by Surface Enhanced Raman Scattering. *J. Colloid Interface Sci.* **2003**, *265*, 234–238.

(118) Zhou, X.; Yan, H.; He, C.; Lu, M.; Hao, R. Comparison of Surface-Enhanced Raman Scattering Spectra of Azo Dye Sudan III on Several Substrates. *Spectrosc. Lett.* **2013**, *46*, 615–619.

(119) Ding, L.-P.; Fang, Y. Influence of the Microstructure of Several Substrates on the SERS Effect of *p*-Hyroxybenzoic Absorbed on Ag Nanoparticles. *Colloids Surf. A Physicochem. Eng. Aspects* **2008**, *316*, 253–257.

(120) Yan, B.; Fang, Y.; Zhao, X.; Liang, L. A Comparative Study on the Adsorption Behaviors of PABA in the Silver Nano-Particles. *J. Mol. Struct.* **2014**, *1074*, 660–665.

(121) Wu, D.; Fang, Y. Surface-Enhanced Raman Scattering of a Series of *n*-Hydroxybenzoic acids (n= P, M and O) on the Silver Nano-Particles. *Spectrochim. Acta A* **2004**, *60*, 1845–1852.

(122) Ma, W.; Fang, Y. Experimental (FT-IR) and Theoretical (DFT) Studies on the Adsorption Behavior of *p*-Nitroaniline (PNA) on Gold Nanoparticles. *J. Nanopart. Res.* **2006**, *8*, 761–767.

(123) Ma, W.; Fang, Y. Experimental (SERS) and Theoretical (DFT) Studies on the Adsorption of *p*-, *m*-, and *o*-Nitroaniline on Gold Nanoparticles. *J. Colloid Interface Sci.* **2006**, *303*, 1–8.

(124) Luo, Z.; Fang, Y. SERS of C_{60}/C_{70} on Gold-Coated Filter Paper or Filter Film Influenced by the Gold Thickness. *J. Colloid Interface Sci.* **2005**, *283*, 459–463.

(125) Niu, Z.; Fang, Y. Surface-Enhanced Raman Scattering of Single-Walled Carbon Nanotubes on Silver-Coated and Gold-Coated Filter Paper. *J. Colloid Interface Sci.* **2006**, *303*, 224–228.

(126) Wang, P.; Fang, Y. The Surface Enhanced Raman Spectroscopic Study of the Adsorption of C_{70} on the Gold Nanoparticles. *J. Chem. Phys.* **2008**, *129*, 134702.

(127) Villa, J. E.; Dos Santos, D. P.; Poppi, R. J. Fabrication of Gold Nanoparticle-Coated Paper and its Use as a Sensitive Substrate for Quantitative SERS Analysis. *Microchim. Acta* **2016**, *183*, 2745–2752.

(128) Villa, J. E.; Poppi, R. J. A Portable SERS Method for the Determination of Uric Acid Using a Paper-Based Substrate and Multivariate Curve Resolution. *Analyst* **2016**, *141*, 1966–1972.

(129) Lee, M.; Oh, K.; Choi, H.-K.; Lee, S. G.; Youn, H. J.; Lee, H. L.; Jeong, D. H. Subnanomolar Sensitivity of Filter Paper-Based SERS Sensor for Pesticide Detection by Hydrophobicity Change of Paper Surface. *Sensors* **2018**, *3*, 151–159.

(130) Enlow, P. D.; Vo-Dinh, T., Detection of Nitro-Polynuclear Aromatic Compounds by Surface-Enhanced Raman Spectrometry. *Anal. Chem.* **1986**, *58*, 1119–1123.

(131) Chen, K.; Leona, M.; Vo-Dinh, K. C.; Yan, F.; Wabuyele, M. B.; Vo-Dinh, T. Application of Surface-Enhanced Raman Scattering (SERS) for the Identification of Anthraquinone Dyes Used in Works of Art. *J. Raman Spectrosc.* **2006**, *37*, 520–527.

(132) Laserna, J.; Sutherland, W.; Winefordner, J. Microspectrometric Investigation of Active Substrates for Surface Enhanced Raman Scattering. *Anal. Chim. Acta* **1990**, *237*, 439–450.

(133) Araújo, A.; Pimentel, A.; Oliveira, M. J.; Mendes, M. J.; Franco, R.; Fortunato, E.; Águas, H.; Martins, R. Direct Growth of Plasmonic Nanorod Forests on Paper Substrates for Low-Cost Flexible 3D SERS Platforms. *Flex. Print. Electron* **2017**, *2*, 1–12.

(134) Park, M.; Hwang, C. S. H.; Jeong, K.-H. Nanoplasmonic Alloy of Au/Ag Nanocomposites on Paper Substrate for Biosensing Applications. *ACS Appl. Mater. Interf.* **2018**, *10*, 290–295.

(135) Berthod, A.; Laserna, J.; Winefordner, J. Analysis by Surface Enhanced Raman Spectroscopy on Silver Hydrosols and Silver Coated Filter Papers. *J. Pharm. Biomed. Anal.* **1988**, *6*, 599–608.

(136) Laserna, J.; Campiglia, A.; Winefordner, J. Surface-Enhanced Raman Spectrometry on a Silver-Coated Filter Paper Substrate. *Anal. Chim. Acta* **1988**, *208*, 21–30.

(137) Laserna, J. J.; Campiglia, A. D.; Winefordner, J. Mixture Analysis and Quantitative Determination of Nitrogen-Containing Organic Molecules by Surface-Enhanced Raman Spectrometry. *Anal. Chem.* **1989**, *61*, 1697–1701.

(138) Cabalin, L.; Laserna, J. Fast Spatially Resolved Surface-Enhanced Raman Spectrometry on a Silver Coated Filter Paper Using Charge-Coupled Device Detection. *Anal. Chim. Acta* **1995**, *310*, 337–345.

(139) Sutherland, W.; Laserna, J.; Winefordner, J. A Spatial Distribution Study of Analyte Concentration in Solid Substrate Surface-Enhanced Raman Spectroscopy. *Spectrochim. Acta A* **1991**, *47*, 329–337.

(140) Sutherland, W.; Winefordner, J. Preparation of Substrates for Surface-Enhanced Raman Microprobe Spectroscopy. *J. Raman Spectrosc.* **1991**, *22*, 541–549.

(141) Ayora, M.; Ballesteros, L.; Perez, R.; Ruperez, A.; Laserna, J. Detection of Atmospheric Contaminants in Aerosols by Surface-Enhanced Raman Spectrometry. *Anal. Chim. Acta* **1997**, *355*, 15–21.

(142) Lee, A. S.; Li, Y. S. Surface-Enhanced Raman Spectra Using Silver-Coated Paper Substrates. *J. Raman Spectrosc.* **1994**, *25*, 209–214.

(143) Cheng, M.-L.; Tsai, B.-C.; Yang, J. Silver Nanoparticle-Treated Filter Paper as a Highly Sensitive Surface-Enhanced Raman Scattering (SERS) Substrate for Detection of Tyrosine in Aqueous Solution. *Anal. Chim. Acta* **2011**, *708*, 89–96.

(144) Raza, A.; Saha, B. In-situ Silver Nanoparticles Synthesis in Agarose Film Supported on Filter Paper and its Application as Highly Efficient SERS Test Stripes. *Forens. Sci. Int.* **2014**, *237*, e42–e46.

(145) Rajapandiyan, P.; Yang, J. Photochemical Method for Decoration of Silver Nanoparticles on Filter Paper Substrate for SERS Application. *J. Raman Spectrosc.* **2014,** *45*, 574–580.

(146) Kim, W.; Kim, Y.-H.; Park, H.-K.; Choi, S. Facile Fabrication of a Silver Nanoparticle Immersed, Surface-Enhanced Raman Scattering Imposed Paper Platform through Successive Ionic Layer Absorption and Reaction for on-Site Bioassays. *ACS Appl. Mater. Interf.* **2015**, *7*, 27910–27917.

(147) Kim, W.; Lee, J.-C.; Shin, J.-H.; Jin, K.-H.; Park, H.-K.; Choi, S. Instrument-Free Synthesizable Fabrication of Label-Free Optical Biosensing Paper Strips for the Early Detection of Infectious Keratoconjunctivitides. *Anal. Chem.* **2016**, *88*, 5531–5537.

(148) Kim, W.; Lee, J.-C.; Lee, G.-J.; Park, H.-K.; Lee, A.; Choi, S. Low-Cost Label-Free Biosensing Bimetallic Cellulose Strip with SILAR-Synthesized Silver Core–Gold Shell Nanoparticle Structures. *Anal. Chem.* **2017**, *89*, 6448–6454.

(149) Lee, J.-C.; Kim, W.; Park, H.-K.; Choi, S. Controlling Successive Ionic Layer Absorption and Reaction Cycles to Optimize Silver Nanoparticle-Induced Localized Surface Plasmon Resonance Effects on the Paper Strip. *Spectrochim. Acta Part A* **2017**, *174*, 37–43.

(150) He, L.; Liu, C.; Tang, J.; Jin, W.; Yang, H.; Liu, R.; Hao, X.; Hu, J. Phase Confinement of Self-Migrated Plasmonic Silver in Triphasic System: Offering 3D Hot Spots on Hydrophobic Paper for SERS Detection. *Appl. Surf. Sci.* **2018**, *450*, 138–145.

(151) Chen, M.; Zhang, Z.; Liu, M.; Qiu, C.; Yang, H.; Chen, X. In-situ Fabrication of Label-Free Optical Sensing Paper Strips for the Rapid Surface-Enhanced Raman Scattering (SERS) Detection of Brassinosteroids in Plant Tissues. *Talanta* **2017**, *165*, 313–320.

(152) Xu, Y.; Man, P.; Huo, Y.; Ning, T.; Li, C.; Man, B.; Yang, C. Synthesis of the 3D AgNF/AgNP Arrays for the Paper-Based Surface Enhancement Raman Scattering Application. *Sens. Actuat. B-Chem.* **2018**, *265*, 302–309.

(153) Yang, C.; Xu, Y.; Wang, M.; Li, T.; Huo, Y.; Yang, C.; Man, B. Multifunctional Paper Strip Based on GO-Veiled Ag Nanoparticles with Highly SERS Sensitive and Deliverable Properties for High-Performance Molecular Detection. *Opt. Express* **2018**, *26*, 10023–10037.

(154) Meng, Y.; Lai, Y.; Jiang, X.; Zhao, Q.; Zhan, J., Silver Nanoparticles Decorated Filter Paper *via* Self-Sacrificing Reduction for Membrane Extraction Surface-Enhanced Raman Spectroscopy Detection. *Analyst* **2013**, *138*, 2090–2095.

(155) Li, Y.; Zhang, K.; Zhao, J.; Ji, J.; Ji, C.; Liu, B. A Three-Dimensional Silver Nanoparticles Decorated Plasmonic Paper Strip for SERS Detection of Low-Abundance Molecules. *Talanta* **2016**, *147*, 493–500.

(156) Desmonda, C.; Kar, S.; Tai, Y. Formation of Gold Nanostructures on Copier Paper Surface for Cost Effective SERS Active Substrate–Effect of Halide Additives. *Appl. Surf. Sci.* **2016**, *367*, 362–369.

(157) Cañamares, M.; Garcia-Ramos, J.; Gomez-Varga, J.; Domingo, C.; Sanchez-Cortes, S. Ag Nanoparticles Prepared by Laser Photoreduction as Substrates for *In-situ* Surface-Enhanced Raman Scattering Analysis of Dyes. *Langmuir* **2007**, *23*, 5210–5215.

(158) Yu, C.-C.; Chou, S.-Y.; Tseng, Y.-C.; Tseng, S.-C.; Yen, Y.-T.; Chen, H.-L. Single-Shot Laser Treatment Provides Quasi-Three-Dimensional Paper-Based Substrates for SERS with Attomolar Sensitivity. *Nanoscale* **2015**, *7*, 1667–1677.

(159) Kang, Y.; Zhang, H.; Zhang, L.; Wu, T.; Sun, L.; Jiang, D.; Du, Y. In-situ Preparation of Ag Nanoparticles by Laser Photoreduction as SERS Substrate for Determination of Hg^{2+}. *J. Raman Spectros.* **2017**, *48*, 399–404.

(160) Wang, C.; Liu, B.; Dou, X. Silver Nanotriangles-Loaded Filter Paper for Ultrasensitive SERS Detection Application Benefited by Interspacing of Sharp Edges. *Sens. Actuat. B-Chem.* **2016**, *231*, 357–364.

(161) Grasseschi, D.; Zamarion, V. M.; Araki, K.; Toma, H. E. Surface Enhanced Raman Scattering Spot Tests: A New Insight on Feigl's Analysis Using Gold Nanoparticles. *Anal. Chem.* **2010**, *82*, 9146–9149.

(162) Webb, J. A.; Aufrecht, J.; Hungerford, C.; Bardhan, R. Ultrasensitive Analyte Detection with Plasmonic Paper Dipsticks and Swabs Integrated with Branched Nanoantennas. *J. Mater. Chem. C* **2014**, *2*, 10446–10454.

(163) Ngo, Y. H.; Li, D.; Simon, G. P.; Garnier, G. Gold Nanoparticle–Paper as a Three-Dimensional Surface Enhanced Raman Scattering Substrate. *Langmuir* **2012**, *28*, 8782–8790.

(164) Kim, J.-H.; Twaddle, K. M.; Cermak, L. M.; Jang, W.; Yun, J.; Byun, H. Photothermal Heating Property of Gold Nanoparticle Loaded Substrates and their SERS Response. *Colloids Surf. A* **2016**, *498*, 20–29.

(165) Lee, C. H.; Tian, L.; Singamaneni, S. Paper-Based SERS Swab for Rapid Trace Detection on Real-World Surfaces. *ACS Appl. Mater. Interf.* **2010**, *2*, 3429–3435.

(166) Lee, C. H.; Hankus, M. E.; Tian, L.; Pellegrino, P. M.; Singamaneni, S. Highly Sensitive Surface Enhanced Raman Scattering Substrates Based on Filter Paper Loaded with Plasmonic Nanostructures. *Anal. Chem.* **2011,** *83*, 8953–8958.

(167) Mehn, D.; Morasso, C.; Vanna, R.; Bedoni, M.; Prosperi, D.; Gramatica, F. Immobilised Gold Nanostars in a Paper-Based Test System for Surface-Enhanced Raman Spectroscopy. *Vibr. Spectrosc.* **2013,** *68*, 45–50.

(168) Ngo, Y. H.; Li, D.; Simon, G. P.; Garnier, G. Effect of Cationic Polyacrylamides on the Aggregation and SERS Performance of Gold Nanoparticles-Treated Paper. *J. Colloid Interface Sci.* **2013**, *392*, 237–246.

(169) Ngo, Y. H.; Li, D.; Simon, G. P.; Garnier, G. Effect of Cationic Polyacrylamide Dissolution on the Adsorption State of Gold Nanoparticles on Paper and their Surface Enhanced Raman Scattering Properties. *Colloid Surf. A* **2013**, *420*, 46–52.

(170) Lin, X.; Lou, X.-T.; Lin, S.; Yang, F.; Lin, D.-Y.; Lu, Z.-W. Chloride Ion-Assisted Self-Assembly of Silver Nanoparticles on Filter Paper as SERS Substrate. *Appl. Phys. A* **2015**, *118*, 799–807.

(171) Dalla Marta, S.; Novara, C.; Giorgis, F.; Bonifacio, A.; Sergo, V. Optimization and Characterization of Paper-Made Surface Enhanced Raman Scattering (SERS) Substrates with Au and Ag NPs for Quantitative Analysis. *Materials* **2017**, *10*, 1365.

(172) Lahr, R. H.; Wallace, G. C.; Vikesland, P. J., Raman Characterization of Nanoparticle Transport in Microfluidic Paper-Based Analytical Devices (μPADs). *ACS Appl. Mater. Interf.* **2015**, *7*, 9139–9146.

(173) Lin, S.; Lin, X.; Lou, X.-T.; Yang, F.; Lin, D.-Y.; Lu, Z.-W. Rapid Fabrication of Self-Assembled Interfacial Film Decorated Filter Paper as an Excellent Surface-Enhanced Raman Scattering Substrate. *Anal. Methods* **2014**, *6*, 9547–9553.

(174) Zhang, K.; Zhao, J.; Xu, H.; Li, Y.; Ji, J.; Liu, B. Multifunctional Paper Strip Based on Self-Assembled Interfacial Plasmonic Nanoparticle Arrays for Sensitive SERS Detection. *ACS Appl. Mater. Interf.* **2015**, *7*, 16767–16774.

(175) Abbas, A.; Brimer, A.; Slocik, J. M.; Tian, L.; Naik, R. R.; Singamaneni, S. Multifunctional Analytical Platform on a Paper Strip: Separation, Preconcentration, and Subattomolar Detection. *Anal. Chem.* **2013**, *85*, 3977–3983.

(176) Fierro–Mercado, P. M.; Hernández-Rivera, S. P. Highly Sensitive Filter Paper Substrate for SERS Trace Explosives Detection. *Int. J. Spectrosc.* **2012**, *2012*, 1–7.

(177) Dai, Z.; Xiao, X.; Wu, W.; Liao, L.; Mei, F.; Yu, X.; Guo, S.; Ying, J.; Ren, F.; Jiang, C. Side-to-Side Alignment of Gold Nanorods with Polarization-Free Characteristic for Highly Reproducible Surface Enhanced Raman Scattering. *Appl. Phys. Lett.* **2014**, *105*, 211902.

(178) Yorov, K.; Grigorieva, A.; Sidorov, A.; Polyakov, A. Y.; Sukhorukova, I.; Shtansky, D.; Grünert, W.; Goodilin, E. Inkjet Printing of Silver Rainbow Colloids for SERS Chips with Polychromatic Sensitivity. *RSC Adv.* **2016**, *6*, 15535–15540.

(179) Wei, W. Y.; White, I. M. Inkjet-Printed Paper-Based SERS Dipsticks and Swabs for Trace Chemical Detection. *Analyst* **2013**, *138*, 1020–1025.

(180) Hoppmann, E. P.; Wei, W. Y.; White, I. M. Highly Sensitive and Flexible Inkjet Printed SERS Sensors on Paper. *Methods* **2013**, *63*, 219–224.

(181) Wei, W. Y.; White, I. M. Chromatographic Separation and Detection of Target Analytes from Complex Samples Using Inkjet Printed SERS Substrates. *Analyst* **2013**, *138*, 3679–3686.

(182) Xiao, G.; Li, Y.; Shi, W.; Shen, L.; Chen, Q.; Huang, L. Highly Sensitive, Reproducible and Stable SERS Substrate Based on Reduced Graphene Oxide/Silver Nanoparticles Coated Weighing Paper. *Appl. Surf. Sci.* **2017**, *404*, 334–341.

(183) Joshi, P.; Santhanam, V. Inkjet-Based Fabrication Process with Control over the Morphology of SERS-Active Silver Nanostructures. *Ind. Eng. Chem. Res.* **2018**, *57*, 5250–5258.

(184) Weng, G.; Yang, Y.; Zhao, J.; Zhu, J.; Li, J.; Zhao, J. Preparation and SERS performance of AuNP/Paper Strips Based on Inkjet Printing and Seed Mediated Growth: The Effect of Silver Ions. *Solid State Commun.* **2018**, *272*, 67–73.

(185) Kim, W.-S.; Shin, J.-H.; Park, H.-K.; Choi, S. A Low-Cost, Monometallic, Surface-Enhanced Raman Scattering-Functionalized Paper Platform for Spot-on Bioassays. *Sens. Actuat. B-Chem.* **2016,** *222*, 1112–1118.

(186) Qu, L.-L.; Song, Q.-X.; Li, Y.-t.; Peng, M.-P.; Li, D.-W.; Chen, L.-X.; Fossey, J. S.; Long, Y.-T. Fabrication of Bimetallic Microfluidic Surface-Enhanced Raman Scattering Sensors on Paper by Screen Printing. *Anal. Chim. Acta* **2013**, *792*, 86–92.

(187) Zhang, R.; Xu, B.-B.; Liu, X.-Q.; Zhang, Y.-L.; Xu, Y.; Chen, Q.-D.; Sun, H.-B. Highly Efficient SERS Test Strips. *Chem. Commun.* **2012**, *48*, 5913–5915.

(188) Li, B.; Zhang, W.; Chen, L.; Lin, B. A Fast and Low-Cost Spray Method for Prototyping and Depositing Surface-Enhanced Raman Scattering Arrays on Microfluidic Paper Based Device. *Electrophoresis* **2013**, *34*, 2162–2168.

(189) Polavarapu, L.; Porta, A. L.; Novikov, S. M.; Coronado-Puchau, M.; Liz-Marzán, L. M. Pen-on-Paper Approach Toward the Design of Universal Surface Enhanced Raman Scattering Substrates. *Small* **2014**, *10*, 3065–3071.

(190) Zhang, W.; Li, B.; Chen, L.; Wang, Y.; Gao, D.; Ma, X.; Wu, A. Brushing, a Simple Way to Fabricate SERS Active Paper Substrates. *Anal. Methods* **2014**, *6*, 2066–2071.

(191) Hoppmann, E. P.; Yu, W. W.; White, I. M. Detection of Deoxyribonucleic Acid (DNA) Targets Using Polymerase Chain Reaction (PCR) and Paper Surface-Enhanced Raman Spectroscopy (SERS) Chromatography. *Appl. Spectrosc.* **2014**, *68*, 909–915.

(192) Hassanain, W. A.; Izake, E. L.; Sivanesan, A.; Ayoko, G. A. Towards Interference Free HPLC-SERS for the Trace Analysis of Drug Metabolites in Biological Fluids. *J. Pharm. Biomed. Anal.* **2017**, *136*, 38–43.

(193) Fornasaro, S.; Dalla Marta, S.; Rabusin, M.; Bonifacio, A.; Sergo, V. Toward SERS-Based Point-of-Care Approaches for Therapeutic Drug Monitoring: The Case of Methotrexate. *Faraday Discuss.* **2016**, *187*, 485–499.

(194) Chamuah, N.; Hazarika, A.; Hatiboruah, D.; Nath, P. SERS on Paper: An Extremely Low Cost Technique to Measure Raman Signal. *J. Phys. D Appl. Phys.* **2017**, *50*, 485601.

(195) Torul, H.; Çiftçi, H.; Çetin, D.; Suludere, Z.; Boyacı, I. H.; Tamer, U. Paper Membrane-Based SERS Platform for the Determination of Glucose in Blood Samples. *Anal. Bioanal. Chem.* **2015**, *407*, 8243–8251.

(196) Gao, X.; Zheng, P.; Kasani, S.; Wu, S.; Yang, F.; Lewis, S.; Nayeem, S.; Engler-Chiurazzi, E. B.; Wigginton, J. G.; Simpkins, J. W. Paper-Based Surface-Enhanced Raman Scattering Lateral Flow Strip for Detection of Neuron-Specific Enolase in Blood Plasma. *Anal. Chem.* **2017**, *89*, 10104–10110.

(197) Semenova, A. A.; Brazhe, N. A.; Parshina, E. Y.; Sarycheva, A. S.; Maksimov, G. V.; Goodilin, E. A. A New Route for SERS Analysis of Intact Erythrocytes Using Polydisperse Silver Nanoplatelets on Biocompatible Scaffolds. *RSC Adv.* **2016**, *6*, 85156–85164.

(198) Arcot, L. R.; Uddin, K. M. A.; Chen, X.; Wenchao, X.; Xianming, K.; Johansson, L. S.; Ras, R. H.; Rojas, O. J. Paper-Based Plasmon-Enhanced Protein Sensing by Controlled Nucleation of Silver Nanoparticles on Cellulose. *Cellulose* **2015**, *22*, 4027–4034.

(199) Ngo, Y. H.; Then, W. L.; Shen, W.; Garnier, G. Gold Nanoparticles Paper as a SERS Bio-Diagnostic Platform. *J. Colloid Interface Sci.* **2013**, *409*, 59–65.

(200) Hu, S.-W.; Qiao, S.; Pan, J.-B.; Kang, B.; Xu, J.-J.; Chen, H.-Y. A Paper-Based SERS Test Strip for Quantitative Detection of Mucin-1 in Whole Blood. *Talanta* **2018**, *179*, 9–14.

(201) Liu, Q.; Wang, J.; Wang, B.; Li, Z.; Huang, H.; Li, C.; Yu, X.; Chu, P. K. Paper-Based Plasmonic Platform for Sensitive, Noninvasive, and Rapid Cancer Screening. *Biosens. Bioelectron.* **2014**, *54*, 128–134.

(202) Saha, A.; Jana, N. R. Paper-Based Microfluidic Approach for Surface-Enhanced Raman Spectroscopy and Highly Reproducible Detection of Proteins Beyond Picomolar Concentration. *ACS Appl. Mater. Interf.* **2014**, *7*, 996–1003.

(203) Kim, W.; Lee, S. H.; Ahn, Y. J.; Lee, S. H.; Ryu, J.; Choi, S. K.; Choi, S. A Label-Free Cellulose SERS Biosensor Chip with Improvement of Nanoparticle-Enhanced LSPR Effects for Early Diagnosis of Subarachnoid Hemorrhage-Induced Complications. *Biosens. Bioelectron.* **2018**, *111*, 59–65.

(204) Park, M.; Jung, H.; Jeong, Y.; Jeong, K.-H. Plasmonic Schirmer Strip for Human Tear-Based Gouty Arthritis Diagnosis Using Surface-Enhanced Raman Scattering. *ACS Nano* **2017**, *11*, 438–443.

(205) Kim, W.; Lee, S. H.; Kim, J. H.; Ahn, Y. J.; Kim, Y.-H.; Yu, J. S.; Choi, S. Paper-Based Surface Enhanced Raman Spectroscopy for Diagnosing Prenatal Diseases in Women. *ACS Nano* **2018**, *12*, 7100–7108.

(206) Huang, Z.; Siddhanta, S.; Zhang, C.; Kickler, T.; Zheng, G.; Barman, I. Painting and Heating: A Nonconventional, Scalable Route to Sensitive Biomolecular Analysis with Plasmon-Enhanced Spectroscopy. *J. Raman Spectros.* **2017**, *48*, 1365–1374.

(207) Li, D.; Ma, Y.; Duan, H.; Deng, W.; Li, D. Griess Reaction-Based Paper Strip for Colorimetric/Fluorescent/SERS Triple Sensing of Nitrite. *Biosens. Bioelectron.* **2018**, *99*, 389–398.

(208) Berger, A. G.; Restaino, S. M.; White, I. M. Vertical-Flow Paper SERS System for Therapeutic Drug Monitoring of Flucytosine in Serum. *Anal. Chim. Acta* **2017**, *949*, 59–66.

(209) Sallum, L. F.; Soares, F. L. F.; Ardila, J. A.; Carneiro, R. L. Determination of Acetylsalicylic Acid in Commercial Tablets by SERS Using Silver Nanoparticle-Coated Filter Paper. *Spectrochim. Acta A* **2014**, *133*, 107–111.

(210) Sallum, L. F.; Soares, F. L. F.; Ardila, J. A.; Carneiro, R. L. Optimization of SERS Scattering by Ag-NPs-Coated Filter Paper for Quantification of Nicotinamide in a Cosmetic Formulation. *Talanta* **2014**, *118*, 353–358.

(211) Li, D.; Zhu, Q.; Lv, D.; Zheng, B.; Liu, Y.; Chai, Y.; Lu, F. Silver-Nanoparticle-Based Surface-Enhanced Raman Scattering Wiper for the Detection of Dye Adulteration of Medicinal Herbs. *Anal. Bioanal. Chem.* **2015**, *407*, 6031–6039.

(212) Wu, M.; Li, P.; Zhu, Q.; Wu, M.; Li, H.; Lu, F. Functional Paper-Based SERS Substrate for Rapid and Sensitive Detection of Sudan Dyes in Herbal Medicine. *Spectrochim. Acta Part A* **2018**, *196*, 110–116.

(213) Qi, L.; Xiao, M.; Wang, X.; Wang, C.; Wang, L.; Song, S.; Qu, X.; Li, L.; Shi, J.; Pei, H. DNA-Encoded Raman-Active Anisotropic Nanoparticles for MicroRNA Detection. *Anal. Chem.* **2017**, *89*, 9850–9856.

(214) Wei, W.; Huang, Q. Rapid Fabrication of Silver Nanoparticle-Coated Filter Paper as SERS Substrate for Low-Abundance Molecules Detection. *Spectrochim. Acta A* **2017**, *179*, 211–215.

(215) Hassanain, W. A.; Izake, E. L.; Schmidt, M. S.; Ayoko, G. A. Gold Nanomaterials for the Selective Capturing and SERS Diagnosis of Toxins in Aqueous and Biological Fluids. *Biosens. and Bioelectron.* **2017**, *91*, 664–672.

(216) Hoppmann, E. P.; Wei, W. Y.; White, I. M. Inkjet-Printed Fluidic Paper Devices for Chemical and Biological Analytics Using Surface Enhanced Raman Spectroscopy. *IEEE J. Sel. Top. Quant. Electron.* **2014**, *20*, 195–204.

(217) Liao, W.-J.; Roy, P. K.; Chattopadhyay, S. An Ink-Jet Printed, Surface Enhanced Raman Scattering Paper for Food Screening. *RSC Adv.* **2014**, *4*, 40487–40493.

(218) Zhu, Y.; Li, M.; Yu, D.; Yang, L. A Novel Paper Rag as 'D-SERS'Substrate for Detection of Pesticide Residues at Various Peels. *Talanta* **2014**, *128*, 117–124.

(219) Zhu, J.; Chen, Q.; Kutsanedzie, F. Y.; Yang, M.; Ouyang, Q.; Jiang, H. Highly Sensitive and Label-Free Determination of Thiram Residue Using Surface-Enhanced Raman Spectroscopy (SERS) Coupled with Paper-Based Microfluidics. *Anal. Methods* **2017**, *9*, 6186–6193.

(220) Wang, K.; Huang, M.; Chen, J.; Lin, L.; Kong, L.; Liu, X.; Wang, H.; Lin, M. A "Drop-Wipe-Test" SERS Method for Rapid Detection of Pesticide Residues in Fruits. *J. Raman Spectrosc.* **2018**, *49*, 493–498.

(221) Lin, S.; Lin, X.; Lou, X.-T.; Yang, F.; Lin, D.-Y.; Lu, Z.-W. Rapid and Sensitive SERS Method for Determination of Rhodamine B in Chili Powder with Paper-Based Substrates. *Anal. Methods* **2015**, *7*, 5289–5294.

(222) Zhu, Y.; Zhang, L.; Yang, L. Designing of the Functional Paper-Based Surface-Enhanced Raman Spectroscopy Substrates for Colorants Detection. *Mater. Res. Bull.* **2015**, *63*, 199–204.

(223) Chen, M.; Yang, H.; Rong, L.; Chen, X. A Gas-Diffusion Microfluidic Paper-Based Analytical Device (μPAD) Coupled with Portable Surface-Enhanced Raman Scattering (SERS): Facile Determination of Sulphite in Wines. *Analyst* **2016**, *141*, 5511–5519.

(224) Li, D.; Duan, H.; Ma, Y.; Deng, W. Headspace-Sampling Paper-Based Analytical Device for Colorimetric/Surface-Enhanced Raman Scattering Dual Sensing of Sulphur Dioxide in Wine. *Anal. Chem.* **2018**, *90*, 5719–5727.

(225) Dou, B.; Luo, Y.; Chen, X.; Shi, B.; Du, Y.; Gao, Z.; Zhao, W.; Lin, B. Direct Measurement of Beta-Agonists in Swine Hair Extract in Multiplexed Mode by Surface-Enhanced Raman Spectroscopy and Microfluidic Paper. *Electrophoresis* **2015**, *36*, 485–487.

(226) Zheng, T.; Gao, Z.; Luo, Y.; Liu, X.; Zhao, W.; Lin, B. Manual-Slide-Engaged Paper Chip for Parallel SERS-Immunoassay Measurement of Clenbuterol from Swine Hair. *Electrophoresis* **2016**, *37*, 418–424.

(227) Durucan, O.; Rindzevicius, T.; Schmidt, M. S.; Matteucci, M.; Boisen, A. Nanopillar Filters for Surface-Enhanced Raman Spectroscopy. *ACS Sensors* **2017**, *2*, 1400–1404.

(228) Han, C.; Li, Y.; Jia, Q.; Bradley, L. H.; Gan, Y.; Yao, Y.; Qu, L.; Li, H.; Zhao, Y. On-Demand Fabrication of Surface-Enhanced Raman Scattering Arrays by Pen Writing,

and their Application to the Determination of Melamine in Milk. *Microchim. Acta* **2017**, *184*, 2909–2917.

(229) Li, D.; Lv, D. Y.; Zhu, Q. X.; Li, H.; Chen, H.; Wu, M. M.; Chai, Y. F.; Lu, F. Chromatographic Separation and Detection of Contaminants from Whole Milk Powder Using a Chitosan-Modified Silver Nanoparticles Surface-Enhanced Raman scattering Device. *Food Chem.* **2017**, *224*, 382–389.

(230) Mekonnen, M. L.; Su, W.-N.; Chen, C.-H.; Hwang, B.-J. Ag@SiO_2 Nanocube Loaded Miniaturized Filter Paper as a Hybrid Flexible Plasmonic SERS Substrate for Trace Melamine Detection. *Anal. Methods* **2017**, *9*, 6823–6829.

(231) Satheeshkumar, E.; Karuppaiya, P.; Sivashanmugan, K.; Chao, W.-T.; Tsay, H.-S.; Yoshimura, M. Biocompatible 3D SERS Substrate for Trace Detection of Amino Acids and Melamine. *Spectrochim. Acta A* **2017**, *181*, 91–97.

(232) Saviello, D.; Alyami, A.; Trabace, M.; Giorgi, R.; Baglioni, P.; Mirabile, A.; Iacopino, D. Plasmonic Colloidal Pastes for Surface-Enhanced Raman Spectroscopy (SERS) of Historical Felt-Tip Pens. *RSC Adv.* **2018**, *8*, 8365–8371.

(233) Figueroa, M.; Pourrezaei, K.; Tyagi, S. Fabrication of Flexible and Porous Surface Enhanced Raman Scattering (SERS) Substrates Using Nanoparticle inks. *AIP Conf. Proc.* **2012**, 1461, 47–53.

(234) Chen, Y.; Ge, F.; Guang, S.; Cai, Z. Low-Cost and Large-Scale Flexible SERS-Cotton Fabric as a Wipe Substrate for Surface Trace Analysis. *Appl. Surf. Sci.* **2018,** *436*, 111–116.

(235) Kong, X.-M.; Reza, M.; Ma, Y.-B.; Hinestroza, J.-P.; Ahvenniemi, E.; Vuorinen, T. Assembly of Metal Nanoparticles on Regenerated Fibres from Wood Sawdust and De-Inked Pulp: Flexible Substrates for Surface Enhanced Raman Scattering (SERS) Applications. *Cellulose* **2015**, *22*, 3645–3655.

(236) Wei, W.; Huang, Q. Preparation of Cellophane-Based Substrate and its SERS Performance on the Detection of CV and Acetamiprid. *Spectrochim. Acta A* **2018**, *193*, 8–13.

(237) Panwar, K.; Jassal, M.; Agrawal, A. K. Ag–SiO_2 Janus Particles Based Highly Active SERS Macroscopic Substrates. *Appl. Surf. Sci.* **2017**, *411*, 368–373.

(238) Kurokawa, Y.; Imai, Y. Surface-Enhanced Raman Scattering (SERS) Using Polymer (Cellulose Acetate and Nafion) Membranes Impregnated with Fine Silver Particles. *J. Membrane Sci.* **1991**, *55*, 227–233.

(239) Ishikawa, H.; Imai, Y.; Kurokawa, Y. Preparation of Ag Particle-Doped Cellulose Acetate Gel Membrane as a Surface-Enhanced Raman Scattering Active Substrate. *Vibr. Spectrosc.* **1995**, *8*, 445–449.

(240) Imai, Y.; Kurokawa, Y.; Hara, M.; Fukushima, M. Observation of SERS of Picolinic Acid and Nicotinic Acid Using Cellulose Acetate Films Doped with Ag Fine Particles. *Spectrochim. Acta A* **1997**, *53*, 1697–1700.

(241) Kurokawa, Y.; Imai, Y.; Tamai, Y. Surface-Enhanced Raman Scattering Observations on Bipyridine, Phthalimide, Phenylethylamine and Theobromine by Using a Fine Silver Particle-Doped Cellulose Gel Film. *Analyst* **1997**, *122*, 941–944.

(242) Imai, Y.; Tamai, Y.; Kurokawa, Y. Surface-Enhanced Raman Scattering of Benzoic and Thiosalicylic Acids Adsorbed on Fine Ag Particle-Impregnated Cellulose Gel Films. *J. Sol-Gel Sci. Techn.* **1998**, *11*, 273–278.

(243) Ke, Y.; Meng, G.; Huang, Z.; Zhou, N. Electrosprayed Large-Area Membranes of Ag-Nanocubes Embedded in Cellulose Acetate Microspheres as Homogeneous SERS Substrates. *J. Mater. Chem. C* **2017**, *5*, 1402–1408.

(244) López-Lorente, A.; Simonet, B.; Valcárcel, M.; Mizaikoff, B. Bare Gold Nanoparticles Mediated Surface-Enhanced Raman Spectroscopic Determination and Quantification of Carboxylated Single-Walled Carbon Nanotubes. *Anal. Chim. Acta* **2013**, *788*, 122–128.

(245) Chen, P.; Cui, L.; Zhang, K. Surface-Enhanced Raman Spectroscopy Monitoring the Development of Dual-Species Biofouling on Membrane Surfaces. *J. Membrane Sci.* **2015**, *473*, 36–44.

(246) Doherty, B.; Brunetti, B.; Sgamellotti, A.; Miliani, C. A Detachable SERS Active Cellulose Film: A Minimally Invasive Approach to the Study of Painting Lakes. *J. Raman Spectrosc.* **2011**, *42*, 1932–1938.

(247) Doherty, B.; Presciutti, F.; Sgamellotti, A.; Brunetti, B. G.; Miliani, C. Monitoring of Optimized SERS Active Gel Substrates for Painting and Paper Substrates by Unilateral NMR Profilometry. *J. Raman Spectrosc.* **2014**, *45*, 1153–1159.

(248) Lu, Y.; Feng, S.; Liu, X.; Chen, L., Surface-Enhanced Raman Scattering Study of Silver Nanoparticles Prepared by Using MC as a Template. *J. Nanomater.* **2013**, *2013*, 984831.

(249) Lee, W. W.; Silverson, V. A.; McCoy, C. P.; Donnelly, R. F.; Bell, S. E. Preaggregated Ag Nanoparticles in Dry Swellable Gel films for Off-the-Shelf Surface-Enhanced Raman Spectroscopy. *Anal. Chem.* **2014**, *86*, 8106–8113.

(250) Lee, W.; Silverson, V.; Jones, L. E.; Ho, Y. C.; Fletcher, N. C.; McNaul, M.; Peters, K. L.; Speers, S. J.; Bell, S. E. Surface-Enhanced Raman Spectroscopy of Novel Psychoactive Substances Using Polymer-Stabilized Ag Nanoparticle Aggregates. *Chem. Commun.* **2016**, *52*, 493–496.

(251) Lee, W. W.; McCoy, C. P.; Donnelly, R. F.; Bell, S. E. Swellable Polymer Films Containing Au Nanoparticles for Point-of-Care Therapeutic Drug Monitoring Using Surface-Enhanced Raman Spectroscopy. *Anal. Chim. Acta* **2016**, *912*, 111–116.

(252) Retko, K.; Ropret, P.; Cerc Korošec, R. Surface-Enhanced Raman Spectroscopy (SERS) Analysis of Organic Colourants Utilising a New UV-Photoreduced Substrate. *J. Raman Spectrosc.* **2014**, *45*, 1140–1146.

(253) Retko, K.; Ropret, P.; Cerc Korošec, R.; Sanchez-Cortes, S.; Cañamares, M. V. Characterization of HPC-Based Photoreduced SERS Substrates and Detection of Different Organic Dyes. *J. Raman Spectrosc.* **2018**, *49*, 1288–1300.

(254) Jiang, F.; Hsieh, Y.-L. Synthesis of Cellulose Nanofibril bound Silver nanoprism for Surface Enhanced Raman Scattering. *Biomacromolecules* **2014**, *15*, 3608–3616.

(255) Chook, S. W.; Chia, C. H.; Chan, C. H.; Chin, S. X.; Zakaria, S.; Sajab, M. S.; Huang, N. M. A Porous Aerogel Nanocomposite of Silver Nanoparticles-Functionalized Cellulose Nanofibrils for SERS Detection and Catalytic Degradation of Rhodamine B. *RSC Adv.* **2015**, *5*, 88915–88920.

(256) Nabeela, K.; Thomas, R. T.; Nair, J. B.; Maiti, K. K.; Warrier, K. G. K.; Pillai, S. TEMPO-Oxidized Nanocellulose Fibre-Directed Stable Aqueous Suspension of Plasmonic Flower-Like Silver Nanoconstruct for Ultra-Trace Detection of Analytes. *ACS Appl. Mater. Interf.* **2016**, *8*, 29242–29251.

(257) Zhang, L.; Li, X.; Ong, L.; Tabor, R. F.; Bowen, B. A.; Fernando, A. I.; Nilghaz, A.; Garnier, G.; Gras, S. L.; Wang, X. Cellulose Nanofibre Textured SERS Substrate. *Colloids and Surf. A* **2015**, *468*, 309–314.

(258) Chen, R.; Zhang, L.; Li, X.; Ong, L.; Soe, Y. G.; Sinsua, N.; Gras, S. L.; Tabor, R. F.; Wang, X.; Shen, W. Trace Analysis and Chemical Identification on Cellulose Nanofibres-Textured SERS Substrates Using the "Coffee Ring" Effect. *ACS Sensors* **2017**, *2*, 1060–1067.

(259) Xiong, Z.; Chen, X.; Liou, P.; Lin, M. Development of Nanofibrillated Cellulose Coated with Gold Nanoparticles for Measurement of Melamine by SERS. *Cellulose* **2017**, *24*, 2801–2811.

(260) Liou, P.; Nayigiziki, F. X.; Kong, F.; Mustapha, A.; Lin, M. Cellulose Nanofibres Coated with Silver Nanoparticles as a SERS Platform for Detection of Pesticides in Apples. *Carbohydr. Polym.* **2017**, *157*, 643–650.

(261) Zhang, S.; Xiong, R.; Mahmoud, M. A.; Quigley, E.; Chang, H.; El-Sayed, M. A.; Tsukruk, V. V. Dual-Excitation Nanocellulose-Plasmonic Membranes for Molecular and Cellular SERS Detection. *ACS Appl. Mater. Interf.* **2018**, *10*, 18380–18389.

(262) Xiong, Z.; Lin, M.; Lin, H.; Huang, M. Facile Synthesis of Cellulose Nanofibre Nanocomposite as a SERS Substrate for Detection of Thiram in Juice. *Carbohydr. Polym.* **2018**, *189*, 79–86.

(263) Oh, K.; Lee, M.; Lee, S. G.; Jung, D. H.; Lee, H. L. Cellulose Nanofibrils Coated Paper Substrate to Detect Trace Molecules Using Surface-Enhanced Raman Scattering. *Cellulose* **2018,** 1–12.

(264) Marques, P. A.; Nogueira, H. I.; Pinto, R. J.; Neto, C. P.; Trindade, T. Silver-Bacterial Cellulosic Sponges as Active SERS Substrates. *J. Raman Spectrosc.* **2008**, *39*, 439–443.

(265) Wei, H.; Rodriguez, K.; Renneckar, S.; Leng, W.; Vikesland, P. J. Preparation and Evaluation of Nanocellulose–Gold Nanoparticle Nanocomposites for SERS Applications. *Analyst* **2015**, *140*, 5640–5649.

(266) Wei, H.; Vikesland, P. J. pH-Triggered Molecular Alignment for Reproducible SERS Detection via an AuNP/Nanocellulose Platform. *Sci. Reports* **2015**, *5*, 18131

(267) Zhou, X.; Zhao, Z.; He, Y.; Ye, Y.; Zhou, J.; Zhang, J.; Ouyang, Q.; Tang, B.; Wang, X. Photoinduced Synthesis of Gold Nanoparticle–Bacterial Cellulose Nanocomposite and its Application for *In-situ* Detection of Trace Concentration of Dyes in Textile and Paper. *Cellulose* **2018**, *25*, 3941–3953.

(268) Park, M.; Chang, H.; Jeong, D. H.; Hyun, J., Spatial Deformation of Nanocellulose Hydrogel Enhances SERS. *BioChip J.* **2013**, *7*, 234–241.

(269) Tian, L.; Jiang, Q.; Liu, K. K.; Luan, J.; Naik, R. R.; Singamaneni, S. Bacterial Nanocellulose-Based Flexible Surface Enhanced Raman Scattering Substrate. *ACS Adv. Mater. Interf.* **2016**, *3*, 1600214.

(270) Tian, L.; Luan, J.; Liu, K.-K.; Jiang, Q.; Tadepalli, S.; Gupta, M. K.; Naik, R. R.; Singamaneni, S. Plasmonic Biofoam: a Versatile Optically Active Material. *Nano Lett.* **2015**, *16*, 609–616.

(271) Ren, S.; Dong, L.; Zhang, X.; Lei, T.; Ehrenhauser, F.; Song, K.; Li, M.; Sun, X.; Wu, Q. Electrospun Nanofibres Made of Silver Nanoparticles, Cellulose Nanocrystals, and

Polyacrylonitrile as Substrates for Surface-Enhanced Raman Scattering. *Materials* **2017**, *10*, 68.

(272) Ogundare, S. A.; van Zyl, W. E. Nanocrystalline Cellulose as Reducing- and Stabilizing Agent in the Synthesis of Silver Nanoparticles: Application as a Surface-Enhanced Raman Scattering (SERS) Substrate. *Surf. Interf.* **2018**, *13*, 1–10.

(273) Kelly, J. A.; Giese, M.; Shopsowitz, K. E.; Hamad, W. Y.; MacLachlan, M. J. The Development of Chiral Nematic Mesoporous Materials. *Acc. Chem. Res.* **2014**, *47*, 1088–1096.

Chapter 3

NCC isolated from discarded cigarette filters

This chapter is adapted from the work published in *Carbohydr. Polym.*, 2017, *175*, 273–281., DOI: 10.1016/j.carbpol.2017.08.008, titled: "Nanocrystalline cellulose isolated from discarded cigarette filters" by **Segun A. Ogundare**, Vashen Moodley and Werner E. van Zyl. Copyright © [2017]. Elsevier. The first author is responsible for all the experimental works, drafting of the manuscript and modification, all through to publication.

3.1 Introduction

The slow rate of photo and biodegradation of discarded cigarette filter (DCF) makes it ubiquitous as an environmental pollutant to both terrestrial and aquatic life. In 2010, an estimated 6.3 trillion cigarettes were consumed, and a significant percentage of the discarded filters were retrieved. By 2025, that number will reach a projected 9 trillion (> 1.5 M tonnes)[1-2] and yet DCF can easily be retrieved during clean-up activities in different designated public settings. With the concept of reverse logistics developed by Terracycle (Canada),[3] DCF are collected and transferred at no additional cost by consumers to the processing plants where it is transformed into plastics.

Although governments worldwide implement legislation towards the reduction of cigarette consumption[4] and to reduce DCF as source of litter,[1] there is clearly an urgent need to recycle this hazardous pollutant, particularly since DCF decomposition studies showed that it could persist between two to ten years under different ambient conditions.[5-6] DCF applications include the designing of energy storage materials[7] and efficient support material for oxygen reduction reactions.[8] The main chemical constituent in DCF is plasticized cellulose acetate from which NCC can be isolated. NCC is currently a highly sought after biopolymeric nanomaterial, which can be isolated from plant, animal and bacterial sources.[9] The economic potential of NCC in various applications[10-14] is due to the distinctive properties its possess, such as: biodegradation, high strength, specific surface area, high crystallinity index, low toxicity and density.[15-17] NCC is typically isolated by acid hydrolysis of cellulose.[18-21]

Research into the isolation of NCC has, more recently, started to focus on the use of recycled cellulosic materials. Such recycled materials can be divided into natural (agricultural) and man-made. This work falls into the latter category and examples that have been utilized include:

newspaper,[20, 22] waste tissue paper,[23] old corrugated containers,[24] wastepaper[25] recycled pulp;[26] recycled wood[27] and harvested bacteria.[28]

This study focused on the isolation and characterization of NCC from cellulose derived from DCF for the first time. The approach adopted involved the recovery of by-product and solvent in order to minimize environmental impact. NCC-DCF was isolated from DCF *via* deacetylation by using NaOH and hydrolysis by using sulphuric acid. The material was characterized with a variety of spectroscopic and microscopic techniques, in addition to elemental composition determination, X-ray diffraction (XRD), surface area and porosity measurements, thermogravimetric analysis (TGA) and differential thermal analysis (DTA) studies.

The objectives of this study were to retrieve and recycle cellulose acetate from DCF and chemically process it to produce NCC.

3.2 Experimental

3.2.1 Materials

Samples DCF were collected on the Westville campus, UKZN, South Africa. Ethanol (99.8 %), sodium hydroxide pellets (NaOH), sulphuric acid (H_2SO_4, 98% w/w), and sodium hypochlorite (NaOCl) were purchased from Sigma-Aldrich (USA). All chemicals were used as received. Double distilled water was used for reactions and dialysis.

3.2.2 Extraction of cellulose from Discarded CF

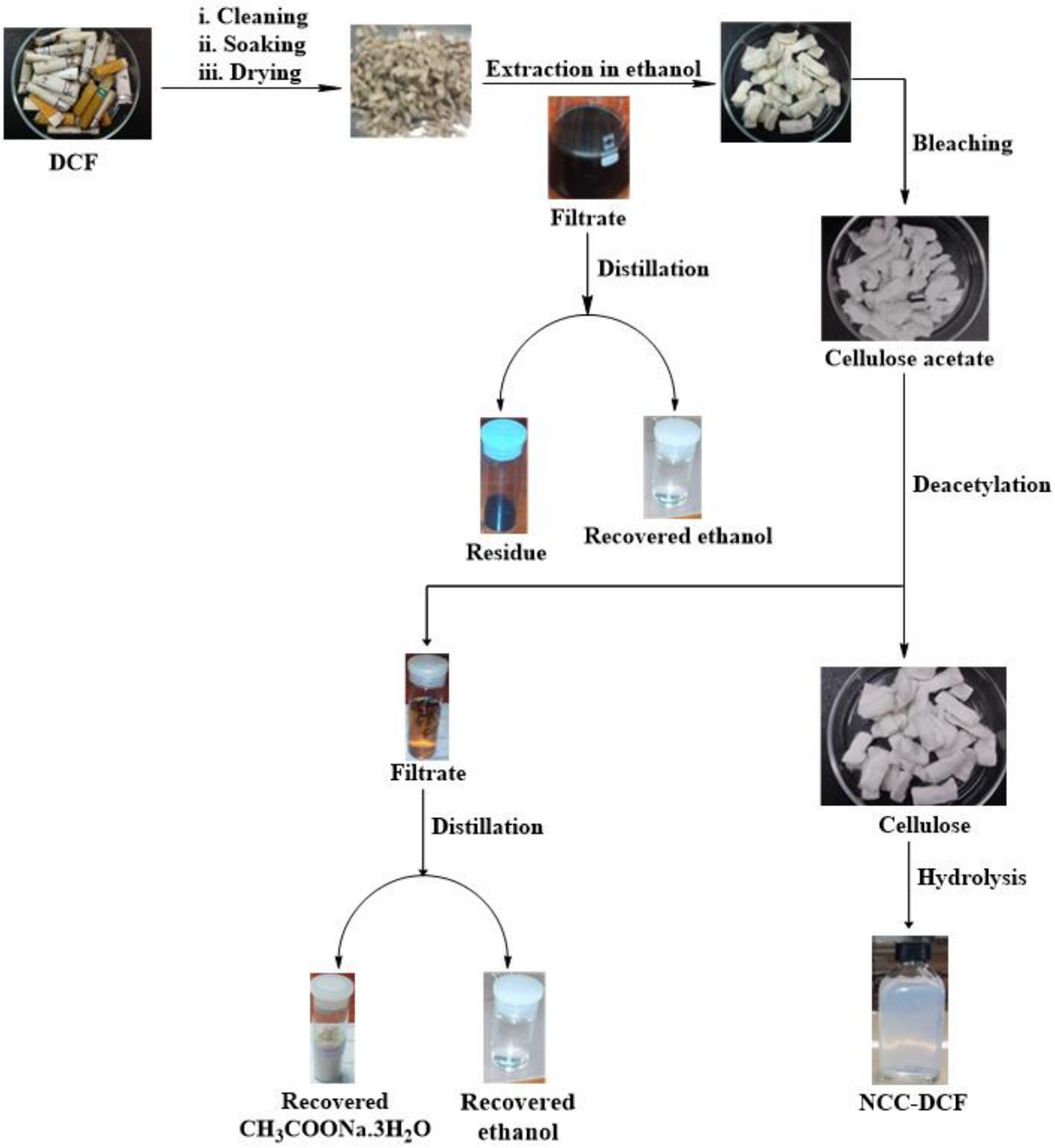
The extraction process is illustrated in Scheme 3.1 below. The filters were, first manually separated from paper and tobacco. Filters (ca. 10 g) were then soaked and washed with water, drained and extracted with ethanol (20 mL/g) for 24 hours at room temperature. After extraction, the cellulose acetate (CA-DCF) obtained was bleached using 1.25 w/v% NaOCl (10 mL/g) for 6 hours at room temperature. The dried CA-DCF obtained was deacetylated by using 1 w/v% of ethanolic NaOH (20 mL/g) at room temperature for 24 hours. NCC-DCF was subsequently isolated *via* acid hydrolysis. Distillation was carried out in order to recover the solvent used for the extraction and the by-product of deacetylation. The percentage yield of the Cel-DCF extracted from DCF was determined as shown in Eq. (3.1).

$$\% \text{ Yield of Cel-DCF} = \frac{\text{weight of extracted Cel-DCF (g)}}{\text{weight of DCF (g)}} \text{ x } 100\% \qquad (3.1)$$

3.2.3 Isolation of NCC-DCF

After the blending of Cel-DCF in a domestic blender, NCC-DCF was isolated by using 20 mL/g (volume acid per mass of cellulose) of 55 wt% sulphuric acid at 45°C in an oil bath for 45 minutes in order to remove the amorphous regions in Cel-DCF. Following the acid hydrolysis, the suspension was diluted 20 times its initial volume with double distilled water at room temperature and centrifuged by using OHAUS Frontier 5706 at 6000 rpm with relative centrifugal force 4427 x g for 10 min. This process was repeated 5 times in order to reduce the sulphuric acid concentration. To avoid aggregation, the suspension was then sonicated by using an ultrasonicator (UP400S, Hielscher, Germany) at 50% amplitude and a 0.5 cycle for 15 minutes to ensure complete dispersion of NCC-DCF before dialysis to a neutral pH. A NCC-DCF suspension (0.45 w/v%, 150 mL) was quickly frozen in liquid nitrogen for 15 minutes and freeze-dried for 72 hours at -60°C and 10^{-3} mbar in an Edwards Modulyo freeze-drier (Crawley, England). Similarly, NCC-DCF suspension (0.45 w/v%, 150 mL) was dried at ambient temperature in order to obtain NCC-DCF film, the ash of the film was obtained after calcination at 700°C in a nitrogen atmosphere (flow rate of 20 mL/min with a heating rate of 10°C/min). The film obtained was reduced to powder with pestle and mortar before characterization. The percentage yield of the isolated NCC-DCF was determined gravimetrically as shown in Eq. (3.2).

$$\% \text{ Yield of NCC-DCF} = \frac{\text{weight of NCC-DCF isolated (g)}}{\text{Weight of Cel-DCF used (g)}} \text{ x } 100\% \qquad (3.2)$$



Scheme 3.1. Stepwise isolation of NCC-DCF from DCF

3.3 Characterization

3.3.1 ^{1}H and ^{13}C NMR spectroscopy

^{1}H and ^{13}C NMR spectra of DCF and CA-DCF were recorded on a Bruker AV 600 (Germany) spectrometer in DMSO-d_6 at 60°C. The degree of substitution (DS) of CA-DCF was calculated from the ^{1}H NMR spectrum with Eq. (3.3):

$$DS = \frac{7 \text{ X } I_{methyl}}{3 \text{ X } I_{HAGU}} \quad (3.3)$$

where I_{methyl} is the peak integral of methyl protons and I_{HAGU} is the peak integral of anhydroglucose unit protons.[29-31]

3.3.2 Fourier transform infrared spectroscopy (FTIR)

The FTIR spectra of DCF, Cel-DCF, the by-product of deacetylation and the isolated NCC-DCF (freeze dried and film) were recorded in the wavelength range of between 380–4000 cm^{-1} at a resolution of 4 cm^{-1} using a Spectrum 100 infrared spectrometer equipped with a universal diamond crystal attenuated total reflection (ATR) accessory (Perkin Elmer, USA).

3.3.3 Morphological structure analysis

The morphological transition from DCF fibres to NCC-DCF was established with the aid of electron. For the TEM study, a JEOL 1010 (Japan) transmission electron microscope (TEM) was used. For the SEM study, a Zeiss Ultra Plus field emission gun scanning electron microscope (FEGSEM) equipped with an energy dispersive X-ray (EDX) detector (Germany) was used. TEM images of the NCC-DCF sample were acquired by using 5 µL of 0.01 w/w% suspension of NCC-DCF deposited on a copper (Cu) TEM-grid. The deposited crystals on the TEM-grid were negatively stained after drying with 5 µL of 2 wt% uranyl acetate for 5 minutes in the dark. The excess uranyl acetate solution was wicked-off with the tip of a Whatman filter paper and the stained crystals on the TEM-grid were dried. The dimensions of 100 randomly selected representative NCC-DCF crystals from the TEM micrographs were measured by using the ImageJ 1.42 software and the data obtained were processed on OriginPro 8 software. Similarly, DCF, Cel-DCF and NCC-DCF (freeze-dried, film and ash) samples for SEM images were deposited separately on conductive carbon tapes stuck to aluminium stubs. Each sample was coated with gold with the aid of a sputter coater in order to minimize charging.

3.3.4 Powder X-ray diffraction analysis

XRD analysis of DCF, Cel-DCF and NCC-DCF (freeze-dried sample and film) was performed by using an X-ray diffractometer (Bruker AXS D8 Advance, Germany), equipped with Cu-Kα radiation source (wavelength = 0.154 nm), operating at 40 kV and 40 mA. The XRD pattern

was recorded over the angular range 2θ = 5–40° at room temperature. The crystallinity index (*CI*) was calculated by using the Segal's method[32-33], as shown in Eq. (3.4).

$$CI\ (\%) = \frac{I_{002} - I_{am}}{I_{002}} \times 100\% \qquad (3.4)$$

where I_{002} is the 2θ = 22° peak associated with the maximum intensity, and I_{am} is 2θ = 18° peak associated with the intensity minimum of the amorphous region of the sample.

Crystallite size (D_{hkl}) was calculated by using the Scherrer's equation[34], as shown in Eq. (3.5); where λ is the X-ray wavelength (0.154 nm), β is the angular width at half maximum intensity, called full width half maximum (FWHM) determined with the aid of a Gaussian fit of the peaks on the diffractograms (Fig. S3.3, Appendix A) of the samples and θ is the Bragg angle. The crystallographic plane adopted for the estimation was 002.

$$D_{hkl}\ (\text{nm}) = \frac{0.89\lambda}{\beta\ cos\ \theta} \qquad (3.5)$$

3.3.5 Thermogravimetric analysis (TGA)

TGA was carried out by using a Simultaneous Thermal Analyzer STA 6000 (Perkin-Elmer, USA). The thermal analyses were conducted by using a sample mass in the range 7–8 mg in a nitrogen atmosphere (flow rate of 20 mL/min), with a constant heating rate of 10°C/min and at a temperature of 40–700°C, the samples were held at 700°C for 5 min. The weight loss (%) at the decomposition temperature and the residual char (%) at 700°C were determined from the TGA curves.

3.3.6 Specific surface area and porosity measurements

Samples were degassed at 90°C under vacuum for 24 h by using a Micromeritics VacPrep 061 sample degassing system (USA). Subsequently, Brunauer–Emmett–Teller (BET) analysis was performed with a surface area and porosity analyzer, Micromeritics Tristar II 3020 2.00 (USA) in a liquid N_2 cooled bath at a temperature of 77 K. Specific surface areas were calculated from the linear region of the isotherms by using the BET equation in a relative P/Po pressure range of between 0.063–0.300. Pore size distributions were derived from the adsorption branch of the isotherms by Barrett–Joyner–Halenda (BJH) method. The total pore volumes were estimated from the amount adsorbed at a relative pressure of P/Po = 0.996.

3.4 Results and Discussion

3.4.1 Nanocrystalline cellulose yield

NCC-DCF was isolated from DCF after ethanolic extraction, bleaching, deacetylation and sulphuric acid hydrolysis. The yield of the Cel-DCF obtained after deacetylation was 60% while the NCC-DCF yield from Cel-DCF was 49%, equivalent to appreciable yield of 29.4% NCC-DCF from DCF. The yield (29.4 %) of the isolated NCC-DCF from DCF is higher than 13.3% for NCC isolated from old corrugated container[24] and 19.0% for NCC isolated from wastepaper.[25] This is not surprising since cigarette filters are produced from refined materials containing less lignin.

3.4.2 NMR and FTIR Spectroscopies

3.4.2.1 NMR Spectroscopy

The ^{1}H and ^{13}C NMR spectra (Fig. 3.1(A and B)) of DCF and CA-DCF demonstrated the efficiency of the adopted method of extraction, no peaks other than cellulose acetate were observed in the spectrum of CA-DCF. The assignment of peaks shown in the ^{1}H and ^{13}C NMR spectra of the CA-DCF were in agreement with literature.[35] Solvent (DMSO-d_6) peaks were observed and appropriately assigned for the spectra.[30-31] The degree of substitution (2.34) and the percentage distribution of the acetyl moiety on C-6 (43 %), C-3 (25 %) and C-2 (32 %) positions were determined by quantitative integration of the methyl (CH_3) and anhydroglucose unit (H_{AGU}) proton peaks in the ^{1}H NMR spectrum of CA-DCF, which showed that the acetyl moiety was most abundant on C-6. This suggested that the primary hydroxyl group on C-6 was the most reactive during acetylation.

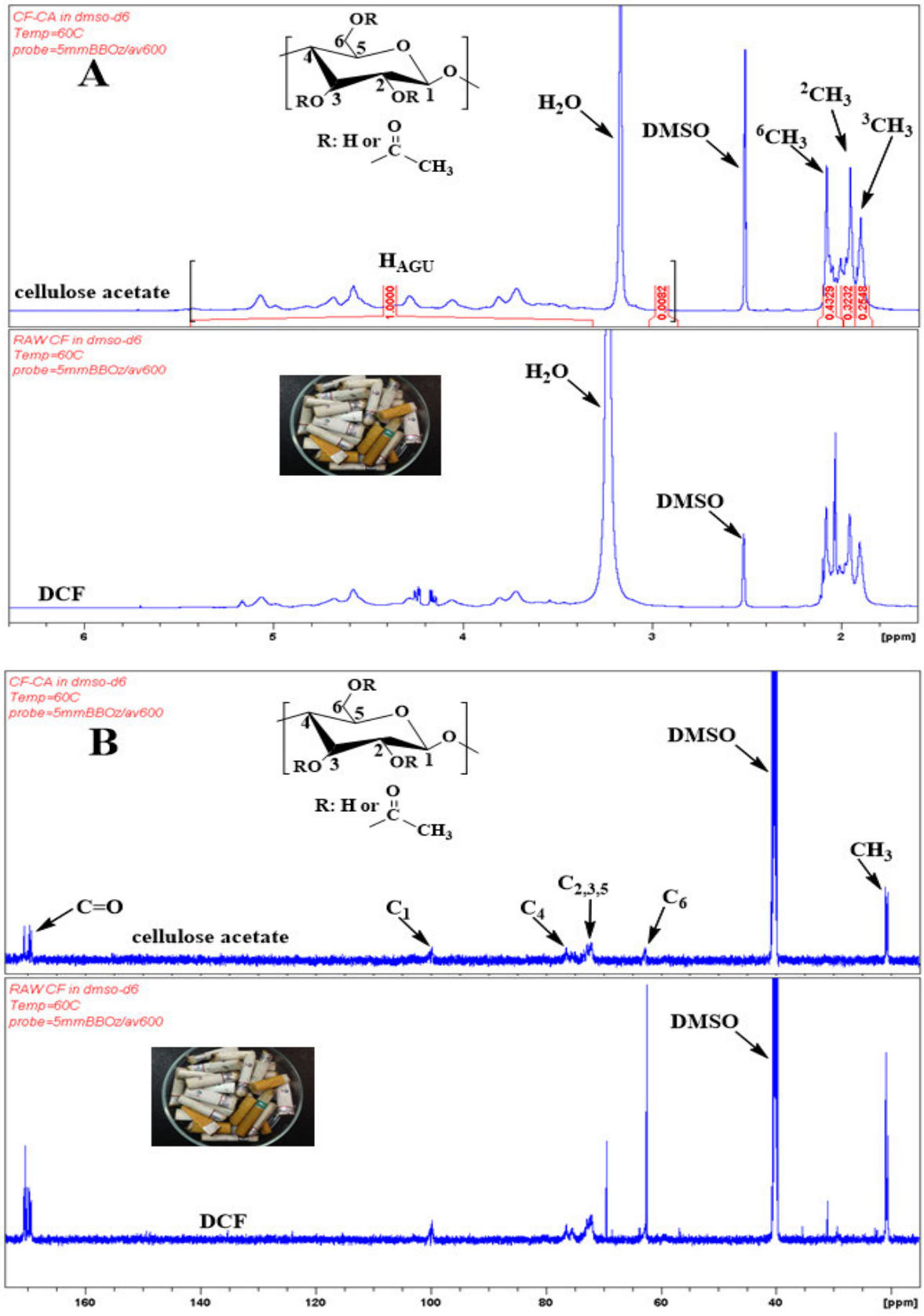


Fig. 3.1: ^{1}H NMR (A) and ^{13}C NMR (B) spectra of CA-DCF and DCF at 60°C in DMSO-d_6.

3.4.2.2 ATR-FTIR spectroscopy

The successful isolation of NCC-DCF from DCF was confirmed by FTIR. Strong absorption bands at 1743 and 1224 cm^{-1} were assigned to C=O stretching and (O)C–O stretching of the acetyl moiety present in the FTIR spectrum of DCF (Fig. 3.2).[36] These bands were characteristic of cellulose acetate, which disappeared on deacetylation as the FTIR spectrum of Cel-DCF showed a broad band at 3340 cm^{-1} which was assigned to O–H stretching and a medium band at 1646 cm^{-1} is associated with the absorbed moisture (H_2O). The identity of the by-product after deacetylation was confirmed to be $CH_3COONa.3H_2O$ (SAT-DCF) since its spectrum (Fig. S3.1, Appendix A) was identical to that of the laboratory reagent $CH_3COONa.3H_2O$ (SAT-LR). The FTIR spectra of the isolated NCC-DCF freeze-dried and film were identical, which suggested that the different methods of drying have no influence on the FTIR response of the isolated NCC. Similarly, these spectra showed identical absorption bands in comparison with the FTIR spectrum of Cel-DCF, but with greater intensities; an indication of increase in crystallinity due to the loss of the amorphous regions.[24] The FTIR absorption bands characteristics of NCC were found in the spectra of NCC-DCF (freeze-dried and film) samples (Fig. 3.2) and assigned (υ/cm^{-1}) as; 3320 (O–H), 2900 ($C–H_{asym}$), 1646 ($H–O–H_{bend}$), 1437 ($CH_{2(symm)}$), 1371 ($C–H_{asymbend}$), 1018 (C–O–C) and 898 ($C–H_{deform}$) modes of the β-glycosidic linkage ($^4C_1$) between the anhydroglucose rings.[37-38]

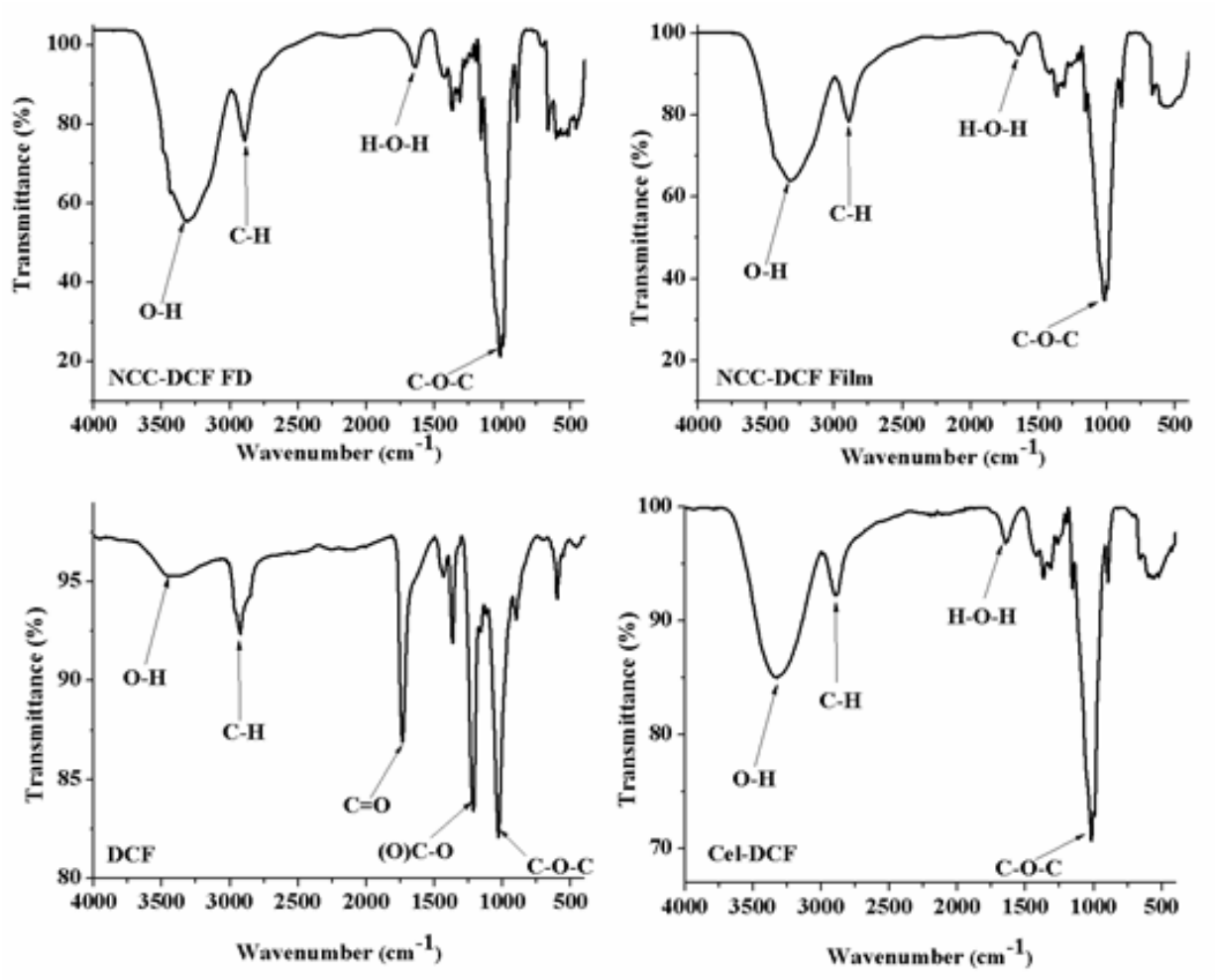


Fig. 3. 2: ATR-FTIR spectra of NCC-CF (film and freeze-dried (FD)), Cel-CF and DCF.

3.4.3 TEM study

The morphological structures of NCC-DCF established with TEM (Fig. 3.3A) showed that the nanocrystals were needle-like with calculated mean length of 143.5 ± 37.4 nm with a standard error of mean (SEM) 3.7 nm, width 8.3 ± 3.3 nm with a SEM 0.3 nm and aspect ratio 17.4 ± 5.7 with SEM 0.6, obtained from 100 randomly selected nanocrystals. The high standard deviations of the dimensions showed that the nanoparticles were polydispersed as revealed by the distributions of the dimensions (Fig. 3.3(B and C)). With an aspect ratio above 10 (the minimum aspect ratio for an ideal stress transfer within the interaction between fibres and matrix), the NCC-DCF isolated has the capacity to provide strong reinforcement and mechanical stability (irrespective of the percentage) when included in polymer.[39-40] The mean length and width (143.5 and 8.28 nm) of the NCC isolated were comparable with mean length and width; 113.0 and 8.50 nm reported for NCC isolated from wood,[27] 121.4 and 5.78 nm

reported for NCC isolated from newspaper,[20] 117.0 and 11.20 nm reported for NCC isolated from rice straw,[41] 200.0 and 7.00 nm reported for NCC isolated from bacteria.[28]

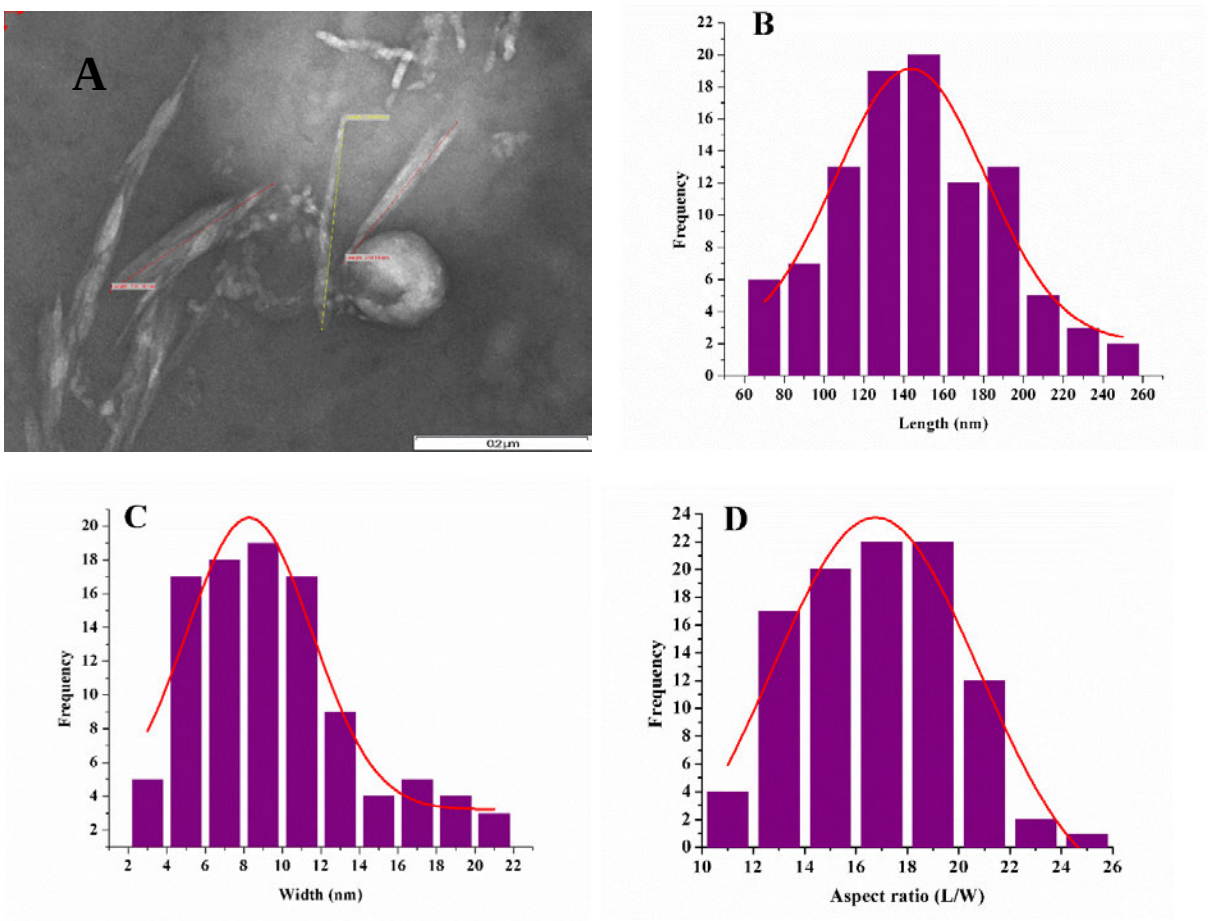


Fig. 3.3: TEM micrograph (A), and the distribution plots for length (B), width (C) and aspect ratio (D) of NCC-DCF.

3.4.4 FEGSEM and EDX study

The FEGSEM micrographs (Fig. 3.4) of DCF, Cel-DCF, and isolated NCC-DCF (freeze-dried and film), showed the morphological transition of DCF fibres to NCC-DCF. From 10 randomly selected samples, the average diameter of DCF fibres after deacetylation increased from 23.78 ± 1.74 µm with a standard error of mean (SEM) of between 0.55 to 26.20 ± 2.39 µm with SEM of 0.76 in the cellulose obtained, the t-test showed that the observed difference was significant as the calculated t-value (2.589) was higher than the critical value (2.101) at 95 % confidence level and degree of freedom 18 for a two-tailed test, as shown in the supplementary information (Appendix A). This attributed to an increase in moisture content, resulting in the swelling of the cellulose. As revealed by FTIR, the number of hydroxyl groups on the fibres increased after deacetylation hence, becoming more hydrophilic. From the micrograph of NCC-DCF freeze-dried sample (Fig. 3.4(C1–3)), the effectiveness of the acid hydrolysis was observed as the

diameter of Cel-DCF fibres were reduced to ~1.79 µm in the self-assemble fibrous freeze-dried NCC-DCF. Self-assemble fibrous NCCs were previously reported.[41] Similarly, Fig. 3.4(D1) also revealed the compact nature and the surface texture of the isolated NCC-DCF films obtained at room temperature. The presence of titanium (Ti) in DCF, Cel-DCF, and isolated NCC-DCF was revealed in the EDX (Fig. S3.2, Appendix A), since peaks corresponding to the binding energies of carbon (C), oxygen (O) and titanium were present in the spectra (Table S3.1, Appendix A). The titanium source was evidently from titania (TiO_2) incorporated into cigarette filters in order to enhance its photo-degradation process on disposal. At high magnification (50 kx), TiO_2 nanoparticles (70–110 nm) were observed to have been exposed on the surface of NCC-DCF freeze-dried (Fig. 3.4(C3)) however these nanoparticles were encapsulated by NCC-DCF in the film (Fig. 3.4(D3)) with size range of between 130–280 nm. This encapsulation attributed to the slow rate of drying at room temperature, which allowed NCC-DCF, to interact with TiO_2 unlike freeze-dried NCC-DCF, where the nanoparticles were instantaneously frozen in liquid nitrogen. The micrograph (Fig. 3.4(E3)) of the ash, rich in Ti (26.44%) obtained after calcination of the film, showed that NCC-DCF was lost, resulting in size reduction of the nanoparticles, to a range of between 110–190 nm. Similarly, the peak corresponding to the binding energy of sulphur (S) from the residual sulphate groups after acid hydrolysis was present in the EDX spectrum of the isolated NCC-DCF (freeze-dried and film).[42] The percentage sulphur content in NCC-DCF freeze-dried (0.78 %) and film (1.25 %) samples were close to 0.85 % that was reported for NCC isolated from cotton but greater than 0.18 % reported for NCC isolated from rice straw *via* sulphuric acid hydrolysis.[41] The difference observed in sulphur content suggested the non-uniformity of sulphate distribution on the surface of the isolated NCC-DCF. The EDX mapping of elements in DCF, Cel-DCF and the isolated NCC-DCF (freeze-dried, film and ash) are shown in the Supporting Information (SI) provided (Fig. S3.2, Appendix A).

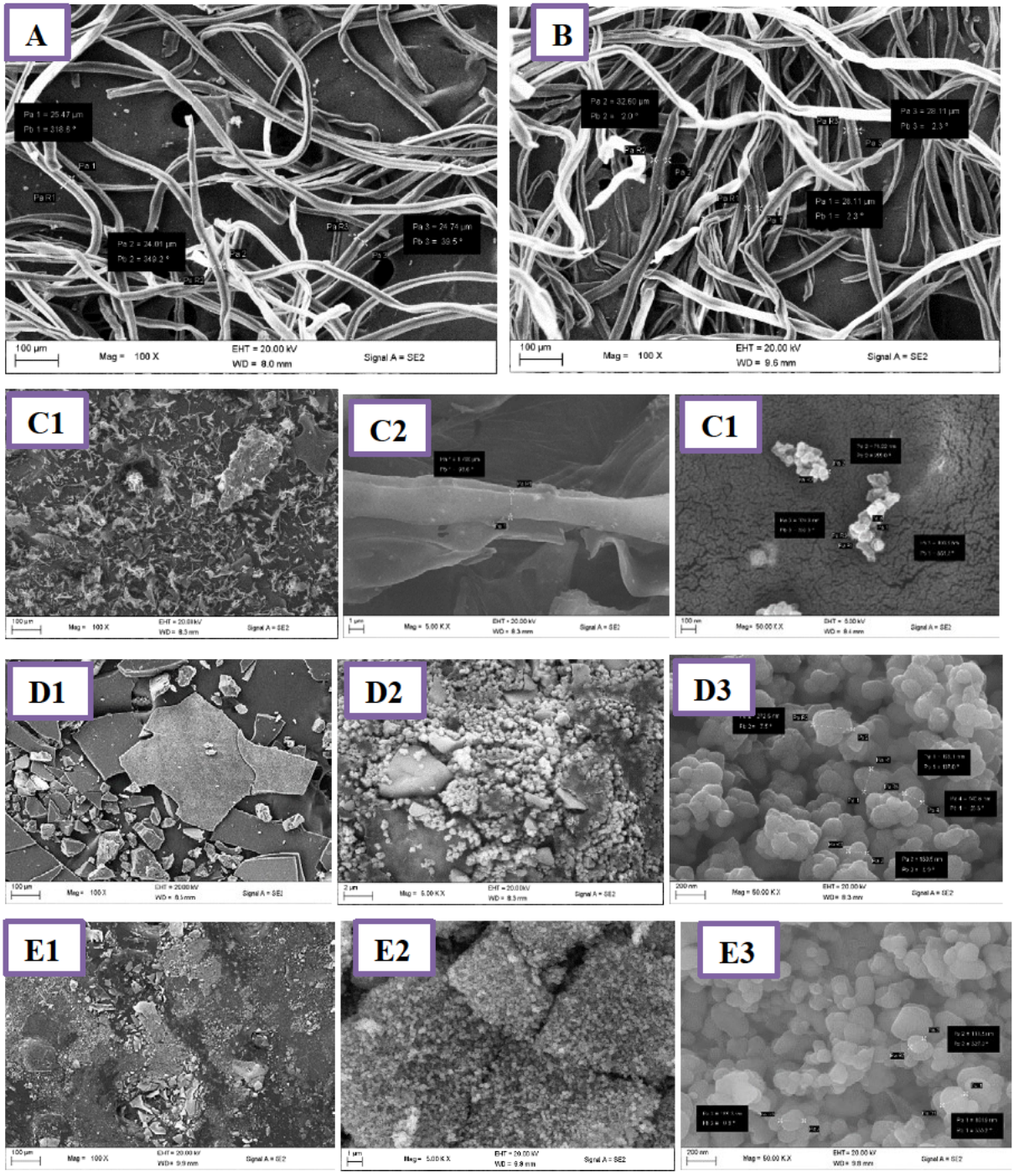
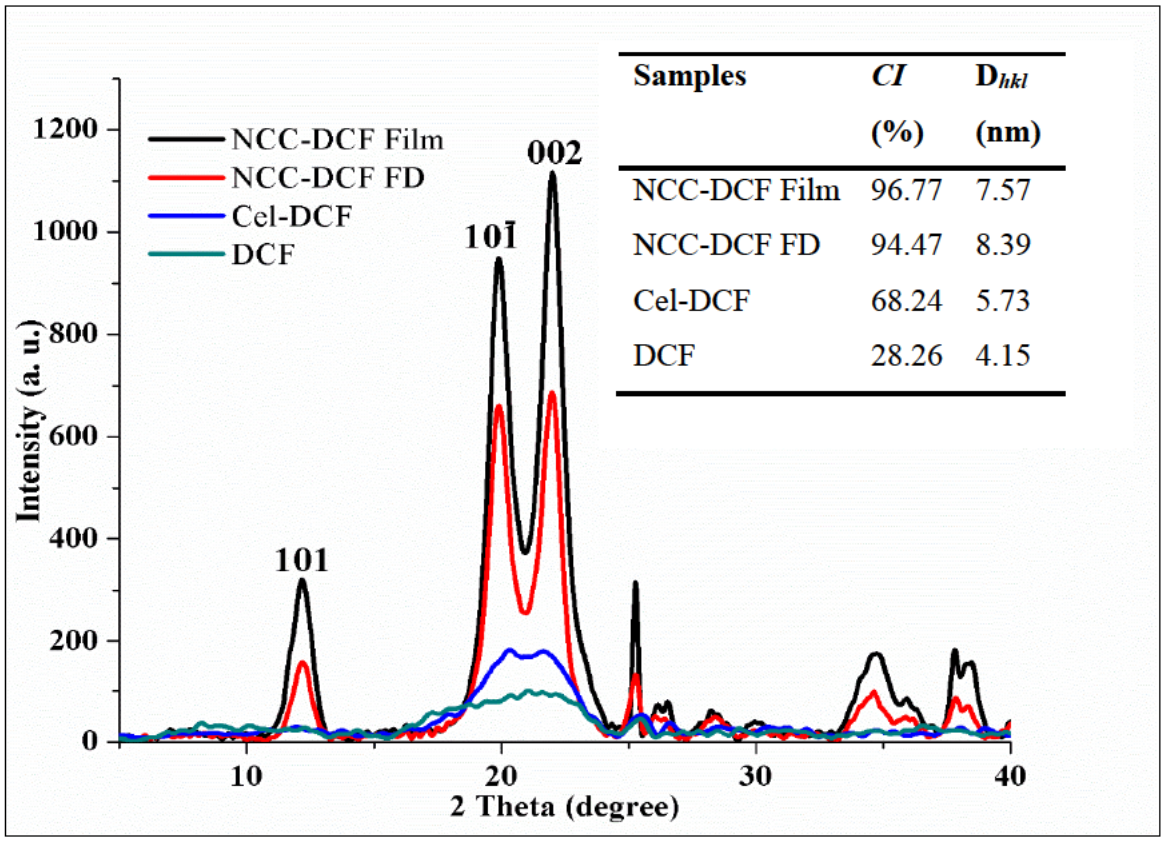


Fig. 3.4: FEGSEM micrographs of DCF (A), Cel-DCF (B), NCC-DCF freeze dried (C1-C3), film (D1-D3) and ash at 700°C (E1-E3).

3.4.5 X-Ray powder diffraction study

The XRD patterns (Fig. 3.5) of the NCC-DCF (freeze-dried and film) showed intense peaks at $2\theta = 12°$ (101), $20°$ ($10\bar{1}$) and $22°$ (002) that are characteristic of cellulose II allomorphs; an indication of the influence of alkaline hydrolysis on the isolated NCC-DCF.[43] These peaks were found to be broad and low in intensities in Cel-DCF. However, DCF showed a very broad

peak at 2θ = 22° and with a crystallinity index (*CI)* of 28.26 % indicated high amorphous content. An increased *CI* (68.24 %, Cel-DCF) was observed after deacetylation. This suggested partial removal of the amorphous regions in the cellulose in the alkaline medium used for the deacetylation. After acid hydrolysis, the isolated NCC-DCF showed a high degree of crystallinity with *CI* of 96.77 % (film) and 94.47 % (freeze-dried). The longer period of drying of NCC-DCF film allows the nanocrystals to pack in more orderly manner than freeze-dried NCC-DCF, where the nanocrystals were instantaneously frozen. The crystallite sizes (D_{hkl}) of the freeze-dried (8 nm) and the film (7 nm) NCC-DCF samples correlated with the average width (8 nm) of NCC-DCF observed under TEM (Fig. 3.3C). The slight variation in D_{hkl} suggested an influence of drying rate on the crystallite dimension. In comparison with D_{hkl} of the DCF, an increase in D_{hkl} was observed after deacetylation and acid hydrolysis (Fig. 3.5, inset Table). The high *CI* and D_{hkl} of the isolated NCC-DCF, showed the effectiveness of the acid hydrolysis in the removal of the amorphous region. The *CI* observed in NCC-DCF was higher than those reported by Danial *et al.,* [25] and Lu & Hsieh[41].



Samples	*CI* (%)	D_{hkl} (nm)
NCC-DCF Film	96.77	7.57
NCC-DCF FD	94.47	8.39
Cel-DCF	68.24	5.73
DCF	28.26	4.15

Fig. 3.5: X-ray diffractograms of NCC-DCF film, freeze-dried (FD), Cel-DCF and DCF. Inset Table: Crystallinity index (*CI*) and crystallite size (D_{hkl}).

3.4.6 Thermogravimetric analysis (TGA) and Differential thermal analysis (DTA)

The thermal behaviours of DCF, Cel-DCF and NCC-DCF (freeze-dried and film) were determined by using the TGA. The thermograms and the DTA curves, shown in Fig. 3.6, revealed comparable, but different rates of thermal degradation profiles. This suggested a similar thermal degradation mechanism, but which proceeded at different rates. The decomposition stages, the corresponding characteristic temperatures, the associated mass losses and ashes left at 700°C, are presented in Table 3.1.

The mass loss observed in the temperature range of between 40–110°C is attributed to the loss of absorbed moisture on the surface. The moisture contents of the NCC-DCF freeze-dried and film samples at 110°C were 1.97 % and 1.77 %, respectively. Cel-DCF showed a moisture content of ~6.78 % unlike DCF, which showed no weight loss at 110ºC. This observed increase in the moisture content of Cel-DCF, correlated well with the increase in hydroxyl groups and fibre diameter observed in the FITR spectra (Fig. 3.2) and the FEGSEM micrograph (Fig. 3.4B) of Cel-DCF. The decrease in the moisture content of the NCC-DCF sample when compared to the Cel-DCF sample, suggested the influence of the removed the amorphous regions in the Cel-DCF sample, hence, on its hydrophilic nature.

During cellulose pyrolysis, several complex reactions, such as: dehydration, decarbonylation, decarboxylation, depolymerization and other related reactions leading to release of gaseous species, including: H_2O, CO, CO_2 and H_2 and CH_4, are involved.[44] Two prominent thermal degradation stages were observed in the DTA curves of the analyzed samples. The freeze-dried sample showed higher peak temperature (T_p) and greater mass loss when compared to the film sample of NCC-DCF at the first stage (Table 3.1) of thermal degradation, which involved the dehydration of the anhydroglucopyranose chain segments. This suggested that the freeze-dried samples showed more resistance to thermal degradation, but the interior (embedded) crystals were more exposed to thermal degradation than those of the film sample. The reduced loss in mass in the film sample correlated with its higher crystallinity. Cel-DCF sample showed the highest T_p at 320ºC and mass loss of 39.55 %. However, DCF sample showed the least peak temperature and mass loss. The high T_p of Cel-DCF suggested greater thermal resistance when compared to DCF, which attributed to influence deacetylation. Unlike Cel-DCF, the sulphate groups on the film and freeze-dried samples of NCC-DCF, negatively influenced their thermal stability, by lowering the activation energy of thermal degradation and when released as sulphuric acid, it further catalyzed the degradation process.[44] In the second stage that involved chain decomposition and oxidative degradation of the interior part of samples, the film sample of NCC-DCF showed greater thermal resistance than the freeze-dried sample. This further

showed that the interior crystals in the film samples were less exposed because of the higher crystallinity. Similarly, Cel-DCF sample showed the highest T_p at the second stage of thermal degradation. The percentage of the ash content at 700°C was highest in the film sample and lowest in DCF. The high ash content in the NCC-DCF film and freeze-dried samples attributed to the dehydration effect of the sulphate group at lower temperature[44] while the difference in the ash content of the film and freeze-dried NCC-DCF sample could be attributed to the drying method that resulted in higher crystallinity for the film obtained at room temperature.

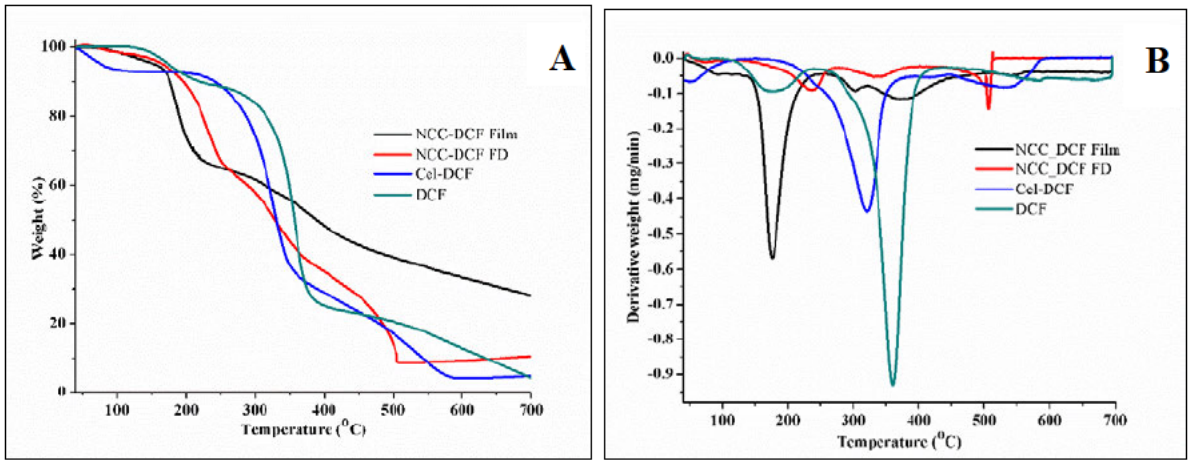


Fig. 3.6: The thermograms (A) and DTA curves (B) of NCC-DCF film, freeze-dried (FD), Cel-DCF and DCF.

Table 3.1. Comparison of thermal analysis data for NCC-DCF (film and freeze-dried), Cel-DCF and DCF.

Sample		T_i (°C)	T_p (°C)	T_f (°C)	Mass loss at T_p (%)	Ash at 700 °C (%)
NCC-DCF Film	Stage 1	138	176	239	9.54	28.04
	Stage 2	320	371	444	47.29	
NCC-DCF FD	Stage 1	143	236	268	26.28	10.52
	Stage 2	281	336	384	52.20	
Cel-DCF	Stage 1	172	320	376	39.55	4.64
	Stage 2	441	536	584	88.96	
DCF	Stage 1	116	174	239	4.85	4.18
	Stage 2	239	359	422	55.53	

Initial temperature (T_i), peak temperature (T_p), final temperature (T_f).

3.4.7 BET measurements

The film and the freeze-dried samples of NCC-DCF showed Type II sorption isotherms, typical for nonporous or macroporous adsorbent material with almost reversible adsorption and desorption loops (Fig. 3.7). The mean BET specific surface area and BJH cumulative volume of pores of the freeze-dried sample, obtained from simultaneously determining the triplicate analysis were, 7.78 ± 0.11 m^2/g and 0.015 ± 0.001 cm^3/g, respectively, were higher than 1.06 ± 0.02 m^2/g and 0.006 ± 0.002 cm^3/g, observed in the film sample obtained in a similar manner. The significant reduction in BET specific surface areas and pore volume of the film sample, suggested a self-assembly nature of the nanocrystals. However, inhibition induced by the narrow confinement in small ice crystals, resulting from the rapid freezing in liquid nitrogen, limited such compact assembly in the freeze-dried sample.[45] The mean specific surface area (7.78 m^2/g) and pore volume (0.015 cm^3/g) of freeze-dried NCC-DCF were close to 8.92 m^2/g and 0.025 cm^3/g observed in a free-dried sample of NCC, isolated from rice straw[41], while the mean specific surface area (1.06 m^2/g) of the film sample was comparable to 1.29 m^2/g that was observed in the NCC dry powder of bleached softwood kraft pulp.[46] The low pore volume observed in isolated NCC-DCF suggested that the nanocrystals were more closely packed *via* strong hydrogen bonding interaction as observed in the SEM micrographs. Similarly, DCF and Cel-DCF fibres showed type II isotherms with a BET surface area of 3.000 and 0.758 m^2/g, respectively. It is proposed that the difference is as a result of the effect of the deacetylation on the surface area of Cel-DCF due to increase in hydrogen bonding.

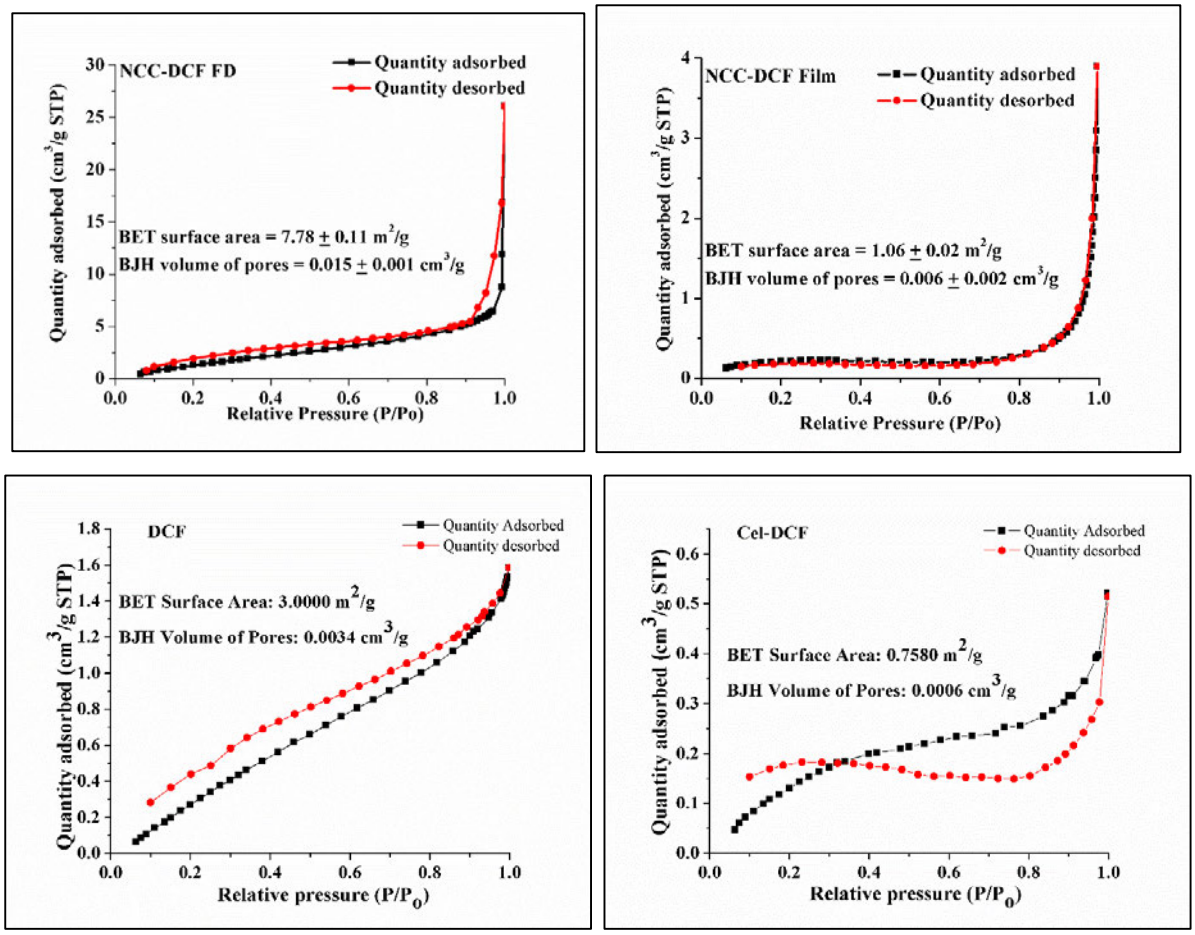


Fig. 3.7: BET Isotherms of NCC-DCF (freeze-dried (FD) and film samples), Cel-DCF and DCF.

3.5 Conclusion

This study has demonstrated the successful isolation of NCC from DCF, for the first time. TEM study showed that the NCC-DCF nanocrystals isolated were needle-like with mean length of 143 nm and a mean width of 8 nm. The higher crystallinity index (94.47 %) of the freeze-dried NCC-DCF sample showed significant improvement in structural organization when compared to the Cel-DCF sample with crystallinity index 68.24 %. FEGSEM showed the self-assembly and compact nature of NCC-DCF, while EDX revealed the presence of residual TiO_2 nanoparticles that were added to DCF in order to aid in the photodegradation process. With adequate logistics on collection by consumers, DCF can be considered a viable source of NCC, which has several demonstrated proof-of-concept and future applications. NCC has numerous applications, including heterogeneous catalysis support in the synthesis of organic compounds[47-48] as well as composites for biomedical purposes.[15] The NCC-DCF isolated sample reported in this study, will be further investigated for such applications.

3.6 References

(1) Novotny, T. E.; Lum, K.; Smith, E.; Wang, V.; Barnes, R. Cigarettes Butts and the Case for an Environmental Policy on Hazardous Cigarette Waste. *Int. J. Env. Res. Pub. He.* **2009**, *6*, 1691–1705.

(2) Slaughter, E.; Gersberg, R. M.; Watanabe, K.; Rudolph, J.; Stransky, C.; Novotny, T. E. Toxicity of Cigarette Butts, and Their Chemical Components, to Marine and Freshwater Fish. *Tob. Control* **2011**, *20*, i25–i29.

(3) https://www.terracycle.ca/en-CA/brigades/cigarette-waste-brigade, accessed 29th April, 2017

(4) Novotny, T. E.; Bialous, S. A.; Burt, L.; Curtis, C.; Costa, V. L. d.; Iqtidar, S. U.; Liu, Y.; Pujari, S.; Tursan d'Espaignet, E. The Environmental and Health Impacts of Tobacco Agriculture, Cigarette Manufacture and Consumption. *B. World Health Organ.* **2015**, *93*, 877–880.

(5) Bonanomi, G.; Incerti, G.; Cesarano, G.; Gaglione, S. A.; Lanzotti, V. Cigarette Butt Decomposition and Associated Chemical Changes Assessed by ^{13}C CPMAS NMR. *PloS one* **2015**, *10*, e0117393.

(6) Robertson, R. M.; Thomas, W. C.; Suthar, J. N.; Brown, D. M. Accelerated Degradation of Cellulose Acetate Cigarette Filters Using Controlled-Release Acid Catalysis. *Green Chem.* **2012**, *14*, 2266–2272.

(7) Lee, M.; Kim, G.-P.; Song, H. D.; Park, S.; Yi, J. Preparation of Energy Storage Material Derived from a Used Cigarette Filter for a Supercapacitor Electrode. *Nanotechnology* **2014**, *25*, 345601.

(8) Kim, G.-P.; Lee, M.; Song, H. D.; Bae, S.; Yi, J. Highly Efficient Supporting Material Derived from Used Cigarette Filter for Oxygen Reduction Reaction. *Catal. Commun.* **2016**, *78*, 1–6.

(9) Wei, H.; Rodriguez, K.; Renneckar, S.; Vikesland, P. J. Environmental Science and Engineering Applications of Nanocellulose-Based Nanocomposites. *Environ. Sci.: Nano* **2014**, *1*, 302–316.

(10) Shatkin, J. A.; Wegner, T. H.; Bilek, E.; Cowie, J. Market Projections of Cellulose Nanomaterial-Enabled Products–Part 1: Applications. *TAPPI J.* **2014**, *13*, 9–16.

(11) Cowie, J.; Bilek, E.; Wegner, T. H.; Shatkin, J. A. Market Projections of Cellulose Nanomaterial-Enabled Products–Part 2: Volume Estimates. *TAPPI J.* **2014**, *13*, 57–69.

(12) Lindström, T.; Aulin, C. Market and Technical Challenges and Opportunities in the Area of Innovative New Materials and Composites Based on Nanocellulosics. *Scand. J. Forest Res.* **2014**, *29*, 345–351.

(13) Abitbol, T.; Rivkin, A.; Cao, Y.; Nevo, Y.; Abraham, E.; Ben-Shalom, T.; Lapidot, S.; Shoseyov, O. Nanocellulose, a Tiny Fibre with Huge Applications. *Curr. Opin. Biotechnol.* **2016**, *39*, 76–88.

(14) Zhu, H.; Luo, W.; Ciesielski, P. N.; Fang, Z.; Zhu, J.; Henriksson, G.; Himmel, M. E.; Hu, L. Wood-Derived Materials for Green Electronics, Biological Devices, and Energy Applications. *Chem. Rev.* **2016**, *116*, 9305–9374.

(15) Rojas, J.; Bedoya, M.; Ciro, Y. In *Cellulose- Fundamental Aspect and Current Trends*; Polleto, M., Ornaghi, H. L., Eds.;Intech, 2015; Chapter 8, pp 193–227.

(16) Jonoobi, M.; Oladi, R.; Davoudpour, Y.; Oksman, K.; Dufresne, A.; Hamzeh, Y.; Davoodi, R. Different Preparation Methods and Properties of Nanostructured Cellulose from Various Natural Resources and Residues: A Review. *Cellulose* **2015**, *22*, 935–969.

(17) Lin, N.; Huang, J.; Dufresne, A. Preparation, Properties and Applications of Polysaccharide Nanocrystals in Advanced Functional Nanomaterials: A Review. *Nanoscale* **2012**, *4*, 3274–3294.

(18) Zhang, P. P.; Tong, D. S.; Lin, C. X.; Yang, H. M.; Zhong, Z. K.; Yu, W. H.; Wang, H.; Zhou, C. H. Effects of Acid Treatments on Bamboo Cellulose Nanocrystals. *Asia-Pac. J. Chem. Eng.* **2014**, *9*, 686–695.

(19) Luzi, F.; Fortunati, E.; Jiménez, A.; Puglia, D.; Pezzolla, D.; Gigliotti, G.; Kenny, J.; Chiralt, A.; Torre, L. Production and Characterization of PLA-PBS Biodegradable Blends Reinforced with Cellulose Nanocrystals Extracted from Hemp Fibres. *Ind. Crop. Prod.* **2016**, *93*, 276–289

(20) Mohamed, M.; Salleh, W.; Jaafar, J.; Asri, S.; Ismail, A. Physicochemical Properties of "Green" Nanocrystalline Cellulose Isolated from Recycled Newspaper. *RSC Adv.* **2015**, *5*, 29842–29849.

(21) Phanthong, P.; Guan, G.; Ma, Y.; Hao, X.; Abudula, A. Effect of Ball Milling on the Production of Nanocellulose Using Mild Acid Hydrolysis Method. *J. Taiwan Inst. Chem. Eng.* **2016**, *60*, 617–622.

(22) Takagi, H.; Nakagaito, A. N.; Bistamam, M. S. A. Extraction of Cellulose Nanofibre from Waste Papers and Application to Reinforcement in Biodegradable Composites. *J. Reinf. Plast. Comp.* **2013**, *32*, 1542–1546.

(23) Maiti, S.; Jayaramudu, J.; Das, K.; Reddy, S. M.; Sadiku, R.; Ray, S. S.; Liu, D. Preparation and Characterization of Nano-cellulose with New Shape from Different Precursor. *Carbohydr. Polym.* **2013**, *98*, 562–567.

(24) Tang, Y.; Shen, X.; Zhang, J.; Guo, D.; Kong, F.; Zhang, N. Extraction of Cellulose Nano-Crystals from Old Corrugated Container Fibre Using Phosphoric Acid and Enzymatic Hydrolysis Followed by Sonication. *Carbohydr. Polym.* **2015**, *125*, 360–366.

(25) Danial, W. H.; Majid, Z. A.; Muhid, M. N. M.; Triwahyono, S.; Bakar, M. B.; Ramli, Z. The Reuse of Wastepaper for the Extraction of Cellulose Nanocrystals. *Carbohydr. Polym.* **2015**, *118*, 165–169.

(26) Filson, P. B.; Dawson-Andoh, B. E.; Schwegler-Berry, D. Enzymatic-Mediated Production of Cellulose Nanocrystals from Recycled Pulp. *Green Chem.* **2009,** *11*, 1808–1814.

(27) Liu, H.; Liu, D.; Yao, F.; Wu, Q. Fabrication and Properties of Transparent Polymethylmethacrylate/Cellulose Nanocrystals Composites. *Bioresour. Technol.* **2010**, *101*, 5685–5692.

(28) Hirai, A.; Inui, O.; Horii, F.; Tsuji, M. Phase Separation Behavior in Aqueous Suspensions of Bacterial Cellulose Nanocrystals Prepared by Sulphuric Acid Treatment. *Langmuir* **2008**, *25*, 497–502.

(29) Cao, J.; Sun, X.; Lu, C.; Zhou, Z.; Zhang, X.; Yuan, G. Water-Soluble Cellulose Acetate from Waste Cotton Fabrics and the Aqueous Processing of all-Cellulose Composites. *Carbohydr. Polym.* **2016**, *149*, 60–67.

(30) Yang, Y.; Xie, H.; Liu, E. Acylation of Cellulose in Reversible Ionic Liquids. *Green Chem.* **2014**, *16*, 3018–3023.

(31) Konwar, L. J.; Mäki-Arvela, P.; Thakur, A. J.; Kumar, N.; Mikkola, J.-P. Sulfonated Carbon as a New, Reusable Heterogeneous Catalyst for One-Pot Synthesis of Acetone Soluble Cellulose Acetate. *RSC Adv.* **2016**, *6*, 8829–8837.

(32) Wang, H.; Zhang, X.; Jiang, Z.; Li, W.; Yu, Y. A Comparison Study on the Preparation of Nanocellulose Fibrils from Fibres and Parenchymal Cells in Bamboo (*Phyllostachys pubescens*). *Ind. Crop. Prod.* **2015**, *71*, 80–88.

(33) Li, J.; Wei, X.; Wang, Q.; Chen, J.; Chang, G.; Kong, L.; Su, J.; Liu, Y. Homogeneous Isolation of Nanocellulose from Sugarcane Bagasse by High Pressure Homogenization. *Carbohydr. Polym.* **2012**, *90*, 1609–1613.

(34) Brito, B. S.; Pereira, F. V.; Putaux, J.-L.; Jean, B. Preparation, Morphology and Structure of Cellulose Nanocrystals from Bamboo Fibres. *Cellulose* **2012**, *19*, 1527–1536.

(35) Pang, J.; Liu, X.; Yang, J.; Lu, F.; Wang, B.; Xu, F.; Ma, M.; Zhang, X. Synthesis of Highly Polymerized Water-Soluble Cellulose Acetate by the Side Reaction in Carboxylate Ionic Liquid 1-Ethyl-3-Methylimidazolium Acetate. *Sci. Rep.* **2016**, *6*, 33725.

(36) Yan, M.; Li, S.; Zhang, M.; Li, C.; Dong, F.; Li, W. Characterization of Surface Acetylated Nanocrystalline Cellulose by Single-Step Method. *BioResources* **2013**, *8*, 6330–6341.

(37) Chen, Y. W.; Lee, H. V.; Juan, J. C.; Phang, S.-M. Production of New Cellulose Nanomaterial from Red Algae Marine Biomass *Gelidium elegans*. *Carbohydr. Polym.* **2016**, *151*, 1210–1219.

(38) Xiang, Z.; Gao, W.; Chen, L.; Lan, W.; Zhu, J.; Runge, T. A Comparison of Cellulose Nanofibrils Produced from *Cladophora glomerata* Algae and Bleached Eucalyptus Pulp. *Cellulose* **2016**, *23*, 493–503.

(39) Deepa, B.; Abraham, E.; Cordeiro, N.; Mozetic, M.; Mathew, A. P.; Oksman, K.; Faria, M.; Thomas, S.; Pothan, L. A. Utilization of Various Lignocellulosic Biomass for the Production of Nanocellulose: A Comparative Study. *Cellulose* **2015**, *22*, 1075–1090.

(40) Mueller, S.; Weder, C.; Foster, E. J. Isolation of Cellulose Nanocrystals from Pseudostems of Banana Plants. *RSC Adv.* **2014**, *4*, 907–915.

(41) Lu, P.; Hsieh, Y.-L. Preparation and Characterization of Cellulose Nanocrystals from Rice Straw. *Carbohydr. Polym.* **2012**, *87*, 564–573.

(42) Bano, S.; Negi, Y. S. Studies on Cellulose Nanocrystals Isolated from Groundnut Shells. *Carbohydr. Polym.* **2017**, *157*, 1041–1049.

(43) Mittal, A.; Katahira, R.; Himmel, M. E.; Johnson, D. K. Effects of Alkaline or Liquid-Ammonia Treatment on Crystalline Cellulose: Changes in Crystalline Structure and Effects on Enzymatic Digestibility. *Biotechnol. Biofuels* **2011**, *4*, 41.

(44) Jiang, F.; Hsieh, Y.-L. Chemically and Mechanically Isolated Nanocellulose and Their Self-Assembled Structures. *Carbohydr. Polym.* **2013**, *95*, 32–40.

(45) Jiang, F.; Hsieh, Y.-L. Assembling and Redispersibility of Rice Straw Nanocellulose: Effect of Tert-Butanol. *ACS Appl. Mater. Interfaces* **2014**, *6*, 20075–20084.

(46) Brinkmann, A.; Chen, M.; Couillard, M.; Jakubek, Z. J.; Leng, T.; Johnston, L. J. Correlating Cellulose Nanocrystal Particle Size and Surface Area. *Langmuir* **2016**, *32*, 6105–6114.

(47) Moodley, V.; Maddila, S.; Jonnalagadda, S. B.; van Zyl, W. E. Synthesis of Triazolidine-3-one Derivatives Through the Nanocellulose/Hydroxyapatite-Catalyzed Reaction of Aldehydes and Semicarbazide. *New J. Chem.* **2017**, *41*, 6455–6463.

(48) Kaushik, M.; Moores, A. Review: Nanocelluloses as Versatile Supports for Metal Nanoparticles and Their Applications in Catalysis. *Green Chem.* **2016**, *18*, 622–637.

Chapter 4

NCC as a reducing- and stabilizing agent in the synthesis of silver nanoparticles: Application as a SERS substrate

This chapter is adapted from the work that was published in *Surfaces and Interfaces.*, 2018, *13*, 1–10., DOI: 10.1016/j.surfin.2018.06.004, titled: "Nanocrystalline cellulose as reducing- and stabilizing agent in the synthesis of silver nanoparticles: Application as a surface-enhanced Raman scattering (SERS) substrate" by **Segun A. Ogundare** and Werner E. van Zyl. Copyright © [2018]. Elsevier. The first author is responsible for all the experimental work, drafting of the manuscript and modification through to publication.

4.1 Introduction

Silver nanoparticles have been explored in many technological areas, including: as catalysts for the degradation of dyes, conductive adhesives, antimicrobial agents, and a variety of consumer goods.[1-3] Silver nanoparticles are of interest due to its unique interaction with light and hence, giving rise to localized surface plasmon resonance (LSPR), which is caused by electromagnetic field of the incident light coupled with the oscillation of conduction-band electrons.[4] LSRP induces resonant scattering and good light absorption, typically leading to several orders of magnitude increase in the near-field enhancement of the local electromagnetic fields.[5-6] Importantly, this phenomenon is primarily caused by size and shapes of the silver nanoparticles (AgNPs).[7-9] The size and shape-dependent properties, have led to a number of applications in optoelectronics,[10] metal mediated- fluorescence,[11]sensors,[12] and surface-enhanced Raman scattering (SERS),[13-14] including SERS application in point-of-care (POC) diagnostics.[15] SERS is a powerful spectroscopic technique and can be applied in diverse areas of science[16-20]. This is due to its highly sensitive detection when compared with conventional spectroscopic techniques.[21-24]

Nanocrystalline cellulose (NCC), which is a sub-category of nanocellulose,[25-27] has attracted increasing attention due to its extraordinary mechanical, thermal and optical properties.[28-30] SERS has been applied to NCC/AuNPs[31] and cellulose-nanofibrils/Ag nanoprism composites[32-33] however in both cases, additional chemicals were needed to reduce the metals.

Scattering and fluorescence interference, which result in low intensity in standard Raman spectroscopy, are easily overcome due to the LSPR of the AgNPs.[33-36]

Chemical reduction of silver salts is the synthetic route, commonly adopted for the preparation of AgNPs. This involves the use of suitable solvents, reducing agents and stabilizing agents.[37-38] within the context of green chemistry, the use of naturally-occurring reducing and stabilizing agents are the preferred choice in forming AgNPs when compared to the alternative highly reactive hazardous chemicals.[39] Cellulose is the most abundant biopolymer on earth and it has been explored in its native and derived states as reducing and/or stabilizing agent in the synthesis of AgNPs.[40] During the course of formation, the hydroxyl groups on the cellulose surface form a complex with silver ions through ion-dipole interaction and prevent aggregation on reduction by coating the AgNP.[41] When cellulose is hydrolyzed, NCC can be isolated.[25] A number of environmental science and engineering applications of nanocellulose-based nanocomposites have been reported.[42] Such NCC materials result in a greater reducing and stabilizing capacity when compared to native cellulose due its higher surface charge and specific surface area. However, NCC is typically used as stabilizer in the presence of other reducing agents, except when surface-modified[43] without which, high temperature in combination with hydrothermal conditions are needed for NCC to function as both reducing- and stabilizing agent.[44-45] It was shown that partial desulphurization of NCC, in the synthesis of AgNPs, improved the nucleation and stabilizing capacity of NCC in the presence of $NaBH_4$ as reducing agent at room temperature.[41] Similarly, an increase in pH of NCC solution also improved its reducing capacity in the preparation of gold nanoparticles (AuNPs) under hydrothermal condition.[46] However, the influence of pH on the reducing and stabilizing capacity of NCC in the preparation of AgNPs without the use of other reducing agents or hydrothermal conditions, has not been previously reported, and this was the basis of the present study. The influence of pH on both the reducing and stabilizing capacity of NCC was investigated in the production AgNPs at 80°C under different pH conditions.

Riboflavin is an organic compound that can be secreted from phytoplankton in natural waters, and has been demonstrated to be an effective sensitizer to enhance the photochemical transformation of many organic compounds in aqueous solutions.[47] Additionally, since riboflavin and river humic acid in a natural environment have a significant influence on the fate of many organic pollutants, including that of polycyclic aromatic hydrocarbons (PAHs),[48] a low cost method for the detection of riboflavin at low concentration levels will be valuable.

The need for a reliable and fast method of detection of trace analytes has made the use of AgNPs as a SERS substrate a useful analytical tool. Here, the use of NCC to serve the dual

purpose as a reducing- and stabilizing agent in the formation of AgNPs for the first time is reported. It is further demonstrated that the formed nanocomposite can be applied as an efficient SERS substrate in the detection of riboflavin.

4.2 Experimental

4.2.1 Materials

Discarded cigarette filters (DCF) were collected on the Westville campus, UKZN, South Africa. Ethanol, sodium hydroxide pellets (NaOH), sulphuric acid (H_2SO_4, 98% w/w), silver nitrate ($AgNO_3$), hydrochloric acid (HCl, 32 % w/w), nitric acid (HNO_3, 69 % w/w), sodium hypochlorite, (NaOCl) and riboflavin (98%) were purchased from Sigma-Aldrich. All chemicals were used as received. Double distilled water was used for reactions and dialysis.

4.2.2 Isolation of NCC

The isolation and characterization of NCC from the cellulose obtained from DCF has been previously reported.[49] Briefly, cellulose was obtained from DCF via ethanolic extraction, NaOCl bleaching and deacetylation with NaOH in ethanol. NCC was isolated by using 20 mL/g (volume acid per mass of cellulose) of 55 wt% sulphuric acid at 45°C in an oil bath for 45 min in order to remove the amorphous regions in cellulose. After 45 min, the suspension was diluted (dilution factor: 20) with double distilled water at room temperature and centrifuged by using OHAUS Frontier 5706 at 6000 rpm with relative centrifugal force 4427 x g for 10 min. This procedure was repeated 5 times in order to reduce the sulphuric acid concentration. Aggregation of nanocrystals was avoided by sonicating the suspension by using an ultrasonicator (UP400S, Hielscher, Germany) at 50% amplitude and a 0.5 cycle for 15 min in order to ensure thorough dispersion of NCC-DCF before dialyzing to neutral pH.

4.2.3 Synthesis of silver nanoparticles

The synthesis of AgNPs was conducted at 80°C by using 10 mL of 0.1 wt% NCC dispersion sonicated for 15 min and adjusted to the desired pH (5, 6, 7, 8, 9 or 10) with 0.1 M NaOH or 0.1 M HCl. Freshly prepared $AgNO_3$ solution (1 mL) of the desired concentration (0.10, 0.15, 0.20, 0.25 or 0.30 M) was added to the stirring NCC dispersion and the temperature was maintained at 80°C for a fixed period (15, 30, 45, 60 or 75 min). The AgNPs obtained in each reaction were washed with double distilled water and centrifuged at 6000 rpm with relative centrifugal force 4427 x g for 10 min in order to remove unreacted $AgNO_3$. This procedure was repeated 5 times in order to ensure complete removal of unreacted $AgNO_3$. Each sample was diluted to 50 mL before UV-vis spectroscopic study and transmission electron microscopic (TEM) imaging. Colloids for SERS application and dry AgNPs for characterization were

prepared at 80°C for 75 min by using 0.30 M $AgNO_3$ and 0.1 wt% of NCC (pH: 10). The obtained AgNPs were similarly washed and centrifuged to remove unreacted $AgNO_3$. The concentration of AgNPs in the colloid was determined with an inductive coupled plasma optical emission spectroscopy (ICP-OES) after a microwave digestion. Dry AgNPs were obtained by drying the colloid at 50°C for 24 hours in an oven. In order to study the thermal effect on morphology of the AgNPs and ascertain the percentage of AgNPs in the dried product, the residual product of the dried AgNPs was obtained following calcination at 600°C in a nitrogen atmosphere (flow rate of 20 mL/min with a heating rate of 10°C/min).

4.3 Characterization of the synthesized AgNPs

4.3.1. UV-vis spectroscopy

The absorption spectra of the various AgNPs samples synthesized were obtained in the wavelength range of between 300–700 nm by using UV-3600 Plus UV-VIS-NIR Spectrophotometer, Shimadzu, Japan. A LAMBDA^{TM} 35 UV/VIS Spectrophotometer, by PerkinElmer, equipped with an integrating sphere was used to acquire the absorption spectrum of AgNPs absorbed on filter paper.

4.3.2 Microwave digestion and ICP-OES analysis

A triplicate analysis was simultaneously performed in order to determine the concentration of AgNPs in the colloid by digesting three separate samples each containing AgNPs colloid and HNO_3 (69 % w/w) in volume ratio 1:5 (colloid: nitric acid) by using a MARS 6 Microwave Reaction System (CEM, USA) at 200°C for 15min. From a 1000 ppm stock solution of Ag^+ ions prepared by using $AgNO_3$, a series of standard solutions (100–0.5 ppm) were prepared by serial dilution and used for calibration on Optima 5300 DV ICP-OES Inductive Coupled Plasma spectrometer (Perkin Elmer, USA) before the determination of Ag^+ ions in the digested AgNPs colloid samples.

4.3.3 Morphological studies

The size, shape and dispersion of the AgNPs were examined with the aid of electron. For the TEM and HRTEM studies, a JEOL 1010 (Japan) transmission electron microscope (TEM) and a JEOL 2100 (Japan) high resolution transmission electron microscope (HRTEM) were used. For the SEM study, a Zeiss Ultra Plus field emission gun scanning electron microscope (FEGSEM) equipped with energy dispersive X-ray (EDX) detector (Germany) was used. TEM and HRTEM images of the AgNP samples were acquired by using 5µL of each sample

deposited on a copper TEM-grid. The diameters of 150 AgNPs were measured from the TEM micrographs by using the ImageJ 1.42 software and the data obtained were processed on OriginPro 8 software. Similarly, dried and calcined product of AgNPs samples for SEM images, were deposited on a conductive carbon tape, stuck to aluminium stubs. The samples were coated with gold with the aid of sputter coater in order to minimize charging and improve conductivity.

4.3.4 Fourier transform infrared spectroscopy (FTIR)

FTIR spectra of samples were obtained in the range of between 380–4000 cm^{-1} at a resolution of 4 cm^{-1} by using Spectrum 100 infrared spectrometer equipped with universal diamond crystal attenuated total reflection (ATR) accessory (Perkin Elmer, USA).

4.3.5 Powder X-ray diffraction analysis

XRD analysis of the dried and calcined product AgNPs were performed by using an X-ray diffractometer (Bruker AXS D8 Advance, Germany), equipped with Cu-Kα radiation source (wavelength = 0.154 nm) operating at 40 kV and 40 mA. The XRD pattern was recorded over the angular range 2θ = 5–80° at room temperature. The crystallite diameter (D_{hkl}) was calculated by using Scherrer's formula as shown in Eq. (4.1), where λ is the X-ray wavelength (0.154 nm), β is the angular full width at half maximum (FWHM) intensity, determined with the aid of a Gaussian fit of the peaks on the diffractogram (Fig. S4.7, Appendix B) of the samples and θ is the Bragg angle. The crystallographic plane adopted for the calculation was (111).

$$D_{hkl}\ (\text{nm}) = \frac{0.89\,\lambda}{\beta \cos\theta} \qquad (4.1)$$

4.3.6 Specific surface area and porosity measurements

AgNPs samples were degassed at 90°C under vacuum for 24 hours by using a Micromeritics VacPrep 061 sample degassing system (USA). Thereafter, BET analysis was carried out with a surface area and porosity analyzer, Micromeritics Tristar II 3020 2.00 (USA) in a liquid N_2 cooled bath temperature of 77.2 K. Specific surface areas were calculated from the linear region of the isotherms by using the BET equation in a relative P/Po pressure range of 0.063–0.300. Pore size distributions were derived from the adsorption branch of the isotherms by Barrett–

Joyner–Halenda (BJH) method. The total pore volumes were estimated from the amount adsorbed at a relative pressure of P/Po = 0.996.

4.3.7 Thermogravimetric analysis (TGA)

TGA of the synthesized AgNPs was performed by using a Simultaneous Thermal Analyzer STA 6000 (Perkin-Elmer, USA). The thermal analysis was conducted by using a sample mass of 15.50 mg in a nitrogen atmosphere (flow rate of 20 mL/min) with a constant heating rate of 10°C/min and at a temperature of between 40–600°C, while the samples were held at 600°C for 10 min. The weight loss (%) at the decomposition temperature and the residual product (%) at 600°C were determined from the TGA curves.

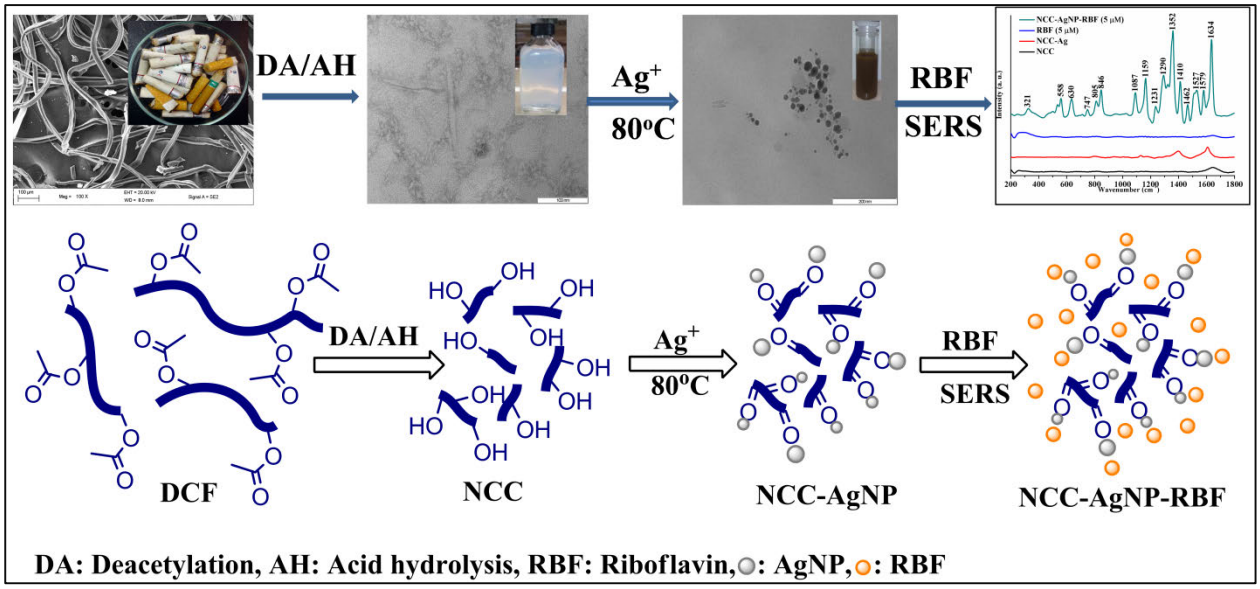
4.4 SERS spectroscopic study

The AgNPs colloid synthesized was used as substrate in the detection of riboflavin. A 100 µM stock solution of riboflavin was prepared and a series of standard solutions (10–10^{-5} µM) were prepared by serial dilution. The SERS spectroscopic study was carried out by using 1 mL of sample solution containing 1:1 volume ratio of AgNPs colloid and riboflavin solution of the desired concentration after incubation period of 30 min at 25°C. A sample cell (8 mm vial) provided for the liquid sample, with dimension 8 mm diameter and 40mm height, was used and SERS spectra were acquired in the range of between 200–1800 cm^{-1} from an Advantage 532™ Raman Spectrometer, equipped with charge coupled device (CCD) detector and NuSpec software (DeltaNu, USA). The laser power was 100 mW at a 532 nm excitation wavelength and integration time of 10 seconds for each acquired spectrum. A triplicate measurement was carried out on each sample and each measurement was obtained from an average of 10 spectra in order to ensure good precision. In order to further explore the SERS potential capacity of the synthesized AgNPs, filter papers (20 by 20 mm) were used to adsorb the AgNPs in the colloid. After 60 min of contacting time of the filter papers with the colloid, the filter papers were washed 5 times with water in order to remove unadsorbed AgNPs. The filter papers were dried at 25˚C temperature and later contacted with various concentrations (10–10^{-5} µM) of riboflavin for a 30 min incubation period, in the dark; thereafter the filter papers were washed 5 times with water and dried in the dark at 25˚C. The SERS signals of the riboflavin adsorbed on the filter papers were acquired in a similar manner to the liquid samples.

4.5 Results and Discussion

4.5.1 Optical study

The good dispersion, high surface area and rich hydroxyl groups on the surface of NCC make it a suitable reducing agent for Ag^+ ions to form AgNPs. During the course of the synthesis, the Ag^+ ions got attached to the hydroxyl groups on the surface of NCC *via* ion-dipole interaction and upon reduction to Ag atoms, coalesced to spherical nanoparticles stabilized by the NCC, resulting to the characteristic yellow colour associated with the formation of AgNPs Scheme 4.1.



Scheme 4.1. Synthesis of AgNPs using NCC isolated from DCF as both reducing and stabilizing agent and SERS application in detection of riboflavin.

The intensity of the colour increased from pH 5 to pH 10, as shown in Fig. 4.1(A1). This attributed to an increase in the concentration of AgNPs synthesized with increase in pH. Similar increase in the colour intensity was observed with increase in time and concentration of $AgNO_3$ (Fig. 4.1(B1 and C1)). However, at pH 10 and 0.30M concentration of $AgNO_3$, aggregated colloid of AgNPs were observed, which suggested that the optimum capacity of the 0.1 wt% NCC suspension used as a stabilizing agent was reached. The UV-vis spectra of the AgNPs synthesized showed characteristic absorption peaks associated with surface plasmon resonance (SPR). With increase in pH, the absorption peaks were slightly shifted in wavelength from 416 nm (pH 5) to 412 nm (pH 10) for 0.10 M concentration of $AgNO_3$ at 75 min (Fig. 4.1(A2)), indicating a decrease in AgNPs sizes with increase in pH.[46] The broad absorption peak at pH 5 (Fig. 4.1(A2)), which gradually changed into narrow peak with the highest

absorbance at pH 10, suggested an improved monodispersity and an increase in the concentration of AgNPs[40], which corroborated the observed increase in colour intensity. The significant role of pH suggested an increase in number of available hydroxyl groups with reducing capacity since more surface-bonded sulphate ions were exchanged[41] and the hydrogen bonds weakened between the NCC as the pH increased.[46] At pH 10 and 0.10 M concentration of $AgNO_3$, the absorption peak was however shifted in wavelength from 406 nm (15 min) to 412 nm after 30 min and subsequently, remained at 412 nm throughout (Fig. 4.1(B2)). Similarly, the absorption peak was gradually shifted with increase in concentration of $AgNO_3$ from a wavelength of 406 nm (0.10 M) to 413 nm (0.30 M) at pH 10 (Fig. 4.1(C2)). The red shifts in the absorption peaks attributed to decrease in AgNPs sizes with increase in time and concentration.[46] The dark brown AgNPs colloid showed an absorption peak at 416 nm (Fig. 4.1(D1and D2)) and remained stable without precipitation. Similar absorption peak was observed when AgNPs was adsorbed on the filter paper (Fig. 4.1(D3)). The UV-vis spectra of the AgNPs synthesized at different time for pH (5–9) and at different concentration for pH (5–9) are presented in Fig. S4.1 and S4.2, respectively in Appendix B.

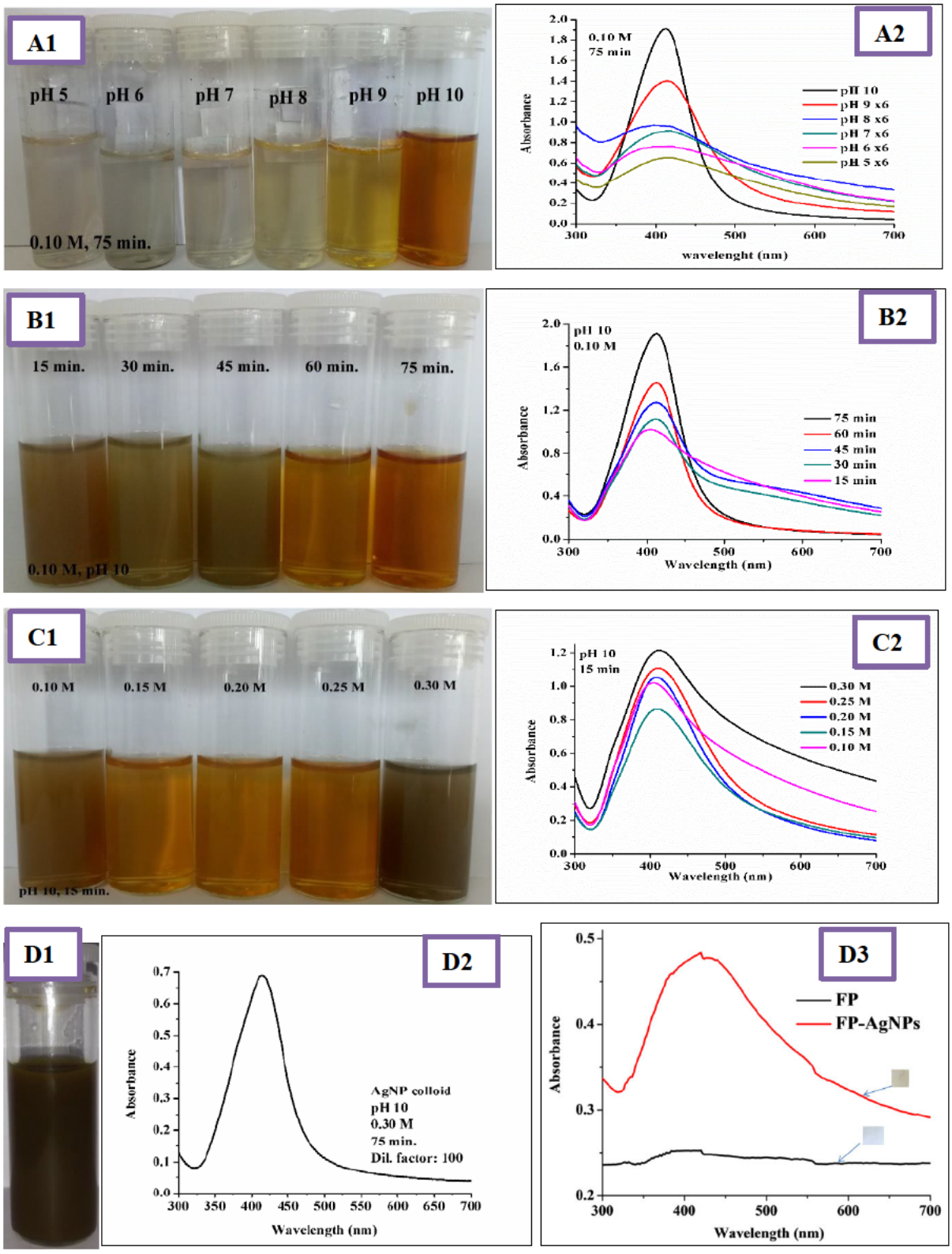


Fig. 4.1: Images and absorption spectra of synthesized AgNPs at different; pHs (A1 and A2), time intervals (B1 and B2), concentrations of $AgNO_3$ (C1 and C2) and AgNPs colloid (D1, D2 and D3). *Note*: Spectra for pH 9 – 5 in A2 were magnified 6 times (x6).

4.5.2 TEM/HRTEM study

NCC isolated from DCF and used in the synthesis of AgNPs were needlelike with a calculated mean length 143.5 ± 37.4 nm, width 8.3 ± 3.3 nm and aspect ratio 17.4 ± 5.7, as was previously reported.[49] The variation in the reaction conditions adopted for the synthesis of the AgNPs showed a significant effect on their dispersion and size distributions, as revealed by the TEM images and histograms in Fig. 4.2(A, B and C). The variation in size distributions as studied by using 0.20 M concentration of $AgNO_3$ and 15 min reaction time, showed a notable increase in population of smaller AgNPs (< 10 nm) with increase in pH (Fig. 4.2A), while the population of the larger aggregates (> 10 nm) diminished gradually with a corresponding decrease in the mean diameter from 19.9 ± 11.1 nm (pH 5) to 4.6 ± 1.6 nm (pH 9). This attributed to an increase in hydroxyl groups with suitable reducing and stabilizing effects since more sulphate ions were exchange with increase in pH.[41] The increase in population of the smaller AgNPs with increase in pH, corroborated the observed increase in intensity of the absorption peak of UV-vis spectra. The increase in population of the smaller AgNPs reached the optimum at pH 9 because the AgNPs coalesced at pH 10, resulting in an increase in the population of the larger aggregates. This suggested that the optimum capacity of the NCC as stabilizing agent was reached. A similar increase in the population of the smaller AgNPs and decrease in mean diameter, were observed with increase in reaction time using 0.10 M $AgNO_3$ at pH 10 (Fig. 4.2B). After 60 min, the population of the larger aggregates increased significantly, indicating coalescence of smaller AgNPs. However, an increase in the concentration of $AgNO_3$ at pH 10 and a 15 min reaction time resulted in a decrease in the population of the smaller AgNPs, with an increase in the mean diameter (Fig. 4.2C). This indicated fast rates of nucleation and coalescence in the presence of high concentration of $AgNO_3$.[44] As revealed by TEM and HRTEM micrographs of the AgNPs colloid (Fig. 4.2D), the AgNPs remained, monodispersed even at pH 10 with lattice fringes of ~0.246 nm, which correlated to the (111) plane of a face-centered cubic (FCC) of Ag metal.[40] The inset of a selected area electron diffraction (SAED) pattern in HRTEM micrograph, showed that the AgNPs were polycrystalline.[44] This result conclusively demonstrated the reducing and stabilizing capability of NCC in the synthesis of AgNPs, under different reaction conditions, hence leading to variation in size.

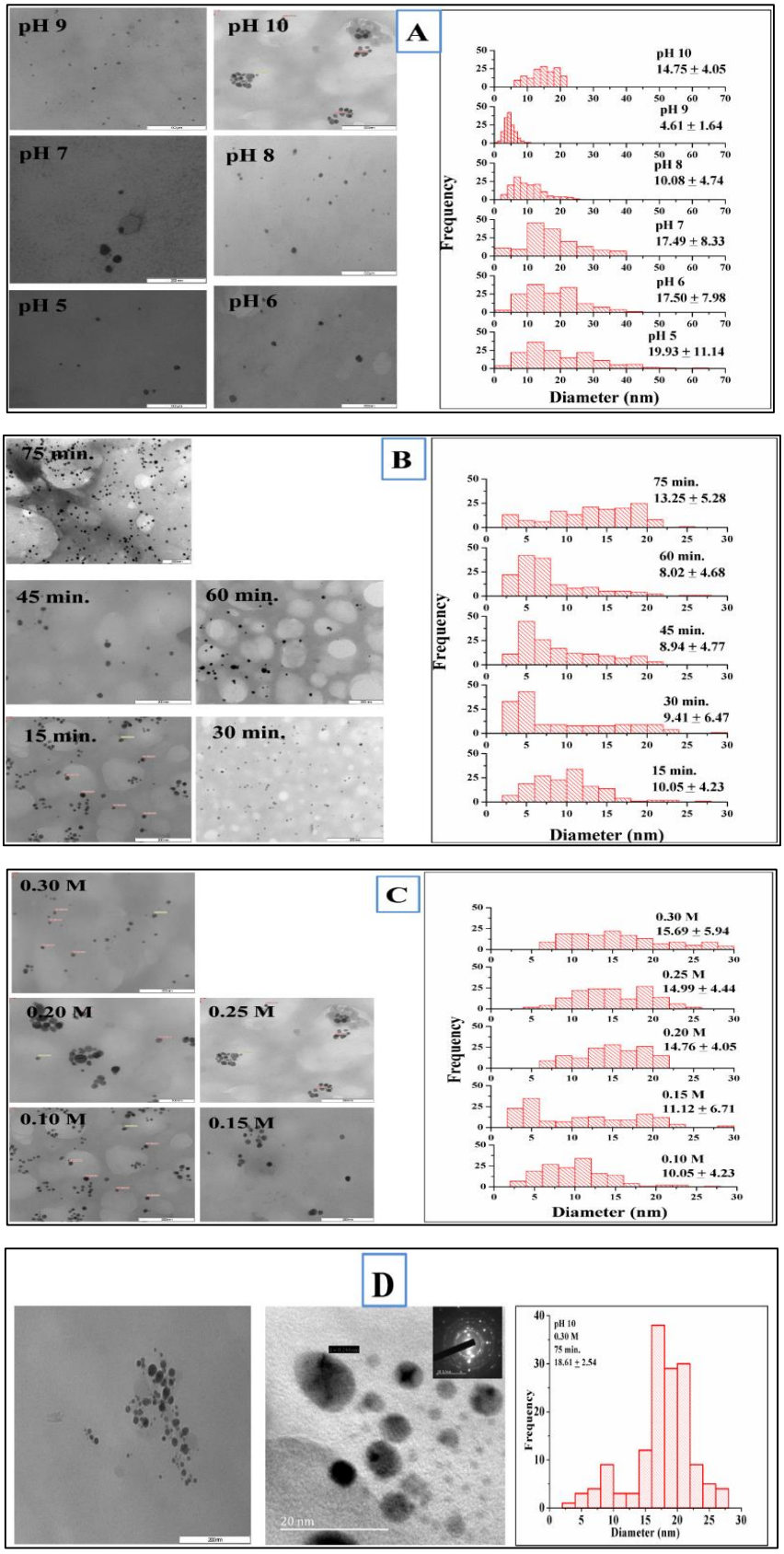


Fig. 4.2: TEM micrographs and Size distributions of synthesized AgNPs for; (A) different pH ($AgNO_3$: 0.20 M, time: 15 min.); (B) time interval ($AgNO_3$: 0.10 M, pH 10); (C) concentration (time: 15 min., pH 10). AgNPs colloid TEM and HRTEM (inset: corresponding SAED) micrographs and Size distributions (D).

5.5.3 FEGSEM and EDX study

The SEM micrograph before calcination (Fig. 4.3(A1)) showed that the synthesized AgNPs remained spherical, as established with TEM (Fig. 4.2), despite the aggregation resulting from drying effect. This demonstrated the significant effect that the NCC has in stabilizing the synthesized AgNPs. However, the SEM micrograph obtained after calcination showed the agglomeration of AgNPs as the NCC was thermally decomposed. This also underscored the significant role of NCC in stabilizing the nanoparticles. The EDX spectra (Fig. 4.3(A2 and B2)) of AgNPs before and after calcination, showed prominent peak for AgNPs with corresponding binding energy of 3 kev.[50] The weight percent of Ag before calcination (81.9 %) increased to 94.17 % after thermal removal of NCC. The presence of carbon, oxygen, sulphur, chlorine and titanium observed in the EDX spectra associated with the NCC except chlorine, which could likely be a trace of chloride in the silver salts. While suphur attributed to surface sulphate after acid hydrolysis, the titanium observed in the EDX spectrum resulted from the residual titania added to aid degradation of cigarette filter on disposal. The EDX mapping of the constituent elements (Fig. S4.3 and S4.4, Appendix B) provided in the supplementary information, showed an even distribution of the elements, which indicated uniform composition of the synthesized AgNPs.

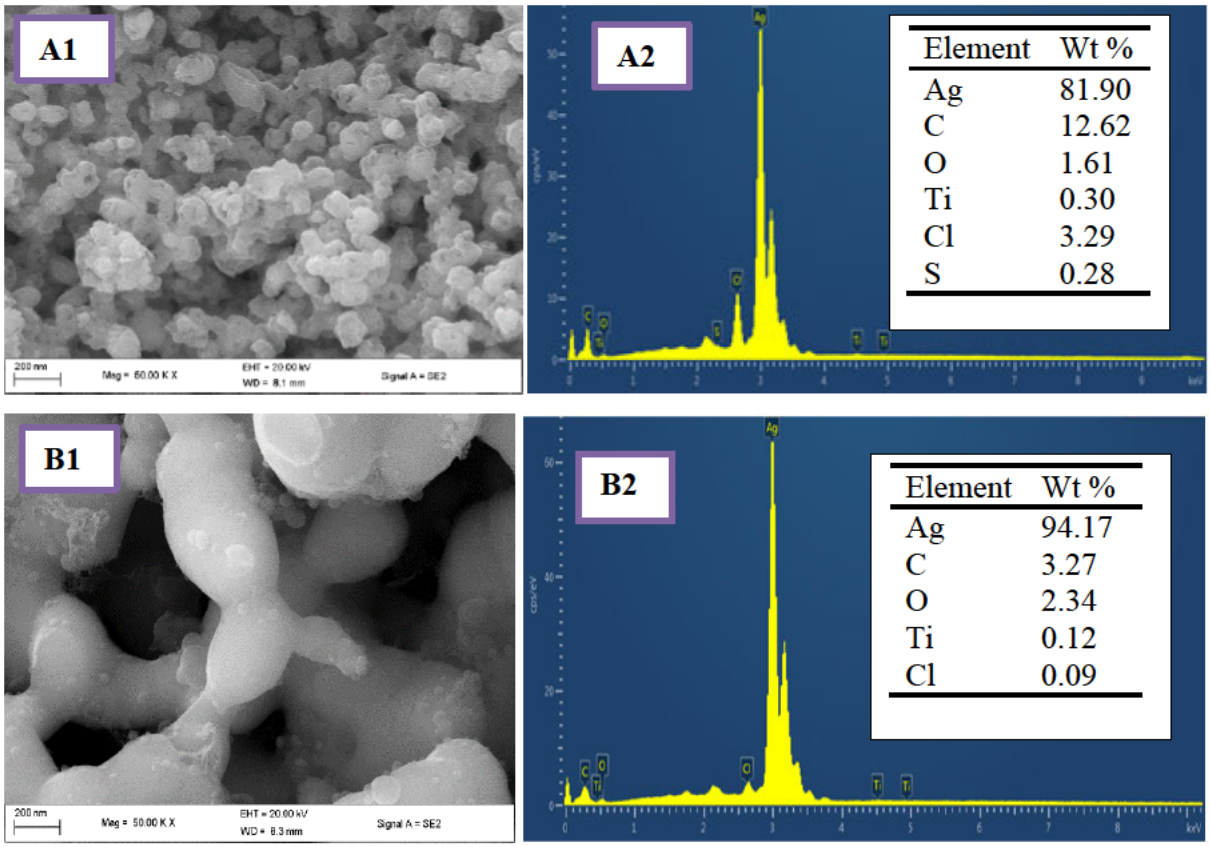


Fig. 4.3: SEM micrographs and EDX spectra of dried AgNPs (A1 and A2) and calcined AgNPs (B1 and B2)

4.5.4 FTIR study

The FTIR spectrum (Fig. 4.4) of dry AgNPs showed absorption peaks characteristics of NCC assigned (υ/cm^{-1}) as: 3320 (O–H), 1646 (H–O–H_{bend}) and 1018 (C–O–C). However, when compared with the FTIR spectrum of the NCC, a weak absorption band at 1740 cm^{-1} assigned to C=O was observed in the spectrum of the AgNPs and slight reduction in intensities of bands at 3320 and 1018 cm^{-1}, which suggested a mild oxidation of the NCC as the silver ions were reduced to AgNPs.[45] This showed the capacity of the NCC as a reducing agent in the synthesis of AgNPs. After calcination, the absorption peaks characteristics of NCC were not observed; an indication that the NCC decomposed during the thermal treatment, which resulted in the agglomeration of AgNPs, as observed in the SEM micrograph of the calcined AgNPs.

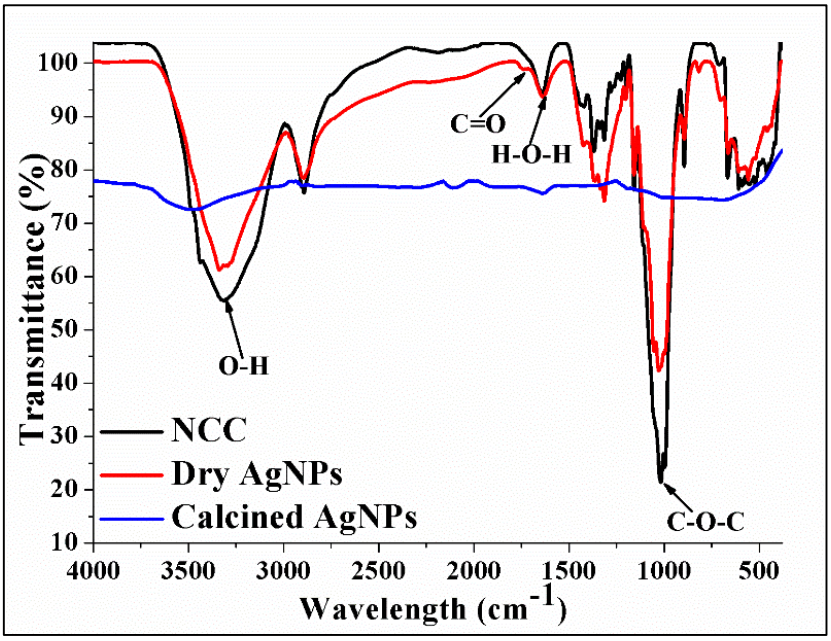


Fig. 4.4: FTIR spectra of NCC, dry and calcined AgNPs.

4.5.5 Powder XRD study

The XRD pattern of the dry AgNPs (Fig. 4.5) showed weak peaks (*) at 2θ = 20º and 22º characteristic of NCC with cellulose II allomorphs, as previously reported.[49] The peaks associated with metallic silver FCC crystal structure were observed at 2θ = 38.1º, 44.3º and 64.5º and are assigned to the diffraction peaks of the (111), (200) and (220) planes of silver crystals.[51] These peaks were observed in the calcined AgNPs with significantly higher intensities and less broadening without the peaks associated with NCC. The increase in intensities indicated the fact that more diffraction from AgNPs after removal of NCC and the less broadening of the peaks, showed an increase in crystallite size with a corresponding decrease in full width at half maximum (FWHM). The calculated crystallite size of the dry AgNPs (11.37 nm), determined by using the (111) crystallographic plane, correlated with the diameter of the AgNPs observed under TEM (Fig. 4.2). However, with the same crystallographic plane (111), the crystallite size was 46.97 nm in the calcined AgNPs, which indicated agglomeration of the nanoparticles after thermal decomposition of the stabilizing NCC. The result of the XRD analysis further established NCC as a suitable stabilizing and reducing agent.

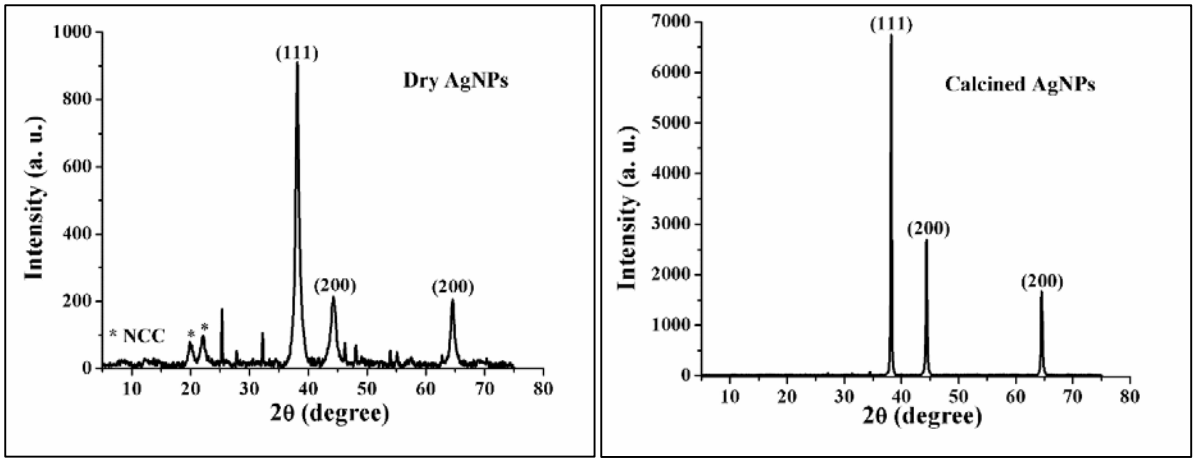


Fig. 4.5: XRD difractogram of the dry and calcined AgNPs.

4.5.6 BET study

The nitrogen adsorption-desorption study of the dry and calcined AgNPs revealed a type II sorption isotherm (IUPAC classification), associated with nonporous or macroporuous materials (Fig. 4.6). The pore size distributions are in the range of between 1.7–300 nm (Fig. 4.6 (inset)) of the dry and calcined AgNPs showed the presence of both meso- (2–50 nm) and macropores (> 50 nm). However, the predominant pore sizes were above 50 nm in diameter, an indication that the AgNPs were largely macroporous.[52] The BET specific surface areas were 4.07 m^2/g (dry AgNPs) and 2.21 m^2/g (calcined AgNPs), while the adsorption cummulative pore volumes were 0.009 cm^3/g (dry AgNPs) and 0.006 cm^3/g (calcined AgNPs). The result of the BET analysis correlated with the observed porous structure of the AgNPs under SEM (Fig. 4.3). As the NCC thermally decomposed, AgNPs coalseaced to large aggregates; resulting in a decrease in the observed BET specific surface area and the adsorption cummulative pore volume of the calcined product. This further showed that the NCC possessed good stabilizing capacity; hence preventing excessive aggregation of the nanoparticles during drying.

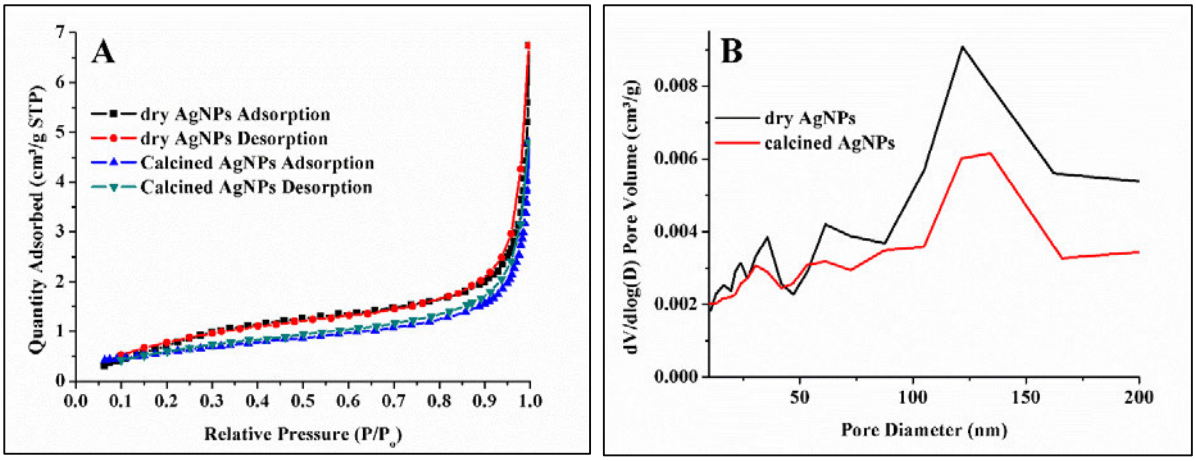


Fig. 4.6: BET isotherms (A) and pore size distributions (B) of dry and calcined AgNPs.

4.5.7 Thermogravimetric and differential thermal analyses (TGA/DTA)

The thermal decomposition profile of the dry AgNPs was studied *via* TGA/DTA with similar conditions employed for calcination in order to provide insight to the formation of the calcined AgNPs. The TGA thermogram (Fig. 4.7A) was comparable to that reported for NCC isolated from DCF[49] but with different rate of thermal degradation. This showed that NCC was the primary component lost during the thermal decomposition, as established with FTIR (Fig. 4.4), FEGSEM (Fig. 4.3) and XRD (Fig. 4.5). Weight loss of 0.5 % at 110ºC showed the low affinity of the dry AgNPs for moisture. The DTA curve (Fig. 4.7B) showed two prominent thermal decomposition stages and a shoulder with peak temperatures at: 145, 225 and 271ºC. The first stage involved the dehydration of the anhydroglucose chain segments, while the second stage involved the chain decomposition and oxidative degradation of the NCC.[49] The observed low decomposition temperatures attributed to the high thermal conductivity of AgNPs, which accelerated the rate of decomposition. The presence of the shoulder, presumably suggested that the crystals of the NCC were not uniformly exposed during the thermal decomposition process. The shoulder ascribed to the late decomposition process of the NCC crystals, sandwiched in between the AgNPs. This is due to the poor heat diffusion, while the main peak suggested the early decomposition of the NCC crystals that are exposed at the surface. The mass residual at 600 ºC was 82.1 %, which correlated with: 82.4 wt% obtained after calcination of dry AgNPs in oven at 600 ºC under nitrogen and 81.9 wt% of Ag obtained from EDX of the dry AgNPs.

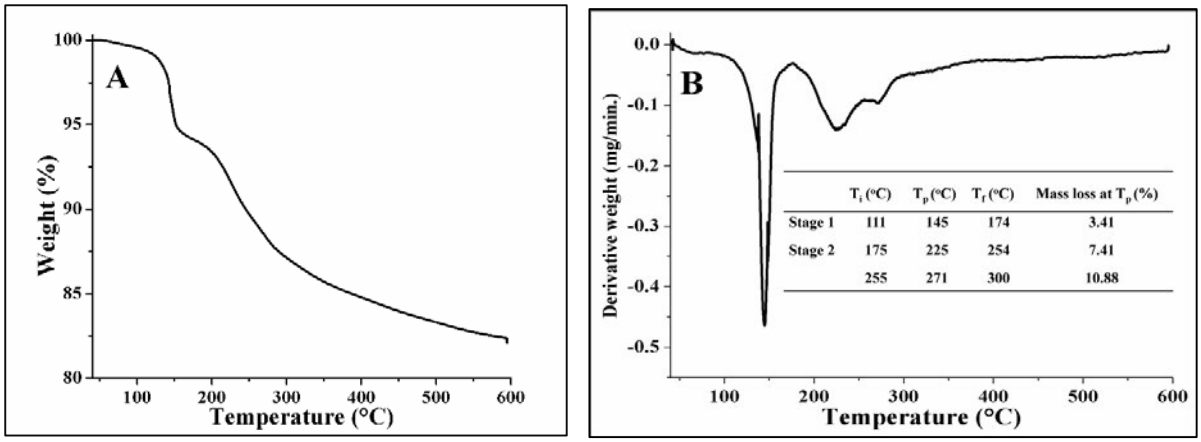


Fig. 4.7: TGA thermogram (A) and DTA curve (B) of dry and Inset: thermal analysis data (Initial temperature (T_i), peak temperature (T_p), final temperature (T_f)).

4.5.8 Detection of riboflavin *via* surface enhanced Raman scattering (SERS)

SERS is one of the preferred analytical concepts in the detection of analytes at micromolar (µM) concentration levels[34-36] and AgNPs have been good substrates especially in the detection of fluorescence analyte molceules with poor Raman signals.[32-33] To this end, a study was carried out in order to determine the suitability of the AgNPs colloid stabilized with NCC isolated from DCF as a substrate in the detection of riboflavin at µmolar concentration range. SERS were acquired by using equal volume of riboflavin solution of appropriate concentration and AgNPs colloid containing 264.94 $\pm$ 15.01 mg/L of Ag, as determined by using ICP OES. The sensitivity of the AgNPs colloid synthesized, as a SERS substrate, was investigated by using riboflavin concentration in the range of between 10–0.00001 µM and the limit of detection, based on the signalto background ratio of 3:1[53], was found to be 0.3 µM. The intensities of SERS signals increased with increase in concentration (Fig. 4.8B). Above 5 µM concentration, the intensities started to decrease. The increase in intensities attributed to an increase in population of the scattering molecules (riboflavin), binding to the AgNPs, through the pyrazine nitrogen and uracil carbonyl oxygen.[54] On saturation, due to the complete surface coverage of the AgNPs, the fluorescence effect from the free riboflavin molecules, interfered with the SERS signal, leading to a reduction in intensity.[54] Prominent peaks in the spectra were (υ/cm^{-1}): 1634 (C–C aromatic stretching), 1527 (C=N stretching), 1410, (C–C + C–N stretching), 1352 (C–N pyrazine ring stretching), 1290 (C=O bending), 1159 (C–N uracil ring stretching), 1087 (C–C uracil ring stretching), 846 (C–H bending), 630 (ring "breathing" of pyrazine and uracil) and 558 (C–C=O bending).[35, 54-56] However, from the plot of intensities of the peaks against concentration (Fig. 4.8C), the most intense peak at all concentrations was at

1352 cm^{-1}. An exponential calibration plot (Fig. 4.8D) of the intensities of this peak (1352 cm^{-1}) against concentration over the range (0.3–5 µM), gave a correlation coefficient, $R^2 = 0.9961$ which showed the capacity of the AgNPs synthesized, as potential SERS substrate in the detection and quantification of florescence analytes at µmolar concentration level. AgNPs absorbed on filter paper showed similar but relatively lower SERS enhanced signals for riboflavin, with a lower detection limit of 0.1 µM (Fig. S4.8B, Appendix B) and a progressive, but non-uniform increase in intensities in the range (0.1–10 µM). The most intense peak was found to be 1352 cm^{-1} and an exponential calibration plot (Fig. S4.8D, Appendix B), gave a lower correlation coefficient, $R^2 = 0.9015$. The non-uniform increase in intensities and the lower correlation coefficient of the paper (solid)-based SERS, compared to that in the liquid state, showed the difference in the characteristics distributions of areas of high SERS enhancement called "hot spots".[57] In the liquid samples, the tendency for the nanoparticles to interact closely within short distances, leading to "hot spot" was higher when compared to solid samples where, the nanoparticles were discretely immobilized. The immobilization of nanoparticles reduces SERS intensities and also the accuracy of detection, especially on the surfaces with non-uniform coating.

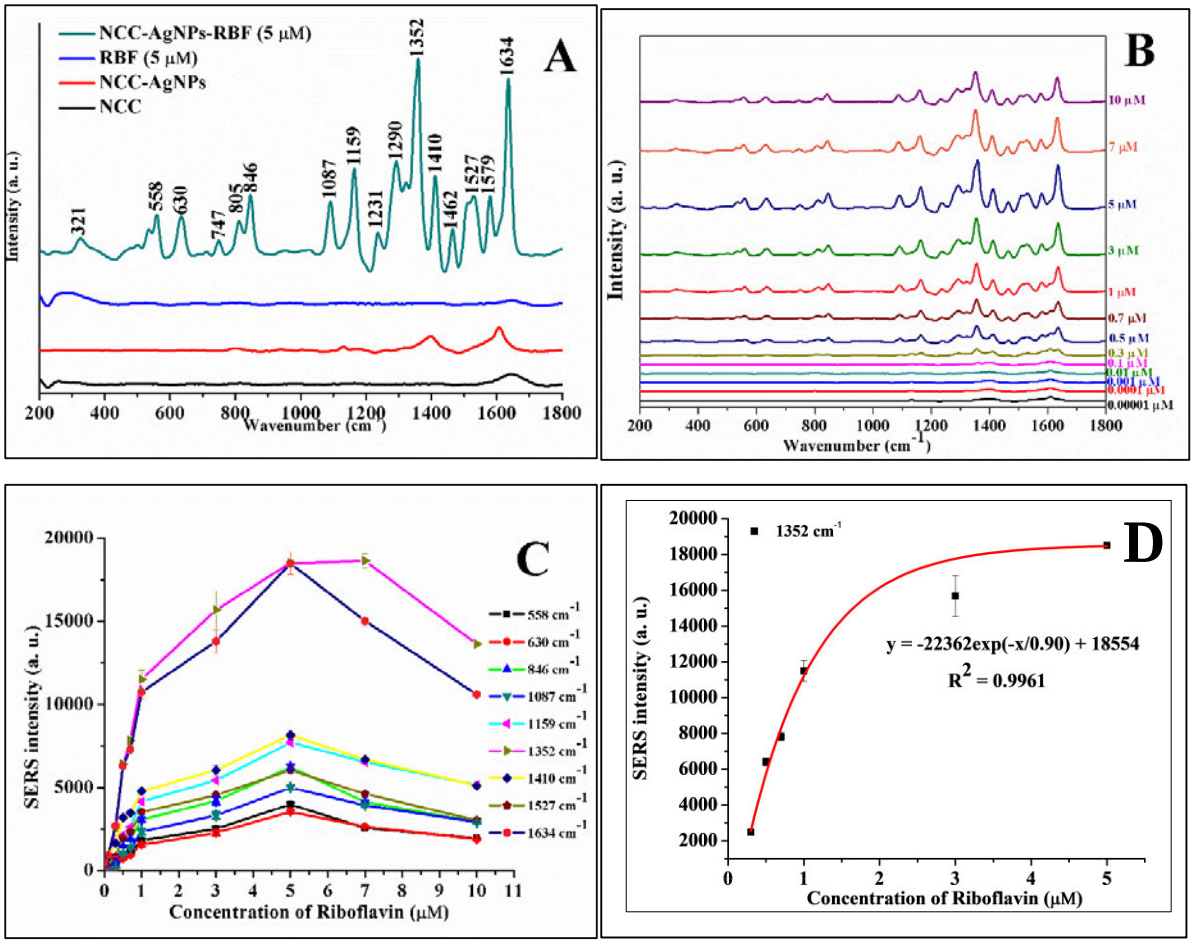


Fig. 4.8: Raman spectra of NCC, NCC-AgNPs, riboflavin (RBF) and SERS spectrum of 5 µM RBF (A), SERS spectra of RBF in concentration range 10–0.00001 µM (B), plots of peaks intensities against concentration (C) and Calibration plot of 1352 cm^{-1}peak intensity against concentration (D).

4.6 Conclusion

The application of NCC isolated from DCF as both reducing and stabilizing agent in the synthesis of AgNPs over a pH range of between 5–10 at 80ºC was successfully demonstrated and the potential of the AgNPs synthesized as SERS substrate, in the detection of riboflavin, was investigated. Variation in yield and size were observed at different pHs, reaction times and concentrations of the Ag precursor. The TEM showed that the AgNPs were spherical in shape and monodispered. Powdered XRD analysis of dry and calcined AgNPs revealed the peaks that are associated with the FCC of Ag on the diffractograms. The removal of the NCC via thermal decomposition resulted in a decrease in BET specific surface area from 4.07 m^2/g (dry AgNPs) to 2.21 m^2/g (calcined AgNPs) and a corresponding increase in the crystallite size from 11.37 nm (dry AgNPs) to 46.97 nm (calcined AgNPs). As a potential substrate, the AgNPs showed excellent SERS in the detection of riboflavin with 0.3 µM limit of detection. The findings of

this study showed the potential in the use of the most littered item (DCF), as a cheap source of NCC, capable of serving as both reducing and stabilizing agent at various pHs, which in turn showed great potential as a SERS substrate in the detection of fluorescence analyte (riboflavin) at μM concentration level.

4.7 References

(1) Shi, Z.; Tang, J.; Chen, L.; Yan, C.; Tanvir, S.; Anderson, W. A.; Berry, R. M.; Tam, K. C. Enhanced Colloidal Stability and Antibacterial Performance of Silver Nanoparticles/Cellulose Nanocrystal Hybrids. *J. Mater. Chem. B* **2015**, *3*, 603–611.

(2) Tulve, N. S.; Stefaniak, A. B.; Vance, M. E.; Rogers, K.; Mwilu, S.; LeBouf, R. F.; Schwegler-Berry, D.; Willis, R.; Thomas, T. A.; Marr, L. C. Characterization of Silver Nanoparticles in Selected Consumer Products and Its Relevance for Predicting Children's Potential Exposures. *Int. J. Hyg. Environ. Health* **2015**, *218*, 345–357.

(3) Formo, E. V.; Potterf, C. B.; Yang, M.; Unocic, R. R.; Leonard, D. N.; Pawel, M. How a Nanostructure's Shape Affects its Lifetime in the Environment: Comparing a Silver Nanocube to a Nanoparticle When Dispersed in Aqueous Media. *Environ. Sci. Technol.* **2016**, *50*, 7082–7089.

(4) Hutter, E.; Fendler, J. H. Exploitation of Localized Surface Plasmon Resonance. *Adv. Mater.* **2004**, *16*, 1685–1706.

(5) Pastoriza-Santos, I.; Liz-Marzán, L. M. Colloidal Silver Nanoplates. State of the Art and Future Challenges. *J. Mater. Chem.* **2008**, *18*, 1724–1737.

(6) Jain, P. K.; Huang, X.; El-Sayed, I. H.; El-Sayed, M. A. Noble Metals on the Nanoscale: Optical and Photothermal Properties and some Applications in Imaging, Sensing, Biology, and Medicine. *Acc. Chem. Res.* **2008**, *41*, 1578–1586.

(7) Millstone, J. E.; Hurst, S. J.; Métraux, G. S.; Cutler, J. I.; Mirkin, C. A. Colloidal Gold and Silver Triangular Nanoprisms. *Small* **2009**, *5*, 646–664.

(8) Xia, Y.; Xiong, Y.; Lim, B.; Skrabalak, S. E. Shape-Controlled Synthesis of Metal Nanocrystals: Simple Chemistry Meets Complex Physics? *Angew. Chem. Int. Ed.* **2009**, *48*, 60–103.

(9) Bastys, V.; Pastoriza-Santos, I.; Rodríguez-González, B.; Vaisnoras, R.; Liz-Marzán, L. M. Formation of Silver Nanoprisms with Surface Plasmons at Communication Wavelengths. *Adv. Funct. Mater.* **2006**, *16*, 766–773.

(10) Kulkarni, A. P.; Noone, K. M.; Munechika, K.; Guyer, S. R.; Ginger, D. S. Plasmon-Enhanced Charge Carrier Generation in Organic Photovoltaic Films using Silver Nanoprisms. *Nano lett.* **2010**, *10*, 1501–1505.

(11) Parfenov, A.; Gryczynski, I.; Malicka, J.; Geddes, C. D.; Lakowicz, J. R. Enhanced Fluorescence from Fluorophores on Fractal Silver Surfaces. *J. Phys. Chem. B* **2003**, *107*, 8829–8833.

(12) Anker, J. N.; Hall, W. P.; Lyandres, O.; Shah, N. C.; Zhao, J.; Van Duyne, R. P. Biosensing with Plasmonic Nanosensors. *Nat. Mater*. **2008,** *7*, 442–453

(13) Willets, K. A.; Van Duyne, R. P. Localized Surface Plasmon Resonance Spectroscopy and Sensing. *Annu. Rev. Phys. Chem.* **2007**, *58*, 267–297.

(14) Laing, S.; Jamieson, L. E.; Faulds, K.; Graham, D. Surface-Enhanced Raman Spectroscopy for in Vivo Biosensing. *Nat. Chem. Rev.* **2017**, *1*, 1–19.

(15) Marks, H.; Schechinger, M.; Garza, J.; Locke, A.; Coté, G. Surface Enhanced Raman Spectroscopy (SERS) for in Vitro Diagnostic Testing at the Point of Care. *Nanophotonics* **2017**, *6* (4), 681–701.

(16) Wei, H.; Abtahi, S. M. H.; Vikesland, P. J. Plasmonic Colorimetric and SERS Sensors for Environmental Analysis. *Environ. Sci.: Nano* **2015**, *2*, 120–135.

(17) Song, W.; Ji, W.; Vantasin, S.; Tanabe, I.; Zhao, B.; Ozaki, Y. Fabrication of a Highly Sensitive Surface-Enhanced Raman Scattering Substrate for Monitoring the Catalytic Degradation of Organic Pollutants. *J. Mater. Chem. A* **2015**, *3*, 13556–13562.

(18) Le Ru, E.; Etchegoin, P. *Principles of Surface-Enhanced Raman Spectroscopy: and Related Plasmonic Effects*, 1st Ed; Elsevier: Amsterdam, 2009.

(19) Kneipp, K.; Moskovits, M.; Kneipp, H. *Surface-Enhanced Raman Scattering-Physics and Applications*. Springer-Berlin, Heidelberg, 2006.

(20) Schatz, G. C.; Valley, N. A. In *Frontiers of Surface-Enhanced Raman Scattering: Single Nanoparticles and Single cells*.Ozaki, Y.; Kneipp, K.; Aroca, R., Eds.; John Wiley & Sons, Inc., 2014, pp 7–14.

(21) Nie, S.; Emory, S. R. Probing Single Molecules and Single Nanoparticles by Surface-Enhanced Raman Scattering. *Science* **1997**, *275*, 1102–1106.

(22) Schlücker, S. Surface-Enhanced Raman Spectroscopy: Concepts and Chemical Applications. *Angew. Chem. Int. Ed.* **2014**, *53*, 4756–4795.

(23) Wu, D.-Y.; Li, J.-F.; Ren, B.; Tian, Z.-Q. Electrochemical Surface-Enhanced Raman Spectroscopy of Nanostructures. *Chem. Soc. Rev.* **2008**, *37*, 1025–1041.

(24) Bell, S. E.; Sirimuthu, N. M. Quantitative Surface-Enhanced Raman Spectroscopy. *Chem. Soc. Rev.* **2008**, *37*, 1012–1024.

(25) Habibi, Y.; Lucia, L. A.; Rojas, O. J. Cellulose Nanocrystals: Chemistry, Self-Assembly, and Applications. *Chem. Rev.* **2010**, *110*, 3479–3500.

(26) Klemm, D.; Kramer, F.; Moritz, S.; Lindström, T.; Ankerfors, M.; Gray, D.; Dorris, A. Nanocelluloses: A New Family of Nature-Based Materials. *Angew. Chem. Int. Ed.* **2011**, *50*, 5438–5466.

(27) De France, K. J.; Hoare, T.; Cranston, E. D. Review of Hydrogels and Aerogels Containing Nanocellulose. *Chem. Mater.* **2017**, *29*, 4609–4631.

(28) Hu, L.; Zheng, G.; Yao, J.; Liu, N.; Weil, B.; Eskilsson, M.; Karabulut, E.; Ruan, Z.; Fan, S.; Bloking, J. T. Transparent and Conductive Paper from Nanocellulose Fibres. *Energy Environ. Sci.* **2013**, *6*, 513–518.

(29) Siqueira, G.; Bras, J.; Dufresne, A. Cellulose Whiskers Versus Microfibrils: Influence of the Nature of the Nanoparticle and its Surface Functionalization on the Thermal and Mechanical Properties of Nanocomposites. *Biomacromolecules* **2008**, *10*, 425–432.

(30) Kelly, J. A.; Giese, M.; Shopsowitz, K. E.; Hamad, W. Y.; MacLachlan, M. J. The Development of Chiral Nematic Mesoporous Materials. *Acc. Chem. Res.* **2014**, *47*, 1088–1096.

(31) Wei, H.; Rodriguez, K.; Renneckar, S.; Leng, W.; Vikesland, P. J. Preparation and Evaluation of Nanocellulose–Gold Nanoparticle Nanocomposites for SERS Applications. *Analyst* **2015**, *140*, 5640–5649.

(32) Jiang, F.; Hsieh, Y.-L. Synthesis of Cellulose Nanofibril Bound Silver Nanoprism for Surface Enhanced Raman Scattering. *Biomacromolecules* **2014**, *15*, 3608–3616.

(33) Soliveri, G.; Ardizzone, S.; Yüksel, S.; Cialla-May, D.; Popp, J.; Schubert, U. S.; Hoeppener, S. Microwave-Assisted Silver Nanoparticle Film Formation for SERS Applications. *J. Phys. Chem. C* **2016**, *120*, 1237–1244.

(34) Guo, H.; Zhang, Z.; Xing, B.; Mukherjee, A.; Musante, C.; White, J. C.; He, L. Analysis of Silver Nanoparticles in Antimicrobial Products Using Surface-Enhanced Raman Spectroscopy (SERS). *Environ. Sci. Technol.* **2015**, *49*, 4317–4324.

(35) Nguyen, A.; Schultz, Z. D. Quantitative Online Sheath-Flow Surface Enhanced Raman Spectroscopy Detection for Liquid Chromatography. *Analyst* **2016**, *141*, 3630–3635.

(36) Saleh, T. A.; Al-Shalalfeh, M. M.; Al-Saadi, A. A. Graphene Dendrimer-Stabilized Silver Nanoparticles for Detection of Methimazole Using Surface-Enhanced Raman Scattering with Computational Assignment. *Sci. Rep.* **2016**, *6*, 32185.

(37) Kaushik, M.; Moores, A. Review: Nanocelluloses as Versatile Supports for Metal Nanoparticles and Their Applications in Catalysis. *Green Chem.* **2016**, *18*, 622–637.

(38) Shervani, Z.; Ikushima, Y.; Sato, M.; Kawanami, H.; Hakuta, Y.; Yokoyama, T.; Nagase, T.; Kuneida, H.; Aramaki, K. Morphology and Size-Controlled Synthesis of Silver Nanoparticles in Aqueous Surfactant Polymer Solutions. *Colloid Polym. Sci.* **2008**, *286*, 403–410.

(39) Dare, E. O.; Oseghale, C. O.; Labulo, A. H.; Adesuji, E. T.; Elemike, E. E.; Onwuka, J. C.; Bamgbose, J. T. Green Synthesis and Growth Kinetics of Nanosilver under Bio-Diversified Plant Extracts Influence. *J. Nanostruct. Chem.* **2015**, *5*, 85–94.

(40) Mochochoko, T.; Oluwafemi, O. S.; Jumbam, D. N.; Songca, S. P. Green Synthesis of Silver Nanoparticles Using Cellulose Extracted from an Aquatic Weed; Water Hyacinth. *Carbohydr. Polym.* **2013**, *98*, 290–294.

(41) Lokanathan, A. R.; Uddin, K. M. A.; Rojas, O. J.; Laine, J. Cellulose Nanocrystal-Mediated Synthesis of Silver Nanoparticles: Role of Sulphate Groups in Nucleation Phenomena. *Biomacromolecules* **2013**, *15*, 373–379.

(42) Wei, H.; Rodriguez, K.; Renneckar, S.; Vikesland, P. J. Environmental Science and Engineering Applications of Nanocellulose-Based Nanocomposites. *Environ. Sci.: Nano* **2014**, *1*, 302–316.

(43) George, J.; Sajeevkumar, V. A.; Ramana, K. V.; Sabapathy, S. N. Augmented Properties of PVA Hybrid Nanocomposites Containing Cellulose Nanocrystals and Silver Nanoparticles. *J. Mater. Chem.* **2012**, *22*, 22433–22439.

(44) Xiong, R.; Lu, C.; Zhang, W.; Zhou, Z.; Zhang, X. Facile Synthesis of Tunable Silver Nanostructures for Antibacterial Application Using Cellulose Nanocrystals. *Carbohydr. Polym.* **2013**, *95* (1), 214–219.

(45) Wu, X.; Lu, C.; Zhang, W.; Yuan, G.; Xiong, R.; Zhang, X. A Novel Reagentless Approach for Synthesizing Cellulose Nanocrystal-Supported Palladium Nanoparticles with Enhanced Catalytic Performance. *J. Mater. Chem. A* **2013**, *1*, 8645–8652.

(46) Wu, X.; Lu, C.; Zhou, Z.; Yuan, G.; Xiong, R.; Zhang, X. Green Synthesis and Formation Mechanism of Cellulose Nanocrystal-Supported Gold Nanoparticles with Enhanced Catalytic Performance. *Environ. Sci.: Nano* **2014**, *1*, 71–79.

(47) Cui, H.; Hwang, H.-M.; Zeng, K.; Glover, H.; Yu, H.; Liu, Y. Riboflavin-Photosensitized Degradation of Atrazine in a Freshwater Environment. *Chemosphere* **2002**, *47*, 991–999.

(48) Larson, R. A.; Stackhouse, P. L.; Crowley, T. O. Riboflavin Tetraacetate: A Potentially Useful Photosensitizing Agent for the Treatment of Contaminated Waters. *Environ. Sci. Technol.* **1992**, *26*, 1792–1798.

(49) Ogundare, S. A.; Moodley, V.; van Zyl, W. E. Nanocrystalline cellulose Isolated from Discarded Cigarette Filters. *Carbohydr. Polym.* **2017**, *175*, 273–281.

(50) Pattanayak, S.; Mollick, M. M. R.; Maity, D.; Chakraborty, S.; Dash, S. K.; Chattopadhyay, S.; Roy, S.; Chattopadhyay, D.; Chakraborty, M. Butea Monosperma

Bark Extract Mediated Green Synthesis of Silver Nanoparticles: Characterization and Biomedical Applications. *J. Saudi Chem. Soc.* **2017**, *21*, 673–684

(51) Goudarzi, M.; Mir, N.; Mousavi-Kamazani, M.; Bagheri, S.; Salavati-Niasari, M. Biosynthesis and Characterization of Silver Nanoparticles Prepared from Two Novel Natural Precursors by Facile Thermal Decomposition Methods. *Sci. Rep.* **2016**, *6*, 32539.

(52) Kruk, M.; Jaroniec, M. Gas Adsorption Characterization of Ordered Organic-Inorganic Nanocomposite Materials. *Chem. Mater.* **2001**, *13*, 3169–3183.

(53) Guideline, I. H. T., Validation of analytical procedures: text and methodology. *Q2 (R1)* **2005**, *1*.

(54) Liang, E.; Göttges, D.; Kiefer, W. Surface-Enhanced Resonance Raman Spectroscopy of Flavins on Silver Nitrate-Modified Cu and Fe as well as Cu-Zn-Pb and Fe-C-Cr-Ni Surfaces. *Appl. Spectrosc.* **1994**, *48*, 1088–1094.

(55) Liu, F.; Gu, H.; Lin, Y.; Qi, Y.; Dong, X.; Gao, J.; Cai, T. Surface-Enhanced Raman Scattering Study of Riboflavin on Borohydride-Reduced Silver Colloids: Dependence of Concentration, Halide Anions and pH Values. *Spectrochim. Acta Part A* **2012**, *85*, 111–119.

(56) Combs, Z. A.; Malak, S. T.; König, T.; Mahmoud, M. A.; Chávez, J. L.; El-Sayed, M. A.; Kelley-Loughnane, N.; Tsukruk, V. V. Aptamer-Assisted Assembly of Gold Nanoframe Dimers. *Part. Part. Syst. Char.* **2013**, *30*, 1071–1078.

(57) Guo, H.; He, L.; Xing, B., Applications of Surface-Enhanced Raman Spectroscopy in the Analysis of Nanoparticles in the Environment. *Environ. Sci.: Nano* **2017**, *4*, 2093–2107

Chapter 5

Silver nanoparticles produced from NCC on SiO_2-supports and their application in malachite green detection by SERS

5.1 Introduction

Surface-enhanced Raman scattering (SERS) was introduced as a concept in 1977 in order to enhance the weak signals associated with Raman scattering of molecules,[1-2] and it has since been developed as an excellent analytical technique, especially for the detection and quantification of molecules at very low concentrations.[3-4] As such, the SERS technique has become a prodigious research focus due to its high sensitivity and promising potential of detecting a single molecule, which has been demonstrated by using plasmonic nanoparticles substrates with "hot spot" (a spatial region of maximum induced electromagnetic field between two or more nanoparticles in close proximity).[5-8] Substrates with nanoarrays of particles in close proximity are synonymous with "hot spots" and they are required for highly sensitive and reproducible SERS of analytes at low concentrations.[9] Plasmonic nanoparticles (typically Ag, Au and Cu) that are capable of generating large localized surface plasmon resonance (LSPR), are considered the quintessential signal enhancers in SERS, but their capacity in this regard is limited when they are monodispersed since isolated nanoparticles provide less induced local magnetic field. This has been established by using computer simulations and also with a negative experimental study by using Ag and Au nanoparticles that were monodispersed and/or encapsulated within silica in order to prevent aggregation.[10]

The need to improve SERS sensitivity and reproducibility requires activation of plasmonic nanoparticle substrates by using aggregating agents, which most often, results in the introduction of interference signals and poor reproducibility due to a decrease in the stability of the substrates.[11] Similarly, anisotropic plasmonic nanoparticles with shapes, such as: cubes, wires, flowers, triangles, rods and plates, have been explored as SERS substrates due to their associated wider range of LSPR which can be tuned to the near infrared region by varying their dimensions.[12-13] This makes them suitable as SERS substrates in biological applications. The well-established methods of synthesizing this class of nanoparticles require the use of different surfactants, reducing- and directing agents, which are often strongly adsorbed to the plasmonic surfaces, thereby limiting the number of available sites for analyte interaction.[13-14] Since SERS

is a surface phenomenon, the passivation of the surfaces limits the optimum performance of these substrates and consequently, makes them less attractive for general use in SERS studies. Generally, the passivation of SERS substrate surfaces is not unique to anisotropic plasmonic nanoparticles, but a common challenge with the use of strong adsorbing surfactant, reducing and directing agents in the synthesis of plasmonic nanoparticles.[15] Therefore, optimum SERS performance of such plasmonic nanoparticles, requires thorough surface cleaning in advance of SERS analysis.[10, 16] This is a necessary step, often carried out by multiple washings *via* centrifugation, which may lead to instability of the resulting colloids. A viable alternative to circumvent this challenge is to avoid the use of a strong absorbing agent in the preparatory steps by adopting a green template[17-18] with extremely low SERS signal interference and also to immobilize the nanoparticles prepared on a support material in order to provide, in high concentration, the much required "hots pots" the without loss of colloidal stability during centrifugation.[19-20]

Nanocrystalline cellulose (NCC) is a biopolymer isolated from plant,[21-22] bacteria[23-24] and tunicate[25-26] cellulose, and in recent times, also from cellulosic waste[27-29] through sulphuric acid hydrolysis.[30-31] NCC has attracted significant research attention[32-34] due to its remarkable mechanical, thermal and optical properties as well as its rich natural surface that is composed of hydroxyl and residual sulphate ester groups, thereby, making it a suitable green template in the synthesis of plasmonic nanoparticles.[35-36] NCC was used as reducing- and stabilizing agent in the synthesis of AuNPs under hydrothermal conditions[18] and chemically modified NCC was also reported to have been used in the synthesis of AgNPs as reducing- and stabilizing agent.[37-38] Previous study showed that nanocomposite of NCC/AgNPs as SERS substrate showed no signal interference, a feature not common to most templates.[39] However, when NCC is used as reducing- and stabilizing agent, it provides a strong stabilizing effect for plasmonic nanoparticles, hence, making them monodispersed in solution and preventing aggregation, even on drying and thus, reducing the number of available "hot spots" for SERS studies.[39] In order to improve the efficiency of AgNPs stabilized with NCC in SERS, the immobilization of the AgNPs on an inert support *via* the *in-situ* synthesis of AgNPs by using NCC as reducing- and stabilizing agent in the presence of Stöber silica was conceptualized. Stöber silica provides a suitable surface area to anchor AgNPs in close proximity in order to generate a "hot spot" without any significant loss of colloidal stability.[40-41] The nanocomposite is applied as an ideal SERS substrate in the detection of malachite green.

Malachite green (MG) is a synthetic dye with extensive applications in the textile, paper and aquaculture industries, where it is used as dye and fungicide.[42] However, it has been reported

that MG has carcinogenic and mutagenesis biases, hence, leading to a ban imposed on its use in China and the USA, while a limit of 2µg/kg was set by European Union in 2004.[43] Due to its illicit use, it is not uncommon to find MG in sea foods and water bodies.[44] As a result, various techniques have been explored for the detection of MG in water; these include a combination of chromatographic and spectroscopic analytical methods.[45] However, these methods are associated with a number of constraints by which include high cost, poor detection limit and a longer duration of analysis, hence, making them unsuitable for real time analysis.[46] More recently, SERS has been employed as an analytical tool in the detection of MG in water and seafood with different substrates, based on Ag and Au nanoparticles.[47-49] However, there is no report on the use of a AgNPs/SiO_2/NCC nanocomposite. Here, the use of NCC as a reducing- and stabilizing agent in the formation of AgNPs clusters, immobilized on SiO_2 is reported. The SERS performance of the composite as a substrate was investigated, and compared with the substrate-free AgNPs/NCC, for the detection of malachite green in water.

5.2 EXPERIMENTAL

5.2.1 Materials

Whatman cellulose filter paper (grade 1) was purchased from GE Healthcare, United Kingdom. Ethanol, sodium hydroxide pellets (NaOH), sulphuric acid (H_2SO_4, 98% w/w), silver nitrate ($AgNO_3$), hydrochloric acid (HCl, 32% w/w), nitric acid (HNO_3, 69% w/w), tetraethyl orthosilicate ((TEOS, 98% w/w), ammonia solution (25% w/w), and malachite green oxalate salt (MG, 95% w/w) were purchased from Sigma-Aldrich. All chemicals were used as received. Double distilled water was used for the reactions and dialysis.

5.2.2 Isolation of NCC

NCC was isolated from Whatman cellulose filter paper by using 20 mL/g (volume acid per mass of cellulose) of 64 wt% sulphuric acid at 45°C in an oil bath for 45 min in order to remove the amorphous regions in cellulose. After 45 min, the suspension was diluted (dilution factor: 20) with double distilled water at room temperature and centrifuged by using an OHAUS Frontier 5706 instrument at 6000 rpm with a relative centrifugal force 4427 x g for 10 min. This procedure was repeated 5 times in order to reduce the sulphuric acid concentration. Aggregation of nanocrystals was avoided by sonicating the suspension by using an ultrasonicator (UP400S, Hielscher, Germany) at a 50% amplitude and a 0.5 cycle for 15 min in order to ensure thorough dispersion of NCC, before dialyzing to neutral pH.

5.2.3 Synthesis of silica (SiO_2)

Silica (SiO_2) nanoparticles were synthesized by using the modified Stöber method.[50] Briefly, a mixture of 10 mL TEOS in 15 mL of ethanol was added to a stirring mixture of water (6 mL), ethanol (15 mL) and ammonia solution (0.5 mL) at 25°C. The stirring continued for 24 hours in order to ensure a complete hydrolysis and condensation. After 24 hours, the colloid was centrifuged by using OHAUS Frontier 5706 at 6000 rpm with relative centrifugal force 4427 x g for 30 min and subsequently washed with water in order to remove the unreacted TEOS. The washing was repeated 5 times and finally, the SiO_2 particles suspension was sonicated by using an ultrasonicator (UP400S, Hielscher, Germany) at a 50% amplitude and a 0.5 cycle for 15 min.

5.2.4 Synthesis of AgNPs/SiO_2/NCC composite

The synthesis of AgNPs/SiO_2/NCC composite was conducted at 80°C by using 10 mL of 0.1 wt% NCC containing 5 mg SiO_2 sonicated for 15 min and adjusted to pH 10 with 0.1 M NaOH. Freshly prepared 0.3 M $AgNO_3$ solution (1 mL) was added to the stirring mixture of NCC and SiO_2. The temperature was maintained at 80°C for 75 min. The composite obtained was washed with double distilled water and centrifuged at 6000 rpm with relative centrifugal force 4427 x g for 30 min in order to remove unreacted $AgNO_3$. This process was repeated 5 times to ensure complete removal of unreacted the $AgNO_3$. The concentration of AgNPs in the colloid was determined *via* inductive coupled plasma optical emission spectroscopy (ICP-OES) after microwave digestion. A dry composite was obtained by drying the colloid at 50°C for 24 hours in an oven. Similarly, AgNPs/NCC was synthesized without SiO_2 by using the same procedure.

5.3 Characterization of the synthesized nanomposites

5.3.1 UV-vis spectroscopy

Absorption spectra were obtained in the wavelength range of between 300–800 nm by using a UV-3600 Plus UV-VIS-NIR spectrophotometer, Shimadzu, Japan.

5.3.2 Zeta potential measurements

The colloidal stability of: NCC, SiO_2, AgNPs/NCC and AgNPs/SiO_2/NCC was determined *via* the measurement of their zeta potentials at 25°C by Smoluchowski modelled Doppler anemometry by using a nanoparticle tracking analyser (NTA) NANOSIGHT (NS500, Malvern

Instruments, Worcestershire, UK). The mean zeta potential was calculated by using the data obtained from five different measurements in each sample.

5.3.3 Microwave digestion and ICP-OES analysis

A triplicate analysis was simultaneously performed in order to determine the concentration of AgNPs in the composites by digesting three separate samples of each nanocomposite, containing sample colloid and HNO_3 (69 % w/w) in a volume ratio 1:10 (colloid/nitric acid) by using MARS 6 Microwave Reaction System (CEM, USA) at 200°C for 20 min. From a 100 ppm stock solution of Ag^+ ions prepared by using $AgNO_3$, a series of standard solutions (1.0–0.05 ppm) were prepared by serial dilution and used for calibration on an Optima 5300 DV ICP-OES Inductive Coupled Plasma spectrometer (Perkin Elmer, USA) before the determination of Ag^+ ions in the digested AgNPs colloids samples.

5.3.4 Morphological studies

The size, shape and dispersion of the NCC, SiO_2 and nanocomposites were investigated with the aid of electron microscopes. For the TEM and HRTEM studies, a JEOL 1010 (Japan) transmission electron microscope (TEM) and a JEOL 2100 (Japan) high resolution transmission electron microscope (HRTEM) were used. For the SEM study, a Zeiss Ultra Plus field emission gun scanning electron microscope (FEG SEM), equipped with energy dispersive X-ray (EDX) detector (Germany), was used. TEM and HRTEM images of the composites were acquired by using 5µL of each sample deposited on a copper TEM-grid. Images of stained samples were obtained after negatively staining the samples on TEM-grid with 2 wt% uranyl acetate for 5 min in the dark. The excess uranyl acetate solution was wicked-off with the tip of filter paper and the stained samples on the grid were allowed to dry. Dimensions of nanoparticles were measured from the TEM micrographs by using the ImageJ 1.42 software and the data obtained were processed on OriginPro 8 software. Similarly, dried samples for SEM images were deposited on conductive carbon tapes and stuck to aluminium stubs, while diluted solutions of (NCC and AgNPs/SiO_2/NCC) samples were also carefully dried on glass, which was stuck to the aluminium stub *via* carbon tape. All samples were coated with gold with the aid of sputter coater, to minimize charging and improve conductivity. EDX spectra were only obtained from dried samples on conductive carbon tape.

5.3.5 Fourier transform infrared spectroscopy (FTIR)

FTIR spectra of samples were obtained in the range of between 380–4000 cm^{-1} at a resolution of 4 cm^{-1} by using Spectrum 100 infrared spectrometer equipped with universal diamond crystal attenuated total reflection (ATR) accessory (Perkin Elmer, USA).

5.3.6 Powder X-ray diffraction analysis

XRD analysis of the NCC, SiO_2 and nanocomposites were performed by using an X-ray diffractometer (Bruker AXS D8 Advance, Germany), equipped with a Cu-Kα radiation source (wavelength = 0.154 nm) operating at 40 kV and 40 mA. The XRD pattern was recorded over the angular range of 2θ = 10–90° at room temperature. The crystallite diameter (D_{hkl}) was calculated by using Scherrer's formula[51], as shown in Eq. (5.1), where λ is the X-ray wavelength (0.154 nm), β is the angular full width at half maximum (FWHM) intensity, determined with the aid of a Gaussian fit of the peaks on the diffractogram (Fig. S5.6, Appendix C) of each sample and θ is the Bragg angle. The crystallographic plane adopted for the calculation was (111). The crystallinity index (*CI*) for the isolated NCC was calculated by using the Segal's method[52-53], as shown in Eq. 5.2, where I_{002} is the 2θ = 23.1° peak associated with the maximum intensity of both amorphous and crystalline region, and I_{am} is 2θ = 18.0° the peak associated with the intensity of the amorphous regions of the sample.

$$D_{hkl}\ (\text{nm}) = \frac{0.89\,\lambda}{\beta \cos\theta} \qquad (5.1)$$

$$CI\ (\%) = \frac{I_{002} - I_{am}}{I_{002}} \times 100\% \qquad (5.2)$$

5.3.7 Thermogravimetric and differential thermal analyses (TGA/DTA)

TGA of the samples were performed by using a Simultaneous Thermal Analyzer STA 6000 (Perkin-Elmer, USA). The thermal analysis was conducted in a nitrogen atmosphere (flow rate of 20 mL/min) with a constant heating rate of 10°C/min and at a temperature of between 25–700°C, while the samples were held at 700°C for 10 min. The weight loss (%) at the decomposition temperature and the residual product (%) at 600°C were determined from the thermograms and the differential thermal analysis (DTA) curves.

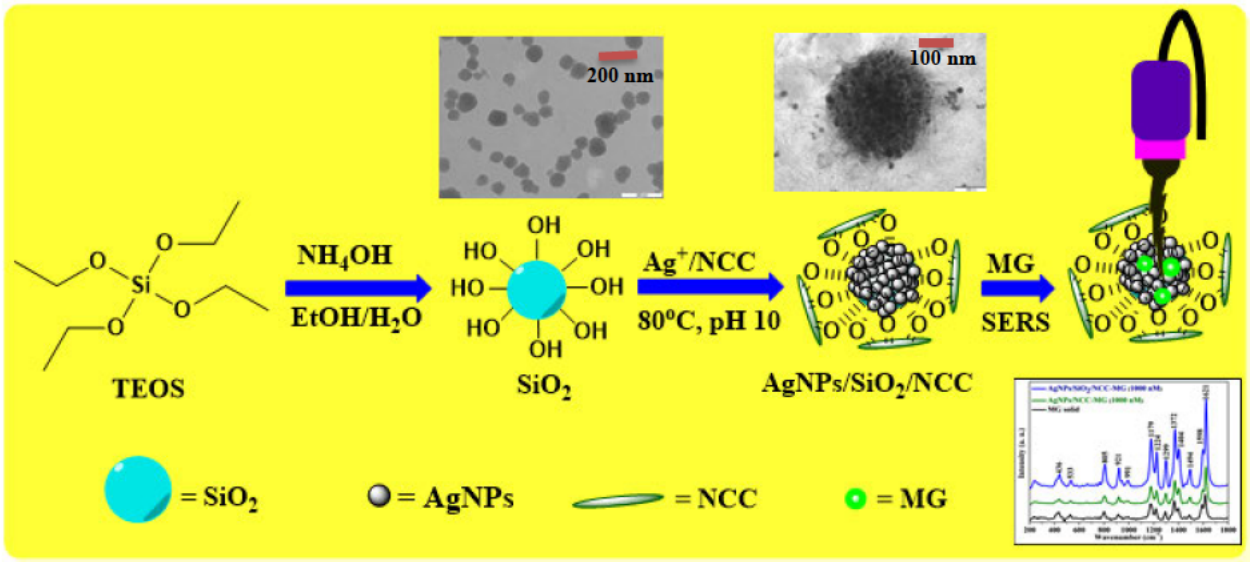
5.4 SERS spectroscopic study

The colloids of the AgNPs/NCC and AgNPs/SiO_2/NCC synthesized were used as substrates in the detection of malachite green (MG). From a 100 µM prepared stock solution of MG, a series of standard solutions (10^4–10^{-3} nM) were prepared by serial dilution. The SERS spectroscopic study was carried out by using 1 mL of sample solution containing a 1:1 volume ratio of colloid and MG solution of the desired concentration after incubation period of 30 min at 25°C. A sample cell (8 mm vial) provided for a liquid sample with dimension 8 mm diameter and 40 mm height was used and SERS spectra were acquired in the wavelength range of between 200–1800 cm^{-1} from an Advantage a 532^{TM} Raman spectrometer equipped with charge coupled device (CCD) detector and NuSpec software (DeltaNu, USA). The laser power was 100 mW at 532 nm excitation wavelength and an integration time of 10 seconds was used for each acquired spectrum. A triplicate measurement was carried out on each sample and each measurement was obtained from an average of 10 spectra in order to ensure good precision.

5.5 Results and Discussion

5.5.1 Synthesis of nanocomposites

The hydrolysis and condensation of TEOS resulted in the formation of quasi-spherical silica nanoparticles with a surface rich in silanol (Si–OH) groups that are capable of absorbing Ag^+ ions in alkaline medium. The addition of $AgNO_3$ solution into a stirring mixture of SiO_2 and NCC at pH 10, led to the adsorption of Ag^+ ions on SiO_2 and NCC surfaces. However, a stronger affinity of silanol ensured a higher density of Ag^+ ions on the SiO_2 surface when compared to NCC with surface hydroxyl groups (C–OH).[54] Moreover, the mean zeta potential of SiO_2 (-40.3 ± 0.3 mV) was lower than -31.7 ± 0.5 mV observed in NCC. This suggests that the surface of SiO_2 possesses stronger electrostatic attraction for the positively charged Ag^+ ions in contrast to NCC.[55-57] Nevertheless, the hydroxyl groups reduced the adsorbed Ag^+ ions on the silica, leading to the formation of dense clusters of AgNPs on the SiO_2 surface, when compared to the monodispersed AgNPs on the NCC surface, as revealed by microscopic studies. The capacity of NCC to reduce the Ag^+ ions on the surface of SiO_2 showed the synergic interaction between them, as illustrated in Scheme 5.1. The clustering of AgNPs on SiO_2 surface assures a greater SERS enhancement since the number of "hot spots" increases.



Scheme 5.1. Graphical illustration of the preparation and application of AgNPs/SiO_2/NCC.

5.5.2 FTIR study

The FTIR spectra of: NCC, SiO_2, AgNPs/NCC and AgNPs/SiO_2/NCC nanocomposites in Fig. 5.1 show the chemical modification resulting from the interaction between the individual constituents in the nanocomposites. The characteristic FTIR absorption bands of NCC were found in the isolated NCC from filter paper and assigned (υ/cm^{-1}) as: 3329 (O–H), 2907 (C–H_{asym}), 1637 (H–O–H_{bend}), 1028 (C–O–C).[28, 58-59] Similarly, these bands were found in the FTIR spectrum of the AgNPs/NCC composite, however, with reduced intensity, as observed in the band associated with O–H and C–O–C vibration modes. The result suggests mild oxidation of the NCC since Ag^+ ions were reduced and coalesced to the AgNPs.[39] The spectrum of AgNPs/SiO_2/NCC showed a similar trend in loss of intensity in the band associated with O–H groups of the NCC. However, the band associated with the vibration of the C–O–C group was overshadowed by a more intense band associated with Si–O–Si bond of the silica. A concomitantly very weak broad band (Fig. 5.1 (inset)) was also observed around 1754 cm^{-1} and was assigned as a carbonyl (C=O) band, which indicated a partial oxidation of the NCC surface hydroxyl groups in the AgNPs/NCC.[18, 60] Similarly, in relation to the C=O vibration, two weak bands were observed at 1754 and 1773 cm^{-1} in the AgNPs/SiO_2/NCC nanocomposite. This presumably, relates to a difference in the degree of interaction of the C=O moiety and by monodispersed AgNPs on NCC and clusters of AgNPs on SiO_2. The FTIR spectrum of the synthesized silica showed characteristic bands assigned (υ/cm^{-1}) as: 1055 (Si–O–Si_{asym}), 798 (Si–O–Si_{symm}) and 442 (Si–O^-_{bend}).[61-63] These bands were observed in the spectrum of

AgNPs/SiO_2/NCC with a narrow shift (~ 5cm^{-1}) to a lower wavenumber and stronger intensities, which suggested the clustering of the AgNPs on the SiO_2 surface.

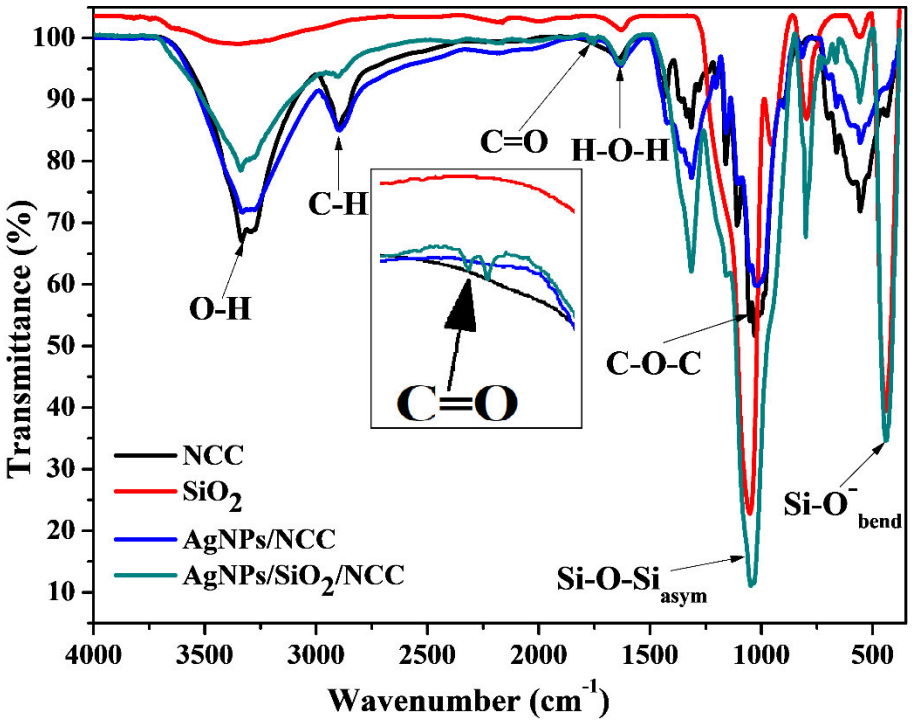


Fig. 5.1: FTIR spectra of NCC, SiO_2, AgNPs/NCC and AgNPs/SiO_2/NCC.

5.5.3 Optical study

The optical properties of the synthesized nanocomposites, in contrast to those of NCC and SiO_2, showed the formation of AgNPs, as revealed by intense yellow-brown and dark brown colours of AgNPs/NCC and AgNPs/SiO_2/NCC, respectively, see Fig. 5.2 (inset). The observed colours were due to the localized surface plasmon resonance (LSPR) of AgNPs in the nanocomposite.[39, 64] The result was further confirmed by the UV-vis absorption study of the nanocomposites. A narrow peak was observed in the UV-vis spectrum of the AgNPs/NCC at 412 nm, while a broad peak was observed in the spectrum of the AgNPs/SiO_2/NCC at approximately the same wavelength, with a shoulder at 490 nm (Fig. 5.2). The absorption peaks showed the presence of freely oscillating electrons, adsorbing the electromagnetic radiation on the surface of the AgNPs.[65] The narrow absorption peak observed in the spectrum of AgNPs/NCC indicated that the synthesized AgNPs were monodispersed and non-aggregated, with spherical morphology, which confirmed the reducing- and stabilizing effect of the NCC.[18, 66] The observed broadness of this peak in the spectrum of AgNPs/SiO_2/NCC, showed that the AgNPs were polydispersed and aggregated, forming clusters and leading to a multipolar plasmon resonance, as reflected by the observed shoulder in the spectrum.[41, 67] This clearly

indicated that the aggregation of the AgNPs on the SiO_2 surface in the nanocomposite and these clusters, should, therefore, provide a stronger SERS effect since the population of "hot spots" increases in the AgNPs/SiO_2/NCC nanocomposite in comparison with AgNPs/NCC.

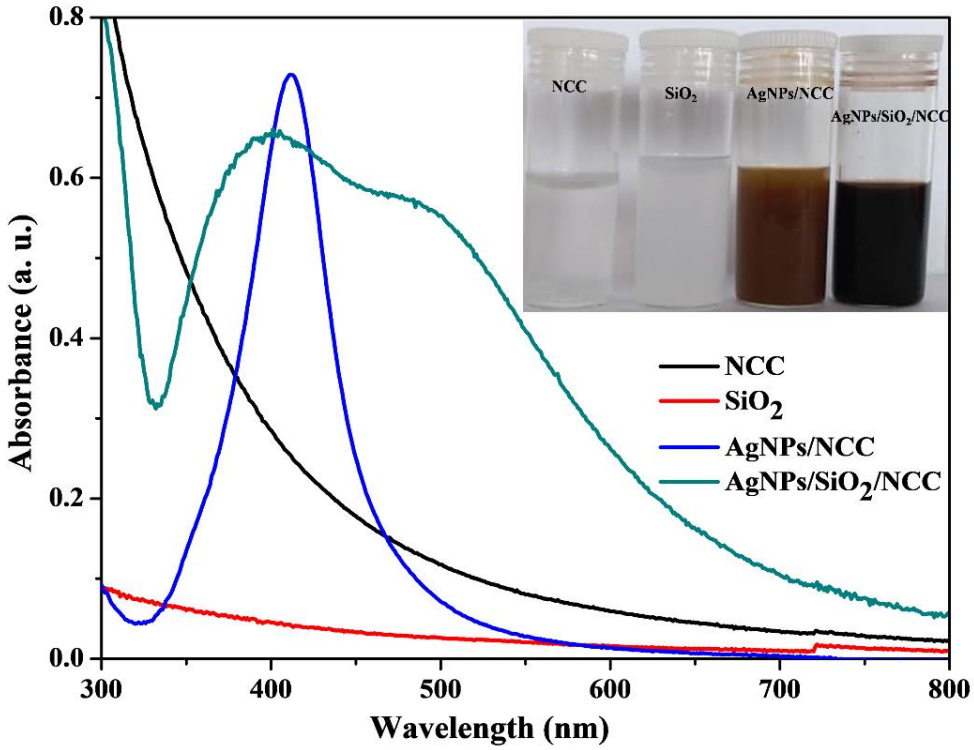


Fig. 5.2: Absorption spectra and images (inset) of NCC, SiO_2, AgNPs/NCC and AgNPs/SiO_2/NCC.

5.5.4 Stability study of colloidal solutions of nanocomposites

The colloidal solutions of: NCC, SiO_2, AgNPs/NCC and AgNPs/SiO_2/NCC (inset: Fig. 5.2) were stable over a period of six months without any noticeable precipitation. The colloidal stability was further confirmed by the calculated mean zeta potential (ζ/mV); -31.7 ± 0.5 (NCC), -40.3 ± 0.3 (SiO_2), -30.5 ± 0.2 (AgNPs/NCC) and -33.2 ± 0.1 (AgNPs/SiO_2/NCC), respectively, which indicated that the absolute values were more than 25 mV, which is the minimum required surface charge on nanoparticles in a stable colloidal solution.[68-69] The charged surface provided the required repulsion between adjacent nanoparticles in order to prevent excess aggregation that can result in the precipitation of coagulated nanoparticles.[70-71] The observed negative potential on NCC was a characteristic of NCC, isolated by sulphuric acid due to the residual sulfone groups left after hydrolysis that are known to provide electrostatic stability for NCC in solution.[27, 51, 72] The zeta potential of SiO_2 resulted from the presence of the abundant negatively charged silanol groups on the surface.[56-57] The slight

reduction in the absolute zeta potential of the nanocomposites when compared with NCC and SiO_2, indicated a synergic interaction between the constituents of the nanocomposites.[41]

5.5.5 TEM/HRTEM study

The TEM micrograph (Fig. 5.3A) of the isolated NCC from filter paper showed that the nanocrystals were needlelike with a calculated mean length of 155.9 ± 51.1 nm, width 12.4 ± 4.0 nm and aspect ratio 11.9 ± 5.0, from 150 randomly selected nanocrystals. The high standard deviation of the dimensions indicated that the nanocrystals were polydispersed, as revealed by the distributions of the dimensions (Fig. S5.1, Appendix C). This result is related to the previous report on the NCC isolated from cigarette filters[28] and comparable to the NCC isolated from other sources *via* similar processes.[58-59, 73] The capacity of the isolated NCC as both reducing- and stabilizing agent was evident from the synthesized AgNPs, which were monodispersed and without agglomeration, as shown by a representative TEM micrograph of AgNPs/NCC in Fig. 3B; the inset shows a stained micrograph, revealing the interaction of the NCC with the AgNPs, attached to the NCC. However, in the presence of silica, the AgNPs were observed to aggregate, forming clusters on the silica surface (Fig. 5.3E), which indicated a stronger affinity of the AgNPs for the silica, surface in comparison with NCC. Nevertheless, the NCC were found to be closely interacting with the silica as revealed by the inset stained sample (Fig. 5.3E). The result suggests a synergy between the NCC and silica, leading to a homogenous distribution of "hot spots" on the silica surface. HRTEM further revealed that the polycrystalline nature of the AgNPs decreased as the selected area electron diffraction (SAED) pattern rings of the AgNPs were observed to diffuse on silica, as shown in the inset in Fig. 5.3F in comparison to the inset in Fig. 5.3C. This showed that the AgNPs were directly attached to the amorphous silica surface, hence, leading to the observed diffusion.[74] The AgNPs cluster formation on the silica in AgNPs/SiO_2/NCC composite resulted in an increase in the calculated mean diameter to 181.8 ± 67.2 nm from 161.3 ± 29.5 nm, in comparison to free silica (Fig. S5.2 (A and B), Appendix C). The HRTEM also revealed lattice fringes of 0.24 nm (Fig. S5.3, Appendix C) for the synthesized AgNPs, which correlated with the (111) plane of a FCC crystal structure of silver metal.[75] The calculated mean diameter of 19.5 ± 5.3 nm in the AgNPs (Fig. S5.2 (C), Appendix C) was comparable to 18.6 ± 2.5 nm that was earlier reported by using the NCC isolated from discarded cigarette filter and used as a reducing- and stabilizing agent *via* similar procedure.[39]

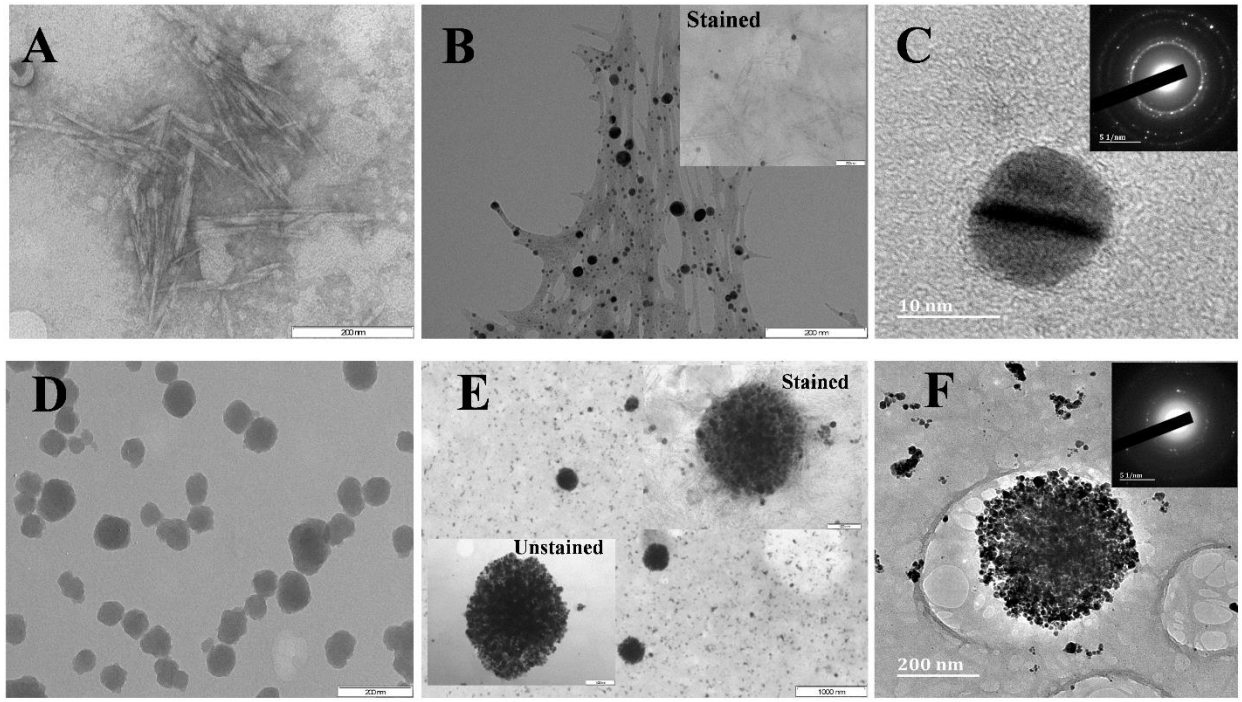


Fig. 5.3: TEM micrographs of NCC (A), AgNPs/NCC (inset: stained sample) (B), HRTEM micrograph of AgNPs/NCC (inset: corresponding SAED) (C), TEM micrographs SiO_2 (D). AgNPs/SiO_2/NCC (inset: corresponding high magnification stained and unstained samples) (E) and HRTEM micrograph of AgNPs/SiO_2/NCC (inset: corresponding SAED) (F).

5.5.6 SEM/EDX study

The SEM micrograph (Fig. 5.4A) of the isolated NCC showed needle-like structures of the nanocrystals, similar to that observed in the TEM micrograph (Fig. 5.3A), however, with a higher degree of aggregation of the nanocrystals on drying.[28, 76] Similarly, the spherical nature of the synthesized silica was revealed by the SEM, as shown in Fig. 5.4B. The surface appeared smoother when compared to the coated silica in Fig. 5.4D. The SEM micrograph of the AgNPs/NCC composite showed an assembly of the AgNPs, which remained spherical as observed in TEM (Fig. 5.3C), despite the aggregation resulting from drying effects: this feature was not observed in solution due to the fact that the NCC prevented such aggregation. A higher degree of aggregation was observed in AgNPs/SiO_2/NCC (Fig. 5.4D) due to presence of silica, which provided a suitable surface for the clustering of AgNPs, thereby leading to a larger population of "hot spots". This further corroborated the observed AgNPs particles in the TEM micrograph of AgNPs/SiO_2/NCC (Fig. 5.3E). The SEM micrograph of a diluted solution of the AgNPs/SiO_2/NCC composite revealed the synergic interaction effect of the NCC with silica. The nanocrystals were observed to interact with the silica, leading to a reduction of Ag^+ ions on the silica surface in the presence of NCC as reducing agent. The synergism was attributed

to the hydrogen bonding interaction that existed between silica and NCC due to the surface silanol and hydroxyl groups on silica and NCC respectively. The EDX spectra showed that the predominant element in both nanocomposites was Ag, with 72.81 and 65.05 wt% of Ag (Table S5.1, Appendix C) observed in AgNPs/NCC and AgNPs/SiO_2/NCC, respectively. The difference was obviously as a result of the 5 mg (10 wt%) mass of silica introduced. Similarly, the EDX mapping of the element showed even distributions of the AgNPs in both composites (Fig. S5.4 and S5.5, Appendix C).

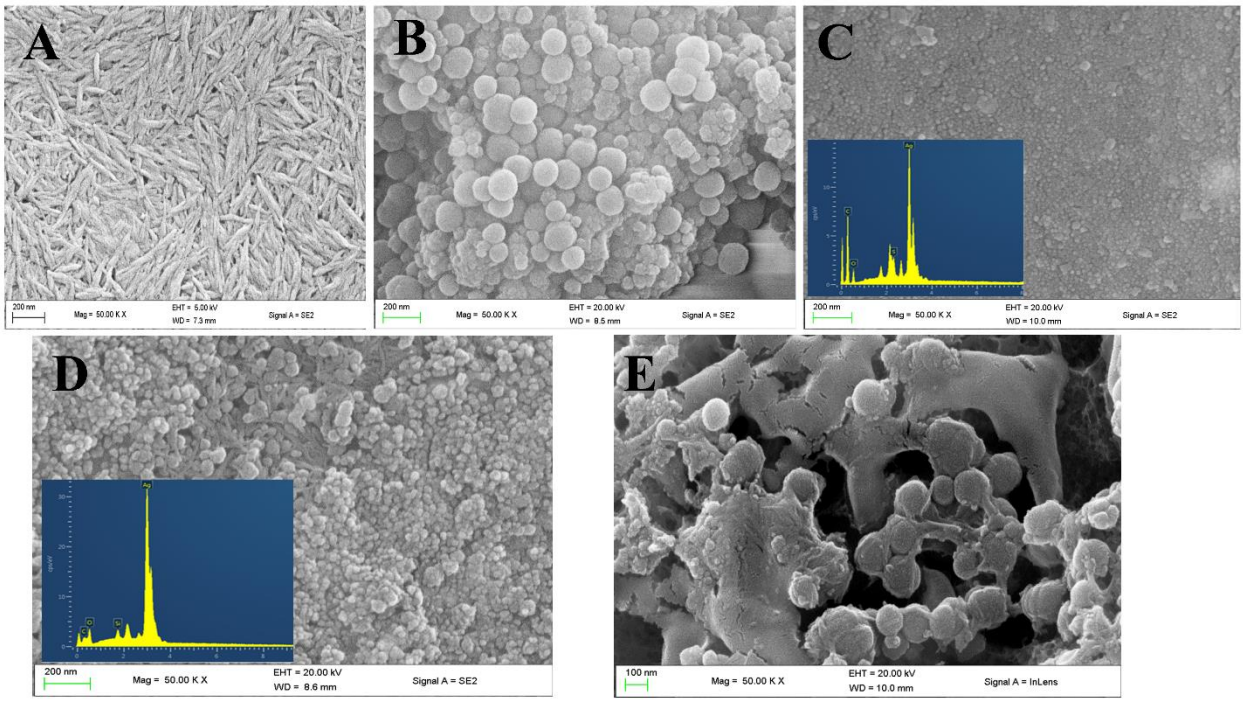


Fig. 5.4: SEM micrographs of dilute NCC dried on glass (A), SiO_2 (B), AgNPs/NCC (inset: corresponding EDX spectrum) (C), AgNPs/SiO_2/NCC (inset: corresponding EDX spectrum) (D) and dilute AgNPs/SiO_2/NCC dried on glass (E).

5.5.7 Powder XRD study

The XRD pattern of the isolated NCC (Fig. 5.5) showed intense peaks at 2θ = 15.1° (101), 16.8° ($10\bar{1}$) and 23.1° (002), characteristics of cellulose I crystal[77-79] with a high crystallinity index of 99.8% and crystallite size of 12.2 nm, comparable to the calculated mean width (12.4 nm) of the nanocrystals in the TEM micrograph Fig. (3A). Similarly, the presence of these peaks was observed in the diffractograms of AgNPs/NCC and AgNPs/SiO_2/NCC nanocomposites, however with reduced intensities since highly intense peaks characteristic of metallic silver FCC structure predominated at 2θ = 38.1° (111), 44.3° (200), 64.4° (220), 77.5° (311) and 81.5° (222).[80-81] The presence of SiO_2 in AgNPs/SiO_2/NCC resulted in a slight broadening of the peaks in comparison with AgNPs/NCC, with a corresponding decrease in

crystallite size from 19.1 nm (AgNPs/NCC) to 15.4 nm (AgNPs/SiO_2/NCC), as calculated by using the (111) crystallographic plane. The result was attributed to the observed aggregation of AgNPs on SiO_2, which showed a diffraction pattern with a very broad peak, centered at 2θ = 23.4°, characteristic of amorphous SiO_2.[62] The crystallite size calculated for the AgNPs in AgNPs/NCC composite correlated with the mean diameter of AgNPs in the TEM micrograph (Fig. 5.3B).

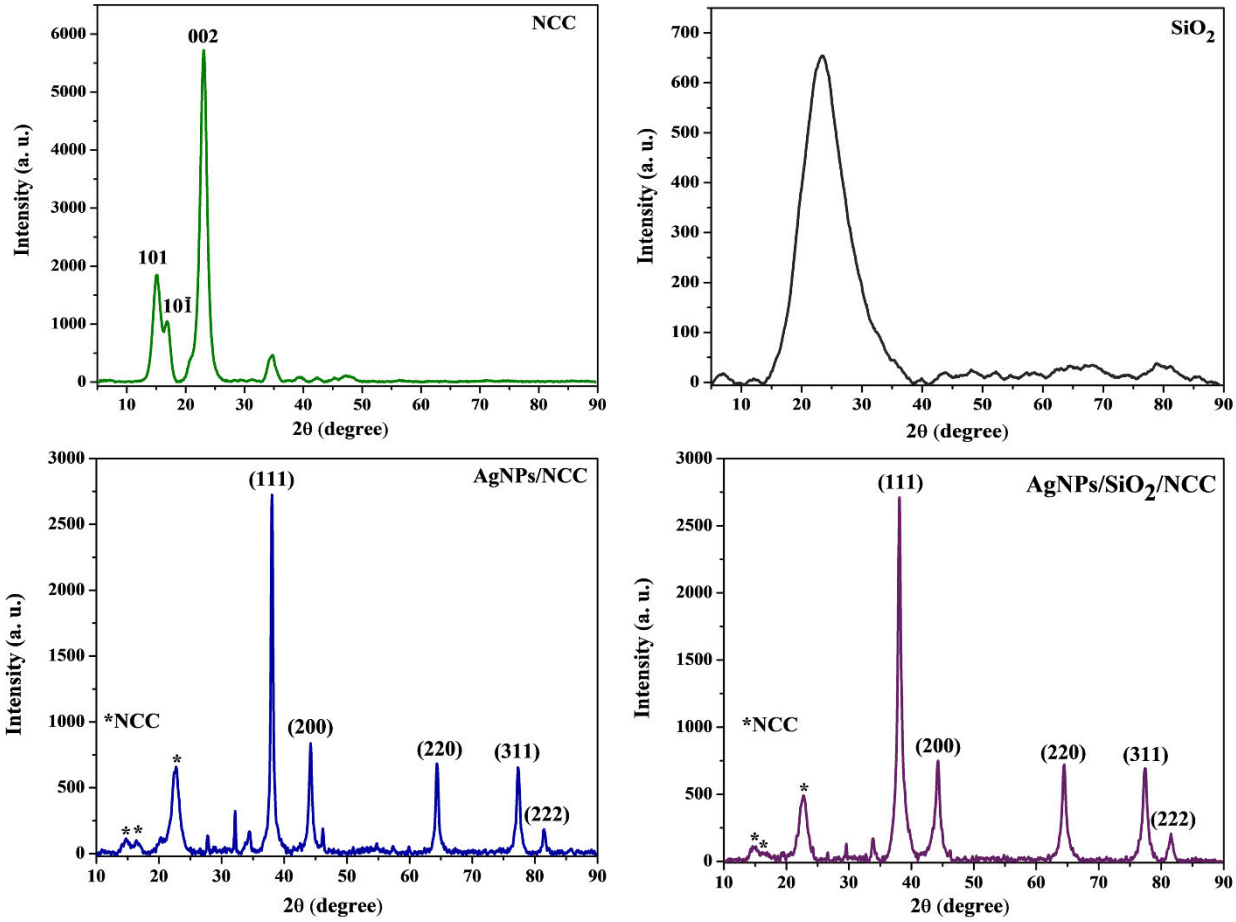


Fig. 5.5: X-ray diffractograms of NCC, SiO_2, AgNPs/NCC and AgNPs/SiO_2/NCC.

5.5.8 Thermogravimetric and Differential thermal analyses (TGA/DTA) study

The thermal behaviour of the isolated NCC, SiO_2, AgNPs/NCC and AgNPs/SiO_2/NCC were determined by TGA/DTA. The thermograms and DTA curves shown in Fig. 5.6 (A and B) revealed the NCC as the principal component that is susceptible to thermal degradation since the thermograms showed comparable, but different rates of the thermal degradation profiles for the NCC, AgNPs/NCC and AgNPs/SiO_2/NCC. The decomposition stages, corresponding to: characteristic temperatures, mass losses and mass residue at 700°C, are shown in Table 5.1. The mass loss below 110°C was associated with the physically absorbed moisture on the

surface of the samples. While the thermogram of SiO_2 showed no significant change above 150°C, the NCC thermogram showed two stages of thermal decomposition, characteristics of nanocellulose[82-83] at peak temperatures of 174°C and 372°C, which involved the dehydration of the anhydroglucose chain segments, chain decomposition and oxidative degradation, as earlier reported.[28, 39] These stages were observed in the thermograms and DTA curves of AgNPs/NCC and AgNPs/SiO_2/NCC composites, however, with reduction in peak decomposition temperature, which is attributed to an increase in thermal degradation (due to high thermal conductivity of AgNPs). The thermal insulating effect of SiO_2 on NCC, resulted in a reduction in the mass loss at the second stage of thermal decomposition of NCC in AgNPs/SiO_2/NCC, when compared to AgNPs/NCC and NCC. The presence of AgNPs and SiO_2 in the nanocomposites, resulted in an increase in the corresponding mass residue at 700°C in comparison with NCC.

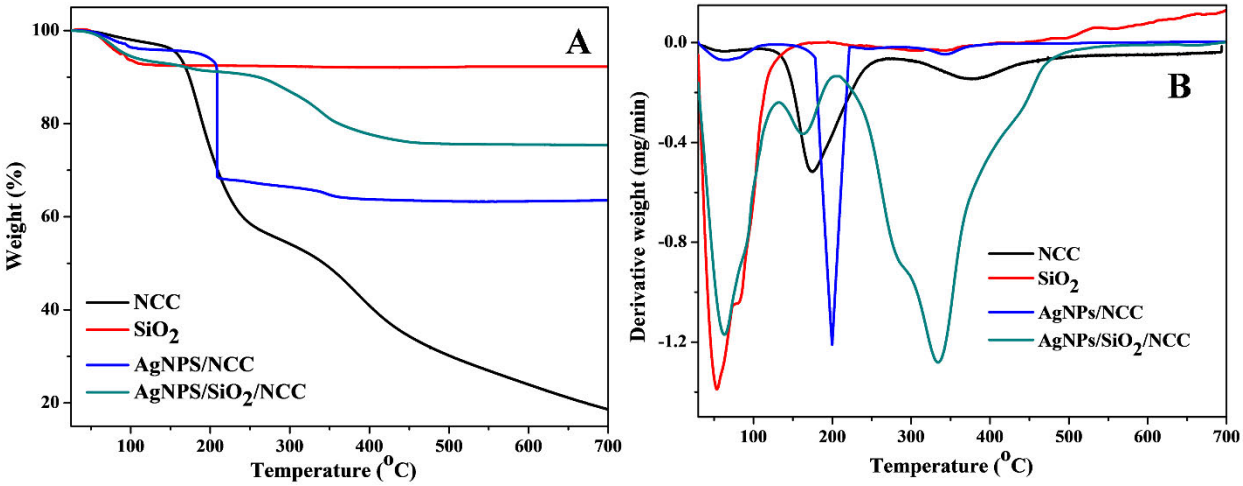


Fig. 5.6: The thermograms (A) and DTA curves of NCC, SiO_2, AgNPs/NCC and AgNPs/SiO_2/NCC.

Table 5.1. Comparison of thermal analysis data for NCC, AgNPs/NCC and AgNPs/SiO_2/NCC

Sample		T_i (°C)	T_p (°C)	T_f (°C)	Mass loss at T_p (%)	Mass at 700 °C (%)
NCC	Stage 1	110	174	268	10.18	18.60
	Stage 2	270	372	507	54.32	
AgNPs/NCC	Stage 1	142	200	223	6.05	63.51
	Stage 2	306	342	384	34.81	
AgNPs/SiO_2/NCC	Stage 1	131	163	202	7.60	75.40
	Stage 2	208	334	498	16.71	

Initial temperature (T_i), peak temperature (T_p), final temperature (T_f).

5.5.9 Detection of malachite green (MG) *via* surface-enhanced Raman scattering (SERS)

The suitability of the synthesized composites as SERS substrates was demonstrated by using MG, a fungicide with genotoxic and carcinogenic predispositions, illicitly used in some aquaculture industries. Prominent peaks characteristics of Raman spectrum of MG were observed to be strongly enhanced by AgNPs/SiO_2/NCC and AgNPs/NCC nanocomposites, even at low concentration, in comparison with Raman spectrum of solid MG (Fig. 5.7E). However, the tri-component nanocomposite AgNPs/SiO_2/NCC showed stronger enhancement of the Raman peaks in comparison with silicaless AgNPs/NCC. This improved enhancement of SERS signal intensities is attributed to the clustering of the plasmonic nanoparticles on SiO_2, leading to a higher population of "hot spots". SERS spectra (Fig. 5.7(A and C)) for each nanocomposite were acquired by using equal volumes of the analyte (MG) of known concentration and colloids of the nanocomposite with 198.16 ± 15.61 mg/L (AgNPs/SiO_2/NCC) and 221.32 ± 14.58 mg/L (AgNPs/NCC) concentrations of Ag metal, respectively, as determined by ICP-OES. The Raman spectra of the neat (without MG) nanocomposites (Fig. S5.7, Appendix C) were weak and showed no significant interference of the peaks associated with MG, thereby leading to a low background noise. Moreover, the background intensity of AgNPs/SiO_2/NCC was lower in comparison with AgNPs/NCC. Prominent peaks in the SERS spectra of MG were (υ/cm^{-1}): 436 (out-of-plane modes of phenyl–C–phenyl), 805 (out-of-plane modes of ring C–H), 911 (C–H out-of-plane bending), 1179 (in-plane modes of ring C–H bending), 1224 (C–H rocking), 1372 (*N*-phenyl stretching) and 1621 (ring C–C stretching).[45, 84-85] These peaks experienced a different degree of enhancement, as revealed by the plots of peak intensities against concentration (Fig. 5.7 (B and D)), which showed that the most enhanced peak was at 1621 cm^{-1}, and the intensities of this peak at different concentrations were thus, used to generate calibration plots (Fig. 5.7F) in order to establish the sensitivity of the nanocomposites. The sensitivity of the nanocomposites investigated by using a 0.001–100 nM concentration range of MG, showed that the limits of detection (LODs) based on a signal-to-background ratio of 3:1[86] were 0.9 and 5.1 nM for AgNPs/SiO_2/NCC and AgNPs/NCC, respectively. The lower LOD observed for AgNPs/SiO_2/NCC demonstrated that with the clustering of the plasmonic nanoparticles, hence leading to formation of "hot spots", the sensitivity of the substrate was significantly improved in comparison with AgNPs/NCC. The LODs observed for the nanocomposites were comparable with 1.0 nM reported by Liao et al., using AuNPs coated on paper with the aid of ink-jet printer,[87] 0.1 nM reported by Shao et al., using a poly(L-lactic acid) nanofibrous paper

adsorbed with plasmonic nanostructures,[88] 100 nM reported by Xiao et al., using reduced graphene oxide/AgNPs[49] and 1.0 nM reported by Zhao et al., using Ag-decorated TiO_2 inverse opal film.[89] Generally, LODs in SERS analysis vary, based on the conditions of measurement, which include: pH, time of incubation, contact time of substrate with laser, method of SERS substrate preparation, plasmonic nanoparticle shape and size.

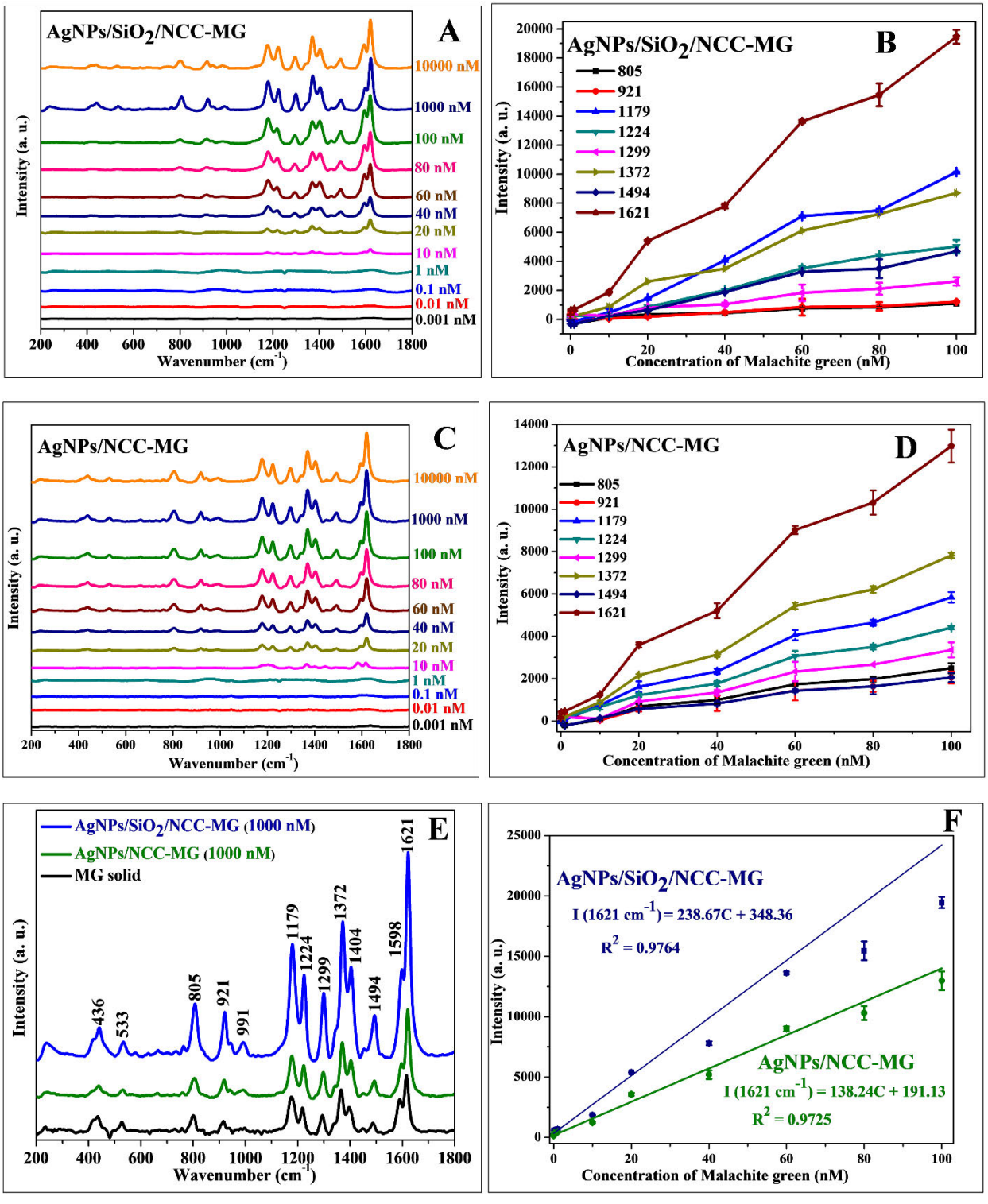


Fig. 5.7: SERS spectra of MG on AgNPs/SiO_2/NCC substrate in a concentration range of 0.001–10000 nM (A) and the corresponding plots of the peak intensities against concentration (B). SERS spectra of MG on AgNPs/NCC substrate in a concentration range of 0.001–10000 nM (C) and the corresponding plots of the peak intensities against concentration (D). Raman spectra of MG, SERS spectra of MG (1000 nM) on the nanocomposites (E) and the calibration plots of 1621 cm^{-1} peak intensity against concentration.

5.6 Conclusion

This study demonstrated a significant improvement in SERS sensitivity and enhancement of AgNPs synthesized by using NCC as a reducing- and stabilizing agent in the presence of Stöber silica. The 3-component nanocomposite provided a suitable surface area for the aggregation of the plasmonic nanoparticles needed to generate "hot spots" without loss of colloidal stability as revealed by zeta potential studies. TEM micrographs revealed the monodispersed nature of the plasmonic nanoparticles with a mean diameter of 19.5 nm in AgNPs/NCC, while the SAED obtained from HRTEM, revealed polycrystallinity. However, the plasmonic nanoparticles assembled into clusters on SiO_2 with a resultant increase in the mean diameter of SiO_2 by approximately 20 nm, in contrast to free SiO_2. The SEM and stained TEM micrographs of AgNPs/SiO_2/NCC showed a synergic interaction between NCC, AgNPs and SiO_2, while EDX spectrum and powder-XRD revealed that the predominant element in the nanocomposites (AgNPs/NCC and AgNPs/SiO_2/NCC) was Ag metal. The nanocomposites produced were relatively stable below 150°C as thermal analysis revealed that the component most susceptible to thermal degradation was NCC. The AgNPs/SiO_2/NCC material showed relatively lower background interference and higher sensitivity when used as a SERS substrate for detection of MG to a limit of 0.9 nM, in contrast with AgNPs/NCC, which showed a LOD of 5.2 nM based, on a signal-to-background ratio of 3:1, which clearly exemplified the enormous impact of "hot spots" associated with the aggregation of the plasmonic nanoparticles.

5.7 References

(1) Albrecht, M. G.; Creighton, J. A. Anomalously Intense Raman spectra of Pyridine at a Silver Electrode. *J. Am. Chem. Soc.* **1977**, *99*, 5215–5217.

(2) Jeanmaire, D. L.; Van Duyne, R. P. Surface Raman Spectroelectrochemistry: Part I. Heterocyclic, Aromatic, and Aliphatic Amines Adsorbed on the Anodized Silver Electrode. *J. Electroanal. Chem.* **1977**, *84*, 1–20.

(3) Zong, C.; Xu, M.; Xu, L.-J.; Wei, T.; Ma, X.; Zheng, X.-S.; Hu, R.; Ren, B. Surface-Enhanced Raman Spectroscopy for Bioanalysis: Reliability and Challenges. *Chem. Rev.* **2018**, *118*, 4946–4980.

(4) Li, J.-F.; Zhang, Y.-J.; Ding, S.-Y.; Panneerselvam, R.; Tian, Z.-Q. Core–shell Nanoparticle-Enhanced Raman Spectroscopy. *Chem. Rev.* **2017**, *117*, 5002–5069.

(5) Nam, J.-M.; Oh, J.-W.; Lee, H.; Suh, Y. D. Plasmonic Nanogap-Enhanced Raman Scattering with Nanoparticles. *Acc. Chem. Res.* **2016**, *49*, 2746–2755.

(6) Ding, S.-Y.; Yi, J.; Li, J.-F.; Ren, B.; Wu, D.-Y.; Panneerselvam, R.; Tian, Z.-Q. Nanostructure-Based Plasmon-Enhanced Raman Spectroscopy for Surface Analysis of Materials. *Nat. Rev. Mater.* **2016**, *1*, 16021.

(7) Radziuk, D.; Moehwald, H. Prospects for Plasmonic Hot Spots in Single Molecule SERS Towards the Chemical Imaging of Live Cells. *Phys. Chem. Chem. Phys.* **2015**, *17*, 21072–21093.

(8) Shiohara, A.; Wang, Y.; Liz-Marzán, L. M. Recent Approaches Toward Creation of Hot Spots for SERS Detection. *J. Photochem. Photobiol., C* **2014**, *21*, 2–25.

(9) Li, M.; Cushing, S. K.; Liang, H.; Suri, S.; Ma, D.; Wu, N. Plasmonic Nanorice Antenna on Triangle Nanoarray for Surface-Enhanced Raman Scattering Detection of Hepatitis B Virus DNA. *Anal. Chem.* **2013**, *85*, 2072–2078.

(10) Zhang, Y.; Walkenfort, B.; Yoon, J. H.; Schlücker, S.; Xie, W. Gold and Silver Nanoparticle Monomers are Non-SERS-Active: A Negative Experimental Study with Silica-Encapsulated Raman-Reporter-Coated Metal Colloids. *Phys. Chem. Chem. Phys.* **2015**, *17*, 21120–21126.

(11) Tebbe, M.; Maennel, M.; Fery, A.; Pazos-Perez, N.; Alvarez-Puebla, R. A. Organized Solid Thin Films of Gold Nanorods with Different Sizes for Surface-Enhanced Raman Scattering Applications. *J. Phys. Chem. C* **2014**, *118*, 28095–28100.

(12) Burrows, N. D.; Vartanian, A. M.; Abadeer, N. S.; Grzincic, E. M.; Jacob, L. M.; Lin, W.; Li, J.; Dennison, J. M.; Hinman, J. G.; Murphy, C. J. Anisotropic Nanoparticles and Anisotropic Surface Chemistry. *J. Phys. Chem. Lett.* **2016**, *7*, 632–641.

(13) Reguera, J.; Langer, J.; de Aberasturi, D. J.; Liz-Marzán, L. M. Anisotropic Metal Nanoparticles for Surface Enhanced Raman Scattering. *Chem. Soc. Rev.* **2017**, *46*, 3866–3885.

(14) Millstone, J. E.; Hurst, S. J.; Métraux, G. S.; Cutler, J. I.; Mirkin, C. A. Colloidal Gold and Silver Triangular Nanoprisms. S*mall* **2009**, *5*, 646–664.

(15) Garcia-Leis, A.; Rivera-Arreba, I.; Sanchez-Cortes, S. Morphological Tuning of Plasmonic Silver Nanostars by Controlling the Nanoparticle Growth Mechanism: Application in the SERS Detection of the Amyloid Marker Congo Red. *Colloid. Surface. A* **2017**, *535*, 49–60.

(16) Pazos-Perez, N.; Garcia de Abajo, F. J.; Fery, A.; Alvarez-Puebla, R. A. From Nano to Micro: Synthesis and Optical Properties of Homogeneous Spheroidal Gold Particles and Their Superlattices. *Langmuir* **2012**, *28*, 8909–8914.

(17) Leng, Y.; Fu, L.; Ye, L.; Li, B.; Xu, X.; Xing, X.; He, J.; Song, Y.; Leng, C.; Guo, Y. Protein-Directed Synthesis of Highly Monodispersed, Spherical Gold Nanoparticles and Their Applications in Multidimensional Sensing. *Sci. Rep.* **2016**, *6*, 28900.

(18) Wu, X.; Lu, C.; Zhou, Z.; Yuan, G.; Xiong, R.; Zhang, X. Green Synthesis and Formation Mechanism of Cellulose Nanocrystal-Supported Gold Nanoparticles with Enhanced Catalytic Performance. *Environ. Sci.: Nano* **2014**, *1*, 71–79.

(19) Chen, C.; Zhou, X.; Ding, T.; Zhang, J.; Wang, S.; Xu, J.; Chen, J.; Dai, J.; Chen, C. Preparation and Characterization of ZnO/SiO_2/Ag Nanoparticles as Highly Sensitive Substrates for Surface-Enhanced Raman Scattering. *Mater. Lett.* **2016**, *165*, 55–58.

(20) Ramanauskaite, L.; Snitka, V. The Synthesis of Controlled Shape Nanoplasmonic Silver-Silica Structures by Combining Sol-Gel Technique and Direct Silver Reduction. *Nanoscale Res. Lett.* **2015,** *10*, 133.

(21) Vuoriluoto, M.; Orelma, H.; Zhu, B.; Johansson, L.-S.; Rojas, O. J. Control of Protein Affinity of Bioactive Nanocellulose and Passivation Using Engineered Block and Random Copolymers. *ACS Appl. Mater. Inter.* **2016,** *8*, 5668–5678.

(22) Sirviö, J. A.; Visanko, M.; Laitinen, O.; Ämmälä, A.; Liimatainen, H. Amino-Modified Cellulose Nanocrystals with Adjustable Hydrophobicity from Combined Regioselective Oxidation and Reductive Amination. *Carbohydr. Polym.* **2016,** *136*, 581–587.

(23) Leitch, M. E.; Li, C.; Ikkala, O.; Mauter, M. S.; Lowry, G. V. Bacterial Nanocellulose Aerogel Membranes: Novel High-Porosity Materials for Membrane Distillation. *Environ. Sci. Tech. Lett.* **2016,** *3*, 85–91.

(24) Sampaio, L. M.; Padrão, J.; Faria, J.; Silva, J. P.; Silva, C. J.; Dourado, F.; Zille, A. Laccase Immobilization on Bacterial Nanocellulose Membranes: Antimicrobial, Kinetic and Stability Properties. *Carbohydr. Polym.* **2016**, *145*, 1–12.

(25) Uetani, K.; Okada, T.; Oyama, H. T. Thermally Conductive and Optically Transparent Flexible Films with Surface-Exposed Nanocellulose Skeletons. *J. Mater. Chem. C* **2016**, *4*, 9697–9703.

(26) Zhang, D.; Zhang, Q.; Gao, X.; Piao, G. A Nanocellulose Polypyrrole Composite Based on Tunicate Cellulose. *Int. J. Polym. Sci.* **2013,** *2013*, 175609

(27) Filson, P. B.; Dawson-Andoh, B. E.; Schwegler-Berry, D. Enzymatic-Mediated Production of Cellulose Nanocrystals from Recycled Pulp. *Green Chem.* **2009**, *11*, 1808–1814.

(28) Ogundare, S. A.; Moodley, V.; van Zyl, W. E. Nanocrystalline Cellulose Isolated from Discarded Cigarette Filters. *Carbohydr. Polym.* **2017**, *175*, 273–281.

(29) García, A.; Gandini, A.; Labidi, J.; Belgacem, N.; Bras, J. Industrial and Crop Wastes: A new Source for Nanocellulose Biorefinery. *Ind. Crop. Product.* **2016**, *93*, 26–38.

(30) Brinchi, L.; Cotana, F.; Fortunati, E.; Kenny, J., Production of Nanocrystalline Cellulose from Lignocellulosic Biomass: Technology and Tpplications. *Carbohydr. Polym.* **2013**, *94*, 154–169.

(31) Klemm, D.; Cranston, E. D.; Fischer, D.; Gama, M.; Kedzior, S. A.; Kralisch, D.; Kramer, F.; Kondo, T.; Lindström, T.; Nietzsche, S. Nanocellulose as a Natural Source for Groundbreaking Applications in Materials Science: Today's state. *Mater. Today*, **2018**, *21*, 720–748.

(32) Zhu, H.; Luo, W.; Ciesielski, P. N.; Fang, Z.; Zhu, J.; Henriksson, G.; Himmel, M. E.; Hu, L. Wood-Derived Materials for Green Electronics, Biological Devices, and Energy Applications. *Chem. Rev.* **2016**, *116*, 9305–9374.

(33) Abitbol, T.; Rivkin, A.; Cao, Y.; Nevo, Y.; Abraham, E.; Ben-Shalom, T.; Lapidot, S.; Shoseyov, O. Nanocellulose, a Tiny Fibre with Huge Applications. *Curr. Opin. Biotechnol.* **2016**, *39*, 76–88.

(34) Klemm, D.; Kramer, F.; Moritz, S.; Lindström, T.; Ankerfors, M.; Gray, D.; Dorris, A. Nanocelluloses: A New Family of Nature-Based Materials. *Angew. Chem Int. Ed.* **2011**, *50*, 5438–5466.

(35) Rezayat, M.; Blundell, R. K.; Camp, J. E.; Walsh, D. A.; Thielemans, W. Green One-Step Synthesis of Catalytically Active Palladium Nanoparticles Supported on Cellulose Nanocrystals. *ACS Sustain. Chem. Eng.* **2014**, *2*, 1241–1250.

(36) Kaushik, M.; Li, A. Y.; Hudson, R.; Masnadi, M.; Li, C.-J.; Moores, A. Reversing Aggregation: Direct Synthesis of Nanocatalysts from Bulk Metal. Cellulose Nanocrystals as Active Support to Access Efficient Hydrogenation Silver Nanocatalysts. *Green Chem.* **2016**, *18*, 129–133.

(37) Shi, Z.; Tang, J.; Chen, L.; Yan, C.; Tanvir, S.; Anderson, W. A.; Berry, R. M.; Tam, K. C. Enhanced Colloidal Stability and Antibacterial Performance of Silver Nanoparticles/Cellulose Nanocrystal Hybrids. *J. Mater. Chem. B* **2015**, *3*, 603–611.

(38) Kaushik, M.; Moores, A. Review: Nanocelluloses as Versatile Supports for Metal Nanoparticles and their Applications in Catalysis. *Green Chem.* **2016**, *18*, 622–637.

(39) Ogundare, S. A.; van Zyl, W. E. Nanocrystalline Cellulose as Reducing- and Stabilizing Agent in the Synthesis of Silver Nanoparticles: Application as a Surface-Enhanced Raman Scattering (SERS) Substrate. *Surfaces and Interfaces*, **2018**, *13*, 1–10.

(40) Zhang, X.; Xiao, X.; Dai, Z.; Wu, W.; Zhang, X.; Fu, L.; Jiang, C. Ultrasensitive SERS Performance in 3D "Sunflower-Like" Nanoarrays Decorated with Ag Nanoparticles. *Nanoscale* **2017**, *9*, 3114–3120.

(41) Wang, C.; Li, M.; Li, Q.; Zhang, K.; Wang, C.; Xiao, R.; Wang, S. Polyethyleneimine-Mediated Seed Growth Approach for Synthesis of Silver-Shell Silica-Core Nanocomposites and Their Application as a Versatile SERS Platform. *RSC Adv.* **2017**, *7*, 13138–13148.

(42) Srivastava, S.; Sinha, R.; Roy, D. Toxicological Effects of Malachite Green. *Aquat. Toxicol.* **2004**, *66*, 319–329.

(43) Jin, Y.; Ma, P.; Liang, F.; Gao, D.; Wang, X., Determination of Malachite Green in Environmental Water Using Cloud Point Extraction Coupled with Surface-Enhanced Raman Scattering. *Anal. Methods* **2013**, *5*, 5609–5614.

(44) Ouyang, L.; Yao, L.; Zhou, T.; Zhu, L., Accurate SERS Detection of Malachite Green in Aquatic Products on Basis of Graphene Wrapped Flexible Sensor. *Anal. Chim. Acta* **2018**, *1027*, 83–91.

(45) Zhang, H.; Sun, L.; Zhang, Y.; Kang, Y.; Hu, H.; Iqbal, J.; Du, Y. Rapid Determination of Illegal Additives Chrysoidin and Malachite Green by Surface-Enhanced Raman Scattering with Silanized Support Based Substrate. *Chin. Chem. Lett.* **2018**, *29*, 981–984.

(46) Xu, K.-X.; Guo, M.-H.; Huang, Y.-P.; Li, X.-D.; Sun, J.-J. Rapid and Sensitive Detection of Malachite Green in Aquaculture Water by Electrochemical

Preconcentration and Surface-Enhanced Raman Scattering. *Talanta* **2018**, *180*, 383–388.

(47) Kim, W.; Lee, J.-C.; Lee, G.-J.; Park, H.-K.; Lee, A.; Choi, S. Low-Cost Label-Free Biosensing Bimetallic Cellulose Strip with SILAR-Synthesized Silver Core–Gold Shell Nanoparticle Structures. *Anal. chem.* **2017**, *89*, 6448–6454.

(48) Wei, W. Y.; White, I. M. Chromatographic Separation and Detection of Target Analytes from Complex Samples Using Inkjet Printed SERS Substrates. *Analyst* **2013**, *138*, 3679–3686.

(49) Xiao, G.; Li, Y.; Shi, W.; Shen, L.; Chen, Q.; Huang, L. Highly Sensitive, Reproducible and Stable SERS Substrate Based on Reduced Graphene Oxide/Silver Nanoparticles Coated Weighing Paper. *Appl. Surf. Sci.* **2017**, *404*, 334–341.

(50) Bae, G. Y.; Min, B. G.; Jeong, Y. G.; Lee, S. C.; Jang, J. H.; Koo, G. H. Superhydrophobicity of Cotton Fabrics Treated with Silica Nanoparticles and Water-Repellent Agent. *J. Colloid Interface Sci.* **2009**, *337*, 170–175.

(51) Brito, B. S.; Pereira, F. V.; Putaux, J.-L.; Jean, B. Preparation, Morphology and Structure of Cellulose Nanocrystals from Bamboo Fibres. *Cellulose* **2012**, *19*, 1527–1536.

(52) Wang, H.; Zhang, X.; Jiang, Z.; Li, W.; Yu, Y. A Comparison Study on the Preparation of Nanocellulose Fibrils from Fibres and Parenchymal Cells in Bamboo (*Phyllostachys pubescens*). *Ind. Crop Products* **2015**, *71*, 80–88.

(53) Jiang, F.; Dallas, J. L.; Ahn, B. K.; Hsieh, Y.-L. 1D and 2D NMR of Nanocellulose in Aqueous Colloidal Suspensions. *Carbohydr. Polym.* **2014**, *110*, 360–366.

(54) Muniz-Miranda, M. SERS-Active Ag/SiO_2 Colloids: Photoreduction Mechanism of the Silver ions and Catalytic Activity of the Colloidal Nanoparticles. *J. Raman Spectrosc.* **2004**, *35*, 839–842.

(55) Wang, W.; Ruan, C.; Gu, B. Development of Gold–Silica Composite Nanoparticle Substrates for Perchlorate Detection by Surface-Enhanced Raman Spectroscopy. *Anal. Chim. Acta* **2006**, *567*, 121–126.

(56) Kwon, S.; Singh, R. K.; Kim, T.-H.; Patel, K. D.; Kim, J.-J.; Chrzanowski, W.; Kim, H.-W. Luminescent Mesoporous Nanoreservoirs for the Effective Loading and Intracellular Delivery of Therapeutic Drugs. *Acta Biomater.* **2014**, *10*, 1431–1442.

(57) Liu, Y.; Deng, C.; Yi, D.; Wang, X.; Tang, Y.; Wang, Y. Silica Nanowire Assemblies as Three-Dimensional, Optically Transparent Platforms for Constructing Highly Active SERS Substrates. *Nanoscale* **2017**, *9*, 15901–15910.

(58) Jiang, F.; Hsieh, Y.-L. Chemically and mechanically Isolated Nanocellulose and Their Self-Assembled Structures. *Carbohydr. Polym.* **2013**, *95*, 32–40.

(59) Mohamed, M.; Salleh, W.; Jaafar, J.; Asri, S.; Ismail, A. Physicochemical Properties of "Green" Nanocrystalline Cellulose Isolated from Recycled Newspaper. *RSC Adv.* **2015**, *5*, 29842–29849.

(60) Wu, X.; Lu, C.; Zhang, W.; Yuan, G.; Xiong, R.; Zhang, X. A Novel Reagentless Approach for Synthesizing Cellulose Nanocrystal-Supported Palladium Nanoparticles with Enhanced Catalytic Performance. *J. Mater. Chem. A* **2013**, *1*, 8645–8652.

(61) Green, W. H.; Le, K. P.; Grey, J.; Au, T. T.; Sailor, M. J. White Phosphors from a Silicate-Carboxylate Sol-Gel Precursor that Lack Metal Activator Ions. *Science* **1997**, *276*, 1826–1828.

(62) Akpotu, S. O.; Moodley, B. Encapsulation of Silica Nanotubes from Elephant Grass with Graphene Oxide/Reduced Graphene Oxide and Its Application in Remediation of Sulfamethoxazole from Aqueous Media. *ACS Sustain. Chem. Eng.* **2018**, *6*, 4539–4548.

(63) Hao, L.; Song, H.; Zhang, L.; Wan, X.; Tang, Y.; Lv, Y. SiO_2/Graphene Composite for Highly Selective Adsorption of Pb (II) ion. *J. Colloid Interface Sci.* **2012**, *369*, 381–387.

(64) Lokanathan, A. R.; Uddin, K. M. A.; Rojas, O. J.; Laine, J. Cellulose Nanocrystal–Mediated Synthesis of Silver Nanoparticles: Role of Sulphate Groups in Nucleation Phenomena. *Biomacromolecules* **2013**, *15*, 373–379.

(65) Li, D.; Dong, M.; Besenbacher, F.; Huang, Y.; Chen, M. The Preparation of a Recyclable Catalyst of Silver Nanoparticles Dispersed in a Mesoporous Silica Nanofibre Matrix. *Rsc Adv.* **2016**, *6*, 65613–65618.

(66) Mochochoko, T.; Oluwafemi, O. S.; Jumbam, D. N.; Songca, S. P., Green Synthesis of Silver Nanoparticles Using Cellulose Extracted from an Aquatic Weed; Water Hyacinth. *Carbohydr. Polym.* **2013**, *98*, 290–294.

(67) Yang, J.-K.; Kang, H.; Lee, H.; Jo, A.; Jeong, S.; Jeon, S.-J.; Kim, H.-I.; Lee, H.-Y.; Jeong, D. H.; Kim, J.-H. Single-Step and Rapid Growth of Silver Nanoshells as SERS-Active Nanostructures for Label-Free Detection of Pesticides. *ACS Appl. Mater. Interfaces* **2014**, *6*, 12541–12549.

(68) Morais, J. P. S.; de Freitas Rosa, M.; Nascimento, L. D.; do Nascimento, D. M.; Cassales, A. R. Extraction and Characterization of Nanocellulose Structures from Raw Cotton Linter. *Carbohydr. Polym.* **2013**, *91*, 229–235.

(69) Cheng, M.; Qin, Z.; Liu, Y.; Qin, Y.; Li, T.; Chen, L.; Zhu, M. Efficient Extraction of Carboxylated Spherical Cellulose Nanocrystals with Narrow Distribution Through Hydrolysis of Lyocell Fibres by Using Ammonium Persulphate as an Oxidant. *J. Mater. Chem. A* **2014**, *2*, 251–258.

(70) Kargarzadeh, H.; Ahmad, I.; Abdullah, I.; Dufresne, A.; Zainudin, S. Y.; Sheltami, R. M. Effects of Hydrolysis Conditions on the Morphology, Crystallinity, and Thermal Stability of Cellulose Nanocrystals Extracted from Kenaf Bast Fibres. *Cellulose* **2012**, *19*, 855–866.

(71) Tonoli, G.; Teixeira, E.; Corrêa, A.; Marconcini, J.; Caixeta, L.; Pereira-da-Silva, M.; Mattoso, L. Cellulose Micro/Nanofibres from Eucalyptus Kraft Pulp: Preparation and Properties. *Carbohydr. Polym.* **2012**, *89*, 80–88.

(72) Hasani, M.; Cranston, E. D.; Westman, G.; Gray, D. G. Cationic Surface Functionalization of Cellulose Nanocrystals. *Soft Matter* **2008**, *4*, 2238–2244.

(73) Danial, W. H.; Majid, Z. A.; Muhid, M. N. M.; Triwahyono, S.; Bakar, M. B.; Ramli, Z. The Reuse of Wastepaper for the Extraction of Cellulose Nanocrystals. *Carbohydr. Polym.* **2015**, *118*, 165–169.

(74) Xiong, R.; Lu, C.; Zhang, W.; Zhou, Z.; Zhang, X., Facile Synthesis of Tunable Silver Nanostructures for Antibacterial Application Using Cellulose Nanocrystals. *Carbohydr. Polym.* **2013**, *95*, 214–219.

(75) Oluwafemi, O. S.; Mochochoko, T.; Leo, A. J.; Mohan, S.; Jumbam, D. N.; Songca, S. P. Microwave Irradiation Synthesis of Silver Nanoparticles Using Cellulose from *Eichhornia crassipes* Plant Shoot. *Mater. Lett.* **2016**, *185*, 576–579.

(76) Lu, P.; Hsieh, Y.-L. Preparation and Characterization of Cellulose Nanocrystals From Rice Straw. *Carbohydr. Polym.* **2012**, *87*, 564–573.

(77) Deepa, B.; Abraham, E.; Cordeiro, N.; Mozetic, M.; Mathew, A. P.; Oksman, K.; Faria, M.; Thomas, S.; Pothan, L. A. Utilization of Various Lignocellulosic Biomass for the Production of Nanocellulose: A Comparative Study. *Cellulose* **2015**, *22*, 1075–1090.

(78) Mueller, S.; Weder, C.; Foster, E. J. Isolation of Cellulose Nanocrystals from Pseudostems of Banana Plants. *RSC Adv.* **2014**, *4*, 907–915.

(79) Mittal, A.; Katahira, R.; Himmel, M. E.; Johnson, D. K. Effects of Alkaline or Liquid-Ammonia Treatment on Crystalline Cellulose: Changes in Crystalline Structure and Effects on Enzymatic Digestibility. *Biotechnol. Biofuels* **2011**, *4*, 41.

(80) Soliveri, G.; Ardizzone, S.; Yüksel, S.; Cialla-May, D.; Popp, J.; Schubert, U. S.; Hoeppener, S. Microwave-Assisted Silver Nanoparticle Film Formation for SERS Applications. *J. Phys. Chem. C* **2016**, *120*, 1237–1244.

(81) Jiang, F.; Hsieh, Y.-L. Synthesis of Cellulose Nanofibril Bound Silver Nanoprism for Surface Enhanced Raman Scattering. *Biomacromolecules* **2014**, *15*, 3608–3616.

(82) Cerrutti, P.; Roldán, P.; García, R. M.; Galvagno, M. A.; Vázquez, A.; Foresti, M. L. Production of Bacterial Nanocellulose from Wine Industry Residues: Importance of Fermentation Time on Pellicle Characteristics. *J. Appl. Polym. Sci.* **2016**, *133*, 43109.

(83) Hu, Y.; Tang, L.; Lu, Q.; Wang, S.; Chen, X.; Huang, B. Preparation of Cellulose Nanocrystals and Carboxylated Cellulose Nanocrystals from Borer Powder of Bamboo. *Cellulose* **2014**, *21*, 1611–1618.

(84) Joshi, P.; Santhanam, V. Inkjet-Based Fabrication Process with Control over the Morphology of SERS-Active Silver Nanostructures. *Ind. Eng. Chem. Res.* **2018**, *57*, 5250–5258.

(85) Polavarapu, L.; Porta, A. L.; Novikov, S. M.; Coronado-Puchau, M.; Liz-Marzán, L. M. Pen-on-Paper Approach Toward the Design of Universal Surface Enhanced Raman Scattering Substrates. *Small* **2014**, *10*, 3065–3071.

(86) Guideline, I. H. T., Validation of analytical procedures: text and methodology. *Q2 (R1)* **2005**, *1*.

(87) Liao, W.-J.; Roy, P. K.; Chattopadhyay, S. An Ink-Jet Printed, Surface Enhanced Raman Scattering Paper for Food Screening. *RSC Adv.* **2014**, *4*, 40487–40493.

(88) Shao, J.; Tong, L.; Tang, S.; Guo, Z.; Zhang, H.; Li, P.; Wang, H.; Du, C.; Yu, X.-F. PLLA Nanofibrous Paper-Based Plasmonic Substrate with Tailored Hydrophilicity for Focusing SERS Detection. *ACS Appl. Mater. Interfaces* **2015**, *7*, 5391–5399.

(89) Zhao, J.; Lin, J.; Li, X.; Zhao, G.; Zhang, W. Silver Nanoparticles Deposited Inverse Opal Film as a Highly Active and Uniform SERS Substrate. *Appl. Surf. Sci.* **2015**, *347*, 514–519.

Chapter 6

Conclusions and future work

6.1 Conclusions

This study has provided an in-depth overview on the significant contributions of cellulose in the development of SERS substrates with numerous applications. It also demonstrated the successful isolation and characterization of NCC from DCF for the first time. Cellulose acetate recovered from cigarette filters was processed into cellulose, in a stepwise process that involved ethanolic extraction, hypochlorite bleaching and alkaline deacetylation. NCC was isolated from the cellulose by sulphuric acid hydrolysis. A number of microscopic and spectroscopic analyses showed the transition of the micro-sized fibres to needlike nanocrystals. The isolated NCC was used as a reducing- and stabilizing agent in the synthesis of AgNPs. The colloidal solution of the synthesized AgNPs was applied as a SERS substrate for the detection of highly fluorescence analyte (riboflavin) at low concentration. Similarly, NCC was isolated from Whatman cellulose filter paper by sulphuric acid hydrolysis and used in the synthesis of AgNPs on SiO_2-support to generate "hot spots". The sensitivity of this nanocomposite (AgNPs/SiO_2/NCC) as a SERS substrate was demonstrated using malachite green. The nanocomposite showed improved signal enhancement and higher sensitivity in contrast with AgNPs/NCC obtained in the absence of SiO_2.

In comparison, the NCC isolated from DCF has cellulose II allomorphs crystalline structure; an indication of the influence of alkaline hydrolysis on the isolated NCC-DCF, while the NCC isolated from Whatman cellulose filter paper has cellulose I allomorphs crystalline structure. However, the FTIR spectra of the NCCs isolated, from the DCF and the filter paper, showed similar absorption bands characteristics of cellulose. The AgNPs synthesized by using the NCCs isolated from the DCF and the filter paper as reducing- and stabilizing agents are spherical in shape with mean diameter of 18.6 and 19.5 nm respectively.

This study, therefore, showed the potential for using one of the world's most littered items (DCF) as a cheap source of NCC, capable of serving as both reducing- and stabilizing agent to form AgNPs, which in turn showed great promise as a SERS substrate. This study also demonstrated the improvement in the sensitivity of NCC-based SERS substrate on SiO_2-support.

6.2 Future work

The potential of NCC, isolated from DCF, can be further explored for the synthesis of bimetallic plasmonic nanoparticles, which can also be investigated as SERS substrates. The possibility of an alternative SERS inert-based material to act as a platform for the aggregation of plasmonic nanoparticles can also be investigated towards improving SERS sensitivity of NCC-based plasmonic substrates. The sensitivity of AgNPs/NCC and AgNPs/SiO_2/NCC can be further investigated by using different laser wavelengths, especially those in the near infrared and infrared region, which showed better signal with fluorescence analytes. The sensitivity of the NCC-based SERS substrates can be similarly investigated by using other analytes of environmental concerns. The unique properties of NCC e.g. its chiral nematic nature can also be explored for the development of improved NCC-based SERS substrate.

Appendices

Appendix A: Supplementary Information to Chapter 3

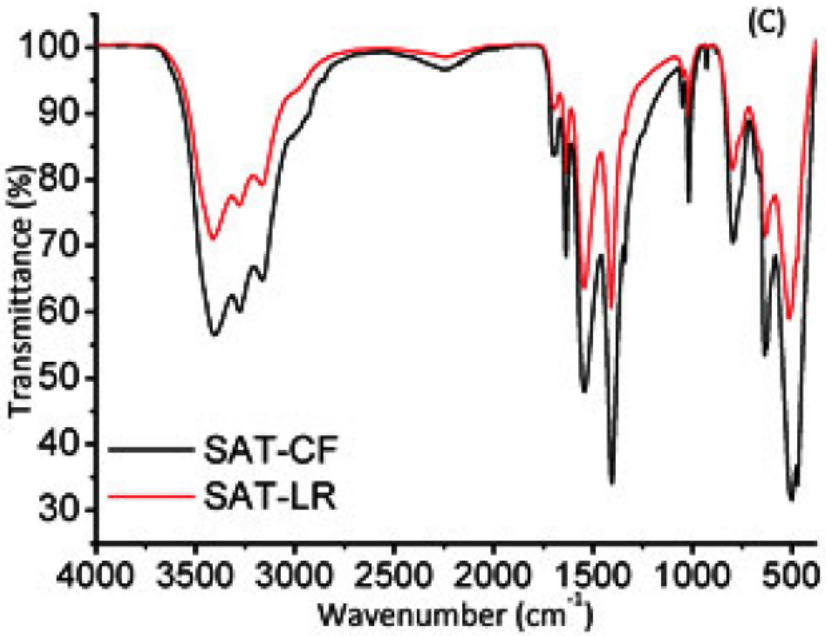
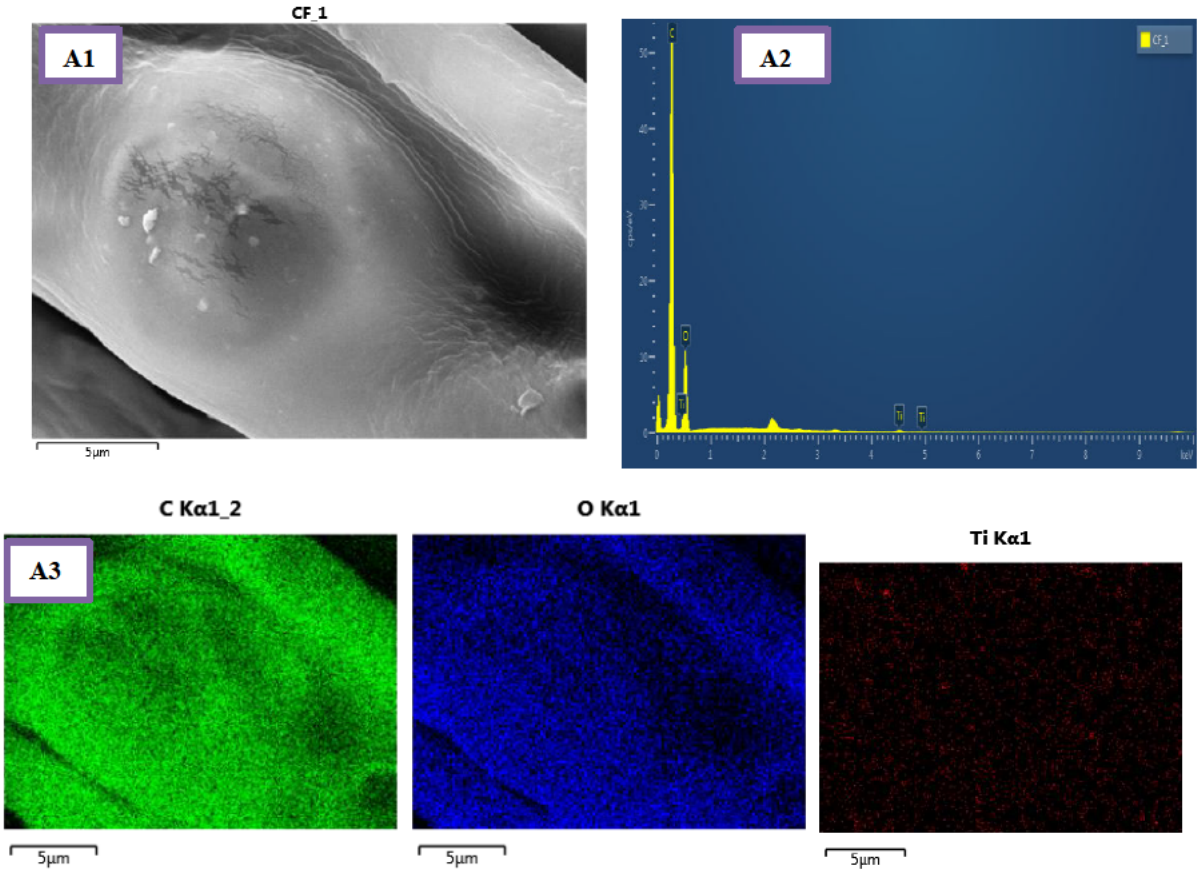
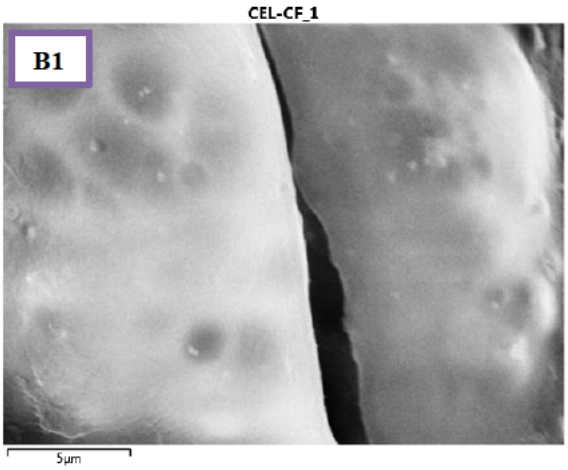
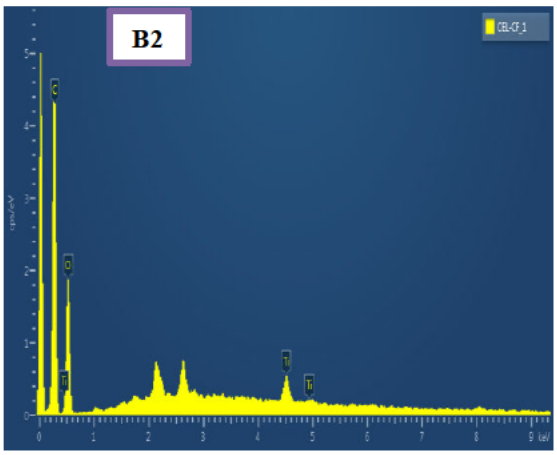
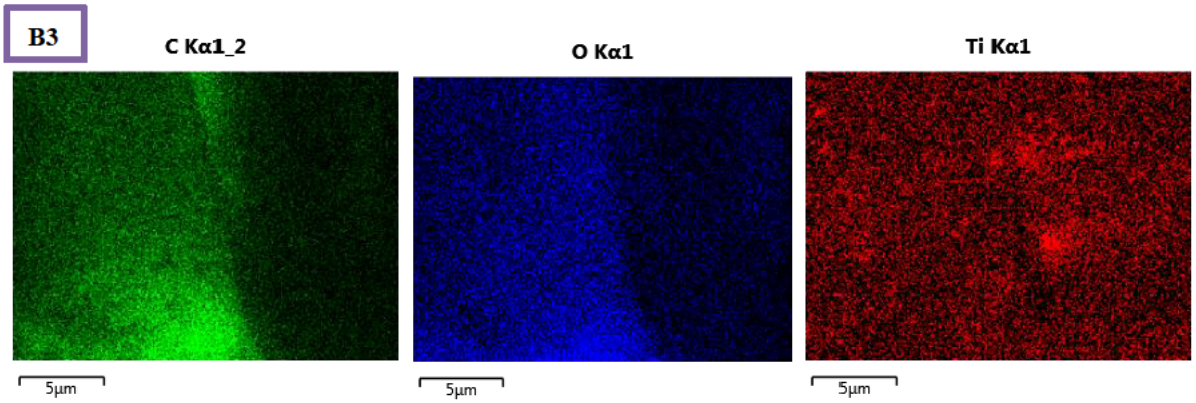


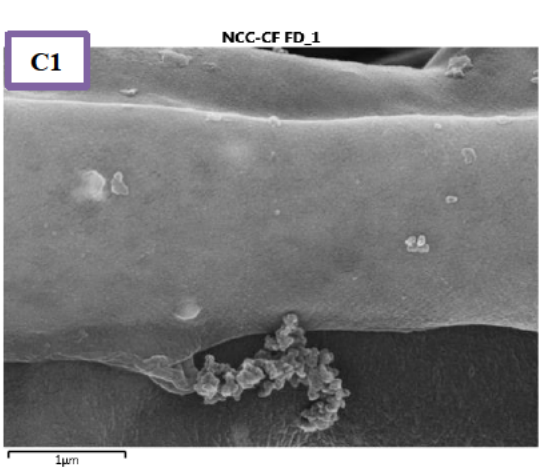
Fig. S3.1: ATR-FTIR spectra of SAT-DCF and SAT-LR. LR (Laboratory reagent).

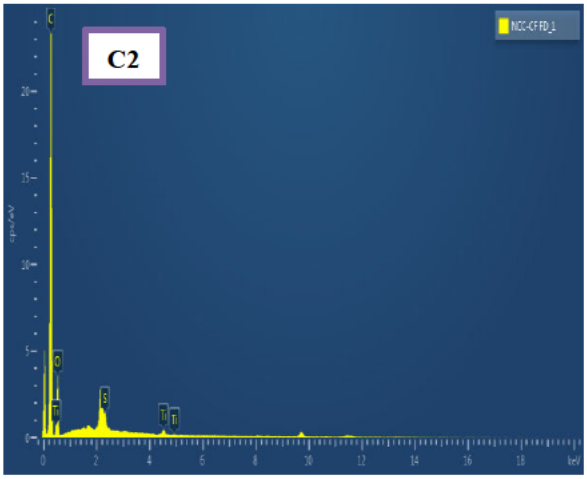


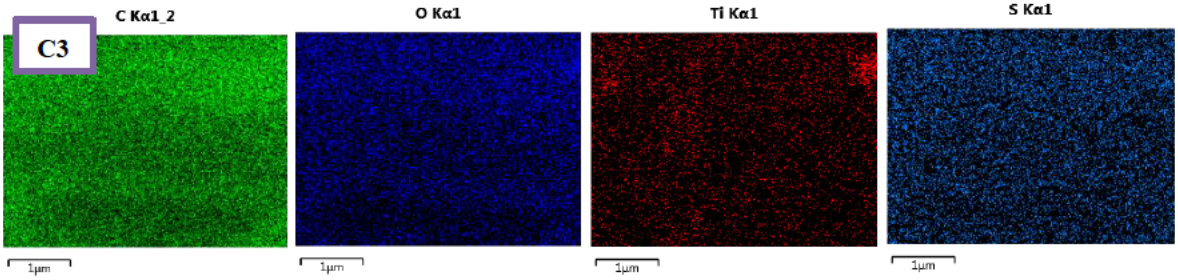

CEL-CF_1
B1
5µm


B2
CEL-CF_1


B3
C Kα1_2
O Kα1
Ti Kα1
5µm
5µm
5µm


NCC-CF FD_1
C1
1µm


C2
NCC-CF FD_1


C3
C Kα1_2
O Kα1
Ti Kα1
S Kα1
1µm
1µm
1µm
1µm

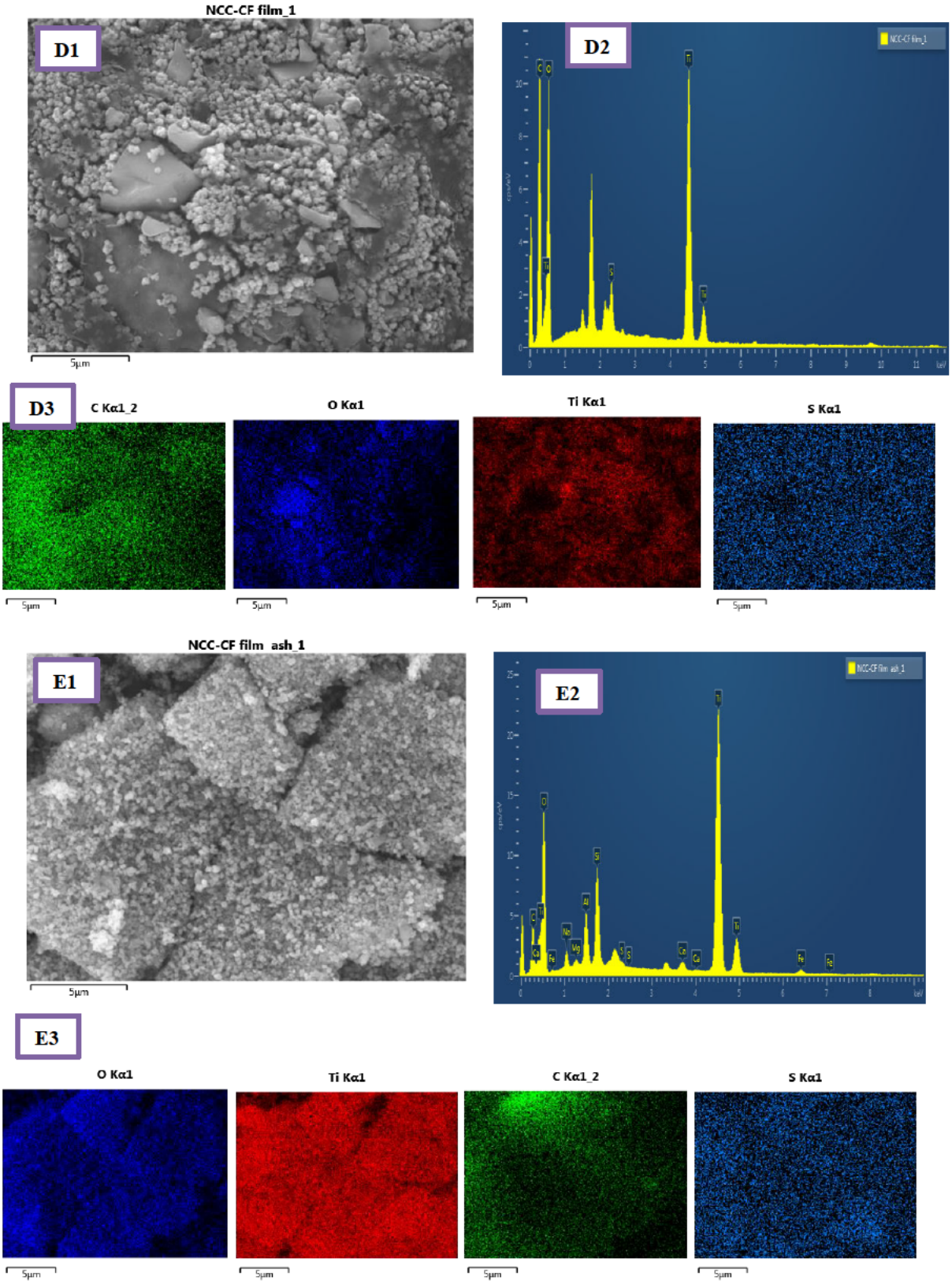


Fig. S3.2: FEGSEM micrographs, EDX spectra and mapping of the constituent elements of DCF (A1-A3), the obtained cellulose (B1-B3), NCC-DCF freeze-dried (C1-C3), NCC-DCF film (D1-D3) and NCC-DCF ash (E1-E3).

Table S3.1. Elemental compositions of: DCF, Cellulose-DCF and NCC-DCF (freeze-dried (FD), film and ash) from EDX

Element	DCF	Cellulose-DCF	NCC-DCF FD	NCC-DCF Film	NCC-DCF Ash
C (wt%)	68.50	60.09	77.40	40.88	18.29
O (wt%)	31.37	37.39	21.39	42.44	45.90
Ti (wt%)	0.13	2.52	0.43	15.43	26.44
S (wt%)	-	-	0.78	1.25	0.18
Others	-	-	-	-	9.19

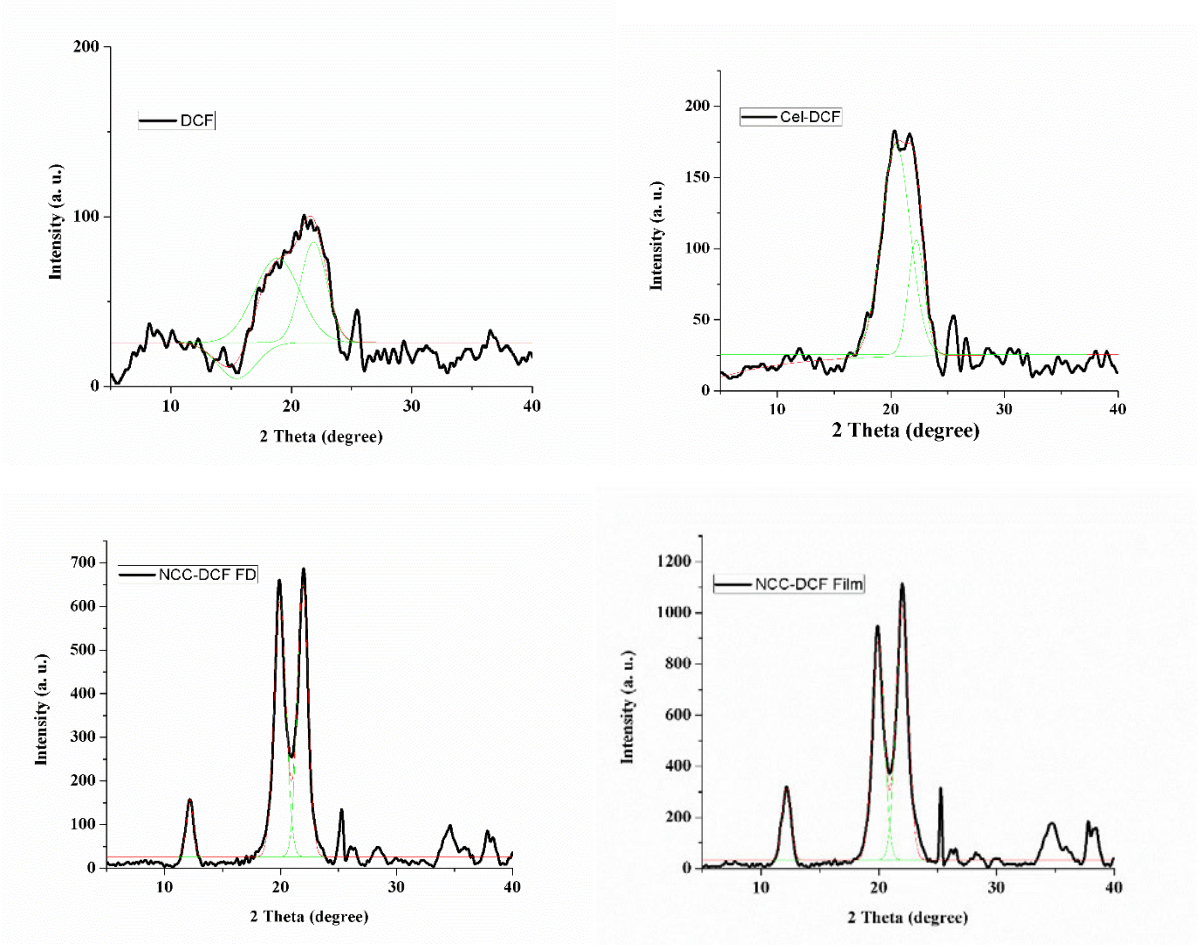


Fig. S3.3: Gaussian fit of the X-ray diffractograms of DCF, the obtained cellulose (Cel-DCF), NCC-DCF freeze-dried (NCC-DCF FD) and film (NCC-DCF Film).

Calculation of t-test to determine the significance difference between the mean fibre widths of DCF and Cel-DCF

	Mean (χ) nm	Standard Dev.(σ) nm	Population (n)	Degree of freedom ($n_{Cel\text{-}DCF} + n_{DCF} - 2$)	Critical value
DCF	23.78	1.74	10	18	2.101
Cel-DCF	26.20	2.39	10		

$$t_{N-2} = \frac{\aleph_{Cel-DCF} - \aleph_{DCF}}{\sqrt{\frac{(n_{Cel-DCF}-1)\sigma^2_{Cel-DCF} + (n_{DCF}-1)\sigma^2_{DCF})}{n_{Cel-DCF} + n_{DCF} - 2}} \sqrt{(\frac{1}{n_{Cel-DCF}} + \frac{1}{n_{DCF}})}}$$

The calculated value of t_{N-2} = 2.589 was greater than critical value (2.101) at 95 % confidence level and degree of freedom 18 for a two-tailed test. Therefore, the difference was significant.

Standard error of mean (SEM) determination

SEM = $\sigma/\sqrt{n}$, confidence interval (*CI*) = $\chi \pm 1.96\sigma/\sqrt{n}$

NCC average dimensions of 100 randomly selected nanocrystals were: length = 143.50 ± 37.43 nm, width 8.28 ± 3.26 nm and aspect ratio 17.44 ± 5.67

Length SEM_{NCC} = 3.74 nm, width SEM_{NCC} = 0.33 nm and Aspect ratio SEM_{NCC} = 0.57

Widths $SEM_{Cel\text{-}DCF}$ = 0.76 and SEM_{DCF} = 0.55

Appendix B: Supplementary Information to Chapter 4

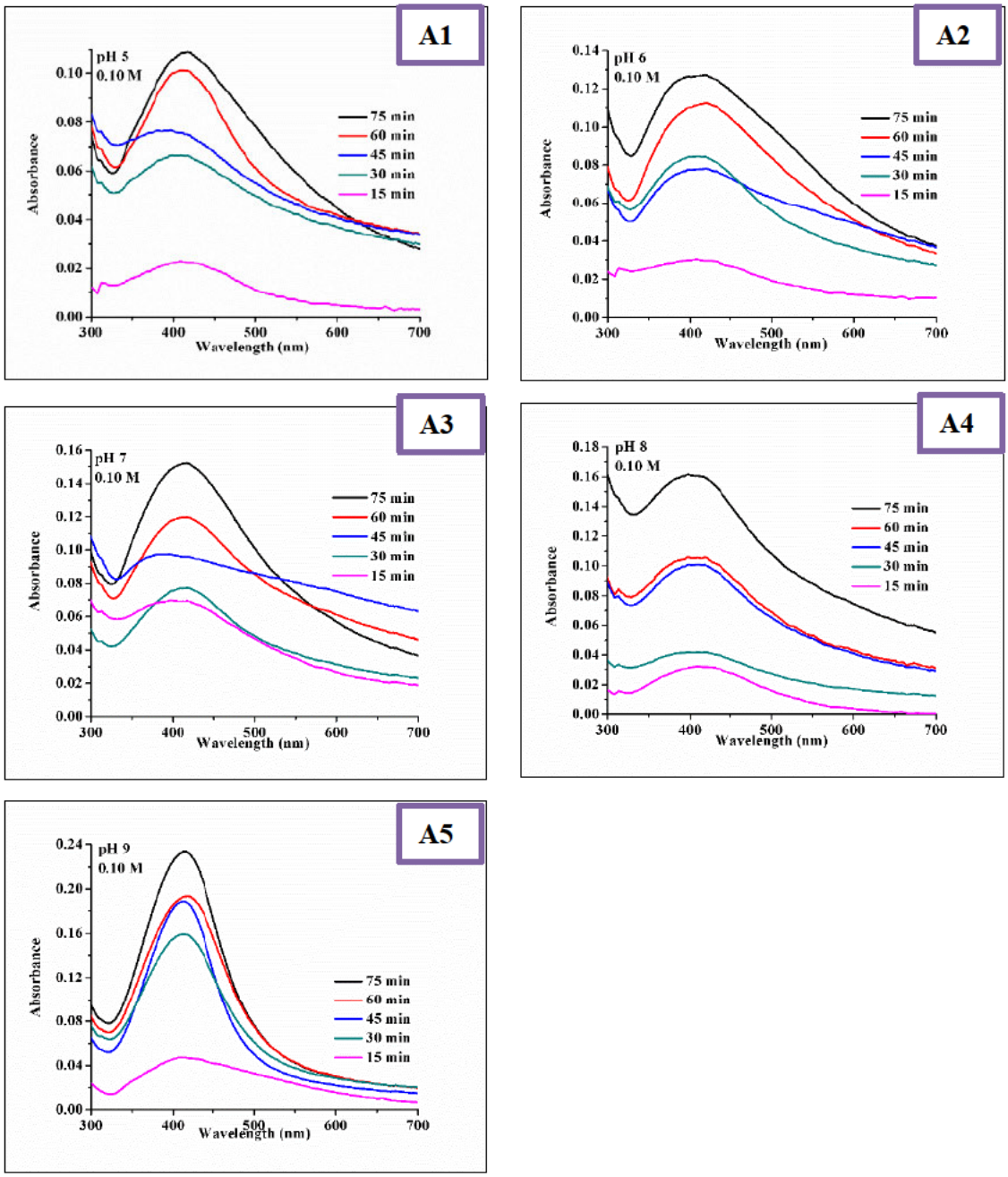


Fig. S4.1: Absorption spectra of synthesized AgNPs at different time intervals for pH 5 (B1), pH 6 (B2) pH 7 (B3), pH 8 (B4) and pH 9 (B5).

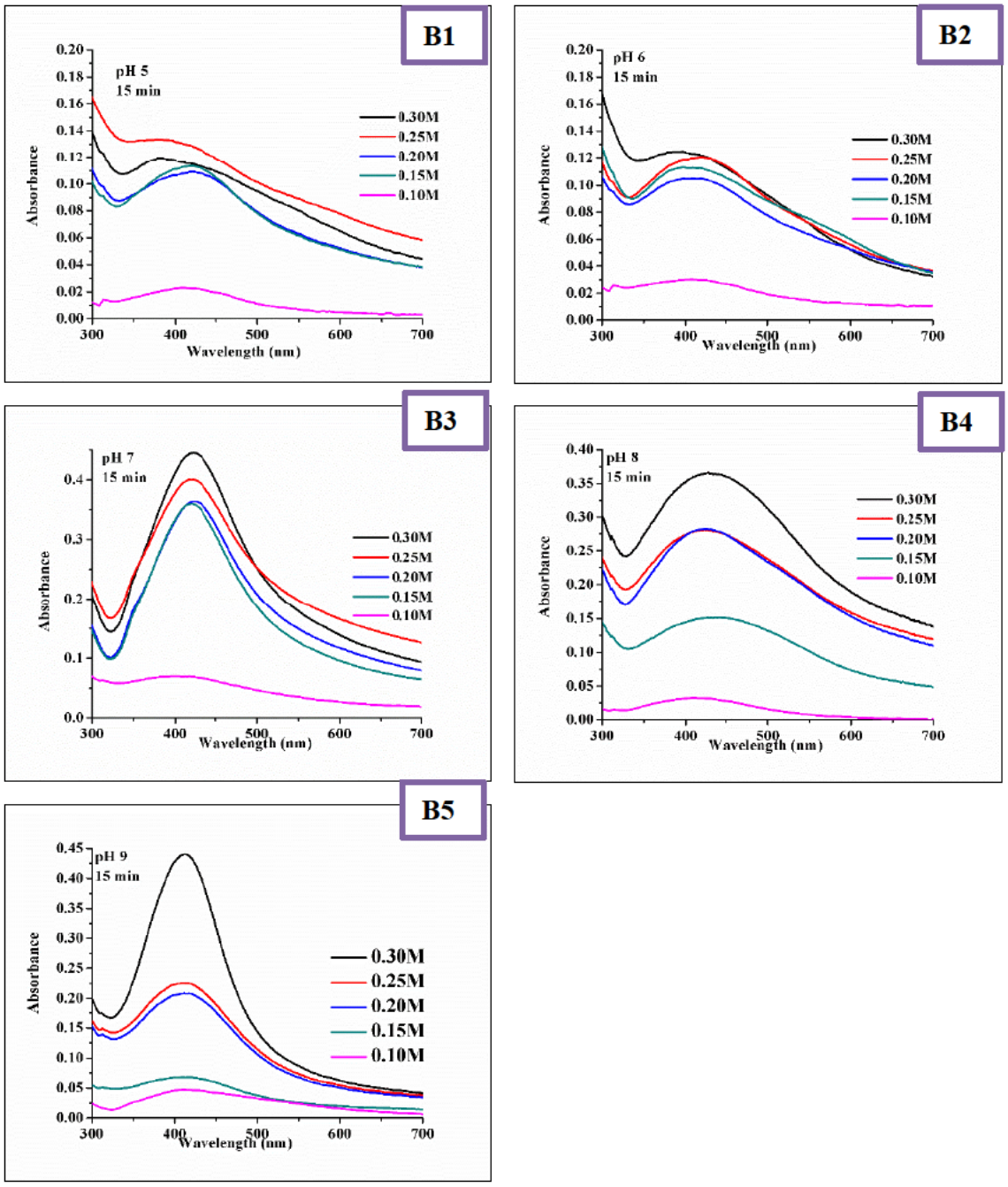


Fig. S4.2: Absorption spectra of synthesized AgNPs at different concentrations for pH 5 (B1), pH 6 (B2) pH 7 (B3), pH 8 (B4) and pH 9 (B5).

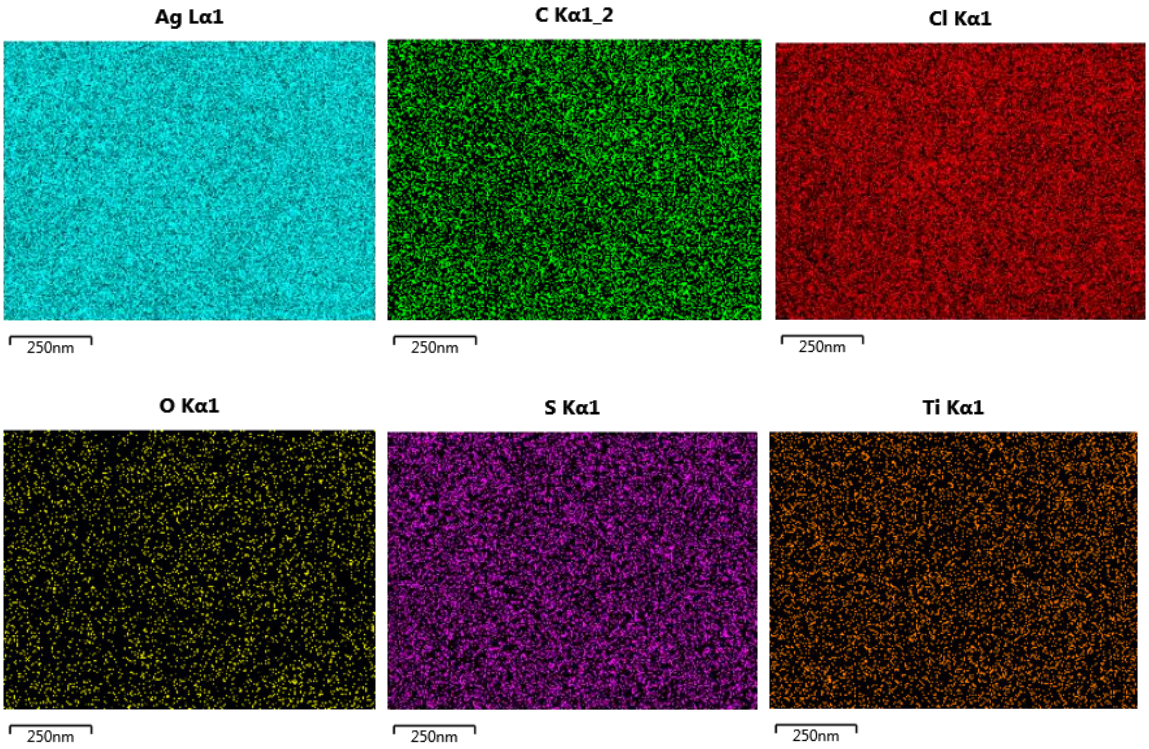


Fig. S4.3: EDX mapping of elements present in the synthesized dry AgNPs.

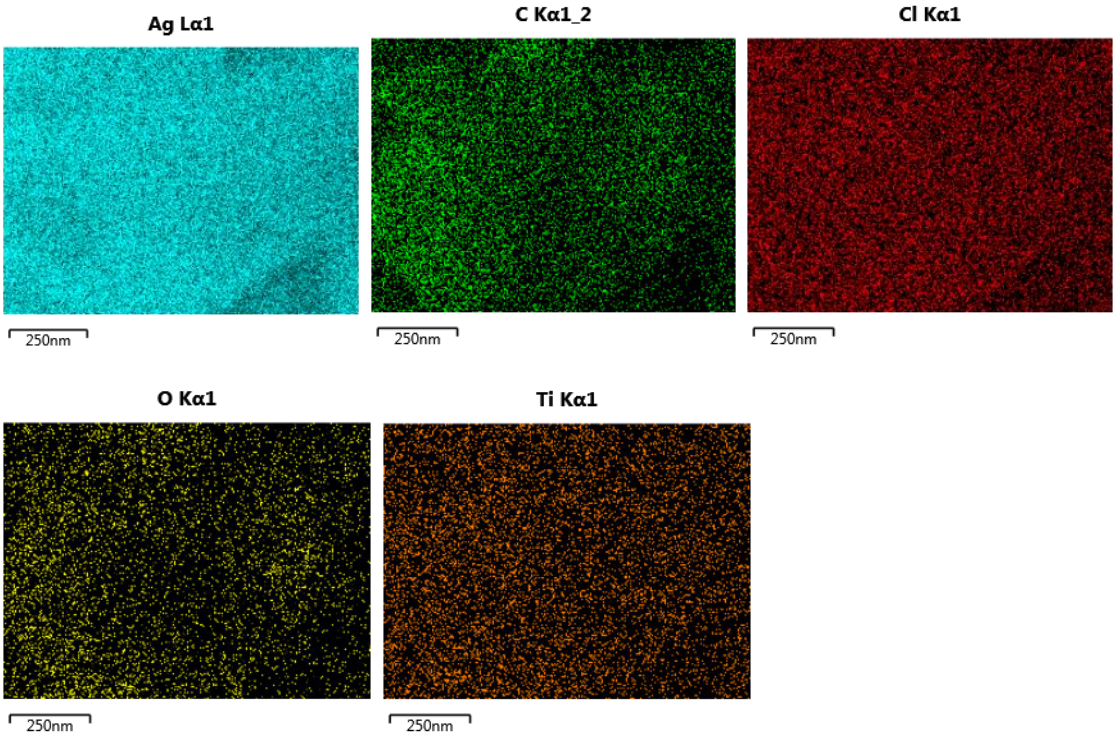


Fig. S4.4: EDX mapping of elements present in the calcined AgNPs.

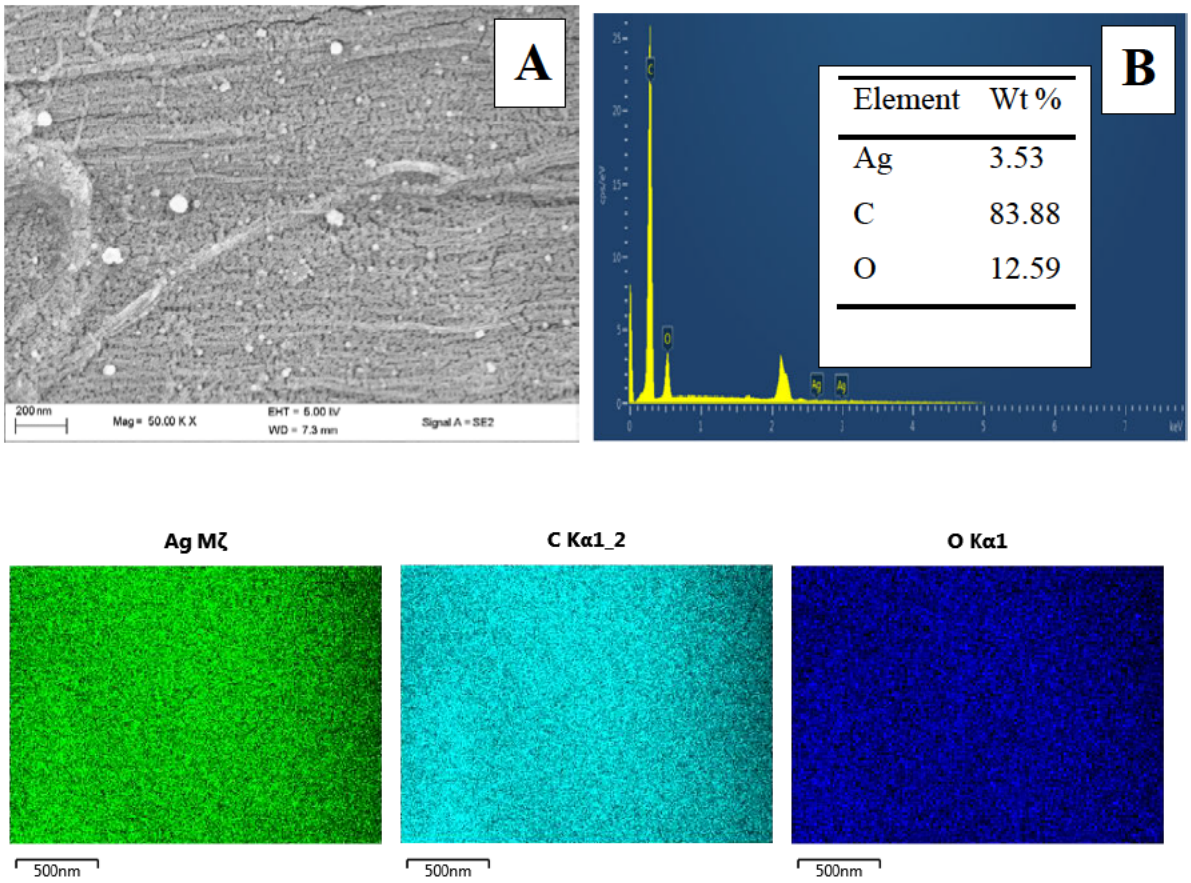


Fig. S4.5: SEM micrograph, EDX spectrum and mapping of the elements present in the AgNPs adsorbed on filter paper.

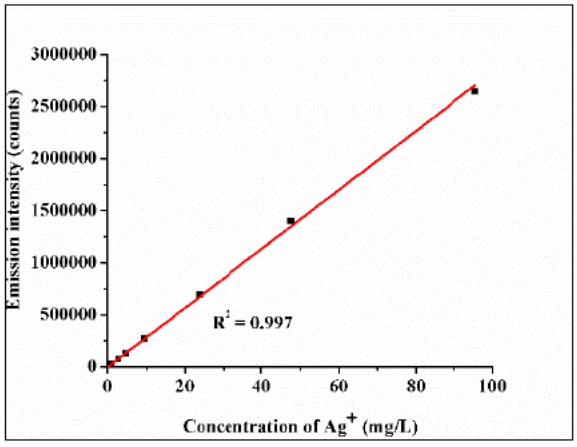


Fig. S4.6: ICP OES calibration for the quantification of AgNPs after digestion.

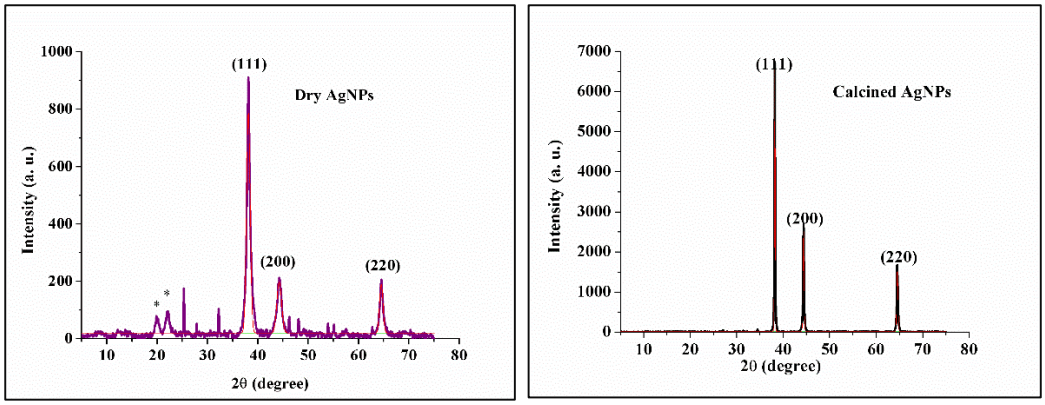


Fig. S4.7: Gaussian fits of XRD diffractograms of dry and calcined AgNPs

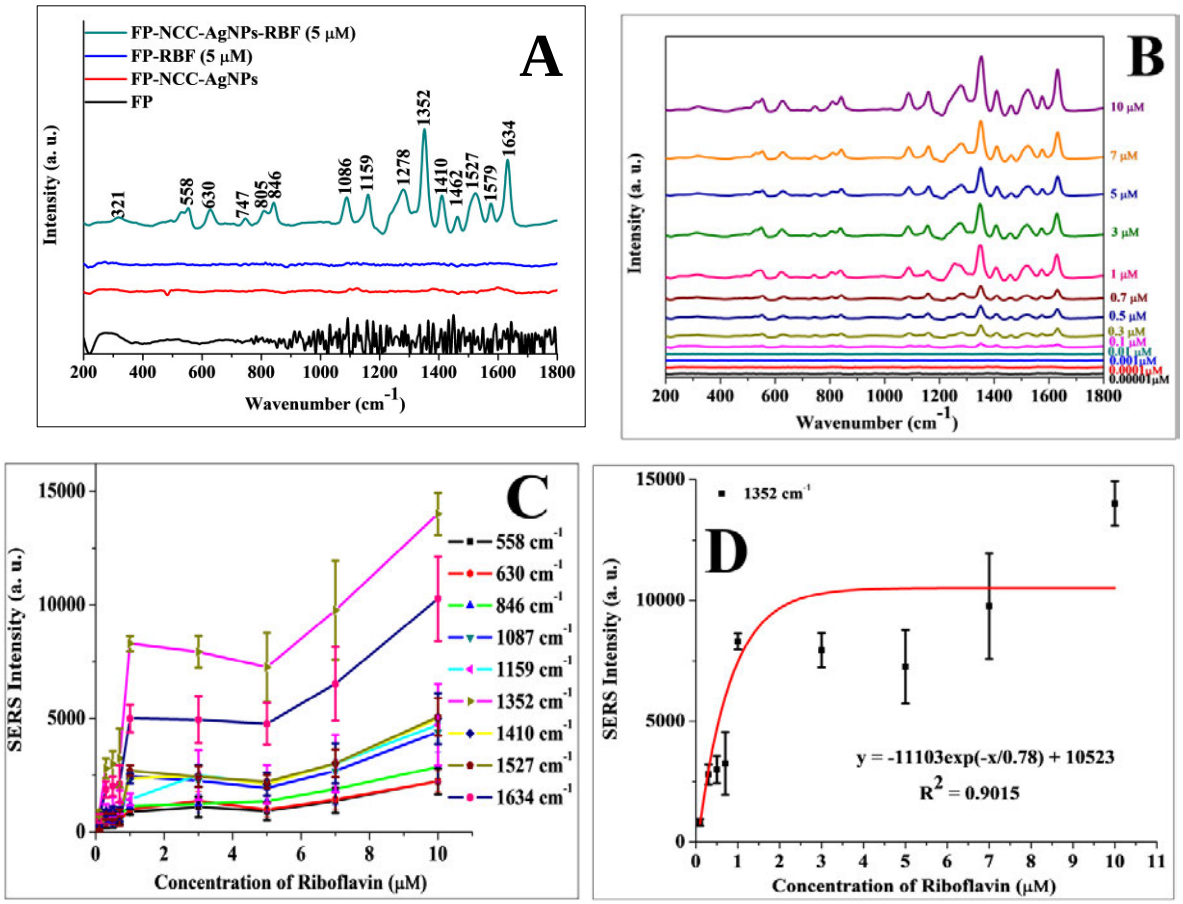


Fig. S4.8: Raman spectra of FP, FP-NCC-AgNPs, FP-riboflavin (RBF) and SERS spectrum of 5 µM RBF (A), SERS spectra of RBF in concentration range 10 -0.00001 µM on filter paper (B), plots of peaks intensities against concentration (C) and Calibration plot of 1352 cm^{-1}peak intensity against concentration (D).

Appendix C: Supplementary Information to Chapter 5

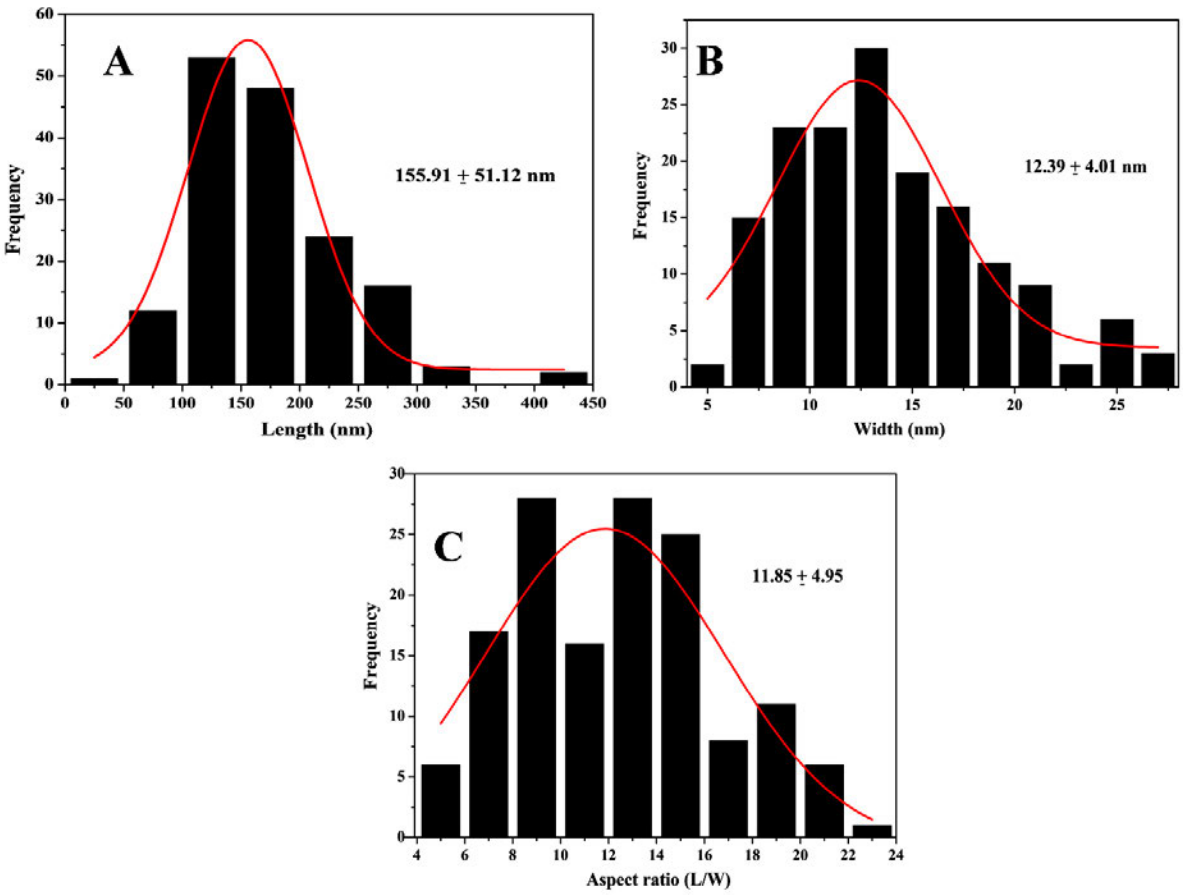


Fig. S5.1: Length (A), width (B) and aspect ratio distributions of isolated NCC from filter paper.

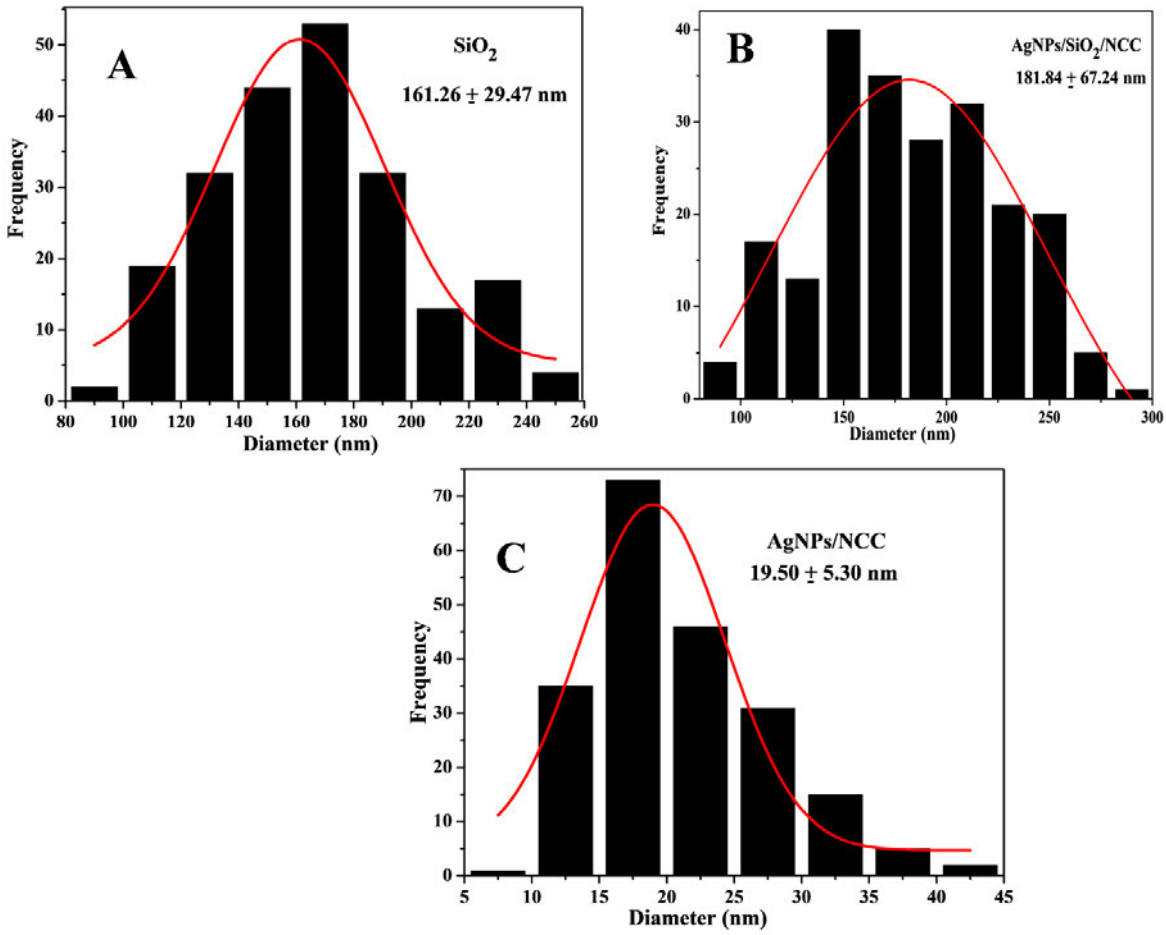


Fig. S5.2: Size distributions of: SiO_2 (A), AgNPs/SiO_2/NCC (B) and AgNPs/NCC (C).

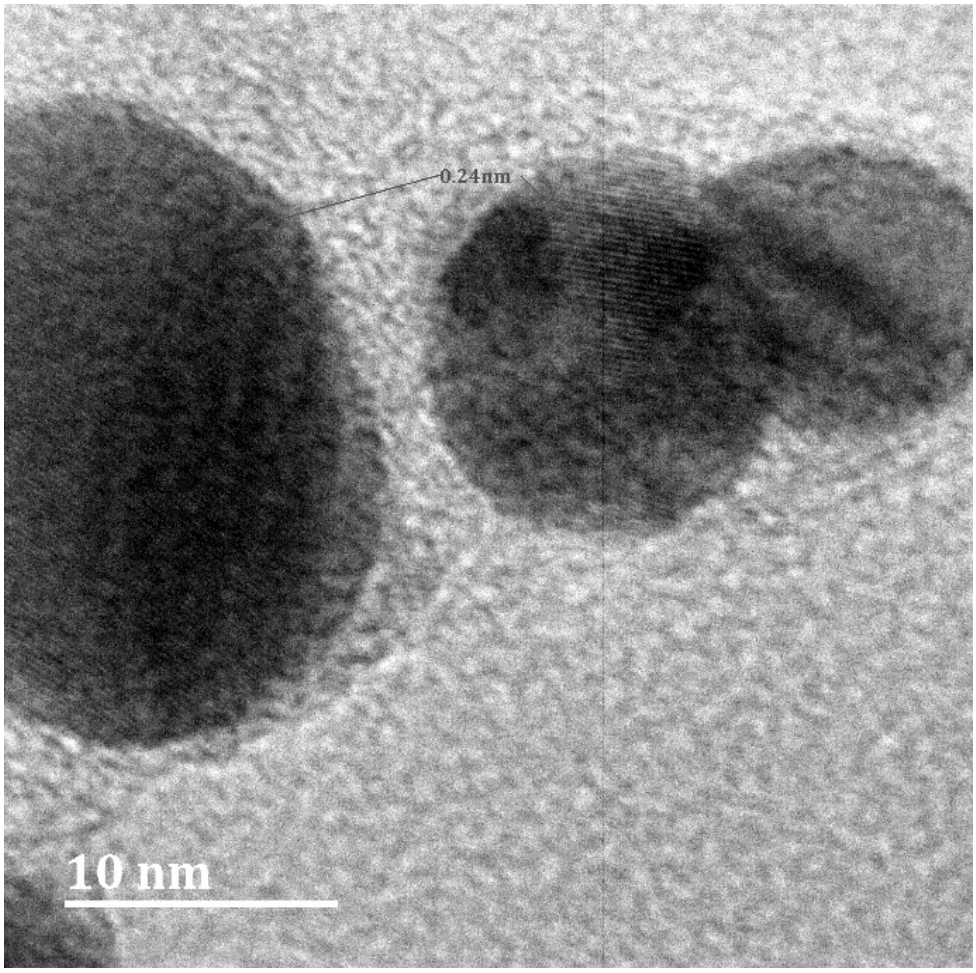


Fig. S5.3: Representative HRTEM micrograph of the AgNPs/NCC showing lattice fringes.

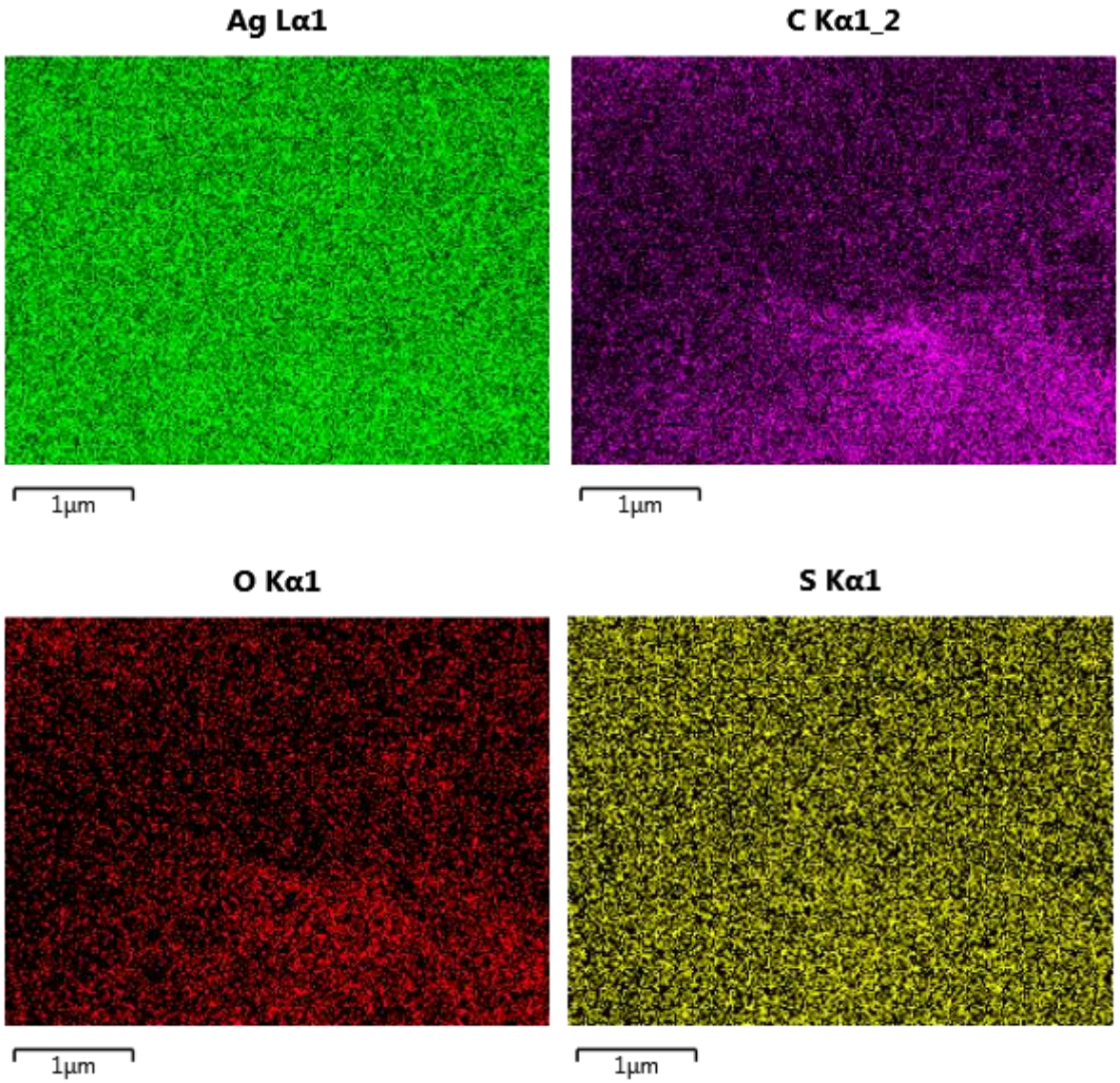


Fig. S5.4: EDX mapping of elements present in the AgNPs/NCC composite.

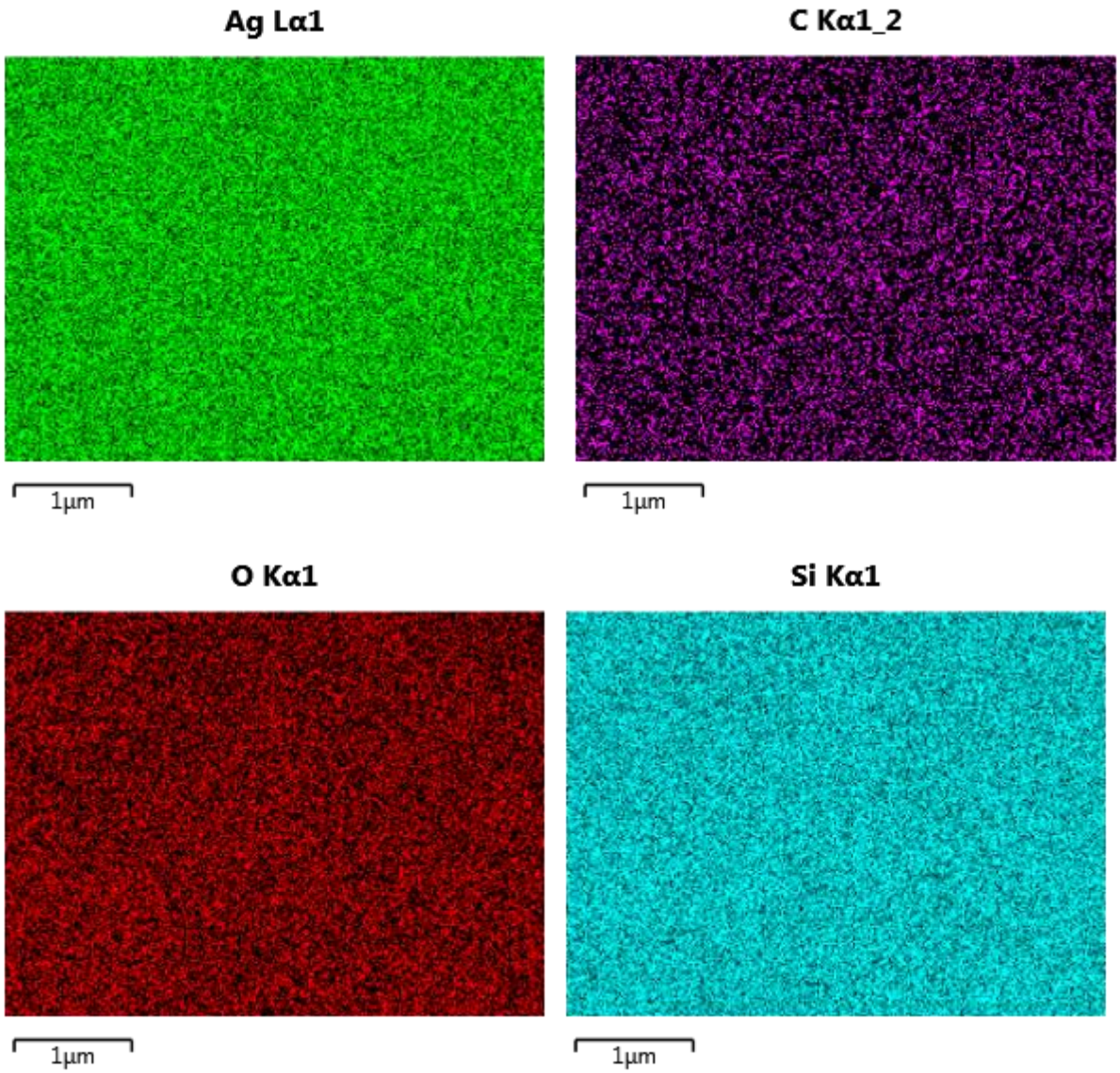


Fig. S5.5: EDX mapping of elements present in AgNPs/SiO_2/NCC composite.

Table S5.1. A representative weight percent of the constituent elements in the nanocomposites

	Wt%	
Element	**AgNPs/NCC**	**AgNPs/NCC/SiO_2**
Ag	72.81	65.05
C	20.53	18.56
O	6.08	12.71
Si	-	3.68
S	0.58	-

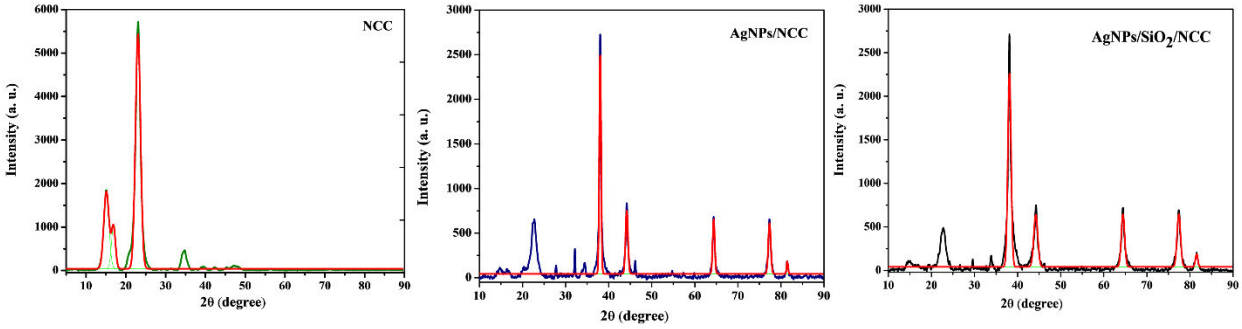


Fig. S5.6: Gaussian fits of XRD diffractograms of NCC, AgNPs/NCC and AgNPs/SiO_2/NCC.

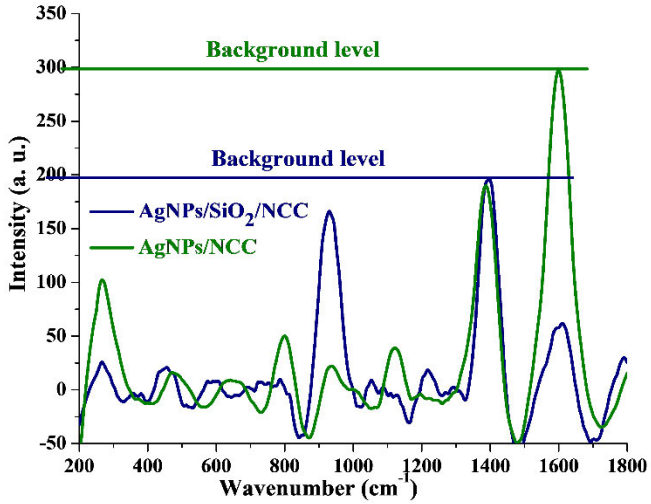


Fig. S5.7: Raman spectra of neat nanocomposites indicating the background intensity levels.

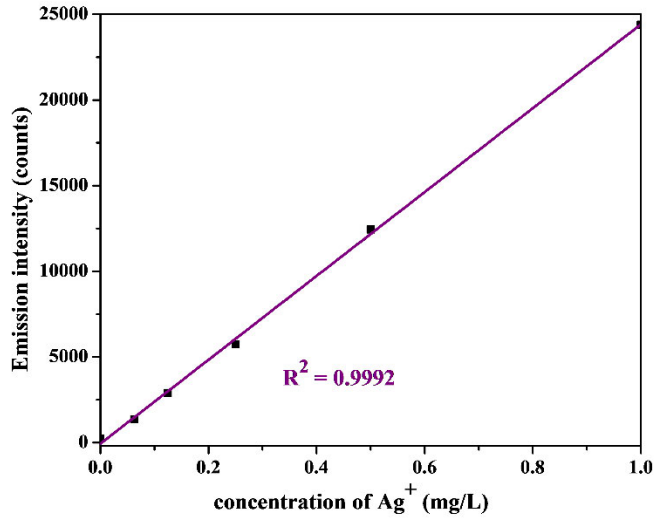


Fig. S5.8: ICP OES calibration for quantification of AgNPs after digestion.